CHEMICAL REVIEWS

Review

Cite This: *Chem. Rev.* XXXX, XXX, XXX–XXX

pubs.acs.org/CR

Nanocarbons for Biology and Medicine: Sensing, Imaging, and Drug Delivery

Nishtha Panwar,[†,#] Alana Mauluidy Soehartono,[†,#] Kok Ken Chan,[†] Shuwen Zeng,[†,‡] Gaixia Xu,[*,§] Junle Qu,[§] Philippe Coquet,[‡,∥] Ken-Tye Yong,[*,†] and Xiaoyuan Chen[*,⊥]

[†]School of Electrical and Electronic Engineering, Nanyang Technological University, Singapore 639798, Singapore

[‡]CINTRA CNRS/NTU/THALES, UMI 3288, Research Techno Plaza, 50 Nanyang Drive, Border X Block, Singapore 637553, Singapore

[§]Key Laboratory of Optoelectronics Devices and Systems of Ministry of Education/Guangdong Province, College of Optoelectronic Engineering, Shenzhen University, Shenzhen 518060, P. R. China

[∥]Institut d'Electronique, de Microélectronique et de Nanotechnologie (IEMN), CNRS UMR 8520—Université de Lille, 59650 Villeneuve d'Ascq, France

[⊥]Laboratory of Molecular Imaging and Nanomedicine, National Institute of Biomedical Imaging and Bioengineering, National Institutes of Health, Bethesda, Maryland 20892, United States

ABSTRACT: Nanocarbons with different dimensions (e.g., 0D fullerenes and carbon nanodots, 1D carbon nanotubes and graphene nanoribbons, 2D graphene and graphene oxides, and 3D nanodiamonds) have attracted enormous interest for applications ranging from electronics, optoelectronics, and photovoltaics to sensing, bioimaging, and therapeutics due to their unique physical and chemical properties. Among them, nanocarbon-based theranostics (i.e., therapeutics and diagnostics) is one of the most intensively studied applications, as these nanocarbon materials serve as excellent biosensors, versatile drug/gene carriers for specific targeting in vivo, effective photothermal nanoagents for cancer therapy, and promising fluorescent nanolabels for cell and tissue imaging. This review provides a systematic overview of the latest theranostic applications of nanocarbon materials with a comprehensive comparison of the characteristics of different nanocarbon materials and their influences on theranostic applications. We first introduce the different carbon allotropes that can be used for theranostic applications with their respective preparation and surface functionalization approaches as well as their physical and chemical properties. Theranostic applications are described separately for both in vitro and in vivo systems by highlighting the protocols and the studied biosystems, followed by the toxicity and biodegradability implications. Finally, this review outlines the design considerations for nanocarbon materials as the key unifying themes that will serve as a foundational first principle for researchers to study, investigate, and generate effective, biocompatible, and nontoxic nanocarbon materials-based models for cancer theranostics applications. Finally, we summarize the review with an outlook on the challenges and novel theranostic protocols using nanocarbon materials for hard-to-treat cancers and other diseases. This review intends to present a comprehensive guideline for researchers in nanotechnology and biomedicine on the selection strategy of nanocarbon materials according to their specific requirements.

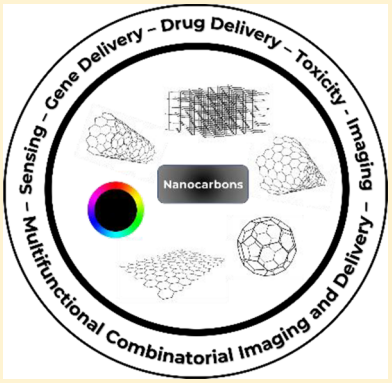

CONTENTS

Received: February 15, 2019

DOI: 10.1021/acs.chemrev.9b00099
Chem. Rev. XXXX, XXX, XXX–XXX

1. INTRODUCTION AND BACKGROUND

1.1. Introduction to Nanocarbon Materials

Nanotechnology plays a key role in scientific innovations of biomedical research.[1−8] The physical and chemical properties of nanomaterials are unique and differ from their bulk counterparts due to their ultrasmall size that ranges from 1 to 100 nm.[9−14] As typical examples, the light-emitting properties of semiconductor quantum dots (QDs) have been widely used for in vitro and in vivo imaging,[15−18] while the strong optical absorption peaks of metallic nanoparticles are very sensitive to the surrounding medium and thus enable colorimetric detection of biomolecules.[19−23] Over the past few years, nanocarbon materials have emerged as promising alternatives to other nanomaterials for various biological applications (e.g., sensing, imaging, and drug delivery) owing to their low intrinsic toxicity, low cost for large-scale production, and versatile surface functionalization.[24−26] In addition, carbon is one of the most abundant elements on earth. Allotropes of carbon at the nanoscale include 0D fullerenes and carbon nanodots, 1D carbon nanotubes/nanohorns and graphene nanoribbons, 2D graphene and graphene oxides, and 3D nanodiamonds. Among all these allotropes, graphene is the most recently discovered in 2004 by Andre Geim and Kostya Novoselov.[27−30]

One persistent challenge with many nanocarbon materials is that they are less well-defined than competing materials in terms of their physical and chemical properties. They are not only less well-defined than molecular species like organic dyes but also less well-defined than QDs, noble metal nanoparticles, and similar nanostructures with potential in biomedical applications. This creates uncertainty in the understanding of their underlying physical and chemical phenomena that define the state of their surfaces, the means by which their surfaces can be functionalized, and mechanisms of their photoluminescence and other properties. Thus, it is important to delineate the characterization methods and understand the physical properties and surface chemistry of nanocarbon materials for seeking regulatory approval of their use in various applications.

Furthermore, the tunable optical and electronic properties of nanocarbon materials, their simple synthesis techniques, and their versatile functionalization compatibility with various ligands and biomolecules, make them immensely useful for applications in biosensing, bioimaging, and drug delivery, both in vitro and in vivo. While such properties cast them as favorable candidates for nanomedicine, the toxicity effects of different nanocarbon materials, and their biodistribution in various tissues and organs must be carefully studied and analyzed before we can predict their success in clinical therapy. For this, a careful and detailed introspection on the factors that affect the intrinsic toxic mechanisms is necessary.

Finally, given that a large number of varying chemical forms constitute the nanocarbon family, delineation of key unifying themes that could serve as systematic design considerations for the synthesis and modifications of nanocarbon materials would be an essentially sourceful toolkit for the scientific community and enable them in designing distinct and explicit strategies for effective use of each of these nanocarbon materials for theranostic applications.

Thus, this review provides a systematical overview of the latest theranostic applications of nanocarbon materials with comprehensive comparison of the characteristics of different

DOI: 10.1021/acs.chemrev.9b00099
Chem. Rev. XXXX, XXX, XXX−XXX

carbon nanomaterials and how these peculiar properties along with the pharmacokinetic and toxicological effects influence their theranostic applications. This review, as it encompasses the research highlights on both in vitro and in vivo sensing, imaging, and drug delivery systems based on various nanocarbon materials, aims to serve as a guideline for researchers to choose and design most efficient functional toolkits for cancer theranostics applications.

1.2. Relationship of Nanocarbon Physics, Properties, and Applications

The two-dimensional atomic thin nanosheet (~0.34 nm) has been viewed as the fundamental building block of nanocarbon materials with sp^2 hybridization like fullerenes (graphene curled up into a sphere with pentagons in the structure) and carbon nanotubes (CNT; single or multiple layer graphene folded into seamless cylinders).[31,32] Since its first successful isolation from the bulk graphite through mechanical exfoliation using Scotch tape, many superior properties of graphene (e.g., zero bandgap with high electrical conductivity and zero effective mass at the Dirac point) have been explored for multidisciplinary research not only in the fields of electronics and optoelectronics but also in biology and medicine.[33−36] For instance, the high charge carrier mobility of graphene (10^6 cm^2/Vs) makes it an attractive enhanced sensing substrate for optical biosensors based on surface plasmon resonance (SPR).[5,37−40] It has been demonstrated that the charge distribution at the graphene-metal interface is dependent on (1) the electron transfer between the metal and the graphene levels and (2) metal−graphene chemical interaction. The charge transfer contribution can be modeled by a plane capacitor model, which yields a simple relation between $N(d)$ and $\Delta E_F(d)$ as[41]

$$N = \pm D_0 \frac{\Delta E_F^2}{2} \quad (1)$$

where $\Delta E_F(d)$ represents the Fermi level shift and $N(d)$ is the number of electrons (per unit cell) transferred from graphene to the metal.

More importantly, graphene has an exceptionally high surface area (up to 2630 m^2/g) with every single carbon atom exposed at the surface. This facilitates highly efficient molecular functionalization in comparison to other carbon nanomaterials. On the basis of this specific structural property, graphene and graphene oxide (GO) nanosheets have been engineered as sensitive signal tags for detection of biomolecules and efficient nanocarriers for targeted imaging/drug delivery.[42−44]

Recently, highly sensitive fluorescence-quenching biosensors with graphene and GO as effective electron/energy acceptors have been demonstrated.[45,46] They were used for detecting biological and chemical samples like DNA, peptide, protein, and even heavy metal ions with low concentrations ranging from 1 nM to 1 pM. Besides high surface area for chemical reactions and molecular functionalizations, nanographene oxide (nGO) materials also exhibit two distinct advantages for biomedical applications: (i) narrow size distribution with good water solubility and biocompatibility and (ii) intrinsic near-infrared (NIR) photoluminescence with little interference of background fluorescence for cellular imaging. The first studies on employing nGOs for targeted bioimaging[47] and drug delivery[3] were reported by Dai and co-workers in 2008. nGOs with an ultrasmall size of 10−50 nm were obtained by multiple sonication steps of the as-made GO nanosheets (50−300 nm) synthesized through the well-known Hummers method.[48] The key step for their ultrahigh water solubility and biocompatibility is the pegylated functionalization of the nGOs by covalent attachment of amino groups in six-arm polyethylene glycol (PEG) to carboxylic groups on GO. Upon further conjugation with specific antibody (Rituxan anti-CD20), targeted cellular uptake of the nGO−PEG−Rituxan was observed by NIR imaging. Moreover, water insoluble anticancer drugs like SN38 and doxorubicin (DOX) were successfully loaded onto the surface of PEG-modified GO by simple physisorption of π-stacking. The drug-loaded graphene nanocomplex showed high cytotoxicity to lymphoma (Raji) and colon cancer (HCT-116) cells.

Although graphene as the basic unit of nanocarbon materials offers numerous advantages for biomedical applications, other nanocarbon materials also exhibit some unique properties and serve as powerful complementary candidates of graphene-based nanomaterials. For example, the internal and external surfaces of CNTs can be used for loading different types of drugs.[49,50] The drugs with high stability during in vitro and in vivo transportation are preferably loaded on the external wall of CNTs, while less stable molecules can be conjugated to the internal cavity of CNTs in order to prolong their therapeutic effects. The high aspect ratio, needle-shaped CNTs allow higher drug loading along the tubes with little effect on their cell penetration process. The structure of carbon nanohorn (CNH) is similar to that of CNT.[51,52] In comparison to CNTs, the application of CNHs benefits more from their laser ablation synthesis methods where no metal catalysts are involved. After preparation, there is no additional purification step to use strong acids for eliminating metal particle or shortening the long fibers. CNHs are usually produced with a high yield of 75% and high purity of 95%.[51] More importantly, their graphitic structure and property are preserved perfectly without any damage by acid treatment.

Different from these one- or two-dimensional carbon nanomaterials, zero-dimensional fullerenes with a spherical and empty cage configuration show a particular advantage for diagnostic imaging applications.[53,54] During their synthesis, metal ions including scandium, yttrium, lanthanum, and gadolinium can be encapsulated into the hollow core carbon cage to form the metal endohedral fullerenes. Inside the endohedral metallofullerenes, electrons are transferred from the metal atoms to the fullerene cages and lead to the off-center position of the metal ions. This novel property is used for enhanced magnetic resonance imaging (MRI) for the diagnosis of diseases like cancer, atherosclerosis, and inflammatory arthritis.[55−58]

Next, three-dimensional nanodiamonds (NDs) can emit bright fluorescence by their intrinsic nitrogen vacancy (NV) center defects and can be easily functionalized with various biomolecules after the ozone purification process with a large number of carboxylic groups on their surface.[59,60] With such optical property and excellent biocompatibility, they have become potential cellular fluorescence markers for the tracking of neuronal differentiation and regenerative capabilities of transplanted stem cells.[61,62] However, their high-pressure, high-temperature preparation procedure and the following separation process are expensive for large-scale production.

The more recently discovered carbon-based nanodots,[63−66] especially graphene quantum dots (GQDs), can overcome this drawback of NDs and are emerging as promising alternatives of

DOI: 10.1021/acs.chemrev.9b00099
Chem. Rev. XXXX, XXX, XXX−XXX

NDs with a relatively low fabrication cost using synthesis methods like thermal plasma jet. The diameter of GQDs normally ranges from 1 to 10 nm with the number of graphene layers less than 10. Because of their small size, GQDs show stable photoluminescence as a result of quantum confinement effects.

1.3. Review Outline

In this review article, we give a detailed discussion on the in vitro and in vivo biomedical applications of different types of nanocarbon materials including graphene, GO, fullerene, CNTs/CNHs, NDs, graphene nanoribbons, and carbon dots (Figure 1). More specifically, we describe the advantages and challenges of using each of these nanomaterials for theranostic applications ranging from biosensing to targeted imaging and drug delivery. In section 2, we review the advances in detections of various "hard-to-identify" biological and chemical analytes (e.g., oligonucleotides, peptide, proteins, hormones, and heavy metal ions) with these nanocarbon materials as either signal amplification tags or enhanced sensing substrates in vitro. Section 2 also gives a systematic description on the use of nanocarbon materials as reporting labels for targeted in vitro imaging, engineering nanocarbon carriers for controlled release and delivery of drugs and genes, and further discusses multifunctional combinatorial imaging and delivery.

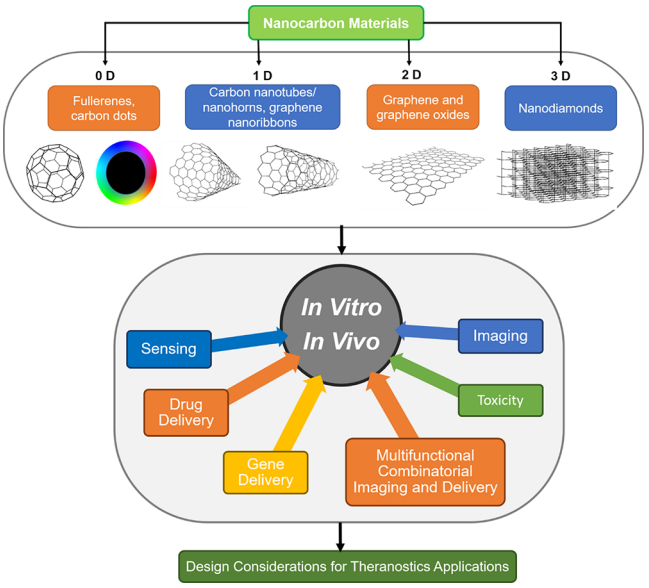

Figure 1. Overview of the review.

Section 3 describes the recent developments in developing nanocarbon platforms for in vivo sensing, imaging, and drug and gene delivery. Section 4 focuses on the in vitro and in vivo toxicological effects of using nanocarbon materials for theranostics applications. Lastly, we define the key unifying themes for defining the utilization protocols of nanocarbon materials for various theranostics applications in section 5. The review ends with a summary and future outlook on how these multifunctional nanocarbon materials can cast an important role in the future clinical translation of these nanoparticles into commercial therapeutic products.

This review aims to promote the awareness of current progress on nanocarbon materials in biology and medicine and to provide a guideline for rational designs of carbon-based theranostic nanoagents/devices. It also encourages the nanomaterials community to develop new clinical nanoapproaches for improving the early diagnosis and treatment of complex illnesses such as cancer, cardiovascular disorders, Alzheimer's disease, Parkinson's disease, and multiple sclerosis.

2. NANOCARBONS FOR IN VITRO APPLICATIONS: SENSING, IMAGING, AND DRUG DELIVERY

2.1. Nanocarbons for in Vitro Sensing

In general, biosensors based on nanocarbon materials can be classified according to its transduction mechanism: (i) electronic biosensors, commonly as field-effect transistors (FETs), (ii) electrochemical biosensors employing nanocarbon material-modified electrodes, and (iii) optical biosensors based on colorimetric detection, fluorescence quenching including Förster resonance energy transfer (FRET), chemiluminescence resonance energy transfer (CRET), and surface plasmon resonance (SPR).

Most notable of electronic sensors is transduction by potentiometric detection, implemented using FETs. FETs provide a route to the realization of miniaturized point-of-care diagnostic systems from the small footprint, fast response, and potential for integration with conventional wafer-scale semiconductor processes. In FETs, carbon materials typically function as the gate material, where a molecular binding event induces a change in the surface potential. Among the carbon nanomaterials, graphene and CNTs in particular have been widely used for FET biosensors due to their superior electronic properties (e.g., ambipolar field effect, high carrier mobility, and high electrical signal-to-noise ratio).[67−71] In the past few years, graphene has been demonstrated to possess properties conducive to attaining higher-performing FETs as compared to CNTs. The higher carrier mobility of graphene-based FET devices (200000 cm^2/Vs) compared to those of CNT-based FET devices (150000 cm^2/Vs)[72,73] promises a much higher resolution and faster response during detection. In contrast to CNTs, graphene provides more structural robustness. The two-dimensional nature of graphene allows for a larger surface area to be functionalized, yielding enhanced detection efficiency and selectivity of the targeted biomolecules.[46] In addition, graphene demonstrates more structural uniformity after synthesis, reducing negative consequences that could arise from structural variations. CNTs, whose performance is strongly dependent on diameter and chirality, are susceptible to greater performance variation attributed to a greater degree of structural variations and stability. Practically, the effective footprint of most graphene sheets limits its scaling. Researchers have concurrently attempted to address the wafer-scale integration of graphene for transistors by epitaxial growth,[74] solution-based methods to increase the sheet size,[75] graphene film transfer,[76] and laser scribing,[77] indicating the potential for low-cost, large-scale graphene-based FETs. Of graphene-based FET biosensors, reduced graphene oxide (rGO) is usually preferred due to its higher conductivity compared to GO and more versatile surface functionalization strategies over pristine graphene nanosheets (GS). More specifically, residual oxygen-containing groups on rGO surfaces can facilitate covalent bonding with amine and carboxyl groups typically present on protein surfaces in biomolecule immobilization. rGOs can be synthesized by a facile chemical reduction of exfoliated GOs with hydrazine. First reported by Boehm et al. in 1962, this method provides a route to a low-cost scaling strategy.[78] In 2014, Cai et al.

DOI: 10.1021/acs.chemrev.9b00099
Chem. Rev. XXXX, XXX, XXX−XXX

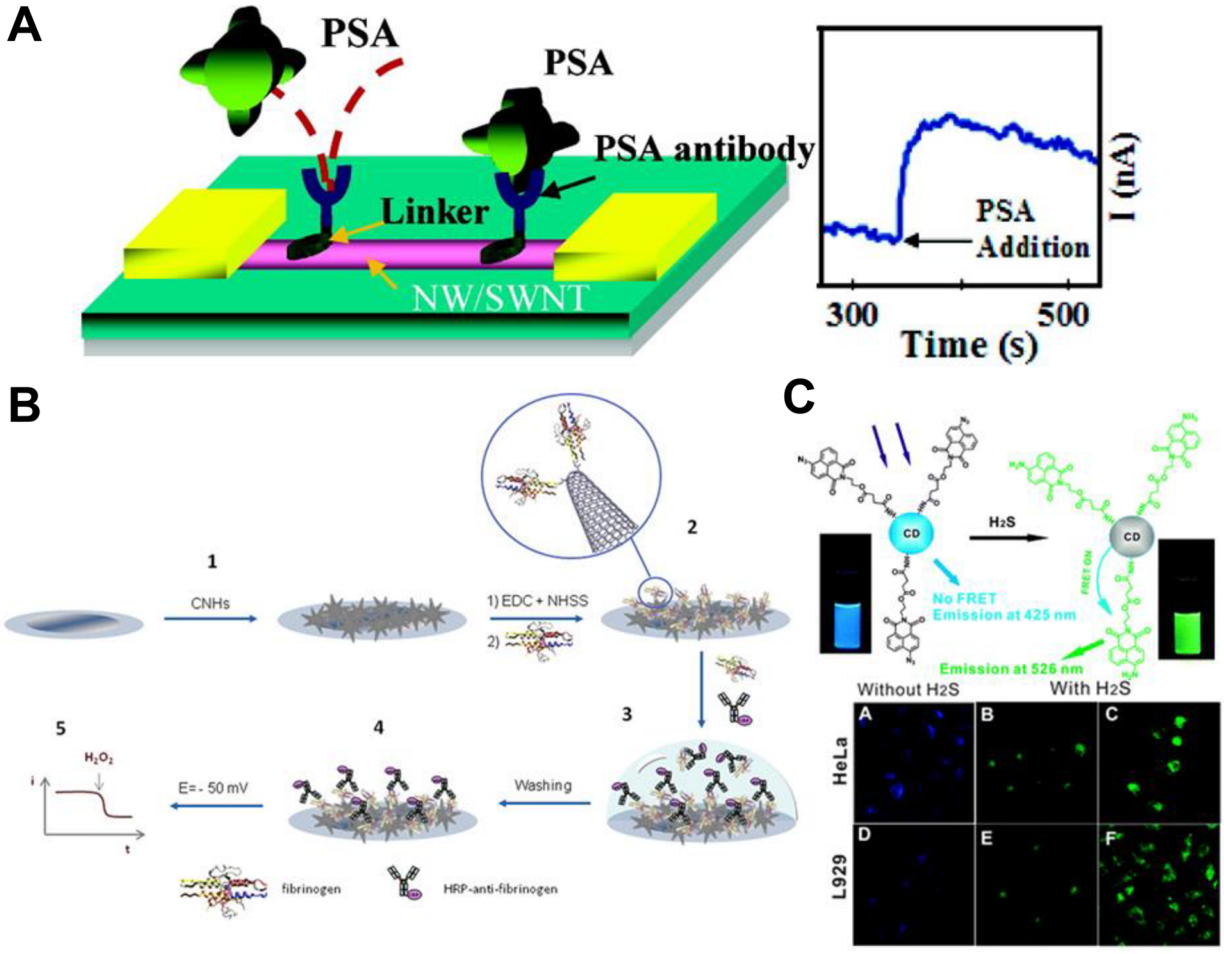

Figure 2. Representative images of carbon nanomaterial-based sensors for in vitro sensing. (A) Schematic of field-effect transistor-based sensing with rGO based on PNA−DNA hybridization achieving a detection limit of 100 fM. Reprinted with permission from ref 185. Copyright 2005 American Chemical Society. (B) Carbon nanohorns as an electrochemical sensor for detecting fibrinogen in human plasma serum and urine and measured by amperometry. Covalent immobilization with carboiimide chemistry is illustrated, along with an indirect competitive immunoassay using HRP-antifibrinogen, where free antibodies reacted to the immobilized analyte. Reprinted with permission from ref 80. Copyright 2014 American Chemical Society. (C) FRET-based ratiometric carbon-dot sensor to quantify hydrogen sulfide (H_2S) in aqueous media, serum, and in live cells with a detection limit of 10 nM. The sensor is reduced to an acceptor in the presence of H_2S, emitting at 526 nm. Fluorescence images of HeLa and L929 cells show the emissions before (A,D) and after H_2S treatment at 30 μM (B,E) and 100 μM (C,F).[81] Reprinted with permission from ref 81. Copyright 2013 Royal Society of Chemistry.

demonstrated an ultrasensitive rGO-based FET biosensor with a detection limit of 100 fM for 22-mer single-stranded DNA (ssDNA).[79] Peptide nucleic acid (PNA), covalently linked to rGO with 1-pyrenebutanoic acid succinimidyl ester, was used to capture the ssDNA target through PNA−DNA hybridization (Figure 2a). Although structurally similar to DNA, PNA consists of a neutral peptide backbone as opposed to the negative deoxyribose phosphate backbone of the former. The neutrality conferred by PNA eliminates electrostatic repulsions during strand hybridization to reduce background noise significantly. This, together with a good sequence-specific affinity of PNA, led to a noteworthy detection limit 1 order of magnitude lower than previously reported graphene-FET DNA biosensors based on DNA−DNA hybridization.

Electrochemical sensors, on the other hand, exploit the charge transfer rates intrinsic to each nanomaterial resulting from electrocatalytic activity.[25,82,83] Compared to conventional analytical techniques such as chromatography and time-of-flight measurements, electrochemistry provides a less time-consuming and cost-efficient alternative for analyzing biomolecules, suitable for deployment in applications such as neuroscience and pharmacology. Nanocarbon materials including CNHs, NDs, and fullerenes have been employed as scaffolds for various biological analytes (e.g., proteins, hormones, glucose, and even bacteria) based on their unique, structure-based mechanical, electrical, and chemical properties.[84−88] For instance, CNHs, known to have more structural defects than CNTs,[51,89] can provide a higher electron transfer efficiency at the CNH-modified electrode and thus a more superior electrochemical detection performance as compared to CNT-based electrochemical biosensors. In addition, the holes on the tips of CNHs can be easily opened under mild oxidation process like H_2O_2 treatment, leading to a much larger effective surface area (from 300 m^2/g to 1400 m^2/g) for functionalization and biomolecular reactions.

Nanocarbon materials have similarly played an important role in the development of next-generation optical biosensors for elemental and biomarker analysis.[5,39,60,90−93] For in vitro studies, the ability to resolve on the single cell level is essential to study the fundamental cellular mechanisms, such as cellular

DOI: 10.1021/acs.chemrev.9b00099
Chem. Rev. XXXX, XXX, XXX−XXX

Table 1. Summary of Carbon-Based Nanomaterials for in Vitro Sensing

target analyte	sensing mechanism	material type	functional group/molecules	material scale	limit of detection	ref
DNA and Oligonucleotides						
12-mer oligonucleotides	FETs	GS (CVD)	probe ssDNA	monolayer	10 pM	101
15-mer oligonucleotides	fluorescence quenching	GO	FAM-labeled MB	monolayer	1 nM	102
	fluorescence quenching	GO	dye-labeled MB	monolayer	1 nM	103
17-mer oligonucleotides	fluorescence quenching	GO (postmixing)	(=O) or (−OH)	monolayer	100 pM	104
18-mer oligonucleotides	FRET	GO	Au NPs labeled ssDNA	monolayer	200 nM	105
	LRET	SWCNH/GO	citrate-functionalized upconversion nanoparticles labeled ssDNA	30−40 nm	0.28 nm	106
20-mer oligonucleotides	AFM and Raman	GNR	(−COOH)	400 nm	<30 μM	107
21-mer oligonucleotides	lateral flow	MWCNT	DNA capture probe	L = 0.5−2 μm	40 pM	108
	fluorescence quenching	GQD	MWCNT and ssDNA probe	3−5 nm	4.2 nm	109
21-mer oligonucleotides (HCV-1)	rolling circle amplification fluorescence quenching	rGO	DP1 DNA probe	monolayer	0.8 pM	45
22-mer oligonucleotides	FETs	rGO	peptide nucleic acid	mono- and multilayer	100 fM	79
	colorimetric detection	GO	Au NPs and DNA probe	mono- and multilayer	8 nM	110
	electrochemical sensing	MWCNT	ssDNA probe	OD = 10−20 nm ID = 5−10 nm L = 0.5−200 nm		111
23-mer oligonucleotides (HIV-1 U5)	fluorescence quenching	GO	dye-labeled ssDNA	monolayer	1 nM	112
23-mer oligonucleotides	fluorescence quenching	AgNCs-GO	cytosine-rich cDNA	1.47 nm monolayer	1 nM	113
	fluorescence quenching	SWCNH	FAM-labeled ssDNA	100 nm	1 nM	114
24-mer oligonucleotides	electrochemical sensing	GO	ssDNA probe	mono- and multilayer	40 nm	115
	fluorescence quenching	GQD	MWCNT and ssDNA probe	3−5 nm	4.2 nm	109
30-mer oligonucleotides	colorimetric detection	GO	hemin and probe ssDNA	monolayer	0.5 nM	116
ssdna with 4−70 Bp	fluorescence quenching	GO	FAM-labeled ssDNA	mono- and multilayer	100 nM	117
polya with 10 Bp	fluorescence measurement	ND	peptide nucleic acid	20 nm	7 per ND	118
EGFR gene mutation (at Exon 19/21)	colorimetric detection	rGO	peptide nucleic acid	monolayer	3.75 nM	119
miRNA						
miRNA-24	electrochemical sensing	MWCNT	DNA capture probe	D = 10−20 nm L = 5−15 μm	1 pM	120
miRNA-7f	photoelectrochemical sensing	SWCNT	(−COOH)	D = 20 nm	34 fM	121
Prostate Cancer Biomarker						
miR-141	electrochemical sensing	rGO	MWCNT/anti RNA·DNA antibody	monolayer	10 fM	82
Protein immunoassay						
BSA	SPR detection	GO	(−COOH)	monolayer	100 pg/mL	122
CRP	CRET	rGO	anti-CRP	monolayer	0.93 ng/mL	123
cysteine	fluorescence quenching	GO	dye-labeled MB	monolayer	60 nM	103
	fluorescence quenching	GO	metallized ssDNA	monolayer	2 nM	124
	electrochemical sensing	GNR	Nafion	27 nm	25 nM	125
D-tryptophan	fluorescence quenching	GO	anthracene-labeled amylose	monolayer	134 nM	126

DOI: 10.1021/acs.chemrev.9b00099
Chem. Rev. XXXX, XXX, XXX−XXX

Table 1. continued

target analyte	sensing mechanism	material type	functional group/molecules	material scale	limit of detection	ref
Protein immunoassay						
L-tryptophan	fluorescence quenching	GO	anthracene-labeled amylose	monolayer	34 nM	126
	electrochemical sensing	SWCNH	pristine	100 nm	50 nM	84
L-tyrosine	electrochemical sensing	SWCNH	pristine	100 nm	400 nM	84
ferritin	optically detected magnetic resonance	ND	(−COO)	20 nm	8−15/ND	100
glutathione	fluorescence turn-on	GQD	nitrogen doped and Hg^{2+}	3.8 nm	87 nM	97
	FRET	CQD	amine group and Au NPs (12.8 nm)	2.5 nm	50 nM	127
bovine IgG	SPR detection	GO	Au NRs and capture antibody	mono- and multilayer	0.075 μg/mL	128
human IgE	FETs	GS	anti-IgE aptamer	monolayer	0.29 nM	129
human IgG	electrochemiluminescence	rGO	PDDA/CdSe QDs	monolayer	0.005 pg/mL	130
	FETs	rGO	anti-IgG/Au NPs	2−5 layer	2 ng/mL	131
	SPR detection	GO	Au NRs and capture antibody	mono- and bilayer	0.075 μg/mL	132
mouse IgG	SPR detection	GO	silver NPs and capture antibody	mono- and multilayer	0.15 μg/mL	133
concanavalin A	SPR detection	GO	phenoxy-derivatized dextran	mono- and multilayer	0.39 μg/mL	134
streptavidin	FETs	rGO	GrBP5-WT peptide	monolayer	50 ng/mL	135
transferrin	SPR detection	GO	Au NRs and capture antibody	mono- and multilayer	0.0375 μg/mL	136
Helicase						
SCV-Nsp13	fluorescence quenching	GO	(=O) or (−OH)	monolayer	0.625 nM	137
Restriction Endonucleases						
Pvuii	fluorescence quenching	GO	(=O) or (−OH)	monolayer	0.05 U/mL	138
Protease						
caspase-3	fluorescence quenching	GO	DEVD peptide and FAM-labeled lysine	monolayer	0.4 nM	139
MMP-2	fluorescence quenching	GO	streptavidin	monolayer	1 nM	140
	fluorescence quenching	GO	FITC-labeled peptide	monolayer	50 pM	141
thrombin	fluorescence quenching	GO	dye-labeled MB	monolayer	5 nM	103
	fluorescence quenching	GO	dye-labeled aptamer	monolayer	2 nM	112
	fluorescence quenching	GO	dye-labeled peptide	monolayer	2 nM	142
	fluorescence quenching	GO	streptavidin	monolayer	0.5 nM	140
	fluorescence quenching	SWCNH	dye-labeled thrombin aptamer	80 nm	100 nM	143
A-chymotrypsin	fluorescence quenching	polymer-coated GO	FITC-labeled peptide	monolayer	0.2 nM	144
Cytokine						
human GM−CSF	SPR detection	MWCNT	capture antibody	0.3−1.3 μm	0.1 ng/mL	145
Cancer biomarker						
Ca 15−3	electrochemical sensing	rGO	N-doped and capture antibody	mono- and multilayer	0.012 U/mL	146
CEA	electrochemical sensing	GO	HRP/nanogold and capture antibody	monolayer	0.01 ng/mL	147
	electrochemical sensing	GO	Fe_3O_4 NPs and capture antibody	monolayer	1 pg/mL	148
	electrochemical sensing	rGO	TB-labeled anti-CEA	mono- and multilayer	0.1 ng/mL	149
	electrochemical sensing	GS (CVD)	magnetic beads and capture antibody	monolayer	5 ng/mL	150

DOI: 10.1021/acs.chemrev.9b00099
Chem. Rev. XXXX, XXX, XXX−XXX

Table 1. continued

target analyte	sensing mechanism	material type	functional group/molecules	material scale	limit of detection	ref
Cancer biomarker						
	SPR detection	rGO	polydopamine and Au NPs	monolayer	500 pg/mL	151
cyclin A_2	fluorescence quenching	GO	(=O) or (−OH)	monolayer	0.5 nM	152
	electrochemical impedance	GO	porphyrin/hexapeptide	monolayer	1.02 pM	153
EGFR	FETs	rGO	APTES/SiO_2 NPs	mono- and multilayer	100 pM	154
Fib	electrochemical sensing	SWCNH	carboxylic group	120 nm	58 ng/mL	80
folate receptor	fluorescence quenching	GO	FAM-labeled ssDNA	monolayer	0.77 ng/mL	155
Her2	FETs	rGO	APTES/SiO_2 NPs	mono- and multilayer	1 pM	154
human telomerase	electrochemiluminescence	rGO	positively charged porphyrin (TAPP)	monolayer	10 cells/mL	156
Pdgf-Bb	electrochemical sensing	fullerene-C_{60}	aptamer and Au NPs	80−150 nm	0.6 pM	157
procalcitonin	electrochemical sensing	SWCNH	HPtC/HRP/thionine and capture antibody	30−70 nm	0.43 pg/mL	158
prostate-specific antigen	electrochemical sensing	rGO	thionine/HRP and capture antibody	monolayer	1 pg/mL	159
	electrochemical sensing	rGO	MNPs and capture antibody	monolayer	2 pg/mL	160
	electrochemical sensing	rGO	QDs and capture antibody	monolayer	3 pg/mL	161
	electrochemiluminescence	GO	chitosan/Au NRs	monolayer	8 pg/mL	162
	electrochemical sensing	rGO	PBSE/Co NPs and capture antibody	monolayer	0.01 ng/mL	163
	FETs	GS	capture antibody	45 ± 5 nm	0.4 fg/mL	164
	photoelectrochemical	rGO	pAb_2-AuNP-Gox and capture antibody	mono- and multilayer	3 pg/mL	165
PSA-ACT	FETs	rGO	capture antibody	monolayer	1.1 fM	166
P53 (S392)	electrochemical sensing	GO	HRP and capture antibody	mono- and multilayer	0.01 nM	167
SCC-Ag	electrochemical sensing	GO	HRP/nanogold and capture antibody	monolayer	1 pg/mL	168
α-fetoprotein	FRET	rGO	capture antibody	monolayer	0.013 nM	169
	electrochemical sensing	SWCNH	HRP/glucose oxidase and capture antibody	*D*: 100 nm	0.33 pg/mL	170
	electrochemical sensing	rGO	thionine and capture antibody	monolayer	5.77 pg/mL	171
	electrochemical sensing	GO	GoldMag NPs, HRP and capture antibody	monolayer	1 pg/mL	172
	electrochemical sensing	GO	Fe_3O_4 NPs and capture antibody	monolayer	1 pg/mL	148
	electrochemical sensing	rGO	PB-labeled anti-α-fetoprotein	mono- and multilayer	0.05 ng/mL	149
	electrochemical sensing	SWCNH	Au NPs and capture antibody	80−100 nm	0.07 pg/mL	173
VEGF	FETs	GS (CVD)	polypyrrole-converted nitrogen-doped	bi- and trilayer	100 fM	174
	electrochemical sensing	GO	Avastin/Fe_3O_4 NPs	monolayer	31.25 pg/mL	175
Hormones						
dopamine	FETs	rGO	(=O) or (−OH)	mono- and multilayer	1 mM	176
	electrochemical sensing	GNR	Fe_3O_4 NPs and Nafion	100 nm	0.33 μM	177
epinephrine	electrochemical sensing	SWCNH	carboxylic group	80 nm	0.1 μM	85
human erythropoietin	SPR detection	MWCNT	capture antibody	0.3−1.3 μm	0.1 ng/mL	145
insulin	fluorescence quenching	GO	FAM-labeled IBA	monolayer	500 nM	178
Chemical samples						
ATP	FRET	GO	aptamer-FAM	monolayer	10 μM	179
	FETs	GS (CVD)	label-free	monolayer	2 μM	180
chloramphenicol	electrochemical sensing	SWCNH	TiO_2 NPs−porphyrin	80 nm	0.9 nM	181
cholesterol	electrochemiluminescence	fullerene-C_{60}	L-cysteine and Au NPs	25 nm	5.7 nM	99
dexamethasone	electrochemical sensing	fullerene-C_{60}	pristine	0.7 nm	55 nM	182
dobutamine	electrochemical sensing	GNR	polyaniline	100 nm	0.1 μM	183

DOI: 10.1021/acs.chemrev.9b00099
Chem. Rev. XXXX, XXX, XXX−XXX

Table 1. continued

target analyte	sensing mechanism	material type	functional group/molecules	material scale	limit of detection	ref
Chemical samples						
ethanol	electrochemical sensing	GO	ADH/polythionine	mono- and multilayer	0.3 μM	184
gallic acid	electrochemical sensing	fullerenol	TvL and Au NPs	1 nm	6 μM	186
H_2S	two-photon fluorescence turn-on	C-Dot	AE-TPEA−Cu^{2+}	5 nm	0.7 μM	187
hydroquinone	electrochemiluminescence	fullerene-C_{60}	L-cysteine and Au NPs	25 nm	15 nM	93
	electrochemical sensing	CNT	laccase and AuNPs		0.1 μM	188
hypoxanthine	electrochemical sensing	SWCNH	Au NPs and xanthine oxidase	80−100 nm	0.61 μM	189
lactate	electrochemical sensing	rGO	lactate oxidase	mono- and multilayer	0.08 μM	190
L-dopa	electrochemical sensing	reduced GNR	few oxygen groups	120 nm	<0.05 mM	191
L-carnitine	electrochemical sensing	MWCNT buckypaper	Au NPs (30 nm)	D = 35−43 nm	2 μM	192
melamine	FRET	C-Dot	Au NPs (13 nm) amide and carboxyl	3−5 nm	36 nM	193
NADH	electrochemical sensing	rGO	(=O) or (−OH)	mono- and multilayer	10 μM	194
	electrochemical sensing	GO	polythionine	mono- and multilayer	0.1 μM	184
	electrochemical sensing	EGO	$CoFe_2O_4$	monolayer	0.38 μM	195
	electrochemical sensing	rGO	Au NPs (20 nm) and PAH	mono- and multilayer	3.5 μM	196
naringin	electrochemiluminescence	SWCNT	β-cyclodextrin	65 nm	0.8 nM	197
urea	electrochemical sensing	ND-NW	nitrogen and Urs−GLDH	80 nm	3.87 mg/dL	198
	capacitive field-effect	SWCNT	PAMAM dendrimer	D = 1.5−3.5 nm and L = 0.5−1.5 μm	0.1 mM	199
xanthine	electrochemical sensing	SWCNH	Au NPs and xanthine oxidase	80−100 nm	0.72 μM	189
bisphenol A	electrochemical sensing	MWCNT	tyrosinase	<100 nm	10 pM	200
folic acid	photoelectrochemical sensing	carbon nanohorns	titanate nanotubes	20 nm	25 pM	201
ALP activity	fluorescent quenching	C-Dot	pyrophosphate anions	3−5 nm	1.1 U/L	202
methotrexate	FRET	C-Dot	N and S codoped	2.81 nm	0.33 nM	91
ganciclovir	electrochemical sensing	MWCNT	DNAand Fe_3O_4	L = 1−2 μm	20 nM	203
levodopa	electrochemical sensing	MWCNT	HRPand p-phenylenediamine	32.9 nm	40 nM	204
ascorbic acid	electrochemical sensing	FC_{60}/FC_{70}/ SWCNT/MWCNT	ascorbate oxidase		0.10, 0.13, 0.20, and 0.22 μM	205
Lung cancer VOC biomarker						
benzene	electrochemical sensing	rGO	PBCD	monolayer	400 ppb	206
Blood Sugar						
glucose	electrochemical sensing	rGO	glucose oxidase	mono- and multilayer	0.1 mM	207
	electrochemical sensing	ERCGr	glucose oxidase	mono- and multilayer	0.02 mM	208
	electrochemical sensing	ERGO/MWCNT	glucose oxidase	mono- and multilayer/ (7−15) × (3−6) × (0.5−200) μm	4.7 μM	209
	electrochemical sensing	CNT	$NiCoO_2$	130−170 nm	1.14 μM	210
	electrochemical sensing	G-CNT	glucose oxidase	30 nm	0.5 mM	211
	electrochemical sensing	SWCNH	Cu microdendrites		17 μM	212
	electrochemical sensing	SWCNT	nafion and GOx	80 nm	6 μM	213
	electrochemical sensing	ND	nitrogen doped and glucose oxidase	25 nm	0.05 μM	214
	electrochemical sensing	ND	nickel (Ni) nanosheets	4−6 nm	0.05 μM	215
	electrochemical sensing	ND	SWCNT and biotin-GOx	2−10 nm	1 μM	216

DOI: 10.1021/acs.chemrev.9b00099
Chem. Rev. XXXX, XXX, XXX−XXX

Table 1. continued

target analyte	sensing mechanism	material type	functional group/molecules	material scale	limit of detection	ref
Chemical samples						
	electrochemical sensing	fullerene-C_{60}	Pd NPs and Cys	25 nm	1 μM	217
	electrochemical sensing	fullerene-C_{60}	GOx/ferrocene and chitosan/ionic liquid	0.7 nm	3 nM	86
	electrochemiluminescence	fullerene-C_{60}	tetraoctylammonium bromide and GOx	100 nm	166.7 nM	218
	electrochemical sensing	fullerene	chit/GOx	20 nm	5 μM	219
	fluorescence quenching	C-Dot	phenylboronic acid	4.5 nm	1.5 μM	220
Metal ions						
Ag^+	fluorescence quenching	GO	dye-labeled MB	monolayer	20 nM	103
	fluorescence quenching	GO	FAM-labeled cytosine-rich SSO	monolayer	5 nM	221
Cu^{2+}	fluorescence quenching	GO	PSICOR-GFP DNA	monolayer	2.5 mM	222
	fluorescence quenching	GO	FAM-modified DNAzyme	monolayer	0.365 nM	223
	fluorescence quenching	GQD	carboxylic group	10−30 nm	0.226 μM	96
Fe^{2+}/Fe^{3+}	dual-peak electrochemiluminescence	C-Dot	TBAB	2.3 ± 0.5 nm	0.7 μM	224
Fe^{3+}	fluorescence quenching	GQD	nitrogen-doped and carboxylic group	3.8 nm	90 nM	225
	fluorescence quenching	C-dots	hydroxyl group	4.73 ± 0.65 nm	0.16 μM	226
Hg^{2+}	fluorescence quenching	GO	dye-labeled MB	monolayer	5.7 nM	103
	fluorescence quenching	GO	ssDNA aptamer	monolayer	0.92 nM	227
	electrochemiluminescence	MWCNT	chitosan and ABEI−Au nanodots	D = 20 nm	3.2 nM	228
	fluorescence quenching	C-Dot	amino and carboxylic group	2−6 nm	226 nM	229
	fluorescence quenching	C-Dot	carboxylic group and methyldimethoxysilane	1.68 nm	845 nM	229
	fluorescence quenching	C-Dot	hydroxyl group	2.5 ± 0.5 nm	20 nM	230
	FRET	C-Dot	GO and T-rich 22-mer oligonucleotide	<10 nm	2.6 nM	231
Pb^{2+}	fluorescence quenching	GO	GR-5 DNAzyme	monolayer	300 pM	232
	fluorescence quenching	GO	aptamer-conjugated QDs	monolayer	90 pM	233
Reactive Oxygen Species						
H_2O_2	electrochemical sensing	SWCNH	PSS and myoglobin	70−85 nm	0.5 μM	234
	electrochemical sensing	ND-NS	HRP	400 nm	59 μM	235
	electrochemical sensing	fullerene-C_{60}	tetraoctylammonium bromide and zinc porphyrin	200 nm	0.81 μM	87
	electrochemical sensing	EGO	$CoFe_2O_4$	monolayer	0.54 μM	195
	electrochemical sensing	MWCNT	AuNPs-PTy and myoglobin		0.01 μM	236
	electrochemical sensing	Fullerene	chitosan and peroxidase		5 μM	237
extracellular H_2O_2	electrochemical sensing	GO	laminin and artificial peroxidase	monolayer	10^{11}/cell	238
	electrochemical sensing	GO	nitrogen-doped	monolayer	175 amol/cell	239
extracellular O_2	electrochemical sensing	GO	accase and ABTS	monolayer	10 μM	240
superoxide anion	ratiometric fluorescence	C-Dot	hydroethidine	3−5 nm	100 nM	241
Toxin						
microcystin-LR	electrochemical sensing	SWCNH	carboxylic group	80−120 nm	0.5 μg/mL	242

DOI: 10.1021/acs.chemrev.9b00099
Chem. Rev. XXXX, XXX, XXX−XXX

Table 1. continued

target analyte	sensing mechanism	material type	functional group/molecules	material scale	limit of detection	ref
Pathogens						
rotavirus	FRET	GO	Au NPs and capture antibody	mono- and bilayer	10^3 pfu/mL	243
	electrochemical sensing	GO film	PSE and capture antibody	multilayer (400 nm)	10^3 pfu/mL	244
Cells						
cardiomyocyte	FETs	rGO	SiNWs	monolayer	2.5×10^5 cells/mL (1.5 μS)	245
HL-1 cells	SGFETs	GS (CVD)	electrolyte	monolayer	2×10^3 cells/mm^2 (100 μV)	246
yeast cells (Sac)	electrochemical sensing	rGO	calcium and Au NPs	monolayer	volume trend in solvents	247
Cancer cells						
HeLa cells	colorimetric detection	GO	hemin and folic acid	mono-and multilayer	10^3 cells/mL	248
	electrochemical sensing	GO	PTCA/aptamer AS1411	monolayer	794 cells/mL	249
Bacteria						
E. coli	electrochemical sensing	rGO	antimicrobial peptide	monolayer	single cell	250
	electrochemical sensing	ND	capture antibody	10−200 nm	$<10^6$ cfu/mL	88
H. pylori	electrochemical sensing	rGO	antimicrobial peptide	monolayer	100 cells in human saliva	250
P. aeruginosa	fluorescence quenching	rGO	chitosan/Fe_3O_4 NPs	mono-and multilayer	400 cfu/mL in blood	251
S. aureus	electrochemical sensing	rGO	antimicrobial peptide	monolayer	single cell	250
	potentiometric measurement	rGO	SA31 aptamer	mono-and multilayer	1 cfu/mL	252
	fluorescence quenching	rGO	chitosan/Fe_3O_4 NPs	mono-and multilayer	100 cfu/mL in blood	251
Geobacter	electrochemical sensing	GO	amine group	mono- and multilayer	1400 CCs per single	253
sulfate-reducing bacteria	electrochemical sensing	rGO	chitosan	monolayer	1.8 cfu/mL	254
V. Parahemolyticus	CRET	GO	dye labeled-hairpin DNA aptamer	monolayer	2230 cells/mL	255

DOI: 10.1021/acs.chemrev.9b00099
Chem. Rev. XXXX, XXX, XXX−XXX

metal regulation. Despite the ability to resolve concentrations on the order of μg to ng/L, conventional methods for trace analysis such as atomic absorption spectroscopy (AAS) and inductively coupled mass spectrometry (ICP-MS), in addition to being bulky and expensive,[94] are unable to analyze on the single cell level.[95] Driven by its simplicity, low-cost, high sensitivity, and utility, carbon-based optical biosensors were extensively researched as an alternative tool to aid scientists in the fundamental cellular studies. Most optical biosensors employing nanocarbon materials monitor changes to the fluorescence signal, termed as fluorescence quenching (off-state) or fluorescence enhancement (turn-on), with these effects induced from interacting with a biomolecule. When employed as a FRET sensor, the distance between the donor and acceptor fluorophores (between 1 and 10 nm) can be measured based on the energy transfer efficiency, creating a powerful means for studying molecular interactions beyond the diffraction limit. As mentioned in section 1.2, GO with a lateral size below 50 nm can emit light in the NIR range. More recently, GQDs with tunable emission wavelengths were used as energy donors in a FRET detection process.[66,96] Interestingly, GOs and GQDs have also been demonstrated to be efficient acceptors due to their unique electronic properties. For instance, Ju et al.[97] found that electron transfer from mercury ions (Hg^{2+}) to the surface of nitrogen-doped GQDs resulted in significant photoluminescence quenching of the GQDs. On this basis, they developed a highly sensitive fluorescence turn-on sensing system for the detection of glutathione (GSH), a critical biomarker for various diseases like malignant tumors, acquired immune deficiency syndrome, and Alzheimer's disease, with a detection limit the could reach as low as 87 nM. Electrochemiluminescence (ECL) is another optical method ideal for biological molecules with low background noise and good temporal control. An amalgamation of electrochemical and chemiluminescent sensing, the approach can be very sensitive to the target biomolecules loaded on the electrodes. Materials such as GOs, CNTs, and fullerenes act as enhanced signal amplification tags in ECL biosensors by facilitating the electron transfer and charge shift between the redox probe and the electrodes.[98] This was demonstrated with spherical fullerenes (C_{60}) functionalized with L-cysteine (L-cys) by Ou et al.[99] to amplify the ECL intensity in cholesterol detection. More importantly, they demonstrated that functionalized fullerenes were good nanomediators for conjugating other amplification nanotags like colloidal gold nanoparticles (Au NPs), which would further enhance the sensitivity of the ECL sensors. Unlike other nanocarbon materials, NDs with NV defect centers have a distinct advantage for optically detected magnetic resonance measurements of metalloprotein molecules like ferritin.[100] When the metalloprotein molecules are adsorbed onto the surface of NDs, electron spins of the NV centers are influenced by the coupling of the metal ion spins in the protein molecule, leading to a reduction of both the coherence and relaxation time of NV spins.

Representative devices presented of the three classifications discussed in this section are shown in Figure 2. In the following sections, we will introduce and discuss in detail various types of novel biosensors based on each of these nanocarbon materials. A detailed summary of carbon-based nanomaterials for in vitro detection is presented in Table 1.

2.1.1. In vitro Protein Detection by Different Nanocarbon Materials. *2.1.1.1. Graphene and Graphene Oxides.* Graphene nanosheets as a zero bandgap 2D atomic layer have unique functional characteristics such as high conductivity, elastic modulus, mechanical strength, and surface area.[256−259] More importantly, they have provided an excellent platform to achieve immunosensing in terms of their low intrinsic toxicity and large surface-to-volume ratios for surface functionalization. According to optical calculations, they could act as long-range energy acceptors with a high energy-transfer rate of d^{-4} dependence on distance.[260] For instance, Wang et al. reported a protease biosensor with peptide-functionalized GOs as fluorescence signal amplification tags.[139] The GO−peptide conjugates could be incubated with live cells with low cytotoxicity and used for real-time monitoring of caspase-3 activations. Caspase-3 molecules are central mediators for cell apoptosis. The detection of caspase-3 can facilitate the drug screening tests through the observation of dysregulated apoptosis. Here, the GOs served as the nanoscale carriers for the peptide cargos with fluorescence quenching molecules. The detachment of the peptides from GO resulted in the release of fluorescent dyes from the GO surface and thus, an enhanced fluorescence signal from previous quenching status. The fluorescence intensity of the GO−peptides increased with an increasing caspase-3 concentration from 7.25 to 362 ng/mL. In addition, the GO−peptides showed a strong fluorescence contrast when transported into the HeLa cells compared to the signals for pure GOs and peptides.

Later, Lee et al. developed a graphene immunosensor based on the CRET effect (Figure 3).[123] Different from the FRET

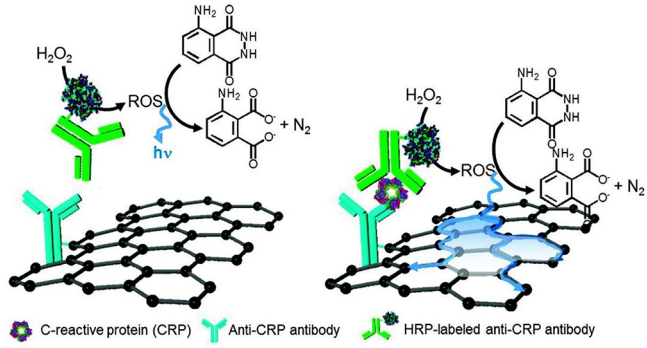

Figure 3. Schematic illustration of a graphene-based CRET platform for the detection of CRP. Anti-CRP antibody-conjugated graphene and luminol that is excited by HRP-catalyzed oxidation are used as an acceptor and a donor, respectively. Reprinted with permission from ref 123. Copyright 2012 American Chemical Society.

sensing mechanism, CRET does not require external excitation light source as the dipole charge transfer occurs from a chemiluminescent donor to the acceptors. C-Reactive proteins (CRPs), key biomarkers for clinical diagnostics of human cardiovascular diseases, were used as target example molecules and detected by chemiluminescence catalytic reaction in the presence of horseradish peroxidase (HRP). The catalytic reaction would produce reactive oxygen species (ROS) like singlet oxygens and thus trigger the strong emission of luminol at 430 nm. The surface of graphene NSs was functionalized with capture CRP antibody to enable the high selectivity and sensitivity to the target CRP molecules. The chemiluminescence of the luminol was quenched by 72% with CRP at a concentration of 1 μg mL^{-1}. A low detection limit of 0.93 ng/mL for the target CRP in human serum samples was obtained through the graphene-CRET sensing platform. The graphene

DOI: 10.1021/acs.chemrev.9b00099
Chem. Rev. XXXX, XXX, XXX−XXX

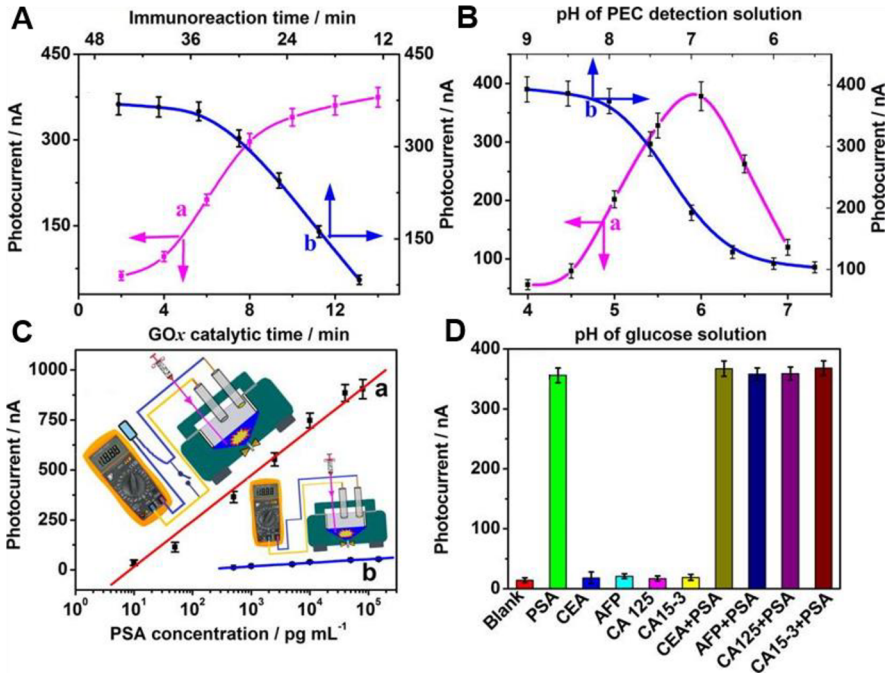

Figure 4. Effects of (A-a) GOx catalytic time, (A-b) the antigen−antibody reaction time, (B-a) pH of GOx catalytic solution, and (B-b) pH of PBS in the PEC detection cell on the photocurrent of self-illuminated PEC immunoassay (0.5 ng/mL PSA used in the case), (C) calibration curves of self-illuminated PEC immunoassay toward various-concentration PSA standards in the (a) presence and (b) absence of external capacitor, and (D) the specificity of PEC immunoassay against of CEA (10 ng/mL), CA 125 (10 U/mL), CA 15−3 (10 U/mL) and α-fetoprotein (10 ng/mL). Reprinted with permission from ref 165. Copyright 2016 American Chemical Society.

NS obtained from hydrothermal deoxygenation was found to exhibit a higher luminescence quenching efficiency than that of GOs as the energy acceptors.

Recently, Shu et al. developed a photoelectrochemical (PEC) immunosensor by using rGOs-$BiVO_4$ photovoltaic hybrid nanomaterials for sensing trace amounts of the prostate cancer biomarker, prostate-specific antigen (PSA).[165] The rGO-$BiVO_4$ nanocomposites were incorporated with a peroxyoxalate chemiluminescence self-illuminated cell and a digital multimeter circuit (Figure 4). During the detection process, an anti-PSA coated microplate was used as the primary capture probes stage, while the second capture probes consisted of glucose oxidase (GOx)/antibody-functionalized Au NPs. The target PSA molecules were sandwiched between the microplate and the Au NPs. The sandwich binding between the antibody and antigen led to the oxidation of glucose and the generation of hydrogen peroxide (H_2O_2) as the Au NPs were also labeled with GOx. The H_2O_2 then triggered the chemiluminescence of the peroxyoxalate system and the following PEC reaction of the $BiVO_4$-rGOs. Therefore, the photovoltaic hybrid nanomaterials triggered a voltage response under light excitation and in the presence of the target PSA molecules, the current signal was observed to increase with a wide concentration range from 10 pg mL^{-1} to 80 ng/mL.

In addition to the fluorescent immunosensors, an aptamer-functionalized graphene-based field-effect transistor (G-FET) for label-free detection of immunoglobulin E (IgE) molecules was designed by Ohno and co-workers.[129] The IgE level in the human serum is related to immune deficiency diseases such as allergic asthma and atopic dermatitis. The aptamers are known as cost-effective artificial oligonucleotides with short sequences (around 3 nm) that are smaller than the Debye length. The use of capture aptamers in their study could maintain the effect of the charged molecules onto the transistor channel. The specific IgE aptamers were attached to the graphene surface through noncovalent π stacking interaction by using a linker molecule of 1-pyrenebutanoic acid succinimidyl ester. The sensing performance of the aptamer-functionalized G-FET was evaluated by measuring the drain current under a 0.1 V drain voltage and 0.1 V top-gate voltage in PBS solutions (pH = 6.8). It is worth noting that a high affinity ratio was obtained between the IgE and G-FET with a low dissociation constant of 47 nM.

Later, Khatayevich et al. demonstrated a G-FET sensor for repeatable 12 cycles with continuous and consistent measurement results.[135] The graphene surface was conjugated with two different types of dodecapeptide peptides (i.e., biotin-labeled GrBP5-WT and SS-GrBP5 mutants) that enhanced the probe-capture ability and significantly reduced the nonspecific attachment on the sensing surface. Detection ability for small biomolecules such as streptavidin over a noise background with human BSA at a high concentration of 50 ng/mL was achieved. More recently, Rodrigo et al. combined the electronic and optical properties of graphene NSs and reported a highly sensitive infrared-plasmonic biosensor for label-free detection of protein molecules (Figure 5).[261] The authors found that the optical spatial confinement in the graphene layers is 2 orders of magnitude higher than that in conventional metallic thin films.

The plasmon resonance excited on the graphene surface could be tuned for detecting different types of target protein molecules by changing the resonance frequencies. The reflected intensity at the specific frequency in the mid-infrared region changed with the refractive index change of the sample solutions, corresponding to the concentration of the target protein molecules. The plasmonic device was fabricated by patterning the graphene nanoribbon arrays (W = 30 nm, P =

DOI: 10.1021/acs.chemrev.9b00099
Chem. Rev. XXXX, XXX, XXX−XXX

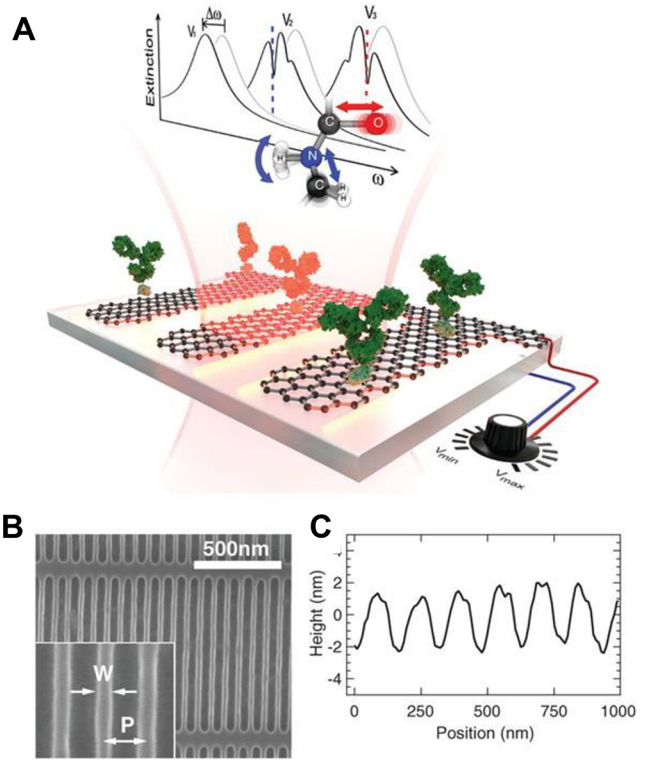

Figure 5. Tunable graphene mid-IR biosensor. (A) Conceptual view of the graphene biosensor. Protein sensing is achieved by detecting a plasmon resonance spectral shift ($\Delta\omega$) accompanied by narrow dips corresponding to the molecular vibration bands of the protein. (B) SEM image of a graphene nanoribbon array. (C) AFM cross-section of the graphene nanoribbon array. Reprinted with permission from ref 261. Copyright 2015 American Association for the Advancement of Science.

80 nm) through electron beam lithography/oxygen plasma etching onto monolayer graphene coated silicon substrate. The localized surface plasmon resonance frequency of the graphene sheets could be tuned from 1450 to 1800 cm^{-1} by changing the bias voltage. When the human IgG antibodies were immobilized onto the sensor surface, a large redshift up to 200 cm^{-1} of the plasmon resonance frequency was obtained.

2.1.1.2. Carbon Nanotubes. Recently, CNTs were reported to be structured as a 2D mat like a buckypaper (BP) and designed as novel electrodes for electrochemical biosensing.[192] The CNT BP show high sensitivity for myoglobin, tryptophan, tyrosine, and L-carnitine samples, all of which are important biomarkers for clinical healthcare applications. For instance, tryptophan is known as the essential amino acid for controlling the nitrogen balance in human bodies. Myoglobins in the blood plasma are indicators of hemoglobin protein for the iron and oxygen binding in red blood cells. A 1000 times sensing signal amplification was observed with the BP when compared with the bare glassy carbon electrodes. The authors also coupled Au NPs and a mediator titrant molecule to the BP electrode. The colloidal Au NPs demonstrated enhanced electrocatalytic effects due to the charge transfer effect from Au NPs to the CNT surface. Strano and group illustrated ultralow and label-free detection of individual proteins in solution from bacteria and yeast.[262] They used nanosensor arrays comprising an aptamer-anchor polynucleotide sequence conjugated to SWCNTs. The nanosensor arrays acted as fluorescent emitters in the NIR window and thus acted as optical sensors for detecting proteins of interest. The demonstrated process of individual protein detection is useful for real-time, single cell analysis including transcription and translation as well as for genetic engineering.

2.1.1.3. Carbon Nanohorns. CNHs have pseudocylindrical structures with both bumps and dips in pentagonal and heptagonal shapes. Their structure defect numbers are larger than those of straight CNTs that allow them to be more easily oxidized and functionalized. The holes at the end of the CNHs can be opened and induced with abundant carboxyl groups. With the opened holes, the inner space of the CNHs is further explored to extend the surface area from 300 to 1400 m^2/g. These advantages of CNHs promise their potential as either signal amplifications or enhanced sensing substrates for molecular detections.[51,114,263] Zhu et al. designed a fluorescent aptasensor based on single-walled CNHs (SWCNHs) for the targeted detection of thrombin molecules (Figure 6A).[143] Here, the SWCNHs were first oxidized by dilute nitric acid through a microwave radiation process. This could make the SWCNHs water soluble due to the carboxyl groups generated on their surface. The oxidized SWCNHs were then noncovalently conjugated with dye-labeled thrombin aptamer by π-stacking force. The fluorescent detection principle is based on the distance-dependent fluorescent effect between the dyes and the oxidized SWCNHs. When the dye-tagged thrombin aptamer was adsorbed onto the oxidized SWCNHs, a significant fluorescence quenching of the dye molecules could be observed. However, the fluorescence could be recovered in the presence of the target thrombin molecules that could lead to a quadruplex conformation of the dye-labeled thrombin aptamer. The fluorescence intensity change showed a linear proportional relationship with the concentration of the target thrombin molecules. A low detection limit of 100 pM was achieved with a good reproducibility (5% standard deviation for the quenching efficiency) (Figure 6B). The high selectivity of the sensors was proven by using 100 nM human IgG and 100 nM bovine serum albumin (BSA) solutions as nonspecific controls (Figure 6C).

In addition to the dye labels, the SWCNHs were found to be efficient energy acceptors for citrate-functionalized upconversion nanoparticles as well. Xu et al. used these novel FRET donor/acceptor nanotags for sensing of acute promyelocytic leukemia biomarkers through a similar "Turn-On" FRET scheme (Figure 6D,E).[106] At the initial stage, the fluorescence of the UCNPs were quenched by SWCNHs resulting from their π-stacking adsorption by a probe ss DNA (5′-NH_2-TCT CAA TGG CTG CCT CCC-3′) functionalized on the UCNP surface. When the complementary target DNA sequences (PML/RARα fusion genes for acute promyelocytic leukemia) were present, the probe and target DNA would form a stable double-helix structures and lead to the separation of the citrate-functionalized upconversion nanoparticles and SWCNHs by weakening the π-stacking interaction. Thus, the fluorescence of the upconversion NPs ($NaYF_4$: 20% Yb, 2% Er@NaYF4) could be turned on. A detection limit of 0.28 nM with a signal noise ratio of 3 for acute promyelocytic leukemia gene could be achieved by this sensing mechanism (Figure 6F,G).

A sandwich immunosensor using bienzyme-functionalized SWCNHs for biocatalyzed precipitation for electrochemical detection of α-fetoprotein molecules was demonstrated by Yang and co-workers.[170] The bienzymes, GOx and HRP could aid the oxidation of the electrochemical active species [4-

DOI: 10.1021/acs.chemrev.9b00099
Chem. Rev. XXXX, XXX, XXX−XXX

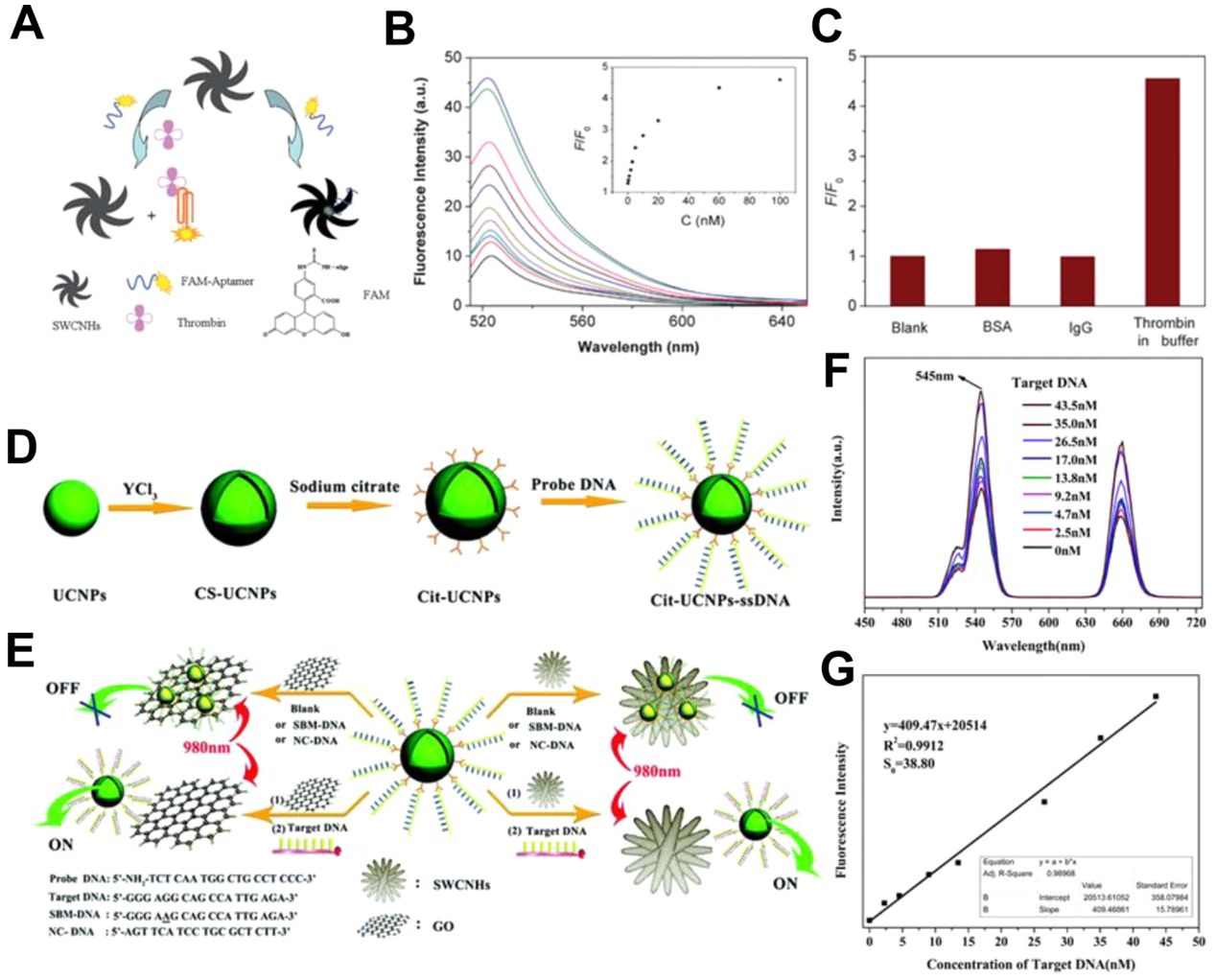

Figure 6. (A) Schematic illustration of oxidized SWCNH as aptasensor for the detection of thrombin. (B) Fluorescence intensity of 50 nM dye−TA in the presence of various concentrations of thrombin. Inset is the F/F_o plotted against the concentration of thrombin, where F and F_o are the fluorescence intensity with and without thrombin, respectively. (C) Fluorescence response of the aptasensor added in blank buffer, 100 nM BSA in buffer, 100 nM IgG in buffer, and 100 nM thrombin in buffer. Reprinted with permission from ref 143. Copyright 2011 Royal Society of Chemistry. (D) Schematic illustration of the preparation of citrate-functionalized upconversion nanoparticles-ssDNA. (E) Schematic illustration of using of LRET-based detection using citrate-functionalized upconversion nanoparticles-ssDNA and SWCNHs for the detection of acute promyelocytic leukemia. (F) The luminescence response of multiplexed citrate-functionalized upconversion nanoparticles-ssDNA-SWCNHs nanoplatform with various concentrations of target DNA. (G) Linear relationship between upconversion luminescence intensity observed at 545 nm versus target DNA concentrations. Reprinted with permission ref 106. Copyright 2016 Royal Society of Chemistry.

chloro-1-naphthol (4-CN)] by H_2O_2. The oxidation resulted in the insoluble precipitates on the surface of the glassy carbon electrode (GCE) and thus a large electrochemical signal change. The GCEs were initially functionalized with Au NPs and graphene (Au-Gra) nanocomposites, followed by the immobilization of the capture α-fetoprotein antibodies (Ab_1). The SWCNHs were conjugated with the capture α-fetoprotein Ab_2 and bienzymes by carbodiimide interactions. The target α-fetoprotein antigen molecules were sandwiched between the Au-Gra nanocomposites and the SWCNHs. The SWCNHs served as efficient signal amplification tags due to their large surface area for sufficient molecular functionalization. They also offered a large space to hold the insoluble precipitates. The immunosensor exhibited a high sensitivity of 0.33 pg/mL and a wide linear detection range from 0.001 to 60 ng/mL. A similar detection scheme was later reported by Liu et al., where they used SWCNHs conjugated with hollow Pt chains as signal amplification tags.[158] A septicemia disease biomarker called procalcitonin was chosen as the target sample molecule. The sensing substrate was functionalized with rGO and Au NPs nanocomposites to enhance the adsorption rate of the capture procalcitonin antibodies (Ab_1), while the SWCNHs-HPtCs were conjugated with procalcitonin Ab_2. A linear detection range of 1.00 pg/mL to 20 ng/mL and a detection limit of 0.43 pg/mL were achieved for this immunosensor.

Ojeda et al. recently developed a CNHs-based disposable electrochemical sensor for quantitative detections of fibrinogen (Fib) in human urine and plasma samples.[80] Fib molecules are plasmatic glycoprotein for hemostatic function in the mammal animals. The healthy level for Fib in human plasma ranges from 1.5 to 4.5 mg/mL. The oxidized CNHs were deposited on SPCEs for the capture of the target Fib. The calibration experiments showed a linear response from 0.1 to 100 μg/mL (r^2 = 0.994) and a detection limit of 58 ng/mL. A long-term shelf time up to 42 days was obtained for the Fib-CNHs/SPCEs. For the urine sample analyses, solid phosphate salts

DOI: 10.1021/acs.chemrev.9b00099
Chem. Rev. XXXX, XXX, XXX−XXX

were used to adjust the pH of the sample solutions to 7.4. Spiked urine samples containing Fib at different concentrations of 0.65, 5.0, and 25.0 μg/mL were tested. For human plasma sample detection, the plasma was diluted in PBS solutions at pH of 7.4 and a mean concentration value of 2.7 ± 0.2 mg/mL Fib was achieved. All these results indicate that the disposable CNH sensors can be used for clinical diagnostics at physiological levels.

More recently, CNHs have been combined with interwove titanate nanotubes for enhanced PEC sensing of folic acid (FA) (Figure 7A).[201] The "dahlia-like" CNHs in hierarchical shapes act as an electron transmission medium to trap and transfer the electrons from the photoexcited titanate nanotubes to the sensing matrix because they possess a high conductivity and a large surface area. The holes generated from the valence band of the photoexcited titanate nanotubes are transferred to the CNHs surface and consumed by the target FA. In this case, a strong photocurrent signal change could be collected through the titanate nanotubes/CNHs-modified GCE. The photocurrent responses linearly increased with the increasing concentration of FA from 1×10^{-10} to 5×10^{-5} M, and a detection limit of $(2.5 \pm 0.005) \times 10^{-11}$ M was achieved (Figure 7B). To further test the selectivity of the sensors to FA molecules, different substances were used as interfering controls including starch, vitamin B1, vitamin B2, sucrose, fructose, K^+, Fe^{3+}, Na^+, and Mg^{2+} with a high concentration of 1×10^{-5} M (Figure 7C). The photocurrent signals induced by these control samples were much lower than that with only 1×10^{-7} M target FA ones.

2.1.1.4. Nanodiamonds. Ermakova et al. designed a protein sensing scheme that used the magnetic responses of NDs to the ferritin molecules.[100] Ferritins are important biomarkers for plants, prokaryotes, and animals due to their iron storage function. The concentration of ferritin in the human serum is critical for homeostasis and metabolism of irons, which makes them an indicator for various diseases such as iron aplastic anemia, thalassemia, chronic hemolytic anemia, hepatitis, hepatoma, and chronic/acute hepatic injury. In this work, the magnetic noise generated from the paramagnetic irons of ferritin molecules were employed as signal contrasts. The ferritin molecules could adsorb to the oxidized ND surface through electrostatic force between the carboxyl groups on the ND and amino groups on the ferritin. An obvious decrease time for the coherence and relaxation process was induced after the ferritin molecules attached to the single ND surface. The authors found that a strong fluctuating spin bath resulted from the thermal fluctuations of the iron electron spins in the ferritin metalloprotein. The induced spin bath would couple to the NV electron spin and led to a significant decrease of the coherence and relaxation time (T_1 and T_2) of the NV spin up to an order of magnitude (T_1 from 41.8 to 5.7 μs and T_2 from 6.0 to 1.6 μs).

2.1.1.5. Carbon Dots. Fluorescent carbon dots (C-dots) have recently become one of the most attractive materials among the nanocarbon family as sensing probes for healthcare and environmental monitoring.[65,66,264,265] Most notably, they can be synthesized through green approaches without the usage of heavy metal ions and organic solvents. Shi et al. reported a carbon quantum dot (CQD)-based dual-mode sensor for both fluorescence and colorimetric sensing of GSH (Figure 8A).[127] The CQDs as fluorescence reporters were conjugated with Au NPs that acted as fluorescence quenchers and colorimetric reporters. The fluorescent CQDs with average

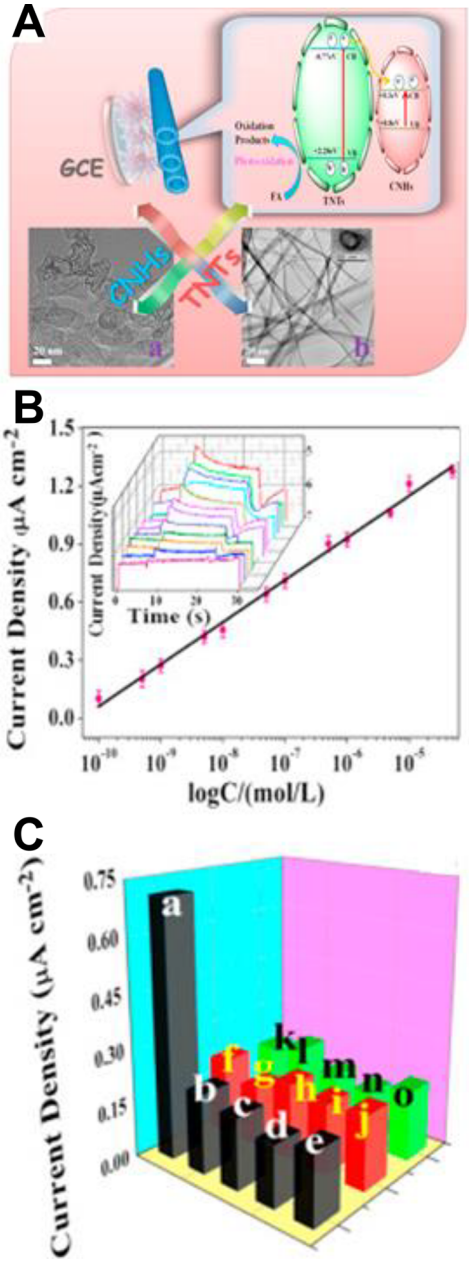

Figure 7. (A) Schematic illustration of the charge transfer on the titanate nanotubes/CNHs/GCE structure under light irradiation. The TEM images shown are CNHs (left) and titanate nanotubes (right). Inset is the high resolution TEM image of titanate nanotubes at the open end. (B) Linear calibration curve of current density and FA concentration. Inset image is the amperometric $I-t$ curve for time-based photocurrent responses. (C) Selectivity result with a–o: K^+, Fe^{3+} fructose, Na^+, vitamin B1, starch, glucose, Mg^{2+}, Zn^{2+}, sucrose, Al^{3+}, vitamin B2, Ca^{2+}, and Fe^{2+}. Reprinted with permission from ref 201. Copyright 2016 Royal Society of Chemistry.

diameter of 2.5 nm were synthesized by using citric acid as the carbon precursor through a microwave process with 2,2′-(ethylene-dioxy)bis(ethylamine) as the coreactant. The detection principle was based on the distance change between the Au NPs and CQDs. In the absence of the target GSH, the Au NPs in the colloidal solutions would be aggregated after mixing with CQDs that resulted in an obvious color change from red to blue and also the fluorescence quenching of the CQDs (Figure 8B). While in the presence of the GSH

DOI: 10.1021/acs.chemrev.9b00099
Chem. Rev. XXXX, XXX, XXX−XXX

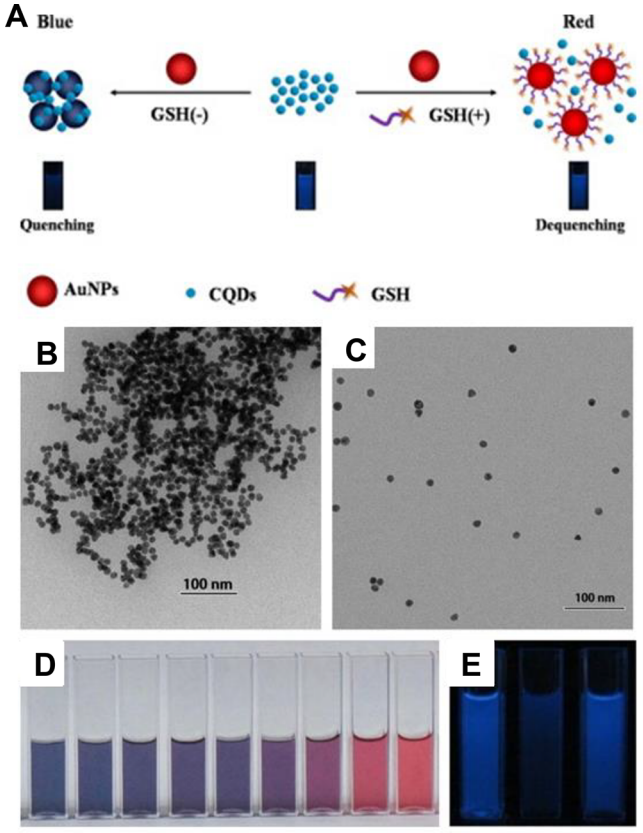

Figure 8. (A) Schematic illustration of the GSH detection using dual-mode colorimetric and fluorometric nanosensor. TEM images of (B) aggregated AuNPs induced by CQDs without addition of GSH; (C) dispersed AuNPs with the addition of CQDs and GSH. (D) Image of CQDs and AuNPs mixture with increasing concentration of GSH from left to right. (E) Image of CQD solution and mixture of CQD and AuNPs without and with the addition of GSH, from left to right. Reprinted with permission from ref 127. Copyright 2014 Elsevier.

molecules, the Au NPs were functionalized and stabilized from aggregation and thus induced the recovery of the color and the fluorescence signals (Figure 8C). The detection limit for target GSH was measured to be 50 nM. The recovered fluorescence intensity of CQD was increased with the increasing concentration of GSH from 0.05 to 3.0 μM (Figure 8D). For the specificity test, 20.0 μM of negative control samples including GSSG, Hcy, and Cys were added into the CQDs/Au NPs conjugates, and no signal responses were obtained even at such high concentrations for these interfering agents (Figure 8E).

In another report, Chan and co-workers developed a facile synthesis method to prepare fluorescent nitrogen and sulfur codoped carbon dots (NS-CDs) for the sensitive detection of ferric ions.[226] The NS-CDs were prepared from citric acid and thiourea using a one-step microwave-assisted pyrolysis and have a dimension of 4.73 ± 0.65 nm. In a neutral environment, the NS-CDs were able to detect ferric ions with a limit of detection of 0.16 μM. In addition, in acidic environment, the NS-CDs were also able to detect ferric ions with a sensitivity of 0.17 μM, with improved selectivity where the interference effect from Cu^{2+}, Co^{2+}, and Ag^{+} ions were reduced by 15%, 18%, and 64%, respectively. This work shows that pH tuning can be employed as a technique to modulate the analytical response of a fluorescent probe.

2.1.2. In Vitro Oligonucleotides Sensing with Different Nanocarbon Materials. *2.1.2.1. Graphene and Graphene Oxides.* Nucleic acid detections with high sensitivity and selectivity have been found to be of great importance for a wide range of bioapplications such as point-of-care disease diagnostics, gene expression profiling, and drug development.[266−270] Among all the graphene-based sensing methods for detecting DNA and RNA oligonucleotides, fluorescence quenching is the most commonly used one due to its rapid response and cost-effectiveness together with picomolar sensitivity and single-nucleotide polymorphism selectivity.[45,271−274] There are three basic elements in a fluorescence biosensor using the quenching ability of graphene, i.e., (i) a capture probe molecule like DNA/RNA aptamer that is complementary to the target oligonucleotide, (ii) a fluorophore as reporter (e.g., organic dye and semiconductor QD), and (iii) graphene/GO as the quencher. The detection process is strongly dependent on the distance between the fluorophore−quencher pairs.[117] First, the fluorophore-labeled capture nucleic acid molecules are tightly bound to the aromatic surface of graphene/GO through noncovalent π-stacking interactions. The binding thus induces fluorescence quenching. The presence of the target DNA/RNA oligonucleotides results in a conformation change of the fluorophore-labeled probe by nucleic acid hybridizations and unbinds the probe from the graphene surface. The fluorescence intensity can then be restored and shows a proportional relationship with the concentration of the target analytes.

In 2009, Lu et al. first reported the use of GO for the quenching of dye-tagged ss DNA (FAM-ssDNA) and demonstrated the feasibility of this principle to detect 23-mer target oligonucleotide sequences (HIV-1 U5) with concentrations ranging from 10 nM to 1 μM.[112] A 97% fluorescence quenching efficiency of GO to the probe molecule was achieved, while the mixtures of probe and GO had a significant fluorescence enhancement after adding the target sequences. They also studied the kinetic behaviors of the adsorption and dissociation of probe ssDNA on/from the graphene surface. It was observed that the adsorption process was much faster (less than 1 min) than that of dissociation (30 min). To further test the selectivity of this method, the authors conjugated a dye-tagged human thrombin-specific DNA aptamer with GO and mixed the probe complex with various protein molecules. The fluorescence intensity change with the addition of target human thrombin (100 nM) was shown to be at least 4-fold larger than those induced by 100 nM tested nontarget analytes (human IgG, human serum albumin, bovine thrombin, and BSA). Later, a postmixing strategy of GO was proposed by He et al. which effectively shortened the fluorescence detection time for ssDNA from 30 min to less than 1 min.[104] To improve the sensitivity and thermal ability of the probe−GO complex, the same group then developed a novel molecular beacon−GO ssDNA probe with this postmixing strategy.[102] Molecular beacons are hairpin-structured ssDNAs that are dual-labeled by a fluorophore (donor) and quencher (acceptor) at each of their two ends. After the introduction of target oligonucleotides, the fluorophore−quencher pair inside the stem−loop structure is detached from each other by the hybridization events. The fluorescence of the probe ssDNA is thus restored with the opened stem−loop. They found that the background interference of molecular beacon fluorescence could be significantly reduced by conjugating GO with the molecular beacon probe even at a

DOI: 10.1021/acs.chemrev.9b00099
Chem. Rev. XXXX, XXX, XXX−XXX

high temperature of 75 °C, leading to a higher signal-to-noise ratio and a lower detection limit of 0.1 nM. A similar DNA sensor that was able to achieve multiplex sensing of different target sequences in a single step as shown in Figure 9 was reported by Zhang et al.[103]

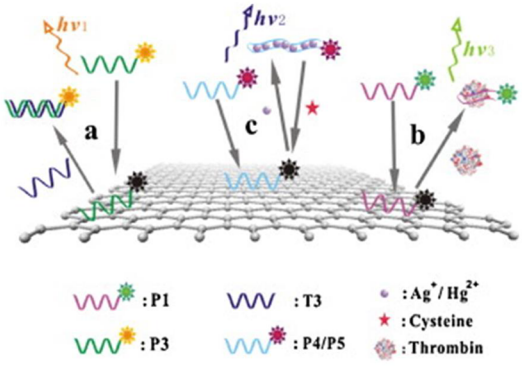

Figure 9. Schematic representation of the ssDNA−GO architecture platform for multiplex targets detection. (a) In the presence of a complementary target T3, P3 reacts with T3 to form a P3−T3 complex, which detaches from the GO surface, resulting in the fluorescence "on" state. (b) P1 assumes the fluorescence "off" state by the formation of probe−GO architecture but switches to the "on" state by the interaction with thrombin. (c) In the presence of Ag^+ or Hg^{2+}, P4 or P5 are self-folded to form the stable C−Ag^+−C or T−Hg^{2+}−T structure, leading to the fluorescence "on" state. However, by continuing to add cysteine to the above solution, the C−Ag^+−C or T−Hg^{2+}−T structure is disrupted by Ag−S or Hg−S bond between cysteine and Ag^+ or Hg^{2+}, switching to the fluorescence "off" state again. Reprinted with permission from ref 103. Copyright 2011 Elsevier.

Fluorescent silver nanoclusters (Ag NCs) were also explored (Figure 10) and used instead of organic dyes as the reporter fluorophores.[113] During the colloidal synthesis process of Ag NCs, the probe ssDNAs can be directly functionalized onto the surface of Ag NCs through their template function for the

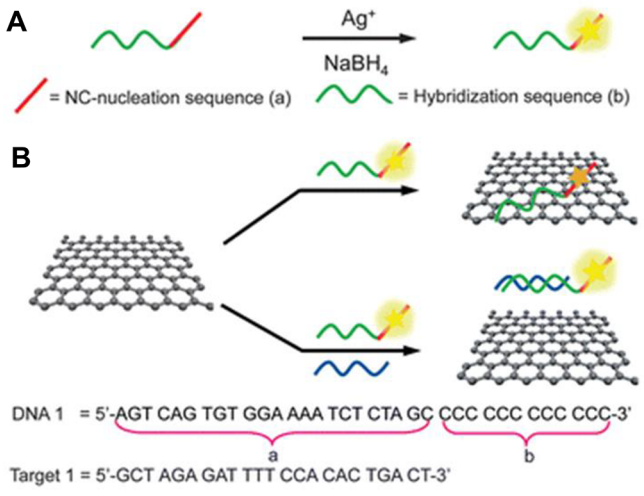

Figure 10. (A) Schematic representation of the preparation of silver nanoclusters on DNA scaffolds in aqueous solution. (B) Schematic illustration of the assay for label-free DNA detection using AgNCs−GO nanohybrid materials. Reprinted with permission from ref 113. Copyright 2012 Royal Society of Chemistry.

silver metallization. On the other hand, Au NPs labeled with target ssDNA could be employed as nanoquenchers with GO as fluorescent signal reporters.[105] The complementary probe ssDNA were covalently bound to the GO surface through carbodiimide chemistry. An 87% fluorescence quenching efficiency was obtained based on this FRET scheme. Recently, Liu et al. designed a fluorescence enhanced graphene-sensing platform that was able to achieve an ultralow detection limit of 0.8 pM for target DNA sequences (Figure 11).[45] This novel

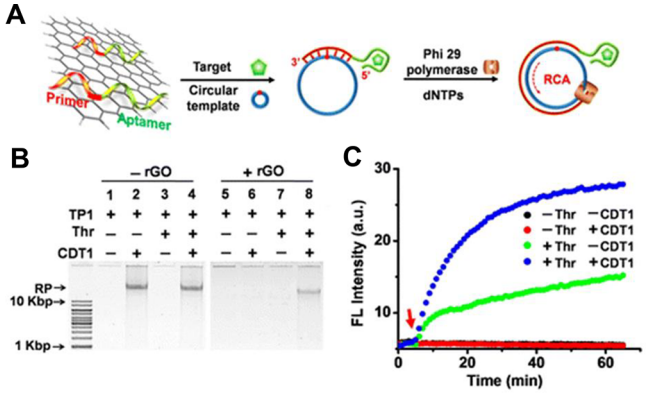

Figure 11. (A) Schematic representation of reduced graphene oxide−aptamer−rolling circle amplification biosensing platform. (b) Analysis of rolling circle amplification products by 0.6% agarose gel electrophoresis. Each reaction was performed for 1 h at 30 °C in 60 μL of target binding buffer (TBB: 20 mM PBS, 150 mM NaCl, 20 mM KCl, 5 mM $MgCl_2$, pH 7.5) containing indicated components of rGO-adsorbed TP1 (250 nM), circular DNA template1 (8 nM), and thrombin (Thr; 200 nM). (c) Time-dependent fluorescence response of reduced GO-adsorbed FAM-labeled TP1 (250 nM) in the presence of Thr (200 nM), circular DNA template1 (8 nM), or both. $\lambda_{ex}/\lambda_{em}$ = 494/518 nm. Reprinted with permission from ref 45. Copyright 2014 American Chemical Society.

platform was based on rolling circle amplification. The rolling circle amplification process was triggered by a probe ssDNA that consisted of an aptamer sequence with a short primer at the end. The probe ssDNAs were bound to the surface of rGOs through π-stacking interaction. rGOs were demonstrated to have a good protection effect for the primer from digesting by cellular nucleases in the absence of the target sequences, while the probe ssDNA with the primer could be released from the graphene surface through hybridizations between the probe aptamer and the target DNA sequence. The release of probe ssDNA made the primer exposed to the circular DNA template and induced the rolling circle amplification reactions. Specific MBs were initially embedded in the circular DNA template and showed enhanced fluorescent signals after binding with the resultant rolling circle amplification products. This approach was applicable to the detection of target analytes in real biological samples even with cell lysates.

Besides fluorescence quenching, graphene-based colorimetric detection is another effective optical sensing method that enables the fast screening of target nucleic acid sequences and gene mutations by the observation with the naked eye.[110,119] For example, GOs were functionalized with hemin and probe ssDNA molecules via π-stacking to form as hybrid nanoassays (Figure 12) for catalyzing color reactions of tetramethylbenzidine with H_2O_2.[116] The hemin−GO nanoassay was initially colloidal-stable and monodisperse due to the electrostatic repulsion of the probe ssDNA. After the hybridization binding

DOI: 10.1021/acs.chemrev.9b00099
Chem. Rev. XXXX, XXX, XXX−XXX

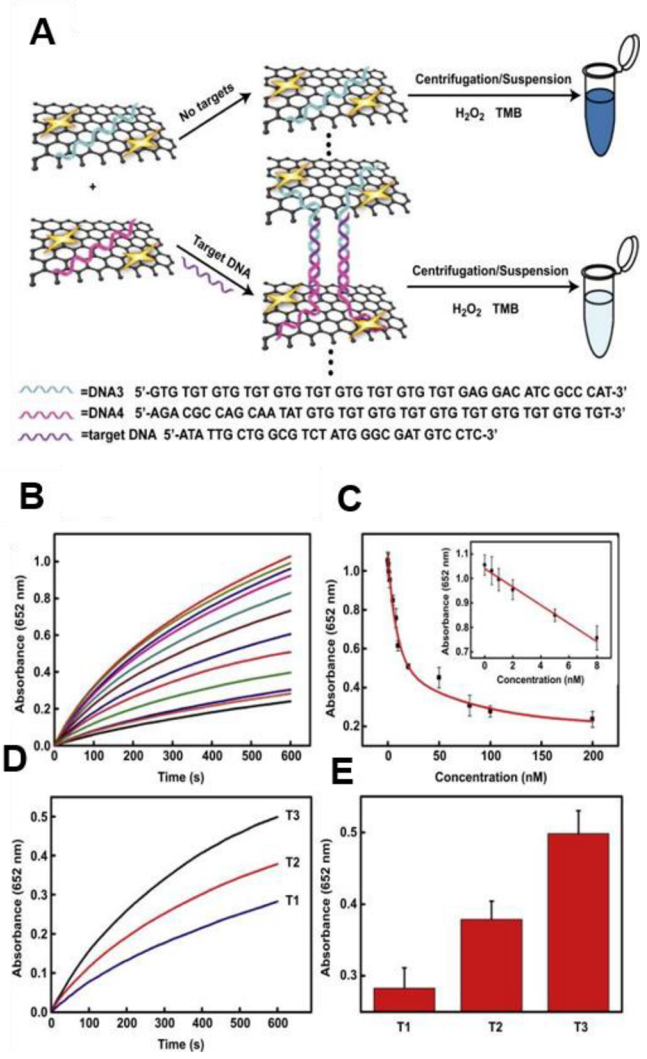

Figure 12. (A) Schematic illustration of procedures for DNA detection. (B) Time-dependent absorbance changes at 652 nm in the presence of different amounts of DNA ranging from 0 to 200 nM (0, 0.5, 1, 2, 5, 8, 10, 20, 50, 80, 100, 200 nM). (C) Calibration curve corresponding to the absorbance for various concentrations of DNA after an interval of 10 min. Inset: the linear plot. (D) Time-dependent absorbance at 652 nm with corresponding supernatant solution of the DNA−GH hybrids with 100 nM T1, 100 nM T2, and 100 nM T3. (E) The corresponding absorbance histograms. Error bars indicated the relative standard deviation of three repeated experiments. Reprinted with permission from ref 116. Copyright 2013 Elsevier.

of the two probe ssDNAs with the target sequences, the hemin−GO nanohybrids aggregated and precipitated at the bottom of the vial through centrifugation. The color change of the supernatant could be precisely measured by the absorbance of the solutions at 652 nm. A detection limit of 0.5 nM for 30-mer oligonucleotides was achieved. Graphene nanoribbons (GNRs) were recently studied for their anisotropic self-assembly function to target ssDNAs with the potential in sequence-specific Raman diagnostics.[107] The interaction between different ssDNAs (e.g., adenine (A), guanine (G), thymine (T), and cytosine (C) nucleotide bases) and GNRs could be distinguished through Raman signal change of the graphene band (G-band). Raman shifts at the G-band of 1603 cm^{-1} were induced by the different amount of charge transferred from the ssDNA to the surface of GNRs.

In addition to the above optical nucleic acid sensors, graphene-based materials have also been exploited for improving the performances of electrochemical and electronic DNA/RNA transducers. Tran et al. developed a 3D interpenetrated network of rGOs and oxidized multiwall carbon nanotubes (oxMWCNTs) coated on gold screen-printed electrodes for electrochemical immunosensing of microRNA-141 (miR-141).[82] miRNAs are small nonprotein-coding ssRNAs with only 18−30 nucleotides that play important roles in biological processes including cellular differentiation, apoptosis, proliferation, and metabolic homeostasis. The early stage discovery of metastatic prostate cancer requires a low detection limit less than 1 pM of miR-141. In this study, a sandwich amplification approach, similar to ELISA, yielded a detection limit of 10 fM for miR-141.

Another more facile electrochemical method for ssDNA detection without the fabrication step of graphene-modified electrodes was demonstrated by Lee and co-workers.[115] GOs labeled with probe ssDNAs were directly mixed with the target ssDNA sequences and then methylene blue, an electrochemical active molecule, during the detection process. The positively charged methylene blue molecules could be conjugated to both the GO surface and the probe ssDNA through electrostatic forces. However, the methylene blue/ssDNA/GO conjugates would precipitate to the bottom of the vials due to the lack of hydrophilic groups after 4 h reaction. The precipitation resulted in the decrease of methylene blue concentrations at the electrode surface. In the presence of the target ssDNAs, probe ssDNAs on the GO surface were hybridized and formed double-stranded DNAs (dsDNAs). The dsDNAs were known to be easily desorbed from the GO, while methylene blue had a lower affinity to dsDNAs to ssDNAs. These two factors led to an increasing amount of methylene blue monodispersed in the reaction solution and around the electrode surface. The methylene blue redox current changes showed a linear relationship with the log of the concentration of the target ssDNA in the range of 100−300 nM and a detection limit of 40 nM. Single-nucleotide polymorphism selectivity could also be achieved by using this graphene-additive electrochemical scheme.

Although several groups have reported the capabilities of G-FETs for electrical detections of ssDNA,[275−277] parts of their sensing principles, especially the electronic properties changes of graphene induced by the target DNA adsorptions, are still under exploration. Lin et al. developed an ultrasensitive liquid-gated G-FET sensor with an electrical detection limit of 10 pM for 12-mer ssDNA oligonucleotides and systematically investigated its sensing mechanisms.[101] In this study, the influences of target ssDNA on the G-FETs were measured based on the Hall Effect through a Van der Pauw configuration with a permanent magnet to generate the magnetic field. Both the complementary and single-base mismatched ssDNA were used as the target analytes. It was observed that the resistance and mobility of the graphene films respectively increased and decreased with an increasing concentration of the two types of target ssDNA. Moreover, the hole carrier density of G-FETs was demonstrated to be more sensitive for the detection of DNA hybridization and single-nucleotide polymorphism identification at a picomolar concentration than the conventional electrical parameters like conductivity change.

More recently, an ultrasensitive graphene-based SPR sensor with a detection limit as low as 1 aM (10^{-18} M) was demonstrated for target ssDNA analytes (Figure 13).[40] In this

DOI: 10.1021/acs.chemrev.9b00099
Chem. Rev. XXXX, XXX, XXX−XXX

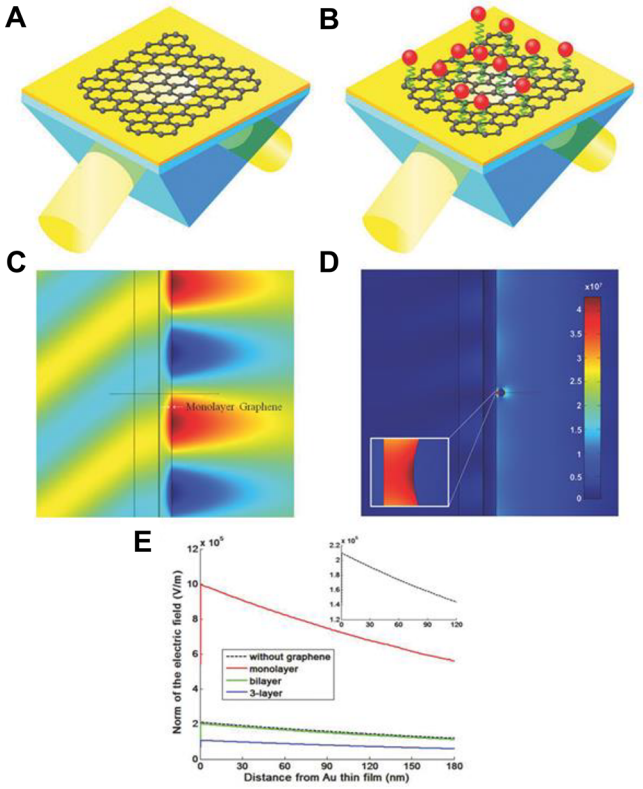

Figure 13. Designs of graphene–gold metasurface architectures. (A) Basic architecture with a layer of graphene deposited on the gold surface. To excite surface plasmon polariton over the graphene–gold interface, a light beam is typically passed through a glass prism and reflected from a 50 nm gold film deposited on one of its facets. (B) Advanced nanoparticle-enhanced architecture with the employment of Au nanoparticles as SPR amplification tags. (C) Finite element analysis (FEA) simulations of resonant monolayer graphene-coated Au sensing film: Electric field in the *y*-component, showing angle of incident light ≈52° and clear evanescent field at the sensing interface. (D) FEA simulations of resonant spherical Au NP coupling to the monolayer graphene-coated Au sensing film: Norm of the electric filed with Au NP (diameter is 30 nm, distance from the sensing film is 5 nm). (E) Cross-section plots for total electric fields along $y = 0$ with different number of graphene layers *L*. Reprinted with permission from ref 40. Copyright 2015 John Wiley and Sons.

study, the plasmon resonance enhancement effect by coating different number of graphene layers on the gold sensing film was theoretically investigated by using both finite element method and transfer matrix method, followed by experimental verifications. The electric field at the monolayer graphene-coated gold sensing interface showed a significant enhancement under the resonance condition up to 400% in comparison to that with bare gold film. Short ssDNA sequences with only 24 bases and a small molecular weight of 7.3 kDa were used for experimental measurements. Sample solutions containing ssDNA molecules with different concentrations ranging from 10^{-16} to 10^{-7} M were respectively flowed on to the CVD graphene-coated gold sensing surface. To further improve the detection sensitivity, Au NPs with optimized diameters were employed as additional signal amplification tags. Because the ssDNA molecules were naturally negatively charged, they could directly capture the positive-charged Au NPs through electrostatic interactions. Finally, positively charged 30 nm Au NPs were flown onto a ssDNA–graphene surface to confirm the enhancement effect by measuring the SPR phase signal change. The phase signal change was further amplified up to 9-fold by the Au NPs, and no significant signal changes were observed for Au NPs followed directly onto the graphene surface in the control experiments.

2.1.2.2. Carbon Nanotubes. In the past decade, CNT-based biosensors have been widely investigated and reported for many theranostic applications.[69,278,279] For example, miRNAs are found to be useful biomarkers and indicators for disease diagnostics. Li et al. designed a label-free electrochemical sensor for the detection of the miRNA-24 by using MWCNT-functionalized GCEs.[120] During the detection process, the guanine oxidation signals through the target miRNAs showed a linear relationship with the concentration of the target molecules. The MWCNTs provide a large surface area and enhance the adsorption efficiency of guanine. Also, they facilitate the electron charge transfer for the electrochemical detection process. This led to a large current leak up to 152.8 μA/cm^2 for the MWCNTs-modified GCE, which is 2.8 times higher than that of the one with bare GCE. By using the sensing scheme, a detection limit of 1 pM and a sensitivity of 4.963 μA/cm^2 decade were achieved. The detection of miRNA using CNTs as signal amplification tags was also reported by Dai's group.[121] They used a PEC sensor based on a hybrid nanostructure consisting of SWCNTs and DNA probe-functionalized CdS QDs. The DNA–CdS QDs were conjugated with oxidized SWCNTs through π-stacking force because both the DNA bases and the CNTs have aromatic ring structures. The hybrid nanostructures served as photo-electrochemically active nanotags. Briefly, the DNA-functionalized QDs would unbind from the oxidized SWCNTs after hybridizing with the target miRNA-7f molecules. Thus, a decreased signal of the photocurrent could be observed. This method provided an alternative strategy to the conventional indirect method for the miRNA sensing that required complex steps. To further enhance the sensing signal, an endonuclease called DNase I was employed to initiate a cyclic enzymatic amplification. The DNase I could cleave the DNA in DNA–RNA conjugates instead of the RNA sequences. The QDs that adsorbed onto the oxidized SWCNTs surface could prevent the DNase I to interact with the DNA probes. The SWCNTs reduced the electron–hole pair recombination of the excited QDs and induced a cathodic photocurrent. A photocurrent decline of 495 nA (up to 60%) was measured after the miRNA/DNA hybridization.

More recently, Shahrokhian et al. developed a hairpin oligonucleotide-conjugated MWCNTs nanoplatform for the electrochemical detection of ssDNA.[111] Here, an external electroactive indicator of $[Fe(CN)_6]^{3-/4-}$ was used as redox probe to monitor the conductivity signal change induced by the MWCNTs. A linear signal change with the logarithm value of the target DNA concentration was observed from 10 pM to 0.1 mM. The specificity of the MWCNT-based sensor was also studied where three types of noncomplementary DNAs or 3-base mismatched ones with a high concentration of 10 nM were flowed onto the CNT sensing surface. No significant DPV responses were observed, which indicated a good selectivity for the sensors for specific sequences. Further, Qiu and workers developed a CNT-based lateral flow sensor for rapid sensing of specific DNA sequences.[108] In their findings, the capture DNA probes with amine moieties were first functionalized to oxidized MWCNTs through diimide-

DOI: 10.1021/acs.chemrev.9b00099
Chem. Rev. XXXX, XXX, XXX–XXX

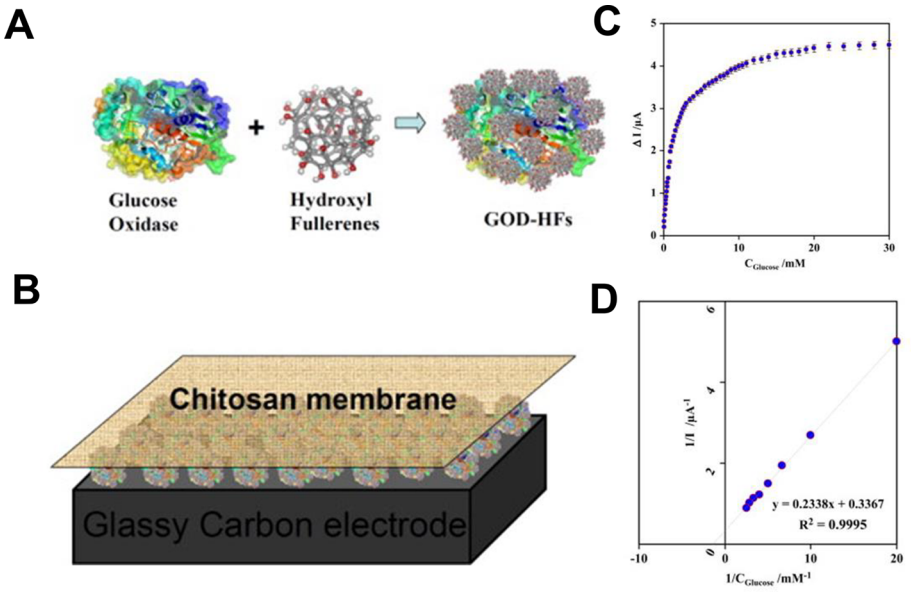

Figure 14. (A) Structure of HFs−GOx. (B) Structure of the device incorporating HFs−GOx passivated with a layer of chitosan membrane. (C) Plot of response current versus concentration of glucose. (D) Lineweaver−Burk plot for the calculation of K_m^{app}. Reprinted with permission from ref 219. Copyright 2014 American Chemical Society.

activated amidation reaction. The target DNA sequence was hybridized with the capture probe on the MWCNTs and formed a sandwich structure. It is worth noting that the MWCNTs were shortened from 5−20 μm to 0.5−2 μm by ultrasonication with strong acids to improve their monodispersity in water. A detection limit of 0.1 nM for the target DNA was obtained which benefited from the efficient lateral flow chromatographic separation and the large surface interaction area of the MWCNT. Following further quantitative analyses, the detection limit could be further improved to 40 pM. This value is 12.5 times lower than that of the Au NPs-based lateral flow sensors. Such MWCNT-based lateral flow sensors have the potential to be used for future on-site and point-of-care diagnostics of genetic and infectious diseases.

2.1.3. In Vitro Glucose Sensing by Different Nanocarbon Materials. *2.1.3.1. Fullerenes.* Wei et al. reported C_{60}-based glucose sensors integrated with GOx, ferrocene, ionic liquid, and chitosan for electrochemical signal enhancement.[86] Because of the high electron transfer rate between the GOx and the C_{60}-modified electrodes, a high sensitivity of 234.67 nA nM^{-1}/cm^{-2} with a detection limit of 3 nM and a fast response time of 0.752 s was obtained. These values were stable for up to seven months under continuous monitoring and testing, showing high reproducibility for the system. Later, a similar glucose electrochemical sensor with hydroxyl fullerenes (HFs) conjugated with GOx was built by Gao and co-workers.[219]

The HFs−GOx nanocomposites were functionalized on the GCE surface and passivated with a layer of chitosan membrane (Figure 14A,B). Chitosan/HFs could effectively maintain the secondary structure of GOx during the detection process and thus achieve the full potential of their catalytic properties. For example, the helix structure of the GOx increased from 15.2% to 20.8% after the functionalization of the chitosan protection layer. More importantly, the percentage of antiparallel structure increased from 35.6% for pure GOx to 40.8% for the GOx−HFs nanocomplex. In this study, the direct electron transfer activities of GOx could be collected and real-time monitored. The redox current linearly changed with an increasing glucose concentration from 0.05 to 1.0 mM and responded with a detection limit of 5 ± 1 μM (Figure 14C). The calculated electron transfer (k_s) rate and apparent Michaelis−Menten rate (K_m^{app}) were 2.7 ± 0.2 s^{-1} and 694 ± 8 μM, respectively (Figure 14D).

Another C_{60}-enhanced glucose sensor was demonstrated by Zhong and co-workers.[217] They fabricated spherical Pd@Cys−C_{60} NPs as signal amplification tags for the electrocatalytic reaction for glucose reduction. In this study, the fullerene was conjugated with Cys to improve the water solubility and biocompatibility. Because Cys is an amino acid that contains NH_2 groups, the amines could be reacted with the π electrons on the surface of fullerene. The Cys−C_{60} nanocomposites were then directly mixed with solutions containing potassium tetrachloropalladate to form the Pd@Cys−C_{60} NPs. An increased oxidation current and a following decreased reduction current were obtained in the presence of glucose samples. A linear amperometric signal range for the sample concentrations ranging from 2.5 μM to 1.0 mM, and a detection limit of 1.0 μM was achieved. The anti-interference ability of the sensors was evaluated with the respective addition of 0.1 mM ascorbic acid, uric acid, fructose, and *p*-acetamidophenol to 0.5 mM glucose samples. No significant current change was observed for these interfering molecules. Recently, Wu et al. developed a nonenzyme electrochemical sensor using a hybrid nanostructure of zinc porphyrin−fullerene (C_{60}) for GCE modification.[87] Two different types of ZnP−C_{60} derivatives were studied, i.e., *ortho*-ZnP−C_{60} (ZnP_o−C_{60}) and *para*-ZnP−C_{60} (ZnP_p−C_{60}). The authors showed that the ZnP_p−C_{60} with a bent conformation exhibited a narrower energy gap and higher electron-transport rate. In the following experiments, the ZnP_p−C_{60} was embedded in a tetraoctylammonium bromide nanofilm and coated on the GCE. The obtained tetraoctylammonium bromide/ZnP_p−C_{60}/GCE were tested with H_2O_2 as target sensing samples. Four clear quasi-reversible redox pairs were obtained during the catalytic reduction process of H_2O_2 without any enzyme

DOI: 10.1021/acs.chemrev.9b00099
Chem. Rev. XXXX, XXX, XXX−XXX

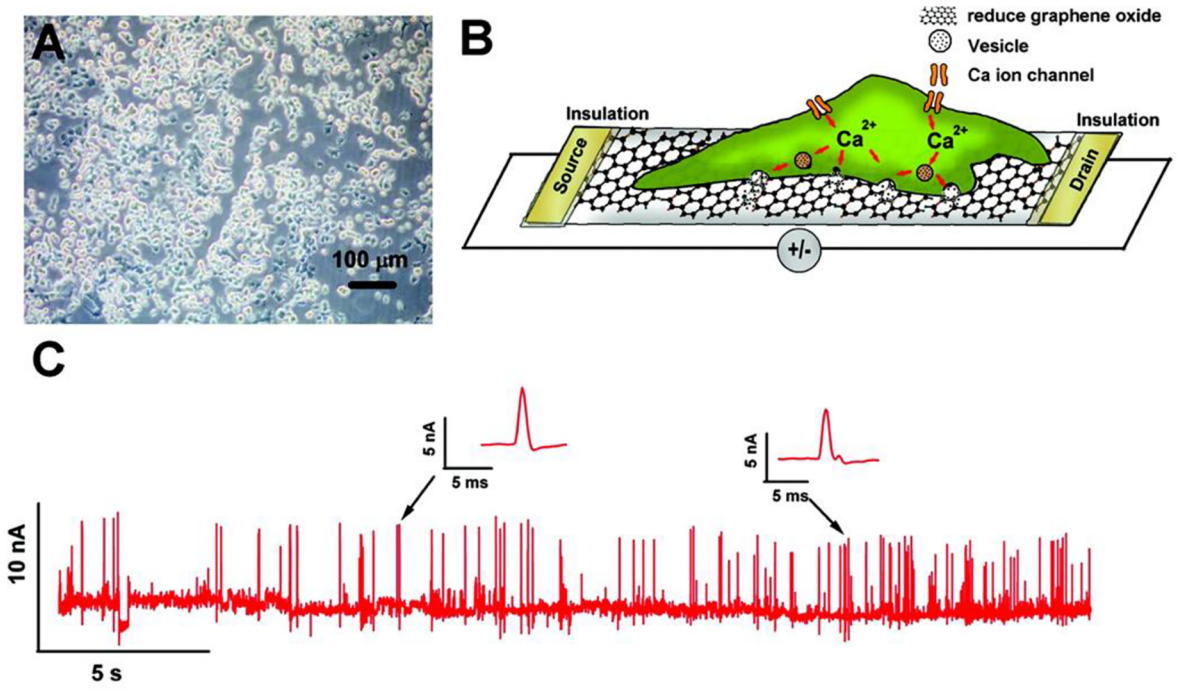

Figure 15. (A) Optical image of PC12 cells grown confluently on poly L-lysine coated rGO−PET device. (B) Schematic illustration of the interface between a PC12 cell and rGO FET. (C) Real-time response of rGO−PET FET to the vesicular secretion of catecholamines from PC12 cells stimulated by high K^+ solution, V_{ds} = 100 mV and V_g = 0 V. The distance between the drain and source electrodes in the device is fixed at 1 cm. Reprinted with permission from ref 176. Copyright 2010 American Chemical Society.

molecules. The catalytic current was proportional to the H_2O_2 concentration and linearly changed from 0.035 to 3.40 mM with a detection limit of 0.81 μM and a high sensitivity of 215.6 μA/mM. Followed by H_2O_2, nitrite solutions were added to induce a reverse oxidation process. The current signal linearly changed with the nitrite concentration range from 2.0 μM to 0.164 mM with a detection limit of 1.44 μM and a high sensitivity of 249.9 μA/mM.

2.1.3.2. Nanodiamonds. Carbon nanohorns (CNHs) have pseudo-3D porous nanostructures based on NDs and SWCNTs as enhanced sensing components coated on the electrodes.[216] The electrodes are first deposited with NDs and SWCNTs, followed by the assembly of pyrene−nitrilotriacteic acid through a dip-coating method. The depositions of NDs on the surface of SWCNTs are spatially controlled and optimized to result in a structure for diffusing biological molecules with sizes ranging from 3 to 10 nm. The 3D scaffolds are strengthened by electrogeneration of a thin layer of polypyrene films. The pyrene−nitrilotriacteic acid functionalization layer creates more attachment spots for the immobilization of biocapturers such as biotin or histidine-labeled proteins. Glucose oxidases labeled with biotin molecules as biocapturers have achieved a high sensitivity of 85.78 mA/M^1 cm^2 for the target glucose molecules. Control experiments carried out with only SWCNT layer in the absence of NDs show lower sensitivity of 20.22 mA/M^1 cm^2 and a much lower maximum current density of 40.44 $\mu A/cm^2$.

A boron-doped diamond (BDD) electrode incorporated with NDs and nickel nanosheets was fabricated by Dai and co-workers for direct glucose detection without enzymes.[215] The NDs electrodeposited on the surface of BDD substrate served as nucleation centers for the following Ni depositions. The sensors exhibited a linear detection range for glucose samples from 0.2 to 1055.4 μM with a detection limit of 0.05 μM. The sensing ability of the ND electrode for quantitative detection of glucose in real human serum (8.6−450.8 μM) was studied as well. The recovery values for glucose in the serum sample solutions were as high as 103.1%. To test the specificity of the sensor, the current responses to negative control solutions of Na_2HPO_4, $CaCl_2$, $NiSO_4$, $Mg(NO_3)_2$, $FeCl_3$, and $Cu(CH_3COO)_2$ were measured and only tiny signal changes were observed (−2.46%, 0.48%, 8.05%, 0.58%, −1.46%, and 3.49%, respectively) in comparison to the glucose ones. For the nontarget interference species in human serum- ascorbic acid, dopamine, L-cysteine, L-lysine, and L-alanine, only small current changes (less than 6%) were recorded.

2.1.3.3. Carbon Dots. Shen et al. fabricated boronic acid-functionalized C-dots for the quantitative determination of blood glucose concentration in human serum.[280] The C-dots were prepared by a facile hydrothermal carbonization process with phenylboronic acid as the carbon source. The boronic acids are known as the recognition groups for glucose. In addition, the inert property of the C-dot surface promises its high specificity toward the target glucose molecules. When the target glucose samples were flowed and mixed with the C-dots, they led to the aggregation of the C-dots due to covalent binding between the boronic acid and *cis*-diols on the glucose and thus resulted in fluorescence quenching. The decreased fluorescence intensity at 408 nm changed linearly for a wide glucose concentration range from 9 to 900 μM with a detection limit of 1.5 μM. This value was improved by at least 1 or 2 orders of magnitude compared to that of the boronic acid nanosensors without C-dots. Different interference assays such as ascorbic acid, uric acid, dopamine, and glutathione were mixed with the target glucose, and no significant fluorescence quenching or enhancement was obtained. The C-dots-based nanosensors show better selectivity against the semiconductor and metallic nanoparticles because the metallic

DOI: 10.1021/acs.chemrev.9b00099
Chem. Rev. XXXX, XXX, XXX−XXX

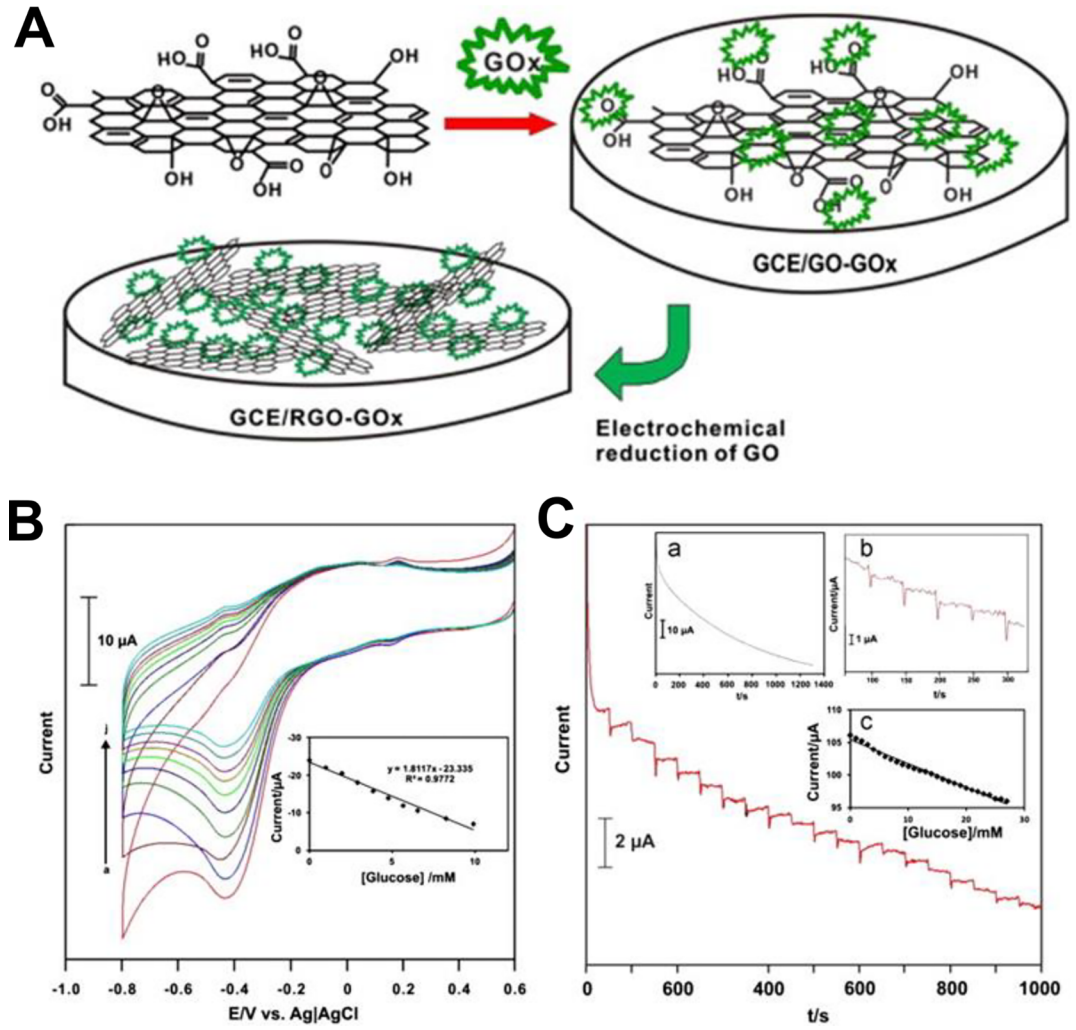

Figure 16. (A) Schematic illustration of the fabrication of RGO−GOx composites. (B) Cyclic voltammograms of GCE/RGO−GOx in oxygen-saturated PBS containing different level of glucose concentration. Inset: linear dependence of I_{pc} versus glucose concentrations. Reprinted with permission from ref 207. Copyright 2012 American Chemical Society.

ions and atoms from these particles are active to the amino and thiol groups present on the interference molecules. As an example of the clinical trial for the C-dots sensor, 20 μL of the serum solutions were measured and the results matched well with a commercial glucose monitor.

2.1.4. In Vitro Detection of Other Biologically Related Molecules by Different Nanocarbon Materials. *2.1.4.1. Graphene and Graphene Oxides.* In addition to DNA/RNA oligonucleotides and protein-related molecules, other important biomarkers such as hormones, glucose in different sensing matrices (e.g., blood serum, urine and saliva), and even volatile organic compounds from exhaled breath can also be detected by using graphene biosensors with improved sensitivity compared to that of the traditional ones.[281−283] For example, He et al. reported the fabrication and patterning of rGO on flexible polyethylene terephthalate (PET) substrates to construct FET sensors (Figure 15).[176] The rGO-FET sensors were used for detecting and tracking the hormonal catecholamine molecules in living neuroendocrine PC12 cells. Because the resulting FET sensors were front-gated or solution gated, the gate voltage falls through a thin double layer capacitance (less than 1 nm) that promises better FET performance to the responses at the rGO solutions' sensing interfaces than the conventional back-gated ones. Before the micropatterning process, the substrates were functionalized with 3-aminopropyltriethoxysilane (APTES) self-assembled monolayers for making the surface positively charged in order to prevent the aggregation of rGOs. Detection of dopamine molecules was demonstrated using these rGO-FET sensors. Dopamine molecules are the main neurotransmitters secreted from the neurons and hormones generated from neuroendocrine cells. Because of the doping effect induced by π-stacking interaction between the dopamines and the rGOs, the increased concentration of dopamine solutions led to a right shift of the Dirac point in the current−voltage curves of the rGO-FET sensors.

Later, Wang and co-workers demonstrated a graphene-based FRET sensor for detecting adenosine triphosphate (ATP) molecules and real-time molecular probing of living cells.[179] The GOs nanoprobes were functionalized with ATP aptamer−carboxyfluorescein (FAM/GOs) to enable the specific targeting ability and further improve the delivery efficiency of the labels. In the absence of the target ATP molecules, the fluorescence of the FAM-labeled ATP aptamers was quenched by the GOs. To obtain the best quenching performance, different concentrations of GO solutions from 1 to 6 μg/mL

DOI: 10.1021/acs.chemrev.9b00099
Chem. Rev. XXXX, XXX, XXX−XXX

were mixed with 100 nM ATP aptamer−FAM solutions. The optimum concentration for GO solutions was found to be 3 μg/mL with a quenching efficiency up to 95.6%. While in the presence of target ATP molecules, the quench could be recovered due to the release of the ATP aptamers from the GO surface because the adsorption between the target ATP and ATP aptamers was much stronger than the binding between the ATP aptamers and the GO nanoprobes. A wide sensing range for ATP solutions with concentrations ranging from 10 μM to 2.5 mM was achieved with a high selectivity against other interfering molecules like CTP, TTP, and GTP. Only the ATP molecules could induce a high fluorescence recovery rate of 85.7%. The in vitro specificity of the aptamer-functionalized GO probes was also tested by incubating them with mice epithelial cells (JB6 Cl 41-5a), and a much stronger FAM fluorescent signal was obtained compared to that of the cells incubated with random DNA oligonucleotides-functionalized FAM/GO probes or pure GO probes.

An electrochemical glucose sensor by using glucose oxidase-conjugated reduced GOs (GOx−rGOs) as signal amplification tags to enhance the charge transfer process was designed by Unnikrishnan and co-workers (Figure 16A).[207] The nanocomposites were drop-cast onto the surface of a GCE and then electrochemically reduced to rGO under a continuous voltage cycling from 0 to 1.5 V (15 cycles) with a scan rate of 50 mV/s. It was found that the anodic and cathodic peak potentials for the RGO−GOx coated GCE would shift to the negative values with increasing pH from 1 to 13. The authors used two different electrochemical approaches to determine the glucose concentrations in the sample solutions. The first one was the traditional electrocatalytic GCE experiment based on cyclic voltammograms. Upon glucose oxidation, the oxygen amount in the PBS would decrease with increasing glucose concentration (Figure 16B). Thus, the oxidation peak current increased with decreasing reduction peak current. In this case, a linear relationship between the peak current and the glucose concentration could be obtained. The second approach was the amperometric measurement by using RGO−GOx functionalized-rotation disk electrode. The current signals collected from this method were more stable than the former electrocatalytic one in terms of a lower drifting value after each glucose addition (Figure 16C). Moreover, a high sensitivity of 1.85 μA/mM cm^2 with a wide detection range from 0.1 to 27 mM was also achieved.

Recently, Nag et al. fabricated an electronic nose-like sensor based on β-cyclodextrin-conjugated rGOs.[206] They demonstrated its ability to distinguish complex lung cancer biomarkers consisting of a series of volatile organic compounds (VOC). Pyrene adamantane molecules were used as linkers to conjugate the rGOs with β-cyclodextrin (rGO@PYAD-CD) through π-stacking interaction. The conjugates were respectively further functionalized with three different groups including mannose (rGO@PYAD-MCD), amino groups (rGO@PYAD-NCD), and perbenzylated cyclodextrin (rGO@PBCD). The rGO@PYAD-MCD had a longer spacer for facile disconnection and also provided the hydroxyl groups, and rGO@PYAD-NCD could reversibly bind with acetone molecules through covalent interactions by its amino groups while rGO@PBCD showed a strong nonpolar property with aromatic ring structures. These cyclodextrin-conjugated rGOs were arranged in three sensor arrays and exposed to 10 VOC biomarkers (benzene, toluene, *p*-xylene, methanol, ethanol, propanol, 2-propanol, acetone, formaldehyde, and water). The principal component analysis (PCA) mapping results showed that the electronic nose-like rGO sensors could differentiate each specific biomarker as 2-propanol out of the other alcoholic VOC or water. The noise of the rGO@PBCD biosensor was eight times lower than that with the pure rGO tags in a signal-to-noise ratio of 88:11 for 400 ppb benzene vapor. Furthermore, Ensafi et al. prepared cobalt ferrite-functionalized GO nanohybrids ($CoFe_2O_4$/GO) for quantitatively determining the concentration of nicotinamide adenine dinucleotide (NADH) and H_2O_2 with high specificity.[195] Under a high temperature reaction of 600 °C, the GO of the hybrids was converted to rGO and then deposited on a GCE to achieve enhanced electrochemical sensing. The Raman spectrum for the resulted nanohybrids indicated that the number of GO sheets ranged between 5 and 10 layers. The surface modification of $CoFe_2O_4$/GO on the GCE were confirmed by the cyclic voltammograms of NADH, where the oxidation peak potential shifted from 712 to 585 mV. To test the anti-interfering and sensing ability of the $CoFe_2O_4$/GO-GCE, the concentration of H_2O_2 was measured in rainwater samples. The current signal changes accurately showed the presence of 30.0 ± 1.8 μmol/L of H_2O_2 in the rainwater sample, which matched well with the concentration determined by the traditional potassium permanganate titration approach. A wide detection range for NADH from 0.5 to 100.0 μmol/L and for H_2O_2 from 0.9 to 900.0 μmol/L was obtained with a respective detection limit of 0.38 and 0.54 μmol/L.

2.1.4.2. Carbon Nanotubes. In addition to electrochemical sensors, capacitive field-effect sensors incorporated with polyamidoamine (PAMAM) dendrimer-functionalized CNTs as a host matrix have also been demonstrated.[199] A layer-by-layer CNT nano thin film was designed for the use of capacitive electrolyte−insulator−semiconductor (EIS) measurement. Urea molecules were chosen as the testing target samples. Two different sensing configurations, comprising the urease enzyme on the top of the CNT thin film [EIS-(PAMAM/CNT)-urease] or sandwiched between the CNT thin film and another CNT layer [EIS-(PAMAM/CNT)-urease-CNT], were respectively used. The sensing signals were collected through the measurements of capacitance−voltage and dynamic constant capacitance for urea samples with concentrations ranging from 0.1 to 100 mM. The sandwiched EIS-(PAMAM/CNT)-urease-CNT sensor showed a sensitivity of 33 mV/decade, which was 2 times those of EIS-urease w/o CNTs and EIS-(PAMAM/CNT)-urease ones. The sensors also showed higher signal stability (only 0.5 mV/min drift), and no irregular signal jumps were observed with increasing urea concentration.

2.1.4.3. Fullerenes. Fullerenes C_{60} and C_{70} exhibit high electron affinities, large surface-to-volume ratios and good adsorption abilities to organic molecules through either covalent or noncovalent bindings.[157,284,285] These characteristics allow them to be functionalized with versatile enzymes as enhanced nanotags or sensing substrates for the ultrasensitive detection of analytes in different chemical and biological matrices including blood serum, milk, juice, and even river water.[186,286] Goyal et al. fabricated a fullerene-C_{60} functionalized pyrolytic graphite electrode for electrochemical determination of dexamethasone concentrations from both pharmaceutical agents (e.g., decaron, demisone, and decdan) and human blood plasma.[182] Dexamethasone is a doping agent that is found to be abused by professional athletes for improving their performances. The accurate and rapid

DOI: 10.1021/acs.chemrev.9b00099
Chem. Rev. XXXX, XXX, XXX−XXX

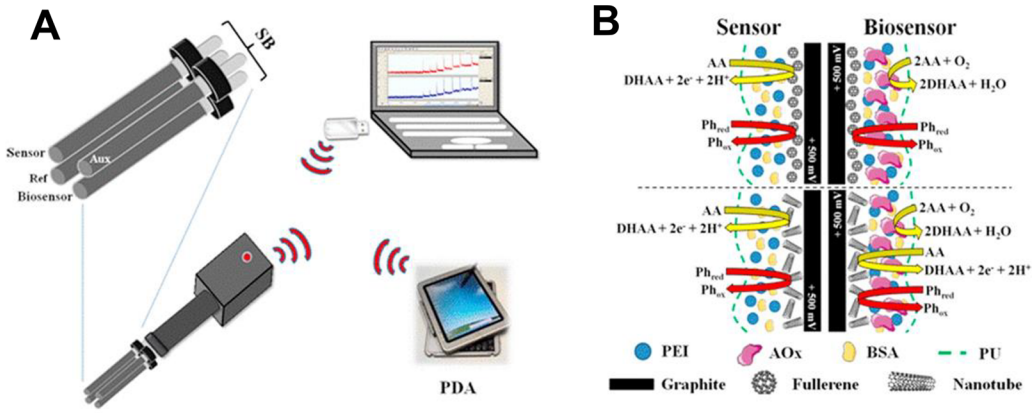

Figure 17. (A) Schematic illustration of the telemetric device interconnected with a laptop or PDA. (B) Schematic illustration of the sensor functionalized with fullerenes or nanotubes. Reprinted with permission from ref 205. Copyright 2012 American Chemical Society.

detection of this type of synthetic steroid molecule is highly desirable out of antidoping concerns. The large electroactive surface area of the fullerene results in a high electron mediation efficiency during the electrocatalytic reduction process of dexamethasone. The sensing signals were acquired during the reduction process of the dexamethasone molecules to generate hydroxyl groups. A pH-dependent peak potential was observed for the fullerene-functionalized GCE with a dE_p/dpH of 59 mV/pH. A wide detection range from 0.05 to 100 μM was achieved with a sensitivity of 0.685 μA/μM and a detection limit of 55 nM for the dexamethasone molecules at pH 7.2. The detection limit was improved by more than 2 orders of magnitude compared to that measured by the traditional differential pulse polarography method.

Besides the above-mentioned fullerene-electrochemical sensors, Barberis et al. designed C_{60} and C_{70}-based two-channel telemetric sensors for simultaneous multiplex detection of ascorbic acid in fruit juices (Figure 17A).[205] It is worth nothing that when the fullerenes were functionalized with the ascorbate oxidases (AOx) (Figure 17B), the selectivity of the sensors for ascorbic acid and phenol was higher than those of single or multiwalled CNTS−AOx-modified sensing devices. This was attributed to the larger surface area of fullerenes that could attach a larger number of AOx molecules. The sensitivity of C_{60} and C_{70}-modified graphite electrodes respectively showed 20% and 50% increases in comparison to the one with bare graphite electrodes to the target ascorbic acid and antioxidant phenol molecules. The fullerene-enhanced telemetric sensors worked under an electric potential of +500 mV and could achieve a detection limit of 0.10 and 0.13 μM with C_{60} and C_{70} as signal amplification tags, respectively. Thus, different fruit juices, including kiwi, blueberry, and orange, could be tested by using the fullerene-telemetric sensors.

2.1.4.4. Nanodiamonds. Nanometer-scaled diamonds (NDs) that contain the NV defect centers have become attractive nanosensor candidates for detecting biological and chemical samples because they exhibit good biocompatibility, strong photoluminescence, and high magnetic responses under ambient conditions.[287−289] The fluorescence of NDs originates from the electronic spin state of their NV centers that promises long coherence time for the optical detection based on single NV center. Gopalan et al. fabricated ND-sponges functionalized with horseradish peroxidase (HRP) enzymes and porous poly(aniline)−poly(2-acrylamido 2-methylpropanesulfonic acid) (PANI−PAMPSA) networks (ND-NS(HRP)) for electrochemical sensing of H_2O_2.[235] The PANI is a conducting polymer which can be conjugated to the amine groups on the surface of NDs together with PAMPSA by *o*-phenylenediamine and 2-vinyl aniline as linker molecules. Because the HRP can simultaneously polymerize aniline and AMPSA, the HRP enzymes get trapped into the PANI−PAMPSA networks in the formation process of ND-NS. On the basis of the amperometric measurements with ND-NS(HRP)-modified electrodes, a high electron transfer rate of 1.85 s^{-1} was obtained for the HRP enzymes entrapped in the ND-NS composites. A linear detection range from 1 to 45 mM for H_2O_2 through an electrocatalytic reduction process was observed with the ND-NS(HRP). A high sensitivity of 129.6 μAM with a low detection limit of 59 μM and a low response time of 5 s was achieved. The specificity of the sensors were further tested by flowing negative control molecules of acetaminophen, ascorbic acid, and dopamine to the sensing surface at a concentration of 0.5 mM with 2 mM target H_2O_2, and no changes in the current responses were observed.

A nitrogen-doped diamond nanowire (N-DNW) substrate for enhanced electrochemical sensing of urea was developed by Shalini and co-workers.[198] The N-DNW electrode was functionalized with urea enzymes consisting of urease and glutamate dehydrogenase (GLDH) molecules through EDC−NHS interactions. The current signal corresponding to the Urs−GLDH/N-DNW electrode showed a linear increase in current with an increasing urea concentration from 10 to 100 mg/dL. Similar signal changes were also observed for human urine samples in PBS with concentrations from 1:9 to 4:6. The Urs−GLDH/N-DNW sensors showed a high sensitivity of 6.18 μA/mg dL/cm^2 and a low detection limit of 3.87 mg/dL with a fast response time of 10 s to target urea molecules. In addition, a long shelf time for the DNW electrode up to 14 days was obtained with 80% enzyme activity, depicting the high stability of the electrode.

Recently, Zhang et al. reported another cost-effective method for the preparation of ND sensing electrodes instead of the expensive CVD approach.[88] They used a sonication-based structuring process that could prevent the functionalized ND from hydrolyses. The authors optimized the solvent for the NDs to achieve the highest surface coverage on the electrode. Different solvents including water, acetone, 2-propanol, ethanol, and methanol were mixed with dimethyl sulfoxide for the modification of ND electrodes through sonication.

DOI: 10.1021/acs.chemrev.9b00099
Chem. Rev. XXXX, XXX, XXX−XXX

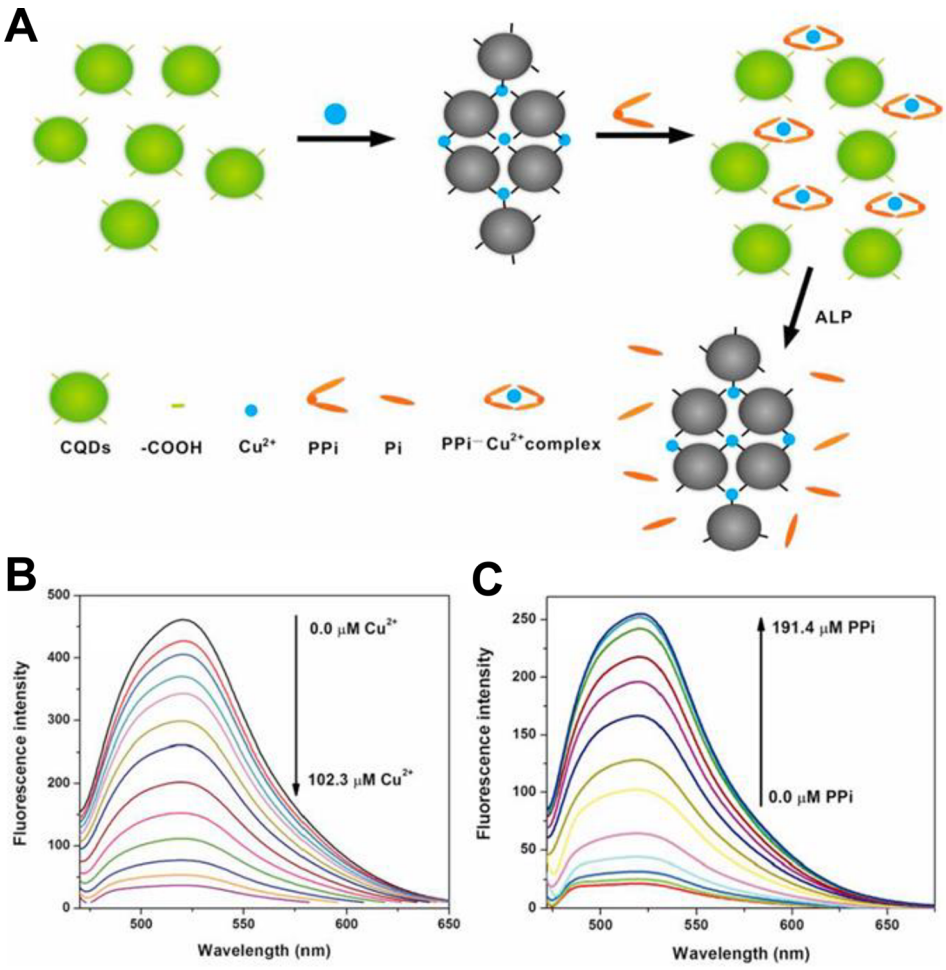

Figure 18. (A) Schematic illustration of the detection strategy for pyrophosphate anions and ALP activity based on aggregation and disaggregation of CQDs. (B) Fluorescence response of CQDs with increasing amount of Cu^{2+}. (C) Fluorescence response of CQD and Cu^{2+} mixture with increasing concentration of pyrophosphate anions. Reprinted with permission from ref 202. Copyright 2012 American Chemical Society.

Among them, the methanol and dimethyl sulfoxide mixtures showed the largest ND surface coverage of 33.6%. The large surface coverage could enhance the capture ability of the biosamples. To further enable the selectivity, the NDs were hydrogenated to conjugate with specific antibodies by UV−alkene interactions. *Escherichia coli O157:H7* bacteria solutions with a concentration of 10^6 cfu/mL were chosen as the target samples for the impedance spectroscopy measurements based on the ND-decorated interdigitated electrodes (ND-IDEs). A high capture efficiency of 800 cells/mm^2 was estimated in the optimized ND-IDEs. The charge transfer resistance was decreased by 38.8% with the ND-IDEs in the presence of the *E. coli* bacteria. This value is improved by 150% compared to the one with traditional redox probes. These results indicate that the ND-IDEs enable highly sensitive detection in low-conductivity sample solutions.

2.1.4.5. Carbon Dots. Carbon quantum dots (CQDs) have also been explored for biosensing applications. Qian et al. designed a CQDs-Cu^{2+} fluorescent assay to real-time monitor the activity of alkaline phosphatase (ALP) (Figure 18A).[202] The concentration of human ALP is used for the diagnosis of diabetes, prostate, and breast cancer. Here, CQDs were combined with pyrophosphate anions as a fluorescent reporter. The abundant carboxyl groups on the CQD surface resulted in significant aggregation when mixed with Cu^{2+} ions, leading to fluorescence quenching (Figure 18B). Because the affinity between pyrophosphate anions and the Cu^{2+} ions was stronger than that between carboxyl groups and Cu^{2+} ions, the presence of pyrophosphate anions would break the CQDs-Cu conjugates and free the CQDs. Thus, a fluorescence recovery could be observed (Figure 18C). On the basis of this scheme, the quenching was strongly dependent on the ALP amounts. A detection range of 16.7−782.6 U/L with a detection limit of 1.1 U/L was achieved for the ALP. It is worth noting that this value is much lower than the ALP level in the human serum ranging from 40 to 170 U/L and can be employed for the clinical diagnosis of blood samples.

A C-dots ratiometric fluorescent sensor for detecting superoxide anions ($O_2^{\bullet-}$) was also designed by Gao and co-workers.[241] The $O_2^{\bullet-}$ are among the primary type of ROS that are highly reactive toward proteins, nucleic acids, and lipids. They have been considered as important markers in cellular pathology for diagnosing diabetes, malignant tumors, and even Parkinson's diseases. The C-dots were conjugated with a hydroethidine (HE) molecule as a selective recognition element to the target $O_2^{\bullet-}$. In the absence of the target $O_2^{\bullet-}$, the hybrid CD-HE nanostructures showed an emission peak centered at 525 nm originated from the C-dots with 488 nm light excitation. After the $O_2^{\bullet-}$ were reacted with the CD-HE, there was a new emission peak at 610 nm that generated

DOI: 10.1021/acs.chemrev.9b00099
Chem. Rev. XXXX, XXX, XXX−XXX

Table 2. Summary of Carbon-Based Nanomaterials for in Vitro Cellular Imaging

cell model	imaging technique	material type	functional group/molecules	material scale	dose	ref
neural precursor	fluorescence	ND	silicon vacancy	100 nm	100 μg/mL	295
ThP-1 macrophages	fluorescence (blue luminescence)	GQD	carboxylic group	15−30 nm	4 μg/mL	296
Hs-578	fluorescence	C-Dot	carboxylic group	3.1 ± 0.3 nm	0.5 mg/mL	297
Human embryonic kidney						
293T	fluorescence	ND	nitrogen vacancy	100 nm	2 mg/mL (1×10^{12} particles/mL)	298
	optical scattering	ND	cationic liposomes	55 nm	1×10^3 particles/cell	299
Stem cells						
mouse P19 (neuronal differentiation)	fluorescence	ND	NV and carboxylic group	120 nm	50 μg/mL	61
Multipotent Stromal						
489-2.1	fluorescence	ND	NV and carboxylic group	100 nm	80 μg/mL	300
Bladder cancer						
BFTC905	fluorescence	ND	MNPs and PAA/FMA	131.7 nm	50 μg/mL	301
Breast cancer						
BCap-37	fluorescence	C-Dot	carboxylic group	3.1 ± 0.3 nm	0.5 mg/mL	297
BT-474	Raman imaging	SWCNT	Her-66 antibody	D = 1.5 nm L = 200−500 nm	0.097 μg/μL	302
MCF-7	fluorescence	GS	gelatin and R6G	monolayer and LD = 80−750 nm	5 μg/mL	303
	fluorescence	fullerene-C_{60}	C_{60}^{3-} ions	5 nm	160 μg/mL	300
	SERS	SWCNT	DTNB-QD-Au NPs-SPION@SiO2@PEI	D = 300 nm L = 0.4−1 μm	20 μg/mL	304
	fluorescence	SWCNT	DTNB-QD-Au NPs-SPION@SiO2@PEI	D = 300 nm L = 0.4−1 μm	20 μg/mL	304
	fluorescence	GQD	carboxylic group	5 nm	2 mg/mL	305
	fluorescence	C-dots	DNA−aptamer	4.8 nm	100 μg/mL	306
MDA-MB-231	fluorescence	ND	fluorescently-labeled oligonucleotide and anti-EGFR	2−8 nm	25 μg/mL	307
	SPECTRL	SWCNH	sodium alginate	50−100 nm	85 μg/mL	308
	fluorescence	SWCNH	QD and PEG	80−100 nm	0.025 mg/mL	309
SK-BR-3	two-photon luminescence	GO	S6 RNA aptamers	monolayer and LD = 10−1000 nm	6.4×10^4 cells/mL	310
	SERS	SWCNT	4ATP-QD-Au NPs and SPION@SiO2@PEI	D = 300 nm L = 0.4−1 μm	20 μg/mL	304
	fluorescence	SWCNT	4ATP-QD-Au NPs and SPION@SiO2@PEI	D = 300 nm L = 0.4−1 μm	20 μg/mL	304
Cervical cancer						
HeLa	fluorescence	GO	fluorescein−PEG	monolayer and LD = 10−1000 nm	2.5 μg/mL	311
	MRI	GO	aminodextran-coated Fe_3O_4 NPs	174.4 nm	5 μg/mL	312
	fluorescence	GO	caspase-3-specific peptide	monolayer and LD < 200 nm	70 μg/mL	139
	Raman imaging	GO	Au NPs (20 nm)	monolayer and LD = 100−400 nm	4 μg/mL	313
	fluorescence	GO	PAA and FMA	40−60 nm	20 μg/mL	314
	fluorescence	GO	PEG	40 nm	0.2 mg/mL	315
	fluorescence	GO	β-cyclodextrin	monolayer and LD = 10−500 nm	0.75 μg/mL	316
	PAT	GO	ICG−FA	200 nm	20 μg/mL	317
	Raman imaging	GO	FA and Ag NPs (15 nm)	monolayer and LD = 50−400 nm	1 μg/mL	318
	Raman imaging	GO	Au NPs (30 nm)	monolayer and 97.67 nm	20−80 μg/mL	319
	fluorescence	rGO	transferrin and SiO_2-coated QDs	125 nm	20 μg/mL	320
	fluorescence	GO	coumarin and SS−DEAC	monolayer and LD = 100−300 nm	20 μg/mL	219
	two-photon luminescence	GO	coumarin and SS−DEAC	monolayer and LD = 100−300 nm	20 μg/mL	219
	fluorescence	ND	NV and carboxyl groups	140 nm	0.8 μg/mL	321

DOI: 10.1021/acs.chemrev.9b00099
Chem. Rev. XXXX, XXX, XXX−XXX

Table 2. continued

cell model	imaging technique	material type	functional group/molecules	material scale	dose	ref
Cervical cancer						
	two-photon luminescence	ND	NV and carboxyl groups	140 nm	0.8 μg/mL	321
	fluorescence (λ_{em} = 510−555 nm and λ_{exc} = 478−495 nm)	ND	PFM−PAAv and Fe@CNP	80−100 nm	47.62 μg/mL	322
	fluorescence	ND	NV	35 nm	0.8 μg/mL	323
	fluorescence	ND	NV and carboxylic group	25 nm	5.7 μg/mL	324
	fluorescence	ND	NV and carboxylic group	46 nm	20 μg/mL	325
	fluorescence	ND	transferrin	100 nm	10 μg/mL	326
	fluorescence	ND	mitochondria antibody	6−8 nm	10 μg/mL	327
	fluorescence	ND	NV	45 nm	20 μg/mL	328
	STED	ND	BSA	30 nm	150 μg/mL	329
	fluorescence	ND	NV and carboxylic group	100 nm	80 μg/mL	300
	direct electron-beam excitation-assisted fluorescence	ND	NV complex and carboxylic group	148.4 ± 42.6 nm	9.03 μg/mL	330
	direct electron-beam excitation-assisted fluorescence	ND	NV and carboxylic group	104.4 ± 26.4 nm	9.38 μg/mL	330
	fluorescence	SWCNH	transferrin and chitosan/CdTe QDs	60−80 nm	182 μg/mL	331
	STED	ND	NV and GNRs	100 nm		332
	dual-color fluorescence	CQD	C−N, N−H, Si−O, and −OH	3.6 ± 1.6 nm	456 μg/mL	333
	fluorescence	GQD	folic acid	2.3 nm	20 μg/mL	334
	fluorescence	GQD	nitrogen doped	3.8 nm	6 μg/mL	97
	MRI	GQD	folate−Gd	5−10 nm	0.15 mM	335
	fluorescence	GQD	folate−Gd	5−10 nm	3 mg/mL	335
	fluorescence	GQD	hypocrellin A and porous silica NPs	30 nm	20 μM	336
	fluorescence	GQD	PEG	88 ± 18 nm	2 mg/mL	337
	fluorescence	C-Dot	nitrogen-doped and carboxylic group	2.97 nm	55 μg/mL	338
	dual-color fluorescence	C-Dot	phosphate	2.7 ± 0.5 nm	200 μg/mL	339
	dual-color fluorescence	C-Dot	hydroxyl group	2.5 ± 0.5 nm	100 μg/mL	230
	multicolor fluorescence	C-Dot	TTDDA and nitrogen-doped	4 nm	100 μg/mL	340
	fluorescence	C-Dot	folic acid	5−10 nm	1 g/mL	341
	fluorescence	C-Dot	ZIF-8	2 nm	30 μg/mL	342
	near-infrared fluorescence	SWCNT	DNA and SDS		0.25 mg/L	343
	fluorescence	C-Dot	ZIF-8	2 nm	30 μg/mL	342
Colorectal cancer						
RKO	fluorescence	ND	MNPs and PAA/FMA	131.7 nm	50 μg/mL	301
Fibroblast						
Embryo						
NIH/3T3	fluorescence	GO	PEG and Zn-doped $AgInS_2$ NPs	monolayer and LD = 63.5−99.4 nm	50 μg/mL	344
	fluorescence	GO	quaternized carbon dot	mono- and bilayer and LD = 10−1000 nm	100 μg/mL	345
	optical scattering	ND	cationic liposomes	55 nm	1×10^3 particles/cell	299
	transient absorption	ND	carboxylic group	35 nm	10^5 cells/cm^2	346
	fluorescence	C-Dot	amino and carboxylic group	2−6 nm	20 μg/mL	229
	fluorescence	ND	silk fibroin	22−70 nm	1 mg/mL	347
Glioblastoma						
C6	fluorescence	C-Dot	amide and carboxyl	3−4 nm	0.83 mg/mL	348
U-87 MG	fluorescence	ND	silica shell and cRGD-Alexa Fluor 488	150 nm	50 μg/mL	349
	fluorescence	rGONR	PEG−cy3−RGD	monolayer and LD = 1 μm	1 μg/mL	350
Gastric carcinoma						
AGS	two-photon luminescence	GO	PEG and transferrin	30 nm	20 μg/mL	351
Liver carcinoma						
Bel-7402	fluorescence	GO	FITC and cRGD-modified chitosan	monolayer and LD = 10−100 nm	20 μg/mL	352
HepG2	Raman imaging	rGO	Au nanoclusters	monolayer	1.75 μg/mL	353
	fluorescence	GO	FITC and cRGD-modified chitosan	monolayer and LD = 10−100 nm	20 μg/mL	352

DOI: 10.1021/acs.chemrev.9b00099
Chem. Rev. XXXX, XXX, XXX−XXX

Table 2. continued

cell model	imaging technique	material type	functional group/molecules	material scale	dose	ref
Liver carcinoma						
	fluorescence	fullerene-C_{70}	tetraethylene glycol and PLLA nanofibers	20 nm	10 wt %	354
	MRI	GO	DTPA−Gd	monolayer and LD = 100−300 nm	25 μM Gd^{3+}	355
	fluorescence	GQD	organosilane and hollow silica spheres	20 nm	200 μg/mL	356
	fluorescence	fullerene-C_{70}	tetraethylene glycol and PLLA nanofibers	20−60 nm	20 wt %	357
Huh-7	fluorescence (green luminescence)	GQD	carboxylic group	7 nm	5 μg/mL	358
SMMC-7721	fluorescence	GO	FITC and cRGD- modified chitosan	monolayer and LD = 10−100 nm	20 μg/mL	352
Lung cancer						
A549	fluorescence	rGO	spiropyran and hyaluronic acid	196 nm	0.1 mg/mL	359
		ND	MNPs and PAA/FMA	131.7 nm	50 μg/mL	301
		fullerene-C_{60}	C_{60}^{3-} ions	5 nm	160 μg/mL	300
		GQD	mesoporous silica NPs	15 nm	50 μg/mL	360
HCC827	fluorescence	ND	TGF	46 nm		361
Lymphoma						
Raji B	fluorescence	GO	PEG and anti-CD20 (Rituxan)	monolayer and LD < 10 nm	0.7 mg/mL	47
Osteoblast						
MC3T3-E1	fluorescence	C-Dot	carboxylic group	12.50 ± 4.03 nm	0.5 mg/mL	362
Ovarian cancer						
A2780	fluorescence	ND	POEGMEMA-st-MAETC-Pt	110 nm	2 μM	363
Pancreatic carcinoma						
AR42J	fluorescence	GO	FITC-labeled octreotide	monolayer and LD = 10−1000 nm	80 μg/mL	364
Panc-1	fluorescence	GQD	HA and human serum albumin NPs	5 nm	10 μg/mL	365
Prostate cancer						
PC3	fluorescence	MWCNT	PEI(FITC)-mAb	D = 10−20 nm; LD = 150 nm	30 μg/mL	366
Renal cancer						
RENCA	fluorescence	SWCNH	$Gd_3N@C_{80}$ and CdSe/ZnS QDs	40−200 nm	25 μg/mL	367
Endothelial cells						
B4G12	near-field scanning microwave microscope	MWCNT		5 μm		368
Bacteria						
E. coli	Raman imaging	ND	lysozyme-carboxylated	131 nm	10 μg/mL	369

from the reaction products of $O_2^{\bullet-}$ and HE. The fluorescence intensity of the products was found to be enhanced by increasing the $O_2^{\bullet-}$ concentration while the peak intensity of 525 nm remained unchanged. Therefore, the change of the $O_2^{\bullet-}$ concentration could be measured by the intensity ratio between the two emission peaks. A wide detection range from 0.5 to 140 μM with a detection limit of 100 nM was achieved by using this scheme. The authors also incubated the CD-HE conjugates into HeLa cells to monitor the $O_2^{\bullet-}$ amounts. Lipopolysaccharides from *E. coli* were employed as a stimulator for ROS production. The results showed that the CD-HEs could accurately monitor the release of $O_2^{\bullet-}$ in the live cells with low cytotoxicity.

Recently, Zhai et al. demonstrated a one-step microwave preparation method for C-dots in aqueous phase with a high quantum yield of 41.4% and their functionalization-free detection for mercury ions (Hg^{2+}).[230] On the basis of the fluorescent C-dots, the authors also developed a portable, pen-like sensor for the detection of heavy metal ions through naked eyes. The carbon precursors used for the C-dots synthesis were ethylenediamines and citric acids. The C-dots showed a significant fluorescent quenching after reacting with sample solutions containing Hg^{2+} ions. The detection limit reached up to 20 nmol/L, and a high selectivity was observed with mixed nontarget ions like Cr^{2+}, Mg^{2+}, Ca^{2+}, $^{+}$, Fe^{2+}, Ag^{+}, and Pb^{2+} even with a high concentration of 0.2 mmol/L. More recently, Wang et al. designed nitrogen/sulfur codoped C-dots with bright-blue emission and used them for sensing the anticancer drug, methotrexate (MTX).[91] It was found that the doping of nitrogen and sulfur could effectively reduce the self-quenching effect and improve the quantum yield compared to those of pure C-dots. The quantum yield of the resulted nitrogen/sulfur codoped C-dots was calculated to be 21.6% using quinine sulfate solutions as reference. The color of the nitrogen/sulfur codoped C-dots solutions was yellow under daylight and turned to bright blue with a UV excitation of 365 nm. Their

DOI: 10.1021/acs.chemrev.9b00099
Chem. Rev. XXXX, XXX, XXX−XXX

fluorescence lifetime was 8.1 ± 0.2 ns, which was long enough for biosensing. The fluorescence quenching was attributed to strong interaction of hydrogen bonds between the target MTX and nitrogen/sulfur codoped C-dots through FRET effect, and a linear detection range for target MTX was obtained ranging from 0.33 nM to 50.0 μM. Interference assays including caffeine, adrenaline, tetracaine, dopamine, uric acid, theobromine, riboflavin, sulfamethoxazole, streptomycin, melamine, and FA were respectively mixed with the nitrogen/sulfur codoped C-dots to evaluate the specificity of the sensors, and no fluorescence quenching was observed for these control molecules.

2.2. Nanocarbons for in Vitro Bioimaging

Despite the merits of semiconductor imaging labels, the presence of heavy metals such as cadmium and lead remains a toxicity concern to the cellular environment. Carbon nanomaterials have been extensively studied as an alternative to cytotoxic nanomaterials and are particularly well-suited for bioimaging applications due to their low toxicity and high biocompatibility.[290−293] One of the distinct advantages nanocarbons lies in its intrinsic versatiliy. Most nanocarbon materials can serve as both fluorescent/Raman/MRI imaging labeles and concurrently as phototherapeutic nanoagents due to its optical absorption capability. Researchers have observed structures such as carbon nanodots, NDs, and CNTs exhibiting bright and multicolor intrinsic photoluminescence emissions. Fluorescent NDs, for example, can be excited by one-photon or two-photon fluorescent microscopy, yielding stable and strong fluorescent intensity that is desirable for continuous cell tracking and long-term in vivo imaging without photobleaching. Furthermore, the large-scale synthesis can be achieved through helium irradiation. Oxidized single-walled carbon nanotubes (SWCNTs), similar to other nanocarbons, can covalently attach with functional groups/molecules for in vitro and in vivo target imaging. The fluorescent emission of SWCNTs can be tailored for the NIR region, preferable for deep tissue imaging due to the high signal-to-noise ratio. Furthermore, biodegradation by neutrophils was observed, demonstrating their low toxicity.[294] Fullerene molecules can be synthesized in controlled size and structure. Their nonphotoblinking and high water-solubility has been recently reported for the imaging of cellular uptake, organ specific binding, and biodistribution. When conjugated with PEG, GOs were found to show intrinsic fluorescent properties that have been used for intracellular imaging. C-dots, of a comparable size to those of semiconductor QDs, have been synthesized from a wide range of green precursors such as glycine, plant leaf, and even ground coffee/tea. To increase imaging efficiency, structure-specific traits, such as its cellular internalization, can be used to carefully engineer dual purpose nanocomposite probes. C-dots are typically internalized into the cytoplasm rather than the nucleus. Meanwhile, the ultrasmall size aids in the nucleus penetration of GOs. When combined, negatively charged GO and C-dots can be used for both cytoplasm/nucleus fluorescent labeling. The use of multifunctional graphene nanoprobes conjugated with magnetic nanoparticles developed through green approaches have also been studied for their applicability as in vitro and in vivo labeling markers. Similarly, single-walled carbon nanohorns (SWCNHs) are able to encapsulate different target species including magnetic nanoparticles as signal amplification tags to enhance MRI imaging. CNHs are known to have greater surface area as compared to CNTs attributed to their open structure, allowing for increased cargo. In this section, we will discuss the in vitro imaging applications of these nanocarbon materials. Table 2 presents a detailed summary of carbon-based nanomaterials in vitro imaging applications.

2.2.1. In Vitro Imaging by Graphene. The single and few-layered graphene nanosheets allow the diversified surface functionalization on the two sides as well as on the edges of the sheet.[370−373] Their high surface area and biocompatibility have enabled their widespread use as both effective fluorescent biomarkers and efficient carriers for an optically active component such as a dye or QD for cellular imaging studies. The most commonly used functional graphene nanoprobes as efficient carriers for bioimaging are the PEG-grafted GOs. For instance, Peng et al. conjugated GOs with fluorescein molecules (Fluo-GOs) for intracellular bioimaging.[311] The fluorescein dye was bound to the surface of GOs through PEG as bridge molecules to maintain their fluorescent intensity and eliminate quenching when directly attached to the GOs. The fluorescent intensity of the GOs-based fluorescent nanoprobes could be tuned by the pH value of their surrounding media. Under light excitation fixed at 494 nm, the emission peak of Fluo-GO red-shifted by 5 nm from that of the pure fluoresceins with an increasing intensity with increasing pH value from 4.6 to 8.0. HeLa cells were used as the target model and cultured respectively with pure GOs, PEG-GOs, and Fluo-GOs with concentrations ranging from 2.5 to 40 mg/L. On the basis of MTT results, the cytotoxicity of the Fluo-GO nanoprobes was found to be less than 20% even with a high concentration at 40 μg/mL, while the cellular metabolism was observed to be recovered in 90% of the cells after 24 h incubation with fresh culture media. For the bioimaging experiments, the authors chose Fluo-GO nanoprobes at a concentration of 2.5 mg/L with PEG-GOs as control groups. Bright-green emission color was shown for the HeLa cells treated with Fluo-GOs for 6 h, while no fluorescence was obtained for the PEG-GOs control group. In addition, the fluorescent intensity of the HeLa cells with Fluo-GOs was not influenced by a significant temperature change from 4 to 37 °C. These results suggested that the direct penetration of the Fluo-GO nanoprobes through the cell membranes instead of endocytosis.

Later, Wang, and co-workers fabricated peptide-functionalized GOs as fluorescent imaging labels.[139] The peptide-functionalized GOs target-specific live cells and were used for caspase-3 activation imaging (Figure 19A). Caspase-3 is known to be closely related to the cell apoptosis process as a main mediator in the cell initiation and propagation stage.[374−376] The study of intracellular protease response to this important biomarker is essential for understanding the pathological principle of dysregulated apoptosis for diseases including heart failure and neurodegeneratives. When the fluorescent dyes were initially attached to the GOs surface, their fluorescence was quenched by the GOs (Figure 19B). After the peptide functionalized GOs penetrated into the cells, the intracellular proteases led to the cleavage of the peptides on the GO surface and thus to the release of the fluorescent dyes. The authors studied both the noncovalent and covalent methods for the conjugation of the peptides/fluorescein to the GO surface. They found that the direct attachment of the peptides onto the GO surface was weak in the cell culture media with abundant protein molecules such as BSA. The peptide sequences were replaced by the other protein molecules as stronger

DOI: 10.1021/acs.chemrev.9b00099
Chem. Rev. XXXX, XXX, XXX−XXX

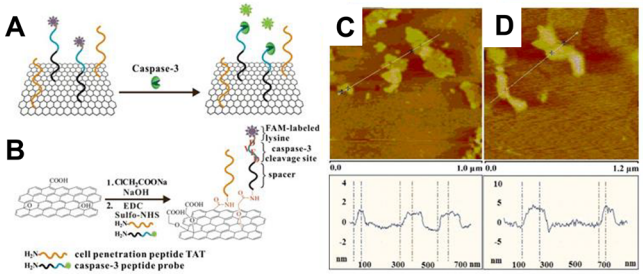

Figure 19. (A) Schematic illustration for the detection of caspase-3 using GO−peptide conjugate. (B) Schematic diagram for the preparation of GO−peptide conjugate. AFM and height profiles of (C) GO and (D) GO−peptide conjugate. (E) Fluorescence images of Hela cells treated with (a1) no STS, (b1) 2 μM STS, (c1) 4 μM STS, (d1) 4 μM STS, and 100 μM inhibitor Z-DEVD-FMK for 4 h after treatment with GO−peptide conjugate, (e1) treated with 4 μM STS after 4 h after incubating with conjugate of GO and nonspecific peptide substrate DEVG. a2−e2 are the overlap of fluorescence and bright-field images of a1−e1. Reprinted with permission from ref 139. Copyright 2010 American Chemical Society.

fluorescence intensity was observed after the nanoconjugates were dispersed into the cell culture medium. Thus, they conjugated the peptide probes onto the GO surface by the covalent method. Moreover, the peptide molecules increased the water solubility and stability of the GOs in the cell culture media. Next, they conjugated the cleavable peptides with the GOs by a commonly used succinimide EDC/NHS method. The obtained peptide−GOs exhibited a weak fluorescent intensity due to the quenching effect of the GOs. BSA molecules were also added to saturate the GO surface with sufficient adsorption of protein molecules. The resulted GOs had a lateral dimension <200 nm with a thickness of 5 nm due to the peptide coverage as compared to 1−2 nm thickness for the pure GOs (Figure 19C,D). By adding caspase-3 with concentrations ranging from 7.25 to 362 ng/mL into the functionalized GO probes, the fluorescence intensity of the solutions at the emission peak of 520 nm quantitatively increased in a linear relationship. The authors then incubated HeLa cells with pure GOs and the targeted peptide/FAM GOs separately at 37 °C for 8 h. After the injection of an apoptosis inducer, staurosporine (STS), the cells treated with pure GOs or only peptides showed no fluorescence, while a bright fluorescence was observed for the targeted peptide GOs probes with FAM labeling. It was also demonstrated that the fluorescent signal could be used for the caspase-3 activation monitoring. Moreover, a stronger fluorescence intensity resulted with the increased amount of STS and no fluorescence was observed in the control group that was incubated with caspase-3 inhibitor (Figure 19E).

Graphene nanoprobes, designed and synthesized by Gollavelli and co-workers using a green method, were demonstrated as fluorescent labels for cellular imaging.[314] The authors reduced the chemically exfoliated GOs to graphene nanosheets through a quick microwave-assisted interaction and magnetized the probes by decomposing ferrocenes into free irons on their surface (Figure 20A). The magnetic graphene nanoprobes were then functionalized with poly(acrylic acid) (PAA) molecules as bridge linkers to load fluorescent dyes of fluorescein *o*-methacrylate (FMA). The synthesized magnetic graphene nanoprobes were reacted with acrylic acid monomer and dispersed in benzoyl peroxide

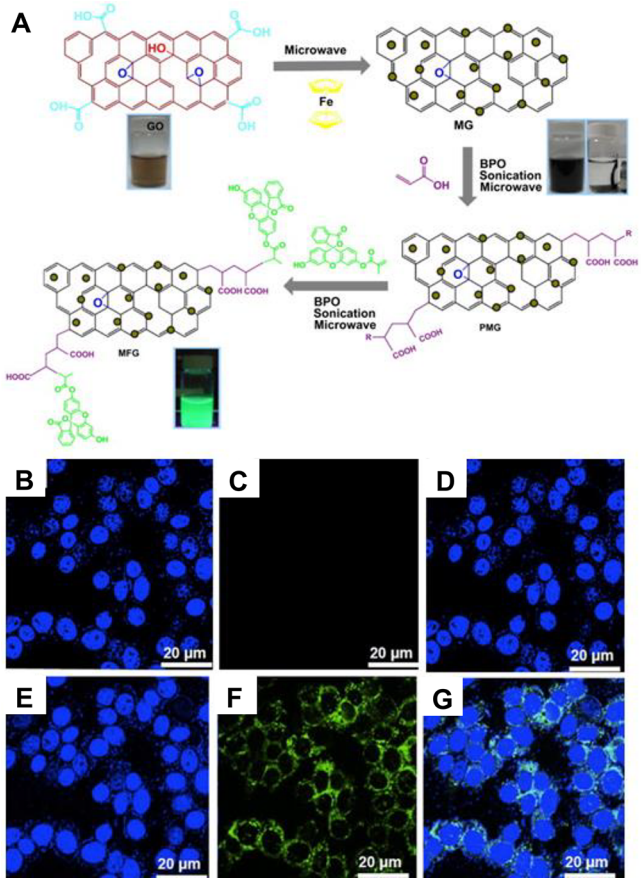

Figure 20. (A) Schematic representation for the preparation of the graphene nanoprobes using a microwave-heated sonication-assisted process and surface modification with acrylic acid and fluorescein *o*-methacrylate. (B−G) CLSM images of control (upper row) and treated (lower row) HeLa cells. (B,E) are nucleus images taken using DAPI filter. (C,F) are green fluorescence images from graphene recorded with a FITC filter. (D,G) is the overlap images of the nucleus images and green fluorescence images. Reprinted with permission from ref 314. Copyright 2012 Elsevier.

solutions, followed by sonication and microwave irradiation. FMA molecules were finally added into the mixtures containing PAA-coated magnetic graphene nanoprobes. It is worth noting that the PAA molecules not only improved the aqueous stability of the graphene probes but also prevented the quenching effect when the fluorescent dyes were directly attached onto the graphene surface. To evaluate the toxicity level of the magnetic graphene nanoprobes, HeLa cells were incubated with the probes with a high concentration of 100 μg/mL. On the basis of the MTT results, the cell viability was maintained above 80% after 24 h, which showed the ultralow cytotoxicity of the probes. The CLSM images with *Z*-scanning in a depth of 0.5 μm showed that the probes were mostly concentrated in the cytoplasmic area and few of them were localized at the lysosomal area (Figure 20B−G). These results indicated that the probes could serve as safe carriers for magnetically guided drug delivery.

Recently, Feng et al. designed a peptide-receptor biosensor based on the fluorescence signal changes induced by GOs and the target molecule, octreotide labeled with fluorescein isothiocyanate (FOC).[364] Octreotide is an FDA-approved clinically used cyclic peptide with eight amino acids that acts in the biological process similar to that of somatostatin. It is

DOI: 10.1021/acs.chemrev.9b00099
Chem. Rev. XXXX, XXX, XXX−XXX

widely employed for the treatment of gigantism, diarrhea, and acromegaly through the secretion inhibition of insulin, glucagon, and growth hormone. In this work, GOs the FOC conjugates showed high adsorption efficiency to the surface of GOs. Their attachment to the GO surface led to a prominent quenching effect of the FITC fluorescent label. More importantly, the fluorescence quenching could be recovered by the addition of antioctreotide solutions that resulted in the release of the FOC. A maximum quenching rate of 78% was observed for GOs with a concentration of 0.8 mg/L. The GO effectively suppressed the fluorescence background during the FOC and AOC interaction and improved the signal-to-noise ratio to a high level of 4.3. The detection limit for the octreotide molecules was estimated to be 2 ng/mL with a linear detection range from 0 to 20 ng/mL. This technique was also demonstrated for the target molecule tumor marker imaging in AR42J gastroenteropancreatic neuroendocrine cancer cells with somatostatin receptor. The FOC solutions with a concentration of 1 μM were added to the cell culture medium and incubated for 1 h at 37 °C. Strong fluorescence on the AR42J cells surface were shown due to the strong interaction between FOC and the tumor receptor of SSTR2. The target ability and specificity were evaluated with CHO cell line as the control group. GOs (80 mg/L) added to the cell culture medium effectively reduced the autofluorescence background noise by the nonspecific protein interaction with FOC in the cells.

Datta et al. reported a hybrid material using GO sheets covalently conjugated with cationic quaternized carbon dots (QCDs) as biocompatible imaging probes.[345] By changing the loading amount of the QCDs to the GO surface, the developed probes were shown to achieve selective target labeling of either the cytoplasm or nucleus in the cells. The QCDs were attached to the GO through electrostatic binding. The weight ratios of the GOs:QCDs were tuned from 0.125 to 0.5. Two specific conjugates were chosen as GO500QCD500 and GO250QCD500. With the increased mass ratio of GOs in the hybrid nanoprobes, the positive charge on the probe surface was decreased. The concentrations of the QCDs were higher than that of the GOs in all the designed probes to ensure homogeneous GO surface coverage density and strong fluorescent intensity. The hybrid nanoprobes showed a slightly reduced fluorescence compared to that of the QCDs alone due to the energy transfer process. Before the cellular imaging experiments, the authors studied the stability and cytotoxicity of the nanoprobes by using mouse fibroblast (NIH/3T3) cells. The cell viability was not changed even with a high dose of 100 μg/mL. The cell internalization process for the pure QCDs and the GO500QCD500/GO250QCD500 hybrid nanoprobes was monitored through optical microscopy. For the pure QCDs, a fast endocytosis process with an easy nucleolemma cross was observed while inhibition of nuclei internalization was observed for the hybrid GO500QCD500 nanoprobes. As with the hybrid GO250QCD500 nanoprobes, there was a distribution of the labels localized at both the nucleus and the cytoplasm. The effective modulation of the cellular penetration was influenced by the zeta-potential of the hybrid nanoprobes with the tunability according to the mass ratios between the QCDs and GOs because the positively charged nanoprobes were easy to interact with the negatively charged lipid membrane that resulted in endocytosis. Moreover, the lateral size of the GOs (in hundred nanometers) was much larger than that of the pure QCDs, which was only a few nanometers. This factor also affected the cell internalization ability of the hybrid nanoprobes.

The use of fluorescence from graphene QDs prepared from plant leaf was also demonstrated by Roy and co-workers for the labeling of various cancer cells. including human cervical cancer cell line (HeLa cells), normal human mammary epithelial cell line (MCF-10A), human breast adenocarcinoma cell line (MCF-7 cells). and apoptotic cells in zebrafish.[305] For the synthesis of graphene QDs, a hydrothermal method was used by adding the extract of neem leaf to DI water and autoclaved for 8 h. After 20 min of centrifugation and 24 h dialysis, the resulting graphene QDs were dried in an oven to a final concentration of 12 mg/mL and an average diameter of 5 nm. Because of the $\pi-\pi^*$ transition in the aromatic sp^2 domains, the absorption peak for the graphene QDs was centered at 265 nm. The fluorescence emission peak of the graphene QDs could be tuned by changing the excitation wavelength. A high photostability was observed for these graphene probes with unchanged fluorescent intensity under 1000 h of continuous light excitation by xenon lamp (450 W/cm^2). For the cellular imaging experiments, an argon laser with a wavelength of 488 nm was used to excite the green and red fluorescence of the graphene QDs inside the cells. Most of the nanoprobes were found to be localized at the cytoplasms and membranes, while no similar fluorescence was observed in the nucleus. This is attributed to the endocytosis penetration and the absence of target receptor groups on the probe surface. A high cell viability of 95% was obtained after cell incubation with the graphene nanoprobes. The graphene QDs were functionalized with annexin V antibody to achieve targeted imaging of the apoptotic cells. The conjugated Ab_{A5}−graphene QDs were found with low toxicity with a concentration of 2 mg/mL up to 72 h. The monitoring of the cell apoptosis is indeed an important modality to study various diseases such as cardiovascular disease and cancers. The red photoluminescence of the Ab_{A5}−graphene QDs were indicative of the apoptotic cells. Thus, the production of highly photostable and low toxicity graphene nanoprobes by the green synthesis method promises the long-term imaging of the apoptosis process in different cells.

2.2.2. In Vitro Imaging by Carbon Nanotubes. Carbon nanotubes are another type of multifunctional nanocarbons that exhibit great potential in biological imaging applications, especially in multicolor and multiphoton imaging.[291,377−380] The SWCNTs show intrinsic fluorescence emission in the NIR wavelength region under excitation by an external light source. Weisman et al. first demonstrated intrinsic NIR fluorescence in SWCNTs and their uptake into macrophage-like cells. NIR fluorescence microscopy at wavelengths above 1100 nm resulted in high contrast images indicating localization of nanotubes in numerous intracellular vesicles.[381] The same group further showed debundled SWCNTs as high-contrast NIR fluorophores for sensitive and selective tracking in mammalian tissues (rabbits).[382]

To further explore the potential of SWCNTs as NIR II labels for biological imaging, Dai and group functionalized them with PEG and conjugated to antibodies such as Rituxan to selectively recognize CD20 cell surface receptor on B-cells with little nonspecific binding to negative T-cells and herceptin to recognize HER2/neu positive breast cancer cells. They particularly observed ultralow NIR autofluorescence for various cells, an advantageous feature over high autofluorescence and large variations between cells lines in the visible

DOI: 10.1021/acs.chemrev.9b00099
Chem. Rev. XXXX, XXX, XXX−XXX

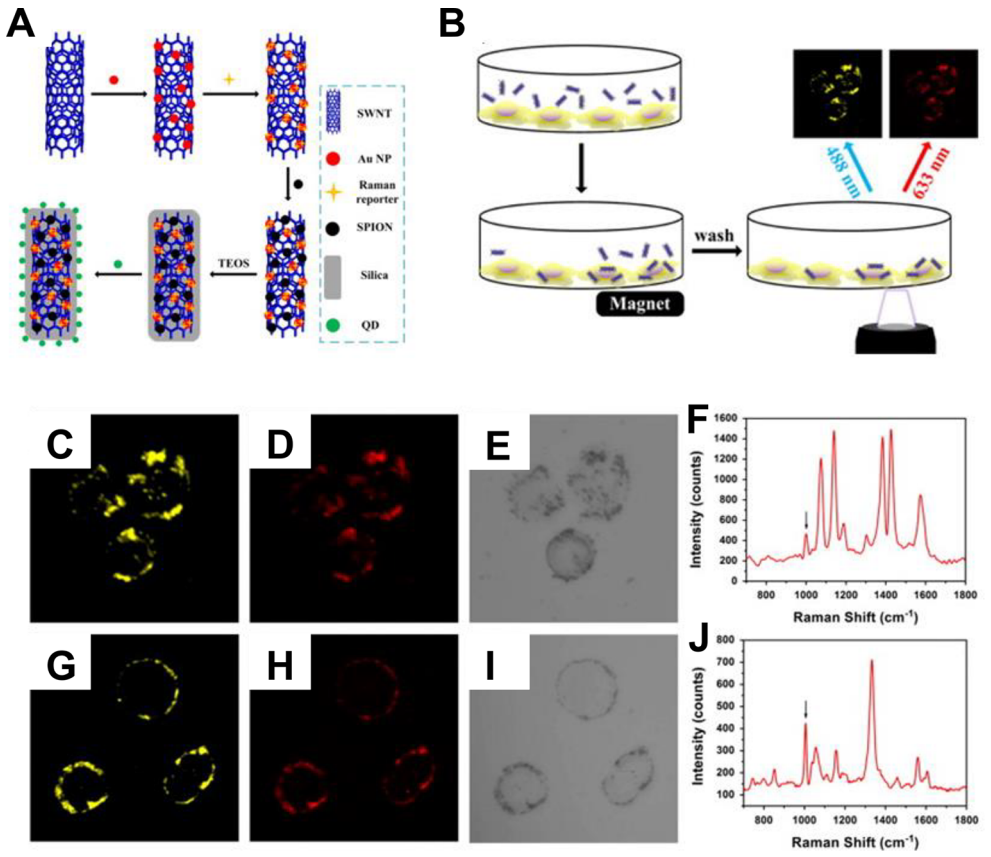

Figure 21. (A) Schematic diagram of the preparation of the multifunctional nanoprobe. (B) Schematic illustration of the magnetic field guided SERS-fluorescence imaging of living cells. (C) Fluorescence image, (D) SERS image, (E) bright-field, and (F) SERS spectrum from SKBR3 cells incubated with 4ATP encoded nanoprobe. (G) Fluorescence image, (H) SERS image, (I) bright-field, and (J) SERS spectrum from MCF7 cells incubated with 4ATP encoded nanoprobe. Reprinted with permission from ref 304. Copyright 2014 Elsevier.

spectrum.[383] Later on, the same group employed an Au/Au substrate for NIR-fluorescence-enhanced (NIR-FE) cellular imaging by using both SWCNTs. They functionalized SWCNTs by the arginine−glycine−aspartic acid (RGD) sequence to selectively tag U87-MG brain cancer cells over MCF-7 breast cancer cells, plated the cells on the Au/Au substrate, and observed an about 9-fold increase in the fluorescence of the SWCNT on U87-MG cells.[384] By taking advantage of the exceptionally stable NIR II fluorescence and negligible autofluorescence background of SWCNTs in the NIR II window, MacKintosh and Schmidt showed noninvasive tracking of kinesin-1 motor proteins in COS-7 cells by imaging the highly stable NIR luminescence of SWCNTs targeted to the cellular protein.[385]

Furthermore, both the carboxylated single-walled and multiwalled CNTs are excellent candidates for targeted live cell imaging as they offer versatile functionalization capabilities to capture molecules through covalent bindings on their surfaces. For example, Wang et al. demonstrated SWCNT functionalization to fabricate a magnetic nanoprobe for guided target bioimaging.[304] To achieve the multifunctional imaging, Au NPs, semiconductor quantum dots (CdSe/ZnS core−shell QDs), and superparamagnetic iron oxide nanoparticles (SPIONs) were used to decorate the SWCNT surface. Au NPs served as surface enhanced Raman scattering (SERS) tags while QDs with fluorescent emission wavelengths at 530 and 580 nm served as fluorescent labels. SPIONs and Au NPs were first functionalized on the SWCNT surface through electrostatic binding. After that, a thin silica layer was coated on the obtained SWCNT for QD functionalization (Figure 21A). To test the SERS signal from the conjugates, two typical Raman molecules, DTNB and 4ATP, were used as reporters to the Au NPs to enhance the Raman peak signals. In this work, a dual-mode in vitro bioimaging in the human breast cancer cells (MCF7 and SKBR3) was demonstrated by using the nanoconjugates for both, SERS and magnetic field guided fluorescent imaging (Figure 21B−J). Strong SERS and fluorescent effect were observed before and after cell internalization in both cell models. In addition, different Raman bands were recorded for the two different reporter molecules. The imaging effects were also enhanced by adding an external magnetic field to the cells labeled by SWCNT nanoprobes. Stronger SERS and fluorescent signals were obtained for the cells that were closer to the magnet because more suspended nanoprobes got assembled by the magnetic field and thus leading to greater penetration of the nanoconjugates inside the cells. The cytotoxicity of the multifunctional SWCNT nanoprobes were also evaluated and the cell viability was larger than 90%, which indicated that the probes were highly biocompatible.

An SWCNT immunoassay, with avidin and biotin functional groups as linker to Raman labels, for cellular imaging was developed by Bajaj and co-workers.[302] Here, the target receptor molecules, Her2, overexpressed in the breast cancer cell model of BT-474, were bound to the capture molecules, Her-66 antibodies, that were linked to the SWCNT surface. Optical and 3D Raman imaging were performed for the cells incubated with the SWCNT probes. The receptor-mediated

DOI: 10.1021/acs.chemrev.9b00099
Chem. Rev. XXXX, XXX, XXX−XXX

immune reaction was confirmed by the reconstructed 3D Raman images based on the Raman G-band peak from 1480 to 1660 cm. To study the target ability of the CNT probes, Raman images were acquired for BT-474 cells incubated with and without the capture antibody. Strong Raman G-band intensity was obtained when the SWCNTs were bound to Her2 receptors, while a significantly reduced signal was obtained when the capture antibody was absent, indicating that the binding between the CNT probes and the receptors were target-specific bindings. The specificity of SWCNTs was also demonstrated through prolonged incubation time of the cells with pristine SWCNTs and the designed probes. Interestingly, most of the pristine SWCNTs were localized at the intracellular vesicles as compared to that of the designed SWCNT probes present in the nucleus.

Recently, Rubio et al. fabricated functionalized multiwalled carbon nanotubes MWCNTs (f-MWCNTs) as fluorescent cell labels for the imaging of Kupffer phagocytic liver cells (KC) and epithelial lung cancer cells (A549).[386] In this study, the MWCNTs were demonstrated for the multiphoton fluorescence emission where the excitation light wavelength was in the NIR region ranging from 750 to 950 nm. The emission intensity exhibited an exponential relationship to the excitation power ranging from 3.7 to 6.7 mW, suggesting nonlinear absorption of photons. It is worth noting that with excitation power below 10 mW, the Raman features of f-MWCNTs at the D-band of 1350 cm^{-1} and G-band of 1590 cm^{-1} showed no change, indicating no laser damage to the nanoprobes. After the addition of MWCNTs solutions into the cell culture media of KC and A549 cells, the cells were examined by multiphoton fluorescence microscopy. The signal intensity for f-MWCNTs inside the cells after 24 h incubation was significantly higher than that with only 4 h incubation. The cellular uptake efficiency of the nanoprobes in the KC cells was found to be higher to that of A549 cells because the KC cells are known to possess an active phagocytosis manner. The f-MWCNTs also acted as cell labels and allowed in vitro tracking through fluorescence lifetime imaging.

More recently, Roxbury and co-workers developed fluorescent labels with pure SWCNTs in the NIR wavelength region with narrow fwhm and good penetration capabilities.[343] They used a spectroscopic technique called wide-field hyperspectral collection method to perform single CNT fluorescence measurement in mammalian live cells and even in the endothelium of zebrafishes. The authors could identify 17 individual SWCNTs with different chiral properties through a single excitation light source while observing 12 CNT species in live cells with an imaging window at 500 nm. The NIR hyperspectral fluorescent microscope was built by inserting a volume Bragg grating into an inverted fluorescence optical microscope with an NIR camera. Thus, the bandwidth could be significantly reduced to 3.7 nm for wavelengths ranging from 844 to 1452 nm as the grating reflected twice of the emission light. To demonstrate the ultraresolution capability of individual SWCNT in the biological environment, human cervical HeLa CCL-2 cancer cells were incubated with 1 mg/L SDC-functionalized SWCNTs for 30 min at room temperature. In the live cells, the SWCNTs could be detected as bright fluorescent objects with a 7 μm median space with each other. From the hyperspectral images, the cell internalization by the SWCNTs was confirmed to be energy-dependent endocytosis and distributed at the endolysosomal pathway when the cells were incubated at a low temperature of 4 °C. Most notably, this imaging method does not require spectral deconvolution because of far-field epifluorescence capture.

2.2.3. In Vitro Imaging by Fullerenes. Fluorescent fullerene nanoparticles (NPs), with size- and surface functional groups-dependent tunable emission peaks, have attracted increasing attention for theranostic applications.[387−390] Researchers have designed and developed several water-soluble fullerene molecules with superior properties for bioimaging, including high cellular uptake efficiency, high biocompatibility, and nonblinking photoluminescent emission. Bai et al. synthesized fullerene C_{60} with ultrasmall size of 5 nm through electrochemically reducing the fullerene thin film to C_{60}^{3-} anions in the acetonitrile solutions containing tetrabutylammonium cations and used them as fluorescent bioimaging agents.[391] The resulting fullerene NPs comprised of a core−shell nanostructure, with a core of C_{60} aggregates coated by a thin layer of C_{60}^{3-} shell to allow water solubility. They exhibited a strong fluorescence emission intensity with a quantum yield of 6%. Because of the small diameter of the C_{60} nanoprobes, the absorption peak was centered at 270 nm. The emission peak could be tuned from 405 to 543 nm by changing the excitation wavelengths, thus enabling multicolor fluorescence. The fullerene nanoprobes showed excellent photostability and low cytotoxicity to live cells with high cellular uptake efficiency. In this work, breast cancer cells (MCF-7) and lung cancer cells (A549) were incubated with 160 μg/mL C_{60} nanoprobes for 24 h. Interestingly, the emission color of the cells labeled with C_{60} nanoprobes were shown to change from blue to green and red under light illumination at 405, 488, and 543 nm. The confocal section images suggested that the probes mostly penetrated to the cytoplasmic region rather than being attached at the cellular membranes. In addition, the cell viability was maintained above 80% even with a high concentration of the C_{60} probes at 100 μg/mL after 3 days incubation. This suggested that the fluorescent C_{60} nanoprobes could be employed for long-term monitoring of the live cells without inducing any damage to the cells.

Recently, Liu et al. designed photoluminescent nanoconjugates by encapsulating fullerene NPs into composite nanofibers for cellular imaging applications.[354] The fabrication process involved blend electrospinning of poly(L-lactide) (PLLA) with the fullerene NPs. PLLA material is a kind of aliphatic polyester with high biodegradability and serves as building scaffolds for tissue anatomical defects and drug delivery vesicles. Under 350 nm excitation, tetraethylene glycol-functionalized C_{60} and C_{70} showed emission peaks at 550 and 575 nm, respectively. After attachment of the fullerene NPs to the nanofibers, the fluorescence peak wavelength blue-shifted with a slightly reduced emission intensity. The fullerene NPs could be tuned to release from the nanofibers with good cell penetration efficiency to act as fluorescent labels. After the incubation of fullerene-loaded nanofibers with human liver carcinoma cells (HepG-2), strong fluorescence emission was observed in the cellular nuclei. The cell viability was estimated to be 96.9% after 48 h incubation with 1 mg/mL fullerene-loaded nanofibers, indicating a low cytotoxicity of the nanoconjugates. Later, the same group employed the tetraethylene glycol-functionalized C_{70} fullerenes for coating on PLLA nanofibers to achieve multifunctional bioapplications including imaging and drug delivery.[357] The authors selected C_{70} fullerene NPs rather than the C_{60} fullerene NPs due to their stronger emission intensity and longer emission peak wavelength at 575 nm. They observed that the HepG-2 cells

DOI: 10.1021/acs.chemrev.9b00099
Chem. Rev. XXXX, XXX, XXX−XXX

retained their complete morphology with integrated nuclei and long spindles after 24 and 48 h incubation. When the PTX drug-loaded fullerene nanofibers were added to the cell culture media, the cell numbers reduced by more than 50% and a round shape morphology was observed. The imaging results suggested that the release rates of the drugs-loaded fullerene increased with the increasing weight ratio of the C_{70} fullerene during the conjugated nanofiber synthesis. Thus, the fluorescent nanoprobes were suitable for the monitoring the guided chemotherapy process in the cancer cells.

2.2.4. In Vitro Imaging by Carbon Nanohorns. SWCNHs were first synthesized and reported by Iijima's group in 1999.[263,392−394] They are closed nanotubules with a diameter usually less than 10 nm and a length of 10−70 nm. The structures of SWCNHs are similar to that of the SWCNTs, while they are rolled into conical shapes rather than the tubular ones. The individual SWCNHs are assembled into a spherical aggregate (40−200 nm) like dahlia flowers by van der Waal forces between their open ends. The dahlia SWCNHs can be produced in low cost and large quantities with minimal cytotoxic effects due to the absence of metal catalysts. With a higher surface-to-volume ratio than the CNTs, the SWCNHs can be functionalized with more target biomolecules or nanoparticles for fluorescence labeling applications.

Zhang et al. synthesized SWCNHs pea pods loaded with trimetallic nitride template endohedral metallofullerenes and semiconductor CdSe/ZnS core/shell QDs to be used as fluorescent labels for both in vitro and in vivo imaging applications (Figure 22A).[367] Two types of metallofullerenes were chosen as the core materials, including $Lu_3N@C_{80}$ that served as X-ray contrast medium and $Gd_3N@C_{80}$ as the radiotherapeutic medium. Through a typical carbodiimide cross-linker chemical process in the presence of *N*-(3-(dimethylamino)propyl)-*N*′-ethylcarbodiimide hydrochloride and *N*-hydroxysulfosuccinimide (sulfo-NHS) solutions, the nanoprobes of $Gd_3N@C_{80}$@SWNH-QDs and $Lu_3N@C_{80}$@SWNH-QDs were obtained. As characterized from the TEM images, the fullerene NPs were clearly observed as bright spots inside the SWCNHs. To test the in vitro MRI imaging ability of the $Gd_3N@C_{80}$@SWNH-QDs, a 2.4 T/40 cm bore MR measuring platform was used. The encapsulation of the endohedral metallofullerenes containing the magnetic Gd^{3+} ions significantly increased the ^1H relaxation efficiency of the biological environments. The T_1-weighted, T_2-weighted, and T_1 mapping results demonstrated that the $Gd_3N@C_{80}$@SWCNHs exhibited a much stronger enhancement effect than the pristine SWCNHs. Moreover, the designed $Gd_3N@C_{80}$@SWCNH-QD nanoprobes were also used as fluorescent labels for live cells. A murine RENCA renal cancer cell line was used as the target cells (Figure 22B). Strong fluorescent emission in the cytoplasm area of the cells confirmed the uptake of the nanoprobes by RENCA cells. These results demonstrated that the $Gd_3N@C_{80}$@SWNH-QD nanoprobes could serve as multimodal imaging agents for both MRI contrast and fluorescent labeling.

On the basis of similar functionalization approaches, Zimmermann et al. fabricated QD-decorated SWCNHs as fluorescent labels and systematically investigated their intracellular transport processes with three different cancer cells (bladder transitional carcinoma cells (AY-27), breast cancer cells (MDA-MB-231), and glioblastoma cells (U-87 MG)).[309] The cell penetration kinetics including the diffusion rate of the

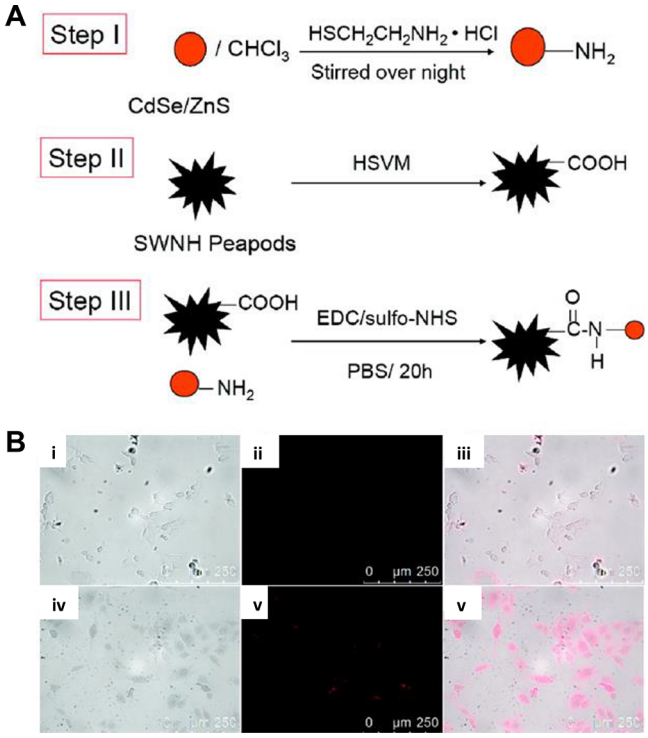

Figure 22. (A) Schematic describing the conjugation of SWNH with CdSe/ZnS QDs. (B) Phase contrast images of RENCA cells (A) without nanoprobe and (D) after 24 h incubation with nanoprobe. Fluorescence images of RENCA cells (B) without nanoprobe and (E) after 24 h incubation with nanoprobe. Overlapped of phase contrast images and fluorescence images (C) without nanoprobe and (F) after 24 h incubation with nanoprobe. Reprinted with permission from ref 367. Copyright 2010 American Chemical Society.

nanoprobes internalization over time and the amount of the nanoprobes uptake over the time was recorded in detail with localization analysis. The multidentate surfaces of the SWCNHs effectively enhanced the binding strength between the QDs and the thiol-coated CNHs. To increase the water solubility of the SWCNHs, the pristine nanohorns were mixed with strong nitric acid for 1 h to generate the oxygen containing chemical groups on their surface. Aminoethanethiol hydrochloride molecules were chosen to functionalize the nanohorn surface with thiol groups due to their short lengths that could induce minimum steric effects. QDs, with a concentration of 1 mg/mL, were then reacted with the thiol-coated SWCNHs. To further improve the dispersibility of the nanoconjugates, PEG molecules with a concentration of 0.5 mg/mL were also added into the sample solution as additional coating shells for reducing the serum protein opsonization in the live cells during fluorescent imaging. The resulting nanoconjugates exhibited a much stronger absorption at 485 nm than those of pure QDs and pure oxidized SWCNHs. Fluorescent emission peaks of the designed probes were blue-shifted compared to that of the pure QDs due to the dielectric coating on the QD surface. To track the cellular distribution after uptake of the nanoprobes, immunofluorescent staining technique with F-actin was used. QD-decorated SWCNHs were observed to internalize not only at the cell membrane surface but also localized at the nuclei and cytoplasm for all the three types of live cells after 1 h. Moreover, the amount of the nanoconjugates kept increasing even 24 h after incubation, indicating the continuous cellular uptake process by the

DOI: 10.1021/acs.chemrev.9b00099
Chem. Rev. XXXX, XXX, XXX−XXX

nanoprobes. Further, no morphological change was induced to the cells during the incubation process, suggesting the low cytotoxicity of the QD-decorated SWCNHs.

More recently, Li and co-workers developed SWCNHs-based fluorescent labels by employing chitosan molecules as linkers for the SWCNHs and QDs through covalent binding.[331] After the coupling of QDs, the fluorescent emission peak of the nanoprobe red-shifted 17 nm from that of the pure CdTe QDs to 610 nm under 355 nm UV light excitation. The maximum fluorescent intensity was obtained with 1.5×10^{-2} mmol CdTe QDs, indicating the complete binding of the QDs with the amino groups on the SWCNH surface. To achieve the targeted bioimaging function, the as-prepared nanoprobes were functionalized with transferrin as the capture molecules to the receptors overexpressed in the HeLa cancer cells. Red fluorescence seen in the live cells after 1 h incubation confirmed the recognition binding of the transferrin on the nanoprobes by the cell receptors. Moreover, the same batch of cells incubated with the nonfunctionalized CNH/QD nanoprobes showed no fluorescence signal. These results demonstrate the excellent specificity of the transferrin-functionalized CNH/QD nanoprobes.

2.2.5. In Vitro Imaging by Nanodiamonds. Fluorescent NDs are sp^3 allotropes of nanocarbon materials with a large number of negatively charged *N*−V defects that serve as fluorescent emission centers.[395−398] These defects are usually generated through high-energy radiation of the diamond. The pronounced advantage of fluorescent NDs compared to the other fluorescent nanocarbons for cell imaging is their nonphotobleaching and nonphotoblinking property in addition to strong fluorescence intensity that can be used for long-term and continuous cell tracking. For instance, Chang et al. fabricated fluorescent NDs with strong emission intensity that was capable of three-dimensional monitoring of single nanoparticle in live cells.[321] The photoluminescence from the defect centers of the NDs (25−140 nm) could be excited through both one-photon and two-photon excitations. Different from the traditional QDs and other fluorescent beads, the fluorescence emission from the NDs was much more stable without any photobleaching and intermittency effects. The emission peak of the resulting 35 nm NDs was at 680 nm with two *N*−*V* center characteristics, i.e., (*N*−*V*)− with a zero-phonon line at 638 nm and (*N*−*V*)0 at 575 nm under a continuous 532 nm laser excitation. Confocal scanning fluorescent images of HeLa cells confirmed the distribution of the internalized NDs. On the basis of quantitative analyses, the two-photon excitation of the ND probes inside the cytoplasm led to better contrast images than those under the one-photon excitation, which is mainly believed to be limited by the aperture diameter of the optical microscopy at one-photon excitation conditions. Finally, single NDs were successfully tracked in the HeLa cell for a long period of 200 s with a diffusion rate of 3.1×10^{-3} $\mu m^2/s$.

Later, Fang and co-workers demonstrated high photostability and biocompatibility of fluorescent NDs for in vitro imaging and tracking by using both stem cells and cancer cells as the test models.[300] Here, NDs with an average size of 100 nm were synthesized and incubated with three different cell models including multipotent stromal cells (489-2.1), preadipocyte cells (3T3-L1), and cervical cancer cells (HeLa). The surface of the NDs was first functionalized with oxygen-containing carboxylate groups after the treatment of strong acids to make them more water soluble. Through different excitation wavelengths in the green, yellow, and orange region, the fluorescent emission peak of the NDs could be tuned in a broad range from 650 to 800 nm. No change in cell morphology was observed during the cell proliferation and growth for all the cell models post incubation with 80 μg/mL of NDs for a long period of 8 days. More specifically, the prometaphase and metaphase of NDs-labeled HeLa cells was monitored. The NDs were observed to be initially localized around the nuclei of the cells after internalization and then redistributed into two daughter cells during the anaphase of the cell cycle. The two daughter cells appeared flattened and adhered well at the bottom of the culture plate (Figure 23A).

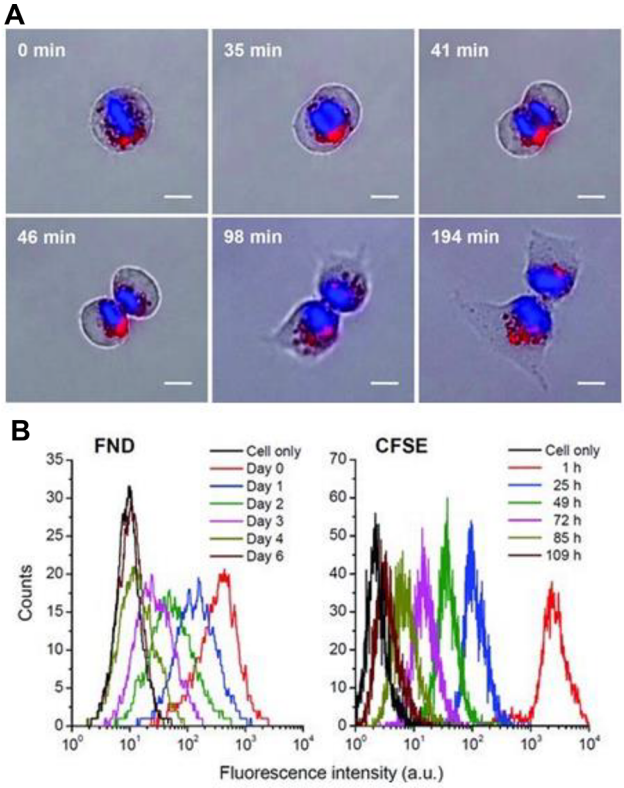

Figure 23. (A) Tracking of ND through the cell cycle of a ND-labeled Hela cells by DIC/epifluorescence microscopy. The cell nucleus is stained with Hoechst 33342 and the red emission is from ND. (B) Comparison studies between ND and carboxyfluorescein succinimidyl ester as long-term cell trackers. Flow cytometry results of ND and CDSE-incubated 3T3-L1 cells at different incubation time. Reprinted with permission from ref 300. Copyright 2011 John Wiley and Sons.

These results confirmed that the fluorescent NDs would not influence the division of the cells after endocytosis. Further, it was recorded that less than 15% of the fluorescent NDs endocytosized in 489-2.1 and HeLa cells were excreted, while 30% were exocytosized from the 3T3-L1 cells. To achieve long-term cell tracking, these low exocytosis rates are preferable for monitoring. To compare the tracking ability of the fluorescent NDs with the commercial fluorescent dye of carboxyfluorescein succinimidyl ester, 3T3-L1 cells were incubated with these two probes under the same conditions (Figure 23B). Notably, the fluorescence intensity of the carboxyfluorescein succinimidyl ester-labeled cells increased immediately after cellular uptake and exponentially decreased in the first 24 h, while the emission intensity of the ND-labeled cells dropped at a much slower rate. These results convincingly

DOI: 10.1021/acs.chemrev.9b00099
Chem. Rev. XXXX, XXX, XXX−XXX

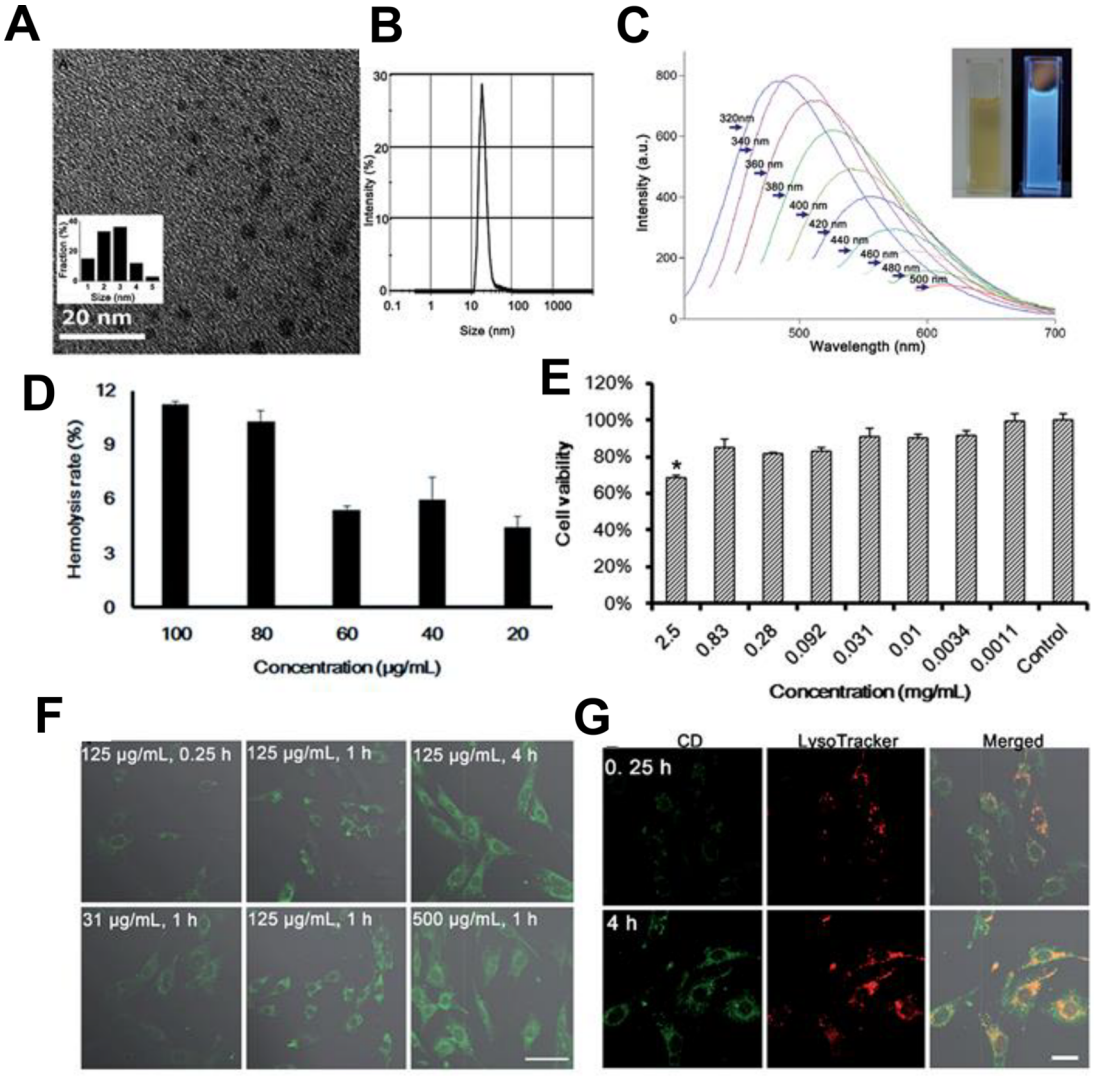

Figure 24. (A) TEM image and (B) DLS distribution of the CD. (C) Excitation-dependent properties of the C-dots when excited under different wavelengths (320−500 nm). Inset is the C-dots solution under bright light and UV illumination, respectively. (D) Hemolysis rate of 2% red blood cells after incubated with various concentration of C-dots for 6 h. (E) Cell viability of C6 cells after being incubated with different concentration of C-dots for 24 h. (F) Cellular uptake of different concentration of C-dots at different times using C6 cell as the cell model. (G) Subcellular localization of C-dots with endosomes after 15 min and 4 h of incubation time. Reprinted with permission from ref 348. Copyright 2014 The Royal Society of Chemistry

present NDs as promising fluorescent labels for long-term continuous tracking labels in live cells.

Fluorescent nanoprobes based on magnetic NDs for labeling and tracking of lung cancer cells (A549) and normal lung fibroblast cells (HFL-1) were reported by Lien and co-workers.[301] The magnetic NDs were obtained by microwave arcing the mixtures of ferrocene nanoparticles and pristine nanodiamond solutions. The resulting magnetic ND probes were then further functionalized with fluorescein *o*-methacrylate by covalent attachment through poly(acrylic acid) molecules. To evaluate the cytotoxicity of the nanoprobes, A549 and HFL-1 cells were incubated with fluorescent magnetic ND probes with different concentrations (from 0.1 to 100 μg/mL) for 24 h. No significant decrease of the cell viability was induced even after 10 days of culture. The fluorescent magnetic ND probes-labeled cells and daughter cells were separated by a magnetic device for further investigation of the ND effect on the cell cycles. From the sodium dodecyl sulfate polyacrylamide gel electrophoresis (SDS-PAGE) analyses, the authors studied the protein expression process of these cells under different generations. It is worth noting that the expression pattern of the proteins together with the cell morphology, growth rate, and viability were not all significantly changed by the internalization of the magnetic ND probes. Recently, Slegerova et al. designed core−shell nanoprobes by coating fluorescent NDs with a polymer shell layer of *N*-(2-hydroxypropyl)methacrylamide.[349] The polymer shell was highly biocompatible and could improve the water dispersibility of the ND probes. These core−shell ND probes were later specifically functionalized with a cyclic RGD peptide as capture molecules for the receptors of integrin $\alpha_v\beta_3$ overexpressed in the U-87 MG glioblastoma cells. The *N*-(2-hydroxypropyl)methacrylamide copolymer shell served as a thin spacer between the ND and the cRGD peptides that could prevent the nonspecific binding and potential aggregation of the NDs after cellular internalization. The resulting peptide ND probes, with an average diameter less than 200 nm, allowed the probe to pass the blood−brain barrier to the tumor

DOI: 10.1021/acs.chemrev.9b00099
Chem. Rev. XXXX, XXX, XXX−XXX

cells. The U-87 MG glioblastoma cells were incubated with 50 μg/mL cRGD-conjugated ND probes for 1 h. The cell viability was maintained at the same level before and after the treatment during the incubation time. From the flow cytometry and confocal image results, the NIR fluorescent intensity of the cRGD-ND-labeled cells was 12 times higher than that of pure ND-labeled ones, confirming the high specificity of the cRGD-ND probes and good cellular uptake efficiencies. The nonphotobleaching effect of the cRGD-NDs was also used to eliminate the background fluorescence noise of the live cells. On the basis of the confocal microscopy images, the cRGD-ND probes were observed to be within the cells rather than only attached at the cell surface.

More recently, Liu et al. functionalized NDs with transforming growth factor (TGF) to target the corresponding receptors in cancer cells.[361] Three-dimensional single-molecule imaging and endogenous protein labeling in live cancer cells were demonstrated based on the internalization of these nanoconjugates. In addition, the TGF-conjugated ND probes showed a higher resolution for the 3D localization than that of traditional fluorescent dyes. TGF molecules were bound to the ND surface by a typical streptavidin−biotin attachment. From the measurement results of fluorescence correlation spectroscopy of the NDs and the absorbance of the TGFs, the number of TGF molecules on the single ND probe was estimated to be 1.2. This indicated that the TGF-ND probes are capable to perform single molecule tracking. The human lung adenocarcinoma cells (HCC827) exhibited strong fluorescence emission intensity after incubation with the TGF-ND probes. To test the specificity of the probes, the cancer cells were pretreated with anti-TGF β receptors that are used to block the binding from the functionalized NDs, followed by incubation of the TGF-ND probes. No fluorescent signals were observed, which confirmed the target ability of the probes to the TGF receptors. Time-lapse cell imaging revealed that the TGF-ND probes penetrated into the cells at a fast diffusion rate for the first 30 min and then slowed down in the following 30 min. In addition, the probes were bound to the TGF-β receptor at the cell surface immediately and thereafter, diffused to the cytoplasm.

2.2.6. In Vitro Imaging by Carbon Dots. Carbon nanodots (C-dots) are relatively new fluorescent nanoparticles from the nanocarbon family.[293,399−401] The size of the C-dots is small and usually less than 10 nm. Similar to the other nanocarbon counterparts, the C-dots show low toxicity and high biocompatibility in biological systems.[402] Currently, many research groups have focused on the improvement of synthesis methods from different carbon precursors to obtain C-dots with longer excitation and emission wavelengths. For example, Ruan et al. synthesized fluorescent C-dots with glycine solution as the precursor through a direct thermal reaction and used them for imaging C6 glioma brain cancer cells.[348] The resultant C-dots had an average diameter less than 5 nm (Figure 24A) with an increased size of 20.78 nm when dispersed in water (Figure 24B). The fluorescent C-dots exhibited a high quantum yield of 29.7%, with tunable emission peaks in the range from 500 to 600 nm (Figure 24C). The functional carboxyl and amino groups on their surface allowed them to be easily conjugated with other target capture molecules. The authors studied the biocompatibility of C-dots by measuring the absorption spectra of the C-dots dissolved in both human plasma and solutions containing blood cells. After incubation of C-dots in human plasma with concentrations ranging from 0% to 50%, the absorbance of the C-dots at 560 nm got significantly increased. This phenomenon was due to the adsorption interaction between the C-dots and serum protein molecules. In addition, the C-dots induced a smaller change in the hemolysis rate (less than 12%) than that led by semiconductor QDs (19.4%) (Figure 24D). As shown in Figure 24E, the cell viability was only decreased to 75.6% even after 24 h incubation of C-dots at a high concentration of 2.5 mg/mL. This concentration was three times higher than that used for in vitro imaging, revealing the low cytotoxicity of the C-dots. Further, the fluorescent intensity of the C-dots-labeled C6 cancer cells strengthened by increasing either the incubation concentration of the C-dots or the incubation time (Figure 24F). The time-lapse fluorescent imaging showed that the number of C-dots localized at the endosomes was large just after 15 min of incubation and then decreased exponentially within 4 h due to diffusion of C-dots to the cytoplasm (Figure 24G).

Later, Wang and co-workers prepared C-dots doped with nitrogen by using streptomycin as the carbon source precursor and demonstrated their capability as fluorescent nanoprobes for the imaging of live cancer cells.[338] The nitrogen-doped C-dots (∼2.97 nm) were obtained from a one-step hydrothermal reaction. The emission peak of the C-dot solution red-shifted with increasing excitation wavelength changing from 333 to 500 nm. The fluorescent lifetime and quantum yield were estimated to be 7.42 ns and 7.6%, respectively. To test the stability of the nitrogen-C-dots in biological conditions with high ionic-strength, the C-dots were mixed with different concentrations of sodium chloride from 0 to 500 mM. The emission intensity of the mixtures was preserved even after 6 h of xenon light excitation of 500 W or after 3 months storage at room temperature. The good stability of the C-dots was also demonstrated by tuning the pH value of the solutions from 3 to 12, indicating that the C-dots were suitable for the general physiological pH environment. The authors proposed that the negatively charged surface groups on the C-dots might lead to electrostatic repulsions that improved their stability under these conditions. A high cell viability of 100% and 78% for HeLa cells was obtained after incubation of the nitrogen-doped C-dots at a low and high concentration of 55 and 825 μg/mL, respectively. A bright fluorescence with green color was detected within the cytoplasm that suggested the penetration of the C-dots to the HeLa live cells.

Recently, Xu et al. fabricated fluorescent phosphate groups-conjugated C-dots by a direct oxidation process and employed them as fluorescent labels for live cells.[339] Here, low-cost sucrose solution was used as the carbon precursor and reacted with phosphoric acid at 60 °C to produce phosphate-functionalized C-dots. The fluorescent emission color of the C-dots could be green and yellow, depending on particles collected from the supernatants or precipitates after the centrifugation of the final reaction solutions. More importantly, the emission intensity of the C-dots increased with the synthesis reaction time and reached to a peak value after 4 h. Further extending the reaction time led to a decrease in the fluorescent intensity. For the cell imaging experiments, the C-dots were added into the cell culture media and incubated with two types of cells (i.e., human gastric normal cell line (GES-1) and human cervical cancer cell (HeLa)) in a concentration of 200 μg/mL. The fluorescent imaging results confirmed the uptake of C-dots by both the cells at the same time.

DOI: 10.1021/acs.chemrev.9b00099
Chem. Rev. XXXX, XXX, XXX−XXX

Table 3. Summary of Carbon-Based Nanomaterials for in Vitro Drug Delivery

cell model	drug type	inhibition rate (%)	material type	functional group/molecules	material scale	dose	ref
Astrocyte							
hippocampal	DEX	50	GO	poly(pyrrole)	mono- and bilayer LD = 450 nm	1 μM	462
Bone marrow stroma							
ST2	DEX		SWCNH	carboxylic group	80−100 nm	1 μg/mL	463
Breast cancer							
4T1	resveratrol	45	rGO	mPEG−NH_2	mono- and bilayer LD = 80 nm	40 μg/mL	417
	DOX	50	ND	carboxylic group	80 nm	1 μg/mL	464
	DOX	50	ND	DSPE−PEG 2K	66.9 nm	0.165 μg/mL	465
	DOX	73	SWCNH	DCA−HPCHS	164 nm	5 μg/mL (with NIR irradiation)	441
EMT6	DOX	82.10	GO	PEG	LD = 100 nm	10 μg/mL	466
MCF-7	CPT/DOX	20	GO	folic acid	mono- and bilayer LD < 150 nm	20 ng/mL	467
	DOX	50	rGO	gelatin	monolayer LD < 750 nm	2 μg/mL	303
	5-FU	75	GO	chitosan	monolayer LD = 100−1000 nm	100 μg/m	468
	DOX	45	rGO	PF127	mono- and bilayer LD = 80 nm	500 μg/mL	469
	PTX	87	GO	6-armed PEG−NH_2	mono- and bilayer LD = 50−200 nm	20 nM	470
	EPI	60	GO	hyaluronic acid	400 nm	20 μg/mL	471
	PTX	46	fullerene AF-1	citrate	128 ± 5 nm	714 ng/mL	430
	DOX	75	fullerene-C_{60}	Gd and tetrahydrofuran	50−100 nm	20 μg/mL	431
	artesunate	78	fullerene-C_{60}	HA and Tf	160 nm	25 μg/mL	433
	4-OHT	80	ND	carboxylic group	278.9 nm	7.5 μg/mL	472
	PTX	50	ND	DNA and mAb	230 nm	17.7 nM	307
	DOX	50	SWCNH	sodium alginate and anti-VEGF mAb	216 nm	25 μM	473
	DTX	50	SWCNH	anti-VEGF mAb	191.2 ± 2.1 nm	2.96 μg/mL	474
MCF-7/ADR	DOX	50	fullerene-C_{60}	FITC	0.7−1 nm	10 μM	475
MDA-MB-231	CPT	50	GO	PVA	monolayer and LD = 100−200 nm	700 nM	425
	CPT	50	MWCNT	PVA	D = 10−20 nm	400 nM	425
	EPI	65	GO	hyaluronic acid	400 nm	20 μg/mL	471
	PTX	50	ND	DNA and mAb	230 nm	43.8 nM	307
	EPI	20	ND	lipid and anti-EGFR	40−110 nm	17.3 wt %	476
	MTX	50	ND	carboxylic group	54.6 ± 0.29 nm	503 nM	477
MDA-MB-231(ABCG2)	MTX	50	ND	carboxylic group	54.6 ± 0.30 nm	78.2 nM	477
MDA-MD-435	SN38	50	GO	PEG	mono- and bilayer LD = 5−50 nm	2 nM	3
Cervical cancer							
HeLa	DOX	50	GO	PEI and Bcl-2 targeted siRNA	mono- and bilayer LD = 200 nm	0.52 μg/mL	478
	DOX	40	GO	Fe_3O_4 NPs-FA	<200 nm	8.8 μg/mL	479
	DXR	65	GO	SS-mPEG	monolayer LD = 146 nm	11.6 μg/mL	480
	DOX	80	rGO	PEG−BPEI	mono- and bilayer LD = 100−200 nm	50 μg/mL	415
	DOX	70	rGO	transferrin and SiO_2-coated QDs	125 nm	5 μg/mL	320
	DOX	55	GO	hyaluronic acid	mono-and bilayer LD = 40−350 nm	6 μg/mL	416
	EPI	70	GO	hyaluronic acid	400 nm	20 μg/mL	471
	DOX	55	fullerene-C_{60}	tetrahydrofuran	20−100 nm	1 μg/mL	481
	DOX	90	fullerene-C_{61}	Gd and tetrahydrofuran	50−100 nm	0.52 μg/mL	431
	DOX	60	fullerene-C_{60}	hydrazone and FA	135 nm	2 μg/mL	432
	DTX	80	fullerene-C_{60} in micelles	diadduct malonic acid	47.7 ± 2.3 nm	1 μg/mL	482
	cisplatin	60	ND	carboxylic group	2−8 nm	37.5 μM	483
	HCPT	50	ND	carboxylic group	40−200 nm	10 μg/mL	449
	DiI dye		ND	mesoporous silica NPs	349 ± 8 nm	2.5 wt %	484
	gliotoxin	65	SWCNT	p53 and chito-oligosaccharide	D = 40−50 nm; L = 1−2 μm	0.125 μM	424
	DOX	74	GQD	PEG	88 ± 18 nm	4 μg/mL	337

DOI: 10.1021/acs.chemrev.9b00099
Chem. Rev. XXXX, XXX, XXX−XXX

Table 3. continued

cell model	drug type	inhibition rate (%)	material type	functional group/molecules	material scale	dose	ref
Cervical cancer							
	DOX	50	GQD	folic acid	2.3 nm	33.7 μg/mL	334
	DOX	80	GQD	folate−Gd	5−10 nm	2.5 μg/mL	335
	5-FU	30	C-Dot	ZIF-8	2 nm	25 μg/mL	342
	DOX	60	C-Dot	folic acid	5−10 nm	0.04 mM	341
	DOX	60	C-Dot	MSPs	3.8 nm	1.5 μg/mL	459
	magnetite nanoparticles	90	CNH	PEI	233 nm	10 μg/mL	485
Colon cancer							
HCT-116	SN38	50	GO	PEG	mono-and bilayer LD = 5−50 nm	6 nM	3
HT-29	DOX	30	ND	carboxylic group	2−8 nm	2.5 μg/mL	486
Diabetes							
RAW 264.7	insulin	125	ND	carboxylic group	1.05−1.69 μm	0.1 μM	487
Glioblastoma							
C6	DOX	55.73	ND	carboxylic group	4−8 nm	4 μg/mL	488
U138	PTX	30	GO	PLA−PEG	mono- and bilayer LD = 0.5−1 μm	24.6 nM	489
U251 (APE-1)	lucanthone	47	O-GNR	PEG−DSPE	W = 100−300 nm; L = 0.5−2.5 μm	5 μM	342
U251MG	DOX	43.57	ND	carboxylic group	4−8 nm	4 μg/mL	488
U87MG	SN38	50	GO	PEG	mono- and bilayer LD = 5−50 nm	50 nM	3
	EPI	50	GO	gadolinium and Let-7 gmiRNA	mono- and bilayer LD = 140−150 nm	1.3 μg/mL	490
	DOX	47.95	ND	carboxylic group	4−8 nm	4 μg/mL	488
	cisplatin	35	ND	RGD peptide and polyglyceryl	63.4 ± 14.9 nm	5 μg/mL	491
Leukemia							
CEM	5-FU	70	GO	chitosan	monolayer LD = 100−1000 nm	200 μg/mL	468
	IBU	50	GO	chitosan	monolayer LD = 100−1000 nm	200 μg/mL	468
L1210FR	taxoid	50	SWCNT	biotin	D = 3 nm; L = 250 nm	0.36 ± 0.04 μg/mL	423
K562	DNR	50	ND	carboxylic group	93.1 ± 8.2 nm	8.1 mM	492
K562/DNR	DNR	50	ND	carboxylic group	93.1 ± 8.3 nm	17.6 mM	492
Liver carcinoma							
BEL 7404 (CP-20)	cisplatin	60	fullerene-C_{82}	Gd and hydroxyl group	50 ± 12 nm	50 μg/mL	493
LT2M	DOX	60	ND	carboxylic group	80 nm	0.5 μg/mL	464
	EPI	50	ND	carboxylic group	89.2 ± 3.3 nm	450 nM	494
HepG2	CPT	50	GO	chitosan	mono- and bilayer LD = 300 nm	29 μM	495
	DOX	45	rGO	Au nanoclusters	monolayer	0.5 μg/mL	353
	DOX	60	GO	Cy−ALG−PEG	94.73 ± 9.56 nm	20 μg/mL	356
	DOX	40	GO	hyaluronic acid	mono- and bilayer LD = 200−300 nm	1 μg/mL	496
	PTX	50	fullerene-C_{70}	tetraethylene glycol and PLLA nanofibers	40 nm	25 μg/mL	357
	DOX	50	ND	carboxylic group	165 ± 1.7 nm	3 μg/mL	220
SMMC-7721	DOX	27.50	SWCNT	lysine and thermo sensitive liposome	232 ± 5.6 nm	2 μg/mL	497
Lung cancer							
A549	MTX	56.70	rGO	gelatin	monolayer and LD = 0.1−1 μm	20 μg/mL	498
	PTX	50.60	GO	6-armed PEG−NH_2	mono- and bilayer L D = 50−200 nm	20 nM	470
	PTX	50	fullerene-C_{60}	DLPC liposome	120−145 nm	410 nM	499
	DOX	50	ND	lecithin	655 ± 11 nm	9.8 μg/mL	500
	PTX	50	ND	carboxylic group	10 nm	100 nM	501
	DOX	40	ND	polyPEGMA	570.6 ± 21.6 nm	160 μg/mL	502
	DOX	60	GQD	mesoporous silica NPs	15 nm	2 μg/mL	360
NCI-H460	cisplatin	60	SWCNH	carboxylic group	80−100 nm	2.5 μM	503
	DXR	40	SWCNH	5PEG	160 nm	5.4 μg/mL	504
	cisplatin	60	SWCNH	carboxylic group	100 nm	5 μM	440
	DXR	50	SWCNH	PEG	80−100 nm	33 μg/mL	505

DOI: 10.1021/acs.chemrev.9b00099
Chem. Rev. XXXX, XXX, XXX−XXX

Table 3. continued

cell model	drug type	inhibition rate (%)	material type	functional group/molecules	material scale	dose	ref
Lymphoma							
Raji	DOX	80	GO	PEG−Rituxan	monolayer LD < 20 nm	10 μM	47
Nasopharyngeal carcinoma							
CNE1	DOX	60	GO	carboxylic group	mono- and bilayer LD < 1 μm	2 mg/mL	506
Neuroblastoma							
N2a	CPT	60	GO	PDEA	mono- and bilayer and LD = 100−200 nm	1 μM	507
	dopamine hydrochloride	74	C-dots	−COOH, −OH, and $-NH_2$	5−10 nm	9 μg/mL	508
Oral cancer							
KB	CPT	50	GO	PVCL	mono- and bilayer LD = 438.5 nm	10 nM	509
	Fe_3O_4	94	CNH	PEI and FA	200−300 nm	10 μg/mL	263
KB-CP20	cisplatin	60	fullerene-C_{82}	hydroxyl group	50 ± 12 nm	50 μg/mL	493
Osteoblast							
MC3T3-E1	DEX		SWCNH	carboxylic group	80−100 nm	20 μg/mL	463
Ovarian cancer							
A2780	cisplatin	50	ND	POEGMEMA	84 nm	1.5 μM	363
A2780cis	cisplatin	50	ND	POEGMEMA	85 nm	1.8 μM	363
OVCAR-3	SN38		GO	PEG	mono- and bilayer LD = 5−50 nm	0.12 nM	3
Pancreatic carcinoma							
Panc-1	gemcitabine	80	GQD	hyaluronic acid and human serum albumin NPs	5 nm	10 μg/mL	365
Prostate cancer							
PC3	cisplatin	65	SWCNT	carboxylic group	D = 1.3−1.6 nm; LD = 100−200 nm	50 μg/mL	510
	DOX	40	MWCNT	PEI(FITC)-mAb	D = 10−20 nm; LD = 150 nm	2 μg/mL	366
	DOX	60	rGO	PEG−BPEI	mono- and bilayer LD = 100−200 nm	50 μg/mL	415
	DTX	65	fullerene-C_{60}	PEI and FA	140 ± 2.7 nm	8 μg/mL	511
	DOX	34	ND	DGEA	89 nm	2 μg/mL	512
	DOX	42	ND	carboxylic group	51.5 nm	1.2 μg/mL	225
CP-r PC-3	cisplatin	30	fullerene-C_{82}	Gd and hydroxyl group	50 ± 12 nm	1 μg/mL	493
DU145	DOX	70	C-dots	PEG−chitosan	182 nm	100 μg/mL	65
Skin cancer							
Melanoma							
B16F1	EPI	55	GO	hyaluronic acid	400 nm	20 μg/mL	471
B16F10	DOX	94.20	fullerene-C_{60}	PEI and hydrazone	181 ± 4.7 nm	4 μg/mL	513
Squamous carcinoma							
A-5RT3	CPT	80	GO	PNIPAM	monolayer LD = 189.6 nm	1 μM	514
SCC7	DOX	80	GO	PEG and Ce6	monolayer LD = 148 ± 18 nm	2.5 μM	414
COS-7	plasmid DNA		C-dots	PDMA−PMPD	2.2 ± 0.3 nm	CD-PDMA80 (16:1); CD-PDMA80-PMPD20 (20:1); CD-PDMA80- PMPD40 (24:1)	515

Furthermore, a short time preparation method for fluorescent C-dots with hydrochloric acid as the carbonization catalyst was developed by Wang and co-workers.[306] The C-dots were synthesized by mixing two amino acids, phenylalanine and tryptophan solutions, for 2 h with hydrochloric acid to effectively accelerate the carbonization time of the dots. It was found that the acidic environment would promote the polymerization process of the carbon precursors from amino acids. The required reaction time to form the C-dots in the absence of the hydrochloric acid was 10 h, which was 5 times longer than that with the acids. By tuning the excitation wavelength in the range of 660−760 nm, the emission peak of the C-dots exhibited an up-conversion fluorescence centered at 435 nm. Further, the obtained C-dots were functionalized with MUC-1 DNA aptamers through the EDC-NHS carbodiimide cross-link reaction to achieve targeted imaging of MCF-7 breast cancer cells overexpressed with MUC-1 receptors. To demonstrate the specificity of the aptamer-conjugated C-dots, human hepatocellular liver carcinoma HepG2 cells with much lower expression of MUC-1 receptors were also incubated with the same concentration (100 mg/mL) of C-dots. From the fluorescence images, the bright-blue fluorescence was only

DOI: 10.1021/acs.chemrev.9b00099
Chem. Rev. XXXX, XXX, XXX−XXX

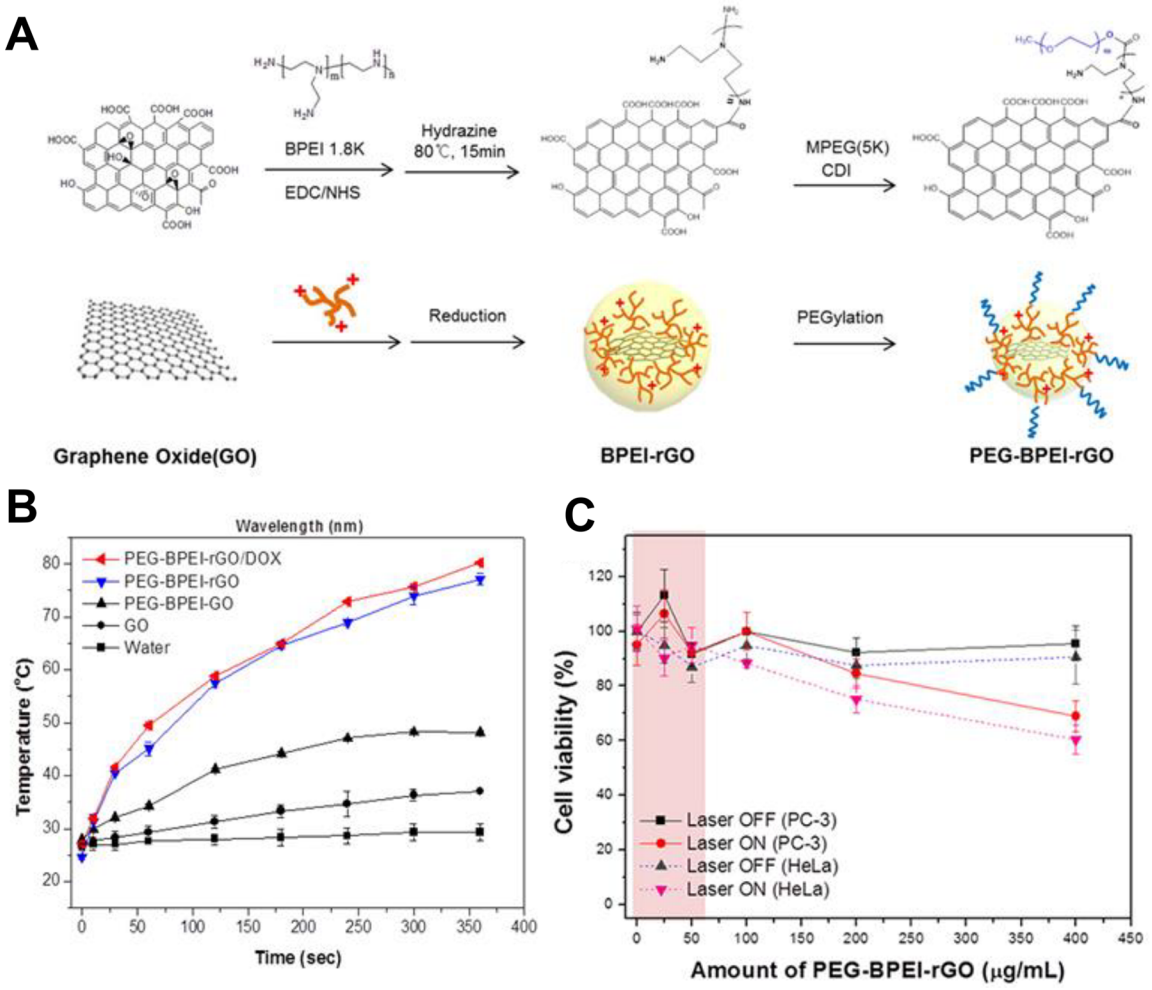

Figure 25. (A) Schematic representation of the synthesis and modification of PEG−BPEI−rGO. (B) Temperature of GO, PEG−BPEI−rGO, and PEG−BPEI−rGO/DOX solutions under NIR irradiation. (C) Cell viability of PC-3 and HeLa cells incubated with different concentration of PEG−BPEI−rGO in the dark and under NIR irradiation. Reprinted with permission from ref 415. Copyright 2013 American Chemical Society.

detected inside the MCF-7 cells while poor fluorescence was observed for the HepG 2 cells.

2.3. In Vitro Therapeutic Delivery

2.3.1. In Vitro Drug Delivery. Conventional drug delivery systems often have the disadvantage of a knock-on of adverse side effects. Inappropriate dosage stemming from low specificity leads to increased cellular toxicity, culminating as adverse side effects experienced by the patient, some of which could be life threatening before causing drug resistance. Such poor outcomes resultant from conventional drug delivery systems have put an impetus on the development of nanocarriers for targeted drug treatments. The efficacy of nanocarriers for such therapeutic applications are undoubtedly complex and dependent on several factors such as its drug loading, targeting, and release capabilities, particle size, and surface properties. These, in turn, would affect the corresponding characteristics concerning delivery in a biological environment such as drug uptake, cellular fate, barrier penetration, and distribution properties.[80,81] One of the major concerns faced in the development early drug carriers was its chemical composition, particularly for semiconductor nanomaterials, whose heavy metals posed a significant toxicity risk. Investigations into biological implications of nanomaterials further revealed effects of its physical properties. For example, surface charges and hydrodynamic radius could affect the biodistribution characteristics by potentially prolonged retention times.[259] The size of the nanoparticle also affects the cellular damage profile. Smaller nanoparticles, with greater penetration capability to the cell nucleus, were found to inflict greater DNA damage.[403]

Nanocarbons, which intrinsically exhibit high surface area, low toxicity, and biocompatibility, naturally lend themselves well as a promising drug delivery carrier.[404−408] Graphene, the 2D allotrope of carbon, can be oxidized to form water-soluble GOs. The large planar surface functional area and carbon hexagonal ring structure can facilitate the loading of aromatic cancer drugs through π-stacking force or hydrogen bonding. GOs have also been reported to be loaded with photosensitizers, such as hypocrellin A and chlorin e6 (Ce6), to achieve photodynamic therapy.

Similarly, CNTs permit versatile functionalization, with the ability to attach anticancer drugs covalently or noncovalently. Drug molecules with multiple aromatic ring π-structures, such as the antibiotic DOX, are easily loaded to the CNT surface through noncovalent interaction. Additionally, structural traits can be exploited to allow for mutlifunctionality. For example, leveraging on the higher optical absorption of MWCNTs in the NIR as compared to SWCNTs, nanoprobes delivered to the

DOI: 10.1021/acs.chemrev.9b00099
Chem. Rev. XXXX, XXX, XXX−XXX

tumor sites can produce heat to destruct the tumor under NIR excitation. Water-soluble fullerene derivatives of C_{60}-$(OH)_n$ protect normal cells by removing free radicals while damaging cancer cells in the presence of sugar derivatives of C_{60} under visible light excitation. DOX molecules bound to the fullerenol surface by amide linkers and show good chemotherapy efficiency.

The structure of SWCNH, similar to that of SWCNT, consists of a conical structure with around 2000 tubules with an average size ranging from 80 to 100 nm. This size is in the optimum range of the enhanced permeability and retention (EPR) effect that ensures accumulation at tumor sites. More importantly, drugs can be loaded at both inner and outer walls of the SWCNHs. The ND tendency to aggregate and cluster when dispersed in aqueous solutions is a unique trait which can improve the loading capacity on their surface or internal pores through $\pi-\pi$ interactions as compared to that of a single ND. Furthermore, the slow and controlled drug release observed with DOX-loaded ND probes has shown to inhibit in vivo tumor growth.

In this section, we will discuss the theranostics applications of in vitro drug delivery systems employing these nanocarbon materials as drug carriers. Detailed summaries of carbon-based nanomaterials for in vitro drug delivery are presented in Table 3.

2.3.1.1. In Vitro Drug Delivery by Graphene. Graphene-based nanomaterials, especially GO nanosheets, have been widely studied as effective nanocarriers for delivering various types of drugs for chemotherapy or multimodal therapy with enhanced photothermal or photodynamic effects.[409−413] Because the GO nanosheets are initially prepared by chemical exfoliating from bulky graphite sheets, they can be readily functionalized with hydrophilic groups or molecules such as carboxyl/hydroxyl/epoxide groups and PEG/polyethylenimine (PEI) molecules, making them biocompatible for nanomedicine applications. Moreover, the large surface area and hexagonal ring structures of GOs significantly improve the loading efficiency of the drugs that contain similar aromatic ring structures, like anticancer drugs DOX and camptothecin (CPT), due to a strong π-stacking interaction. For instance, Miao et al. reported the use of PEG-functionalized GOs (pGOs) as both effective anticancer drug carriers and photosensitizers for photodynamic cancer treatment.[414] The pGOs conjugated with photosensitizer Ce6 showed a significantly improved delivery rate to the cancer cells in comparison to that with only Ce6. The loading efficiencies of the Ce6 and DOX molecules were determined based on their quenching effect to the pGOs. According to the fluorescent measurement results, the loading efficiency for Ce6 was 51.9 ± 5.1% and even higher for DOX at 61.7 ± 4.4%. In this study, SCC cancer cells were employed as a target cell model for monitoring the delivery of the Ce6/DOX/pGO. The flow cytometry results showed that the cellular delivery rate for Ce6 was up to 96.2 ± 1.7% for the DOX:Ce6 ratio of 1:2. In vivo drug delivery of the Ce6/DOX/pGO nanoconjugates was also confirmed by the disruption effect of SCC tumor nuclei under LED illumination at a wavelength of 660 nm. It is worth noting that the nanoconjugates could be accumulated at the tumor sites for more than 72 h. The in vivo toxicity of the pGOs was tested by intravenously injecting with a high concentration of 80 mg/kg. The survival of all mice injected with pGOs indicated low acute toxicity, while the pure GOs without PEG functionalization resulted in 100% fatality to the mice.

Later, Kim et al. designed an rGO nanocarrier for controlled drug delivery/release through photothermal triggering in the cytosol.[415] The authors compared the drug loading efficiency between the rGOs and GOs. The PEG and branched PEI molecules were capped at the surface of rGOs to improve their solubility and biocompatibility (Figure 25A). Anticancer drug molecules with aromatic ring structures, like DOX, could directly adsorb onto the surface of the PEG−BPEI−rGOs through π-stacking and hydrophobic interaction, leading to a higher loading efficiency (100%) than that of PEG−BPEI−GO without reduction (only 10%). The PEG−BPEI−GO loaded with DOX led to aggregations and the PEG−BPEI−rGO loaded with DOX remained monodispersive. This suggested that the PEG−BPEI functionalized rGOs were more suitable as drug carriers in the cellular environment. To investigate the NIR absorption efficiency for the GOs, an 808 nm laser with a power density of 6 W/cm^2 was used to illuminate the solutions. Both the PEG−BPEI−rGO and PEG−BPEI−rGO/DOX exhibited a higher increase in temperature in comparison to that with pure GO or unreduced PEG−BPEI−GO solutions (Figure 25B). The results indicated that the light energy had been effectively absorbed by the functionalized rGO solutions and transferred to molecular vibration energies for thermal generation. For in vitro studies, the PEG−BPEI−rGO/DOX nanodrugs were stimulated by the presence of GSH and NIR light irradiation. The photothermal effect of the PEG−BPEI−GO and their reaction to the proton sponge effect of GSH were observed and led to a high cancer cell-killing efficacy (Figure 25C). Moreover, the release of the drug could be stimulated by multiple factors including GSH concentration, pH value, and the photothermal disruption of the endosomes. GSH molecules were found to break the binding between DOX and the rGO sheets, and the low pH value resulted in an increased hydrophilicity of the DOX molecules and thus reduced binding efficiency to the GO surface.

Recently, Wu and co-workers functionalized GO with adipic acid dihydrazide (ADH) and HA through covalent binding between amine groups.[416] The GO nanosheets were synthesized by chemically oxidizing graphite followed with ultrasonication process. The HA-conjugated GO nanosheets showed negligible cytotoxicity to HeLa cancer cell models after the receptor-specific endocytosis even at a high concentration of 200 μg/mL. Low in vivo toxicity of the HA-GOs were confirmed by the hematological and histological results after injecting high concentration of HA-GOs up to 10 mg/kg to mice for 10 days. The maximum drug loading efficiency was 81.5%, indicating 815 mg DOX molecules were loaded on 1 g of GO-HA. The pH-dependent release of DOX molecules from the GO-HA surface in PBS buffer solutions was monitored at 37 °C. It was found that only 6.8% and 10.9% drugs were released at a pH value of 7.4 and 6.3, while a significantly increased value of 26% was obtained at a pH value of 5.2 due to the higher hydrophilicity of DOX in low pH solutions. The target cellular uptake of the DOX-loaded GO-HA was tested by using two different cancer cell models: (i) HeLa cells with high concentration of the CD44 receptor proteins that could be conjugated with the HA molecules and (ii) negative control of L929 cells with low levels of CD44. After 3 h incubation with GO-HA/DOX solutions, strong fluorescence in the red region was observed in the HeLa cells and no obvious fluorescent signals were obtained inside the L929 cells. The anticancer effect of the GO-HA/DOX conjugates were evaluated by incubating with the HeLa cells

DOI: 10.1021/acs.chemrev.9b00099
Chem. Rev. XXXX, XXX, XXX−XXX

for 12 h. A significant cytotoxic effect of GO−HA/DOX solutions was obtained in comparison to that with GO-HA.

GO-based drug delivery carriers with surface coating of cytamine PEGylated alginate (Cy-ALG−PEG) brushes through covalent binding of disulfide bridge functional groups were demonstrated by Zhao and co-workers.[356] The PEG brushes on the GO surface not only effectively prevented the leakage of the DOX drug molecules in the physiological environments but also prolonged the blood circulation times of the drug carriers. The 3D GO-Cy-ALG−PEG nanocomplex was prepared by mixing 40 mg of Cy-ALG−PEG with 200 mL of GO solutions with a concentration of 1 mg/mL and then sonicating by 15 min. A high DOX loading and encapsulation efficiency of 97.64 ± 3.36% and 0.9764 ± 0.2358 mg/mg was achieved for the 3D GO nanocomplex. This is attributed to both, the π-stacking interaction of GO and DOX and the electrostatic binding of the ALG and DOX molecules. By using a liver cancer cell (HepG2) as a target cell model, GO-Cy-ALG−PEGs with different concentrations from 0 to 200 μg/mL were added into the cell culture medium. A high cell viability ranging from 103.9 ± 4.1% to 93.4 ± 3.2% indicated low cytotoxicity of the nanocomplex. The authors also studied the in vitro controlled drug release of the GO nanocomplex by simulating the pH and GSH concentrations in normal and cancer cells. For the case of normal tissues, the pH value is around 7.4 and the GSH concentration is 10 μmol/L, while these values change to 4.5−6.5 and 10 mmol/L, respectively, in the tumor tissues. In the presence of GSH, the cleavage of disulfide bond between the amine groups of Cy and the carboxyl groups of GOs enabled the controlled release function of the 3D nanocarriers specifically at the tumor sites. After 32 h incubation, the release percentage in the physiological environment with pH = 7.4 and 10 μmol/L GSH was 14.15% and increased to 21.45% with a higher GSH concentration of 10 mmol/L at the same pH value. The DOX-loaded GO-Cy-ALG−PEG solutions were then incubated with HepG2 cells with a dose of 30.0 μg/mL. Confocal laser scanning microscopy (CLSM) imaging results revealed that the DOX was successfully released to the cytosol and accumulated at the cell nuclei with 10 mM GSH. After 6 h incubation, the apoptosis rates for the free DOX and DOX-loaded GO-Cy-ALG−PEGs were 99.91% and 99.96%, respectively.

More recently, Chen et al. fabricated PEG−rGO nanosheets from a single-step green method without toxic organic agents and used them for photothermally triggered drug delivery.[417] The PEG−rGO nanosheets were simply prepared through mixing the methoxypolyethylene glycol amine (mPEG−NH_2) with the GO nanosheets at a reaction temperature of 90 °C. While reacting with the PEG molecules, the GO nanosheets were reduced to rGO by the amino groups and functionalized with mPEG. This PEGylated process improved their hydrophilicity and made the PEG−rGO water-soluble. Similar to DOX, resveratrol is also an anticancer drug molecule with aromatic ring structures and can induce the cell apoptosis for different cancer cells. The resveratrol molecules absorb NIR light and thus can be excited to produce fluorescence. The loading efficiencies for PEG−rGO and PEG−GO were 175.6 and 78.8 w/w%, respectively, suggesting a 2-times improvement in the PEG−rGO carriers due to the noncovalent binding of π-stacking force. A reduction in the intensity of the resveratrol fluorescence was recorded with the increasing concentration ratio of the PEG−rGOs from 0 to 160 μg/mL. Furthermore, an 8- and 14-times enhancement of the drug loading efficiency for rGO and PEG−rGO was obtained compared to that of GO nanosheets at an excitation wavelength of 808 nm. The PEG−rGO nanosheets could also absorb NIR light and transfer the light energy to thermal heat. It was observed that the temperatures of PEG−rGOs and resveratrol-loaded PEG−rGO solutions were increased from 39 to 60 °C under 5 min of NIR irradiation (power density of 0.6 W/cm^2). The NIR absorbance rate of PEG−rGO was enhanced by 14-times compared to that with PEG−GO. The generated heat would break the π-stack binding and detach the resveratrol molecules from the rGO surface. The in vitro drug release controlled by NIR light illumination was carried out with 4T1 cancer cells with 22 μg/mL PEG−GO, PEG−rGO, and resveratrol-loaded PEG−rGO (resveratrol concentration of 40 μg/mL). A high cellular drug uptake of 32.6% was achieved in the case of PEG−rGO. No cell apoptosis was induced for the PEG−GO and PEG−rGO solutions even at a higher concentration of 22 μg/mL, while a significant apoptosis rate was obtained in the presence of NIR irradiation, which confirmed the photothermally controlled anticancer drug release from the PEG−rGO carriers.

2.3.1.2. In Vitro Drug Delivery by Carbon Nanotubes. In addition to GO nanosheets, CNTs are also promising candidates for delivering anticancer drugs and biomolecules to target cells.[418−421] Their surface properties for drug loading efficiency and capacity are determined by different structure types (single-walled or multiwalled) or the conjugation with different hydrophilic molecules for specifically recognizing the receptors overexpressed in the target cells.[422] The functionalized CNT nanocarriers not only improve the cellular uptake efficiency but also minimize the potential cytotoxicity effects with a controlled manner for in vitro drug release. For instance, Chen et al. designed a tumor-targeted drug nanocarrier using SWCNTs functionalized with tumor-recognition segments including biotin and a spacer molecule and conjugated with the anticancer drug of taxoid.[423] The taxoid drug was linked to the surface of SWCNT through a cleavable linker and would only break and detach in the cancer cell environment with high concentration of GSH. The disulfide bond of the cleavage linker between the drug and SWCNT reacted with the thiol groups of GSH and formed a sulfhydryl group that led to the release of the free taxiod molecules. The GSH concentrations in the normal cells were typically in the range from 1 to 2 μM but much higher in the cancer cells, ranging from 2 to 8 mM. Biotin molecules here served as the recognizing moieties for the receptors overexpressed on the surface of leukemia cancer cells (L1210FR). To test the enhanced specificity of the biotin-SWCNTs, both the SWCNTs and biotin-SWCNTs were further conjugated with fluorescent dye molecules of fluorescein isothiocyanate (FITC). The fluorescent intensity of the biotin-SWCNTs treated cells was much higher than that of the pure SWCNTs, indicating an improved permeability of the biotin-SWCNTs due to the receptor-mediated endocytosis process. The tumor cell target ability of the FITC-biotin-SWCNTs was confirmed by simultaneously incubating the biotin receptor overexpressing L1210FR cell and the negative control of a human lung fibroblast cell WI128. A much stronger fluorescence intensity was observed in L1210FR cells than that of WI38 cells. This demonstrated a higher cellular uptake efficiency of the biotin-SWCNT-taxoid drug carriers. Further, the IC_{50} value of the biotin-SWCNT-taxoid was 0.36 μg/mL, which was much lower than that of 50 μg/mL for the

DOI: 10.1021/acs.chemrev.9b00099
Chem. Rev. XXXX, XXX, XXX−XXX

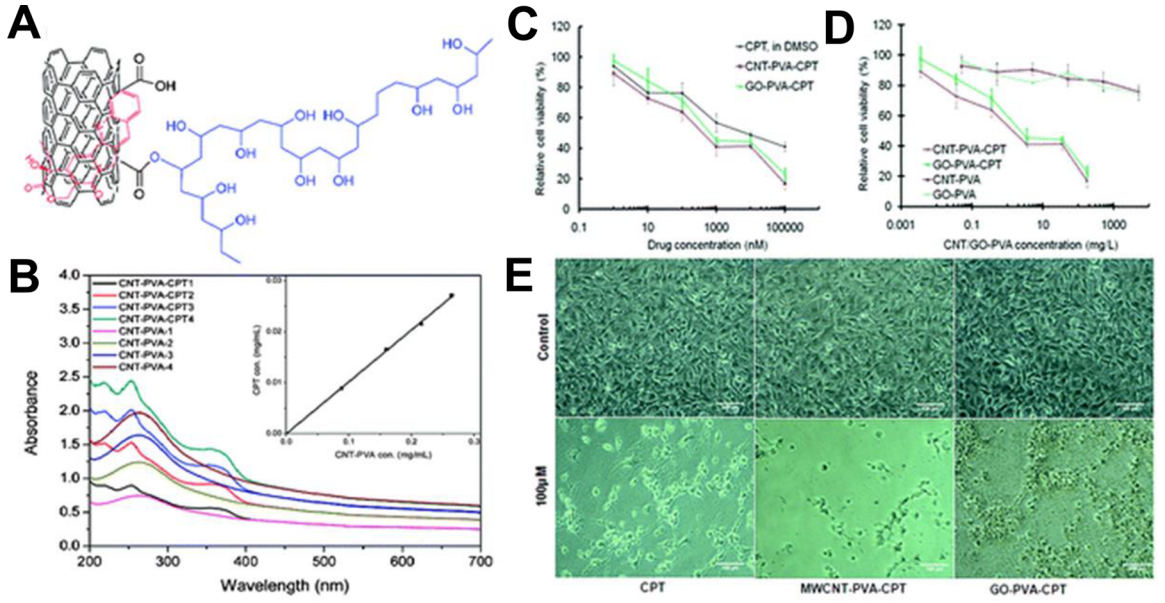

Figure 26. (A) Schematic describing the loading of CPT on MWCNT-PVA. (B) UV spectra of MWCNT-PVA and MWCNT-PVA-CPT with different concentrations. (C) Cell viability of MDA-MB-231 cells cultured with free CPT, MWCNT-PVA-CPT, and GO-PVA-CPT at different concentration. (D) Cell viability of MDA-MB-231 cells cultured with MWCNT-PVA and GO-PVA with and without CPT, respectively. (F) Microscopy images of MDA-MP-231 cells after being treated with CPT, MWCNT-PVA-CPT, and GO-PVA-CPT. Reprinted with permission from ref 425. Copyright 2011 The Royal Society of Chemistry.

untargeted L1210 and WI38 cell models, indicating enhanced cancer cell killing efficacy.

Later, Bhatnagar et al. developed a SWCNT drug delivery carrier with polymer molecules of chitooligosaccharide (COS) as the capping agent.[424] The capping of COS molecules was achieved through a coupling reaction with EDC to form an amide bond on the SWCNT surface that could enhance the biocompatibility of the CNT carriers and reduce their intrinsic toxicity. Gliotoxin (GTX) was employed as the drug cargo. Different capture moieties such as FA, p53, and lysozyme were conjugated to the SWCNT surface to achieve selective targeting of different cancer cells. Two cancer cells models, breast cancer cells (MCF-7) and cervical cancer cells (HeLa), were used for testing the cytotoxicity of the incorporated SWCNT drug carriers of SWCNTs-COS-GTX-FA, SWCNTs-COS-GTX-p53, and SWCNTs-COS-GTX-lysozyme. The cytotoxicity of the COS-SWCNTs before drug loading was studied by incubating the mammalian cells with the nanoconjugates at concentrations from 0.125 to 1 μM. No significant decrease of the cell viability was observed. All the SWCNTs-COS-GTX-FA, SWCNTs-COS-GTX-p53, and SWCNTs-COS-GTX-lysozyme drug nanocarriers resulted in high cell apoptosis rates. Among these carriers, the SWCNTs-COS-GTX-p53 exhibited the highest cytotoxicity to HeLa and MCF-7 cells. The authors attributed this to the high percentage of p53 protein overexpression (larger than 50%) in most types of cancer cells. Following drug treatment, the cell viability dropped to 73.46% after 4 h of incubation and then to 68.9% after 12 h. These results confirmed that the functionalized SWCNTs carriers could release the GTX drugs in a controlled manner and gradually increase the cell apoptotic rates.

In another report, water-soluble MWCNTs with hydrophilic molecules of poly(vinyl alcohol) (PVA) as the surface coating layer were prepared by Sahoo and co-workers.[425] Anticancer drug molecules of CPT were adsorbed to the surface of MWCNTs due to π-stacking interaction and used for chemotherapy of human skin and breast cancer cells (Figure 26A). In this study, the MWCNTs were oxidized by strong acid mixtures including H_2SO_4 and HNO_3 with a volume ratio of 3:1. Thus, abundant carboxyl groups on the surface of MWCNTs were available that allowed the surface functionalization of the PVA molecules by a carbodiimide-activated esterification process. The CPT drug molecules were loaded onto the PVA-MWCNT through simply mixing the CPT dissolved in the DMSO solutions with the PVA-MWCNT solutions. The loaded CPT drug had an absorption peak at 369 nm (Figure 26B), and thus the loaded amount could be calculated from the absorption intensity. The cell apoptosis rates of the CPT-PVA-MWCNTs were monitored by a human breast cancer cell model of MDA-MB-231 treated with the CNT drug carriers at different concentrations ranging from 0 to 500 mg/L. It is worth noting that even with a high concentration of 500 mg/L, the pure CNT carriers without drug loading showed a very low cytotoxicity to the cells with a cell viability rate larger than 80% (Figure 26C,D). On the other hand, the CPT-loaded PVA-MWCNTs exhibited a 50% growth inhibition concentration (IC_{50}), with a concentration of 400 nM that was 15 times lower than that with the free CPT drugs in DMSO solutions (Figure 26E).

Recently, Wu et al. prepared MWCNTs with functional molecules of PEI and prostate stem cell antigen (PSCA) monoclonal antibody (mAb) for specifically targeting cancer cells that overexpressed prostate stem cell antigen like prostate PC-3 cancer cells.[366] The resulting MWCNT-PEI-mAb nanocomplex with a small average length of 150 nm served as effective drug delivery carriers for chemotherapy of tumors. Before the covalent binding of the prostate stem cell antigen monoclonal antibody (mAb_{PSCA}) onto the MWCNT surface, the PEI-MWCNTs were conjugated with a commonly used dye molecule of FITC through amine bonds in order to track the loading and release of drugs for in vitro and in vivo study.

DOI: 10.1021/acs.chemrev.9b00099
Chem. Rev. XXXX, XXX, XXX−XXX

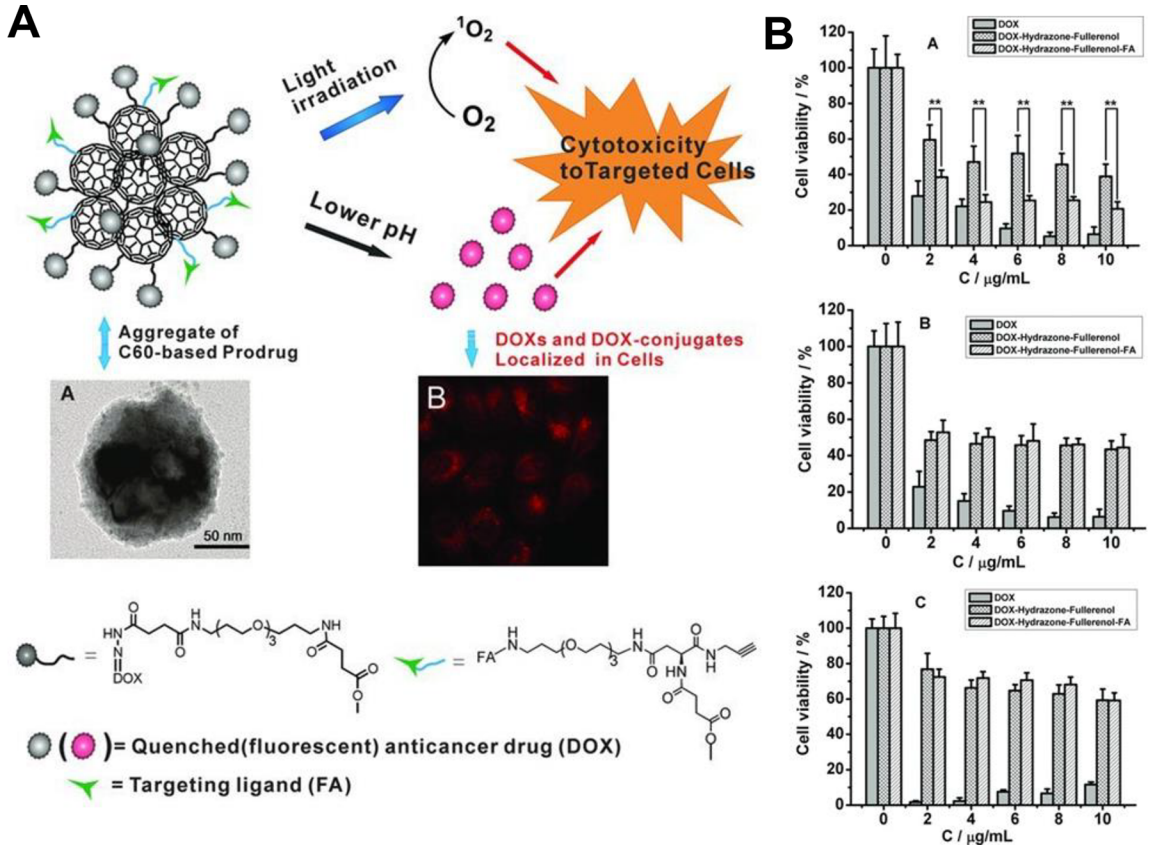

Figure 27. (A) Schematic diagram of the fullerene-based aggregate with dual cancer actions. Inset A is the HRTEM image of a DOX−hydrazine−fullerenol−FA-aggregate. Inset B is the fluorescence microscopy of HeLa cells, where DOX has been released from the nanocarrier. (B) Cell viability of HeLa (top), L929 (middle), and A549 (bottom) treated with DOX, DOX−hydrazone−fullerenol−FA and DOX−hydrazone−fullerenol particles. Reprinted with permission from ref 432. Copyright 2013 John Wiley and Sons.

The intrinsic cytotoxicity of the PEI-MWCNT-FITC-mAb carriers without the cancer drug loading was evaluated by incubating them with two different cancer cell models of MCF-7 and PC-3. For both of the models, the cell viabilities remained larger than 85% after 24 h upon treatment with a high concentration of the CNT nanocomplex (200 μg/mL), indicating the low toxicity of the CNT carriers. The selective cellular uptakes of the CNT carriers were monitored by the fluorescent intensity of the PC-3 and MCF-3 cells. With a dose of 10 μg/mL of PEI-MWCNT-FITC-mAb, much stronger fluorescence signals were observed for the PC-3 cells while a relative lower signal was obtained for the MCF-7 cells with low expression of prostate stem cell antigens. DOX anticancer drug molecules were used as a chemotherapy model as the cargo for the carriers. The loading amount of DOX molecules were found to increase with their increasing concentrations and saturated at 300 mg/g. The release of DOX molecules from the CNT carriers was pH-dependent and could be triggered by a low pH value of 5.2, similar to the physiological conditions in the cancer cells. After a 1.5 h incubation time of the 30 μg/mL DOX-loaded PEI-MWCNT-FITC-mAb, the DOX molecules accumulated mainly in the cytoplasm of the PC-3 cells and after 3 h, most of them were located in the cell nuclei. In comparison to the negative control of MCF-7 cells, the DOX-loaded PEI-MWCNT-FITC-mAb induced a significantly higher toxicity to the target PC-3 cells with prostate stem cell antigen receptors, which linearly increased with the dose of the drug carriers.

2.3.1.3. In Vitro Drug Delivery by Fullerenes. Fullerenes are one of the pioneering carbon allotropes that have been extensively studied as potential candidates for clinical drug delivery applications.[426−429] To overcome the challenge of traditional phospholipid liposome nanocarriers with low loading efficiency and low physical stability to hydrophobic drug molecules, researchers attempted to functionalize novel C_{60} fullerene nanocarriers with amphiphilic dendrimer groups to reduce their cytotoxicity and improve the target specificity with different cancer receptor ligands. For example, Partha et al. designed the fullerene-based nanocarriers as buckysomes for the delivery of hydrophobic drug molecules.[430] The buckysomes were formed by self-assembling amphiphilic fullerene AF-1 and heated at 70 °C, resulting in diameters ranging from 100 to 200 nm. Because of the heating of AF-1 structures, a large number of hydrophobic areas are exposed on the surface of the buckysomes. Hydrophobic paclitaxel (PTX) anticancer drug molecules were used as a delivery cargo to test the delivering ability of the buckysomes. A fluorescence dye of fluorophore DiI was functionalized onto the surface of buckysomes in order to monitor and confirm the in vitro drug delivery. Mouse macrophage cells were incubated with the dye-conjugated buckysomes and cell internalization of the buckysomes carriers was confirmed by comparing the fluorescent imaging results. The authors attributed the cellular uptake process of the buckysomes to the endocytosis that was similar to the uptake of traditional liposome carriers because the size of the buckysomes was in the same range as that of liposomes. Further, A431 epidermoid cancer cells were used to

DOI: 10.1021/acs.chemrev.9b00099
Chem. Rev. XXXX, XXX, XXX−XXX

demonstrate that the buckysomes could accumulate inside the cell nuclei and did not attach to the cell membranes. To quantitatively evaluate the efficacy of the PTX-loaded buckysomes for killing the cancer cells, MCF-7 breast carcinoma cells were employed as the target chemotherapy models. The cell viability was found to decrease with increasing PTX concentration from 28.6 to 714 ng/mL after 24 h incubation and even dropped more significantly after 72 h incubation. In contrast, the empty buckysomes without drug loading induced negligible cytotoxicity for all the test cell models including macrophage, A431, and MCF-7 cells.

Later, Wei et al. demonstrated that water-soluble fullerene C_{60} derivative, C_{60}(Nd) nanoparticles could serve as drug carriers for sensitive chemotherapeutic applications due to their effective autophagy and cell-killing functions.[431] The C_{60} and its derivative C_{60}(Nd) were fabricated by evaporating tetrahydrofuran from the mixtures containing water and C_{60}/C_{60}(Nd) dissolved in tetrahydrofuran solutions. To test the intrinsic cytotoxicity of C_{60} and C_{60}(Nd), two types of cancer cells were used, i.e., HeLa and DOX-resistant MCF-7 cells. These cells were treated with fullerene solutions with different concentrations. From the results of propidium iodide (PI) staining assays, both C_{60} and C_{60}(Nd) solutions induced a low cytotoxicity at a lower dose while they led to 85% cell death for HeLa cells and 70−90% cell death for MCF-7 cells at a high dose of 2 μg mL $^{-1}$. To study the enhancement effect of C_{60}/C_{60}(Nd) nanoparticles for DOX chemotherapy, the 0.5 μg mL $^{-1}$ DOX drugs that could not induce cell death were mixed with the C_{60}/C_{60}(Nd) solutions at a low concentration of 0.2 μg/mL. The mixtures were shown to exhibit a higher cell killing efficacy than that of the DOX molecules alone for the HeLa cells. Moreover, the C_{60}(Nd) nanoparticles induced a higher toxicity enhancement effect than that of pure C_{60} nanoparticle solutions. The improvement on cell-killing effect of C_{60}/C_{60}(Nd) nanoparticles was also observed for DOX-resistant MCF-7 cells. In addition, the fullerene nanocarriers, particularly the C_{60}(Nd), demonstrated high ROS levels in the cancer cells that led to the autophagy process.

A multifunctional fullerene (C_{60}) drug carrier with controlled release ability was reported by conjugating the DOX molecules through a cleavable bond and a target ligand molecules of FA on the fullerene surface (Figure 27A).[432] The size of the fullerene carriers was maintained at 135 nm even after surface functionalization and drug loading. To prepare the drug-loading fullerene nanocarriers, the fullerenols were first linked with succinic acid and then covalent bound with a hydrophilic linker oligo(ethylene glycol) of EG3-tri(ethylene oxide). DOX drug molecules were finally bound to the fullerene surface through carboxylic hydrazone molecules that was sensitive to acidic conditions. The FA molecules were conjugated to the fullerene surface via amidation reactions. The EG3 molecules on the fullerene surface could reduce the nonspecific binding between the nanoparticles and other biomolecules while their hydrophilic property ensured the stability of the nanoparticles in the physiological conditions. The DOX-loaded fullerenol nanocarriers had a fixed diameter of 135 nm in a wide concentration range from 4 to 4000 μg/mL. HPLC results indicated that at least five DOX groups were conjugated on one fullerene carrier, indicating a high loading efficiency of 26 wt %. Three different cancer cell models including L929, A549, and HeLa were used for the cellular uptake and cytotoxicity studies. The cells were treated with hydrazine−fullerenol−FA solutions with concentrations ranging from 0 to 30 μg/mL. No significant cell death was observed for the cells, suggesting the low toxicity of the empty carriers (Figure 27B). Because the HeLa cells are FA-receptor positive while the L929 and A549 are FA-receptor negative, the specificity of the DOX-loaded fullerene carriers could be investigated by monitoring their cytotoxicities after incubating with these cells. When treated with the same concentration of the DOX-loaded fullerenol nanocarriers, the cell viability of the FA-receptor positive HeLa cells decreased significantly while it remained the same for FA-receptor negative L929 and A549 cells.

More recently, Zhang et al. functionalized the fullerene C_{60} with HA and transferrin (Tf) for delivering an iron-dependent anticancer drug of artesunate (AS).[433] A high loading efficiency of 162.4% was achieved in terms of the weight ratio between the AS and the HA-Tf-conjugated fullerenes. The conjugation of the C_{60} with HA molecules could effectively reduce their cytotoxicity and improve the biocompatibility of the C_{60}-based drug carriers. The AS drugs are known to be toxic to tumor cells both in vitro and in vivo due to the flexible endoperoxide bridge cleavage in the presence of iron ions. The cleavage induces the release of free radicals and thus leads to apoptosis of the tumor cells. The HA-C_{60} particles were highly stable and monodispersive in different biological media including cell culture medium, DI water, and even plasma solutions from the mice. After 2 h incubation, the MCF-7 cells treated with AS-loaded HA-C_{60}-Tf showed a 99.7% internalization rate while the one with only AS-loaded HA-C_{60} was 47.4%. These results indicated that the transferrin molecules coated on the fullerene nanoparticles could enhance the cellular uptake rate of the carriers due to the receptor-mediated endocytosis process as the Tf (CD71) receptors were overexpressed in the MCF-7 cells. The cell viability was reduced to 76.8 ± 3.84% and 52.6 ± 2.63% in the case of incubation with AS-loaded HA-C_{60} and HA-C_{60}-Tf nanocarriers while being maintained at a high value of 97.6 ± 2.16% with empty nanocarriers of HA-C_{60}. Most notably, the transferrin molecules could also deliver the intracellular iron ions into the MCF-7 cells and thus activate the oxidizing process of the AS drugs to generate harmful ROS. Overall, the higher cellular uptake efficiency and the iron-mediated drug release process were attributed to the higher cytotoxicity and anticancer effect for the HA-C_{60}-Tf nanocarriers than that with pure HA-C_{60} ones.

2.3.1.4. In Vitro Drug Delivery by Carbon Nanohorns. SWCNHs that possess similar structures as those of CNTs also allow the multifunctionalization of target ligands and drug molecules on both the inner and outer tube walls.[434−439] After oxidation, the hole of the SWCNHs can be opened and filled with functional carboxyl groups at the edges that provide covalent binding sites for different drug molecules. The intrinsic cytotoxicity of SWCNHs is found to be lower than that of the CNTs due to the less-contaminated production reaction in the absence of metal catalysts. In addition, the SWCNHs only assemble to a spherical conjugate with an average diameter less than 100 nm while the CNTs are easily aggregated to form long bundles in a length scale of micrometers in biological solutions. Thus, the smaller size of SWCNHs in the physiological environment is more suitable to achieve a higher cellular uptake and targeted delivery efficiency to the tumor cells. For example, Ajima et al. fabricated SWCNHs as nanocarriers for cisplatin (CDDP) through a nanoprecipitation approach.[440] The SWCNHs were oxidized with the holes opened at one end and then mixed with CDDP.

DOI: 10.1021/acs.chemrev.9b00099
Chem. Rev. XXXX, XXX, XXX−XXX

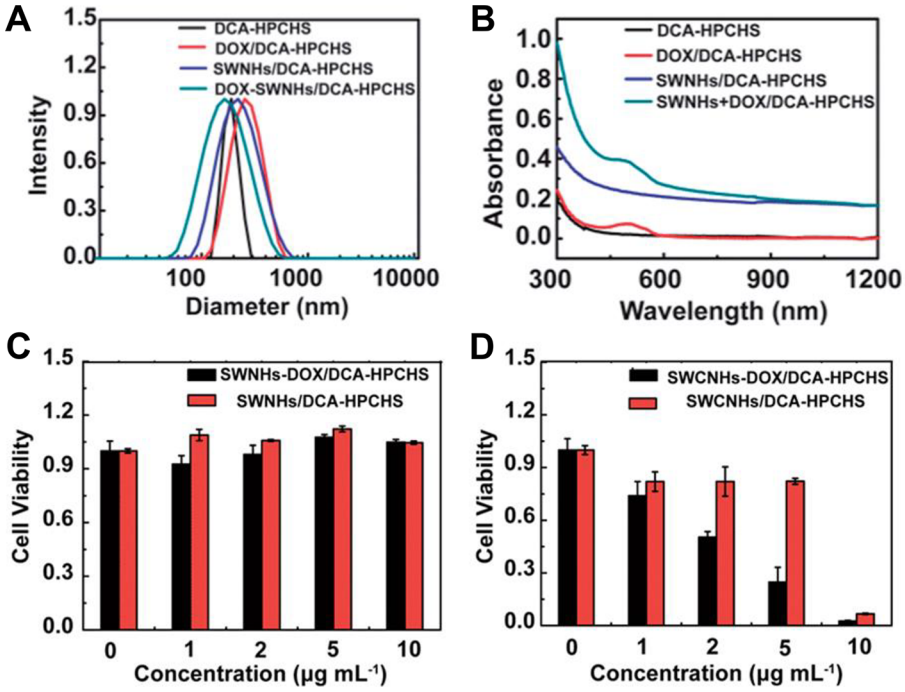

Figure 28. (A) Size distribution and (B) absorption spectra of DCA−HPCHS, DOX/DCA−HPCHS, SWNH/DCA−HPCHS, and DOX-SWNH/DCA−HPCHS measured using DLS. Cell viability of 4T1 cells treated with SWNH/DCA−HPCHS and DOX-SWNH/DCA−HPCHS (C) with and (D) without NIR light irradiation. Reprinted with permission from ref 441. Copyright 2014 Royal Society of Chemistry.

The loading efficiency for the CDDP onto the SWCNHs could reach up to 46%, and the release percentage of the CDDP drug was 60% for dimethylformamide and 100% for water as the solvents. The anticancer efficacy was improved by 4−6 times compared to that of the free CDDP drugs. On the basis of the atomic absorption spectrum results, the loading rate of the CDDP onto the SWCNHs surface was 46% with water as the solvent and 15% with dimethylformamide as the solvent. The CDDP drug release from the SWCNHs was measured via a dialysis cellulose tube in cell culture medium. It was observed that 100% of the free drugs were diffused from the tube within 5 h, while the CDDP-loaded SWCNHs had a slower release time of 150 h to reach the 100% release. This indicated a much confined drug profile inside the narrow space of the SWCNHs. To evaluate the anticancer efficacy of the CDDP-loaded SWCNHs carriers, a human lung cancer cell model of NCI-H460 was used as a target example for the in vitro delivery studies. After 24 h incubation, the CDDP-loaded SWCNHs could induce a 50% drop of the cancer cell viability with a dose that was only 1/6 of free CDDP drugs that was required for the same death rate. The authors suggested that the improvement of the anticancer efficacy of the SWCNHs drug carriers was due to the attachment of the SWCNHs to the cells that increased the localized release amount of the CDDP drugs.

Later, Chen et al. functionalized the DOX-loaded SWCNHs with amphiphilic deoxycholic acid modified hydroxypropyl chitosan (DCA−HPCHS) molecules and achieved NIR light-enhanced cellular uptake rate of the DOX carriers.[441] The DOX molecules were loaded onto the SWCNH surface through π-stacking force between the anthraquinone ring of DOX and the hexagonal ring structure of SWCNHs. Before conjugation, the DOX molecules were reacted with triethylamine for neutralization in order to enhance the loading of the DOX onto the SWCNH surface. DCA−HPCHS ligands were then attached to the DOX-loaded SWCNHs through a vacuum evaporation method. The average diameter of the resulted DOX-loaded SWCNHs/DCA−HPCHS was 164 nm (Figure 28A), which was smaller than that of the SWCNHs/DCA−HPCHS (220 nm) due to decreased aggregation between the SWCNHs through hydrophobic−hydrophobic bindings. The absorption peaks for the SWCNHs and the DOX drugs were located at the NIR region and 488 nm, respectively (Figure 28B). Thus, the amount of the DOX molecules loaded onto the SWCNH surface could be calculated through the absorbance at the 488 nm with the SWCNHs/DCA−HPCHS as the background. The cytotoxicity of the DOX-loaded SWCNH nanocarriers was monitored by incubating them with 4T1 cells. Different concentrations of empty SWCNH nanocarriers and DOX-loaded SWCNH nanocarriers from 1 to 10 μg/mL exhibited negligible toxic effect to the cancer cells (Figure 28C). However, the cell viability of cells incubated with DOX-loaded SWCNHs at a concentration of 5 μg/mL dropped by 73% under 808 nm light irradiation (power density of 0.6 W cm^{-2}) with a generated heating temperature of 43 °C (Figure 28D). The much smaller drop of 13% for the empty SWCNH nanocarriers indicated that the photothermal effect alone at 43 °C was not enough to kill the cancer cells. The enhanced cellular uptake of the DOX-loaded SWCNHs under NIR light irradiation was confirmed by flow cytometry analysis. Notably, the release amount of DOX did not increase under laser irradiation because the fluorescence intensity of the DOX-loaded SWCNHs before and after the irradiation remained at the same level.

CNH-supported liposome nanoparticles were also demonstrated as antinicotine vaccine carriers by Zheng and co-workers.[442] The CNHs were initially negatively charged and served as assembly scaffolds for cationic liposome nanoparticles. The conjugates were then functionalized with hapten-bound proteins. Here, CNHs were demonstrated to overcome

DOI: 10.1021/acs.chemrev.9b00099
Chem. Rev. XXXX, XXX, XXX−XXX

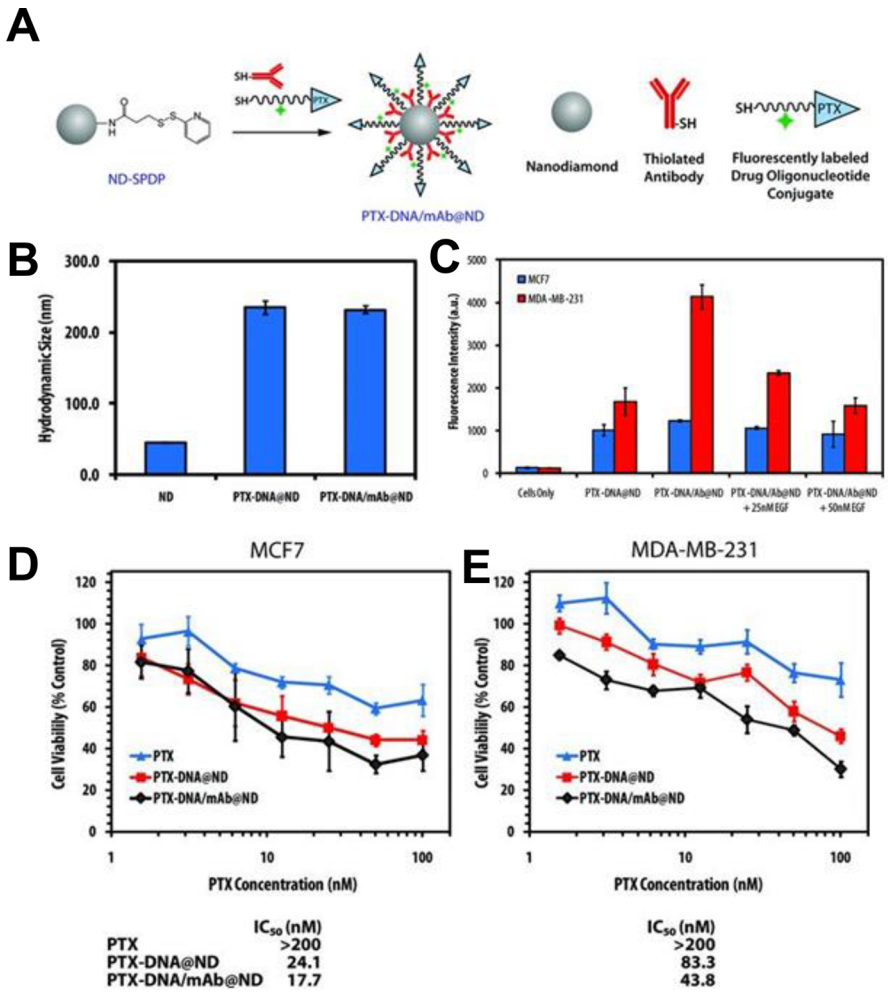

Figure 29. (A) Schematic illustrating the preparation of PTX−DNA/mAb@NDs. (B) Hydrodynamic size of NDs and its conjugate measured using DLS. (C) Quantitative analysis of PTX−DNA@ND and PTX−DNA/mAb@ND in MCF7 and MDA-B-231 cells using flow cytometry analysis. (D,E) Cell viabilities of MCF-7 and MDA-MB-231 cells 48 h treated with PTX, PTX−DNA@ND, and PTX−DNA/mAb@ND. Corresponding IC_{50} values are listed below the graph. Reprinted with permission from ref 307. Copyright 2011 John Wiley and Sons.

the challenge of avoiding precipitation or flocculation of the conventional drug carriers in the physiological environment while using pure liposomes. The thiol-Nic-BSA protein vaccines were mixed with maleimide−PEG functionalized CNH-supported liposome nanoparticles with a molar ratio of 1:8. The nicotine hapten, specific to the nicotine molecules, was conjugated with the BSA molecules through covalent binding between the carboxylic acid groups on the hapten and the amino groups on the BSA. The increasing hapten−BSA molar ratio resulted in an obvious decrease of the surface lysines on the BSA which confirmed the increasing number of hapten molecules attached on each BSA molecule. The hapten−BSA carriers were bound to the surface of liposome through reactions between the maleimide of the PEG-functionalized lipid surface and a sulfhydryl group at the primary amines of the BSA. With 50 times excess nicotine−hapten, one BSA molecule could conjugate with 15 nicotine haptens and with 200 times excess of 2-iminothiolane, one nicotine-BSA molecule could conjugate with five thiol groups. The designed vaccine carrier was in the desirable size range for the liposomes (<300 nm) for cellular uptake by the major antigen presenting cells, especially by the dendritic cells. Confocal fluorescent imaging results confirmed a much higher monodispersive profile and smaller size of the CNHs-supported liposomes than those of pure liposomes.

Recently, Chechetka et al. designed CNHs that were functionalized with PEI and FA as nanocarriers for magnetite nanoparticles (MNPs).[263] The drug carriers were used as multifunctional anticancer nanovectors. The CNHs with an average diameter of 150 nm were first oxidized by oxygen gas flow at a flow rate of 200 cm^3/min and a pressure of 760 Torr at a high temperature of 500 °C to induce the opened holes at the walls of the CNH surface. The oxidized CNHs were then mixed with 50 mg of $Fe(OAC)_2$ powder dissolved in 20 mL of ethanol to form the MNPs-CNHs. The PEI molecules were further coupled to the MNPs-CNH surface through a cross-linking process with carbodiimide EDC and sulfo-NHS. The conjugates were then bound with FA molecules by the carbodiimide mediation process. The diameter of the resulted PEI-MNPs-CNHs ranged from 200 to 300 nm, which was larger in size than the MNPs-CNHs alone because the PEI molecules had large hydrophilic and hyper-branched polymer groups. The aqueous solutions containing these nanovectors showed a significant temperature increase after NIR light illumination and radio frequency radiation. The cellular uptake and intracellular localization of the nanocarriers were quantitatively studied with two different cancer cell lines: (i)

DOI: 10.1021/acs.chemrev.9b00099
Chem. Rev. XXXX, XXX, XXX−XXX

human embryonic (FHs173We) cell, which is FA-receptor negative, and (ii) human epidermal carcinoma (KB) cell, which is FA-receptor positive. The KB cells exhibited a higher cellular uptake rate due to the overexpression of FA receptors on the KB cell surface. Moreover, the rate could be further improved by using a magnet with the magnetic force that interacted with the magnetite nanoparticles inside the nanocarriers. To evaluate the anticancer effect of the FA-PEI-MNPs-CNHs carriers, KB cells were treated with the conjugates at different concentrations ranging from 5 to 50 μg/mL for 24 h. Under the magnetic field induced by a magnet close to the cell culture dish, the cytotoxicity of the FA-PEI-MNPs-CNHs carriers was significantly increased to 36% at the concentration of 50 μg/mL. It is worth noting that the cell death rate could reach up to 94% with both the NIR laser irradiation and radio frequency induction, and no significant cytotoxicity was observed for normal cells like human embryonic cells (FHs173We) with lower expression of FA receptors.

2.3.1.5. In Vitro Drug Delivery by Nanodiamonds. NDs with diameters ranging from 2 to 8 nm are other promising candidates as drug carriers for their advantages including chemical inertness, unique surface electrostatics, biocompatibility, functionalization versatility, and nonbleaching fluorescence.[443−448] The use of NDs also enables to overcome the challenge of transporter-mediated multidrug resistance and intracellular tracking. The natural fluorescence of NDs is reported to be strong enough as fluorescent labels for cancer cells and can be further enhanced by the introduction of NV defects to their structures. Also, the detonation synthesis method for the NDs is cost-effective for producing nanoparticles with small sizes and narrow distributions. Both noncovalent and covalent bindings of functional groups such as oligonucleotides, antibodies, folic acids, and other drug molecules onto the ND surface have been recently achieved. For instance, Li et al. designed ND-based delivery vectors for anticancer drug molecules of 10-hydroxycamptothecin (HCPT) and studied their loading efficiency and releasing profile in HeLa cells.[449] Here, NDs with diameters of 2−10 nm were prepared through detonation methods and then dispersed in DI water by sonication for 30 min. During the synthesis process, carboxyl and hydroxyl groups were generated on the resulted NDs. To evaluate the cytotoxicity of the pure NDs, different cancer cell models including A549, HeLa, and K562 cells were incubated with the ND solutions at a high concentration of 100 μg NDs/mL. No significant decrease of the cell viability was observed for the cells. A low loading rate of 0.4 wt % was obtained for the direct adsorption of HCPT to the ND surface. However, the loading efficiency could be enhanced by up to 50% by adding NaOH solutions; 38 wt % of HCPT molecules from the ND surface were released after 24 h and the released amount gradually decreased with a value of 10 wt % after 120 h. In total, 90% HCPT molecules were released. The HCPT−ND conjugates were then injected into the cell culture media of the HeLa cells. A high cancer cell death rate was induced by the nanoconjugates with a concentration of 50 μg/mL.

Later, Zhang et al. functionalized the ND surface with dye-labeled drug−DNA oligonucleotides to achieve multimodal cancer therapies and enhanced anticancer efficacy (Figure 29A).[307] PTX molecules were chosen as the chemo-drug cargos and used to induce cancer cell death through the disruptions of the tubulin polymerization in the cell division process. To improve the loading efficiency of the PTX molecules onto the ND surface, a thiolated DNA oligonucleotide strand (poly dT with 20 bases) with a dodecyl amine group at one end was bound to the carboxyl group of PTX molecules through amine coupling to form PTX−DNA complex. Both the PTX−DNA complex and the anti-EGFR mAbs as the specific target ligands were coupled to the SPDP-functionalized NDs. The average diameter of the resulting PTX−DNA−NDs was 230 nm based on the DLS measurements (Figure 29B). The cellular uptake of the PTX−DNA−NDs was studied by employing two breast cancer cell models: (i) positive group of MDA-MB-231 cells with overexpressed EGFR and (ii) MCF-7 cells with normally expressed EGFR. The high selectivity of the NDs carriers for the target MDA-MB-231 cells was confirmed by a 150% fluorescence signal enhancement in comparison to those incubated with PTX−DNA−NDs without target anti-EGFR ligands (Figure 29C). Moreover, the cell viability of the pure NDs for a high concentration of 200 μg/mL remained larger than 90% while dropped by 50% with PTX−DNA−NDs with target mAbs at a concentration of 45 μg/mL and a PTX amount of 43.8 nM. The targeted and untargeted PTX−DNA−NDs in MCF8 cells showed IC_{50} values of 17.7 and 24.1 nm, respectively (Figure 29D). The anti-EGFR functionalized PTX−DNA−NDs enhanced the cytotoxicity to the target MDA-MB-231 cells by nearly 2-fold, as the IC_{50} value of PTX for the untargeted NDs was 100 nM (Figure 29E).

Cisplatin-ND nanocarriers for enhanced anticancer treatment for A2870 ovarian cancer cells were also demonstrated by Huynh and co-workers.[363] The ND surface was initially reacted with oxidizing mineral acids under high temperature to generate a large number of carboxyl groups. The oxidized COOH-NDs were then functionalized with the cisplatin directly as a negative control to those later conjugated via polymer linkers. The cisplatin drugs were loaded on the ND surface by first deprotonating the carboxyl groups by NaOH and then mixed with *cis*-diaquodiamino platinum(II). Two ovarian cancer cell models including A2780 and cisplatin-resistant A2870cis were used to investigate the cytotoxicity of the Pt-loaded ND drug carriers. After the cellular take, the cisplatin drugs were released from the ND surface due to ligand exchange process between carboxyl and chlorides. The activated cisplatin could bind to the DNA and induce the cell apoptosis. The POEGMEMA-coated ND carriers showed a lower IC_{50} value of 1.5 and 1.8 μM for A2780 and A2870cis than that of free cisplatin drugs and the ND carriers without polymer coatings.

Recently, Xiao et al. developed ND-DOX nanovectors for killing the lung tumor cells of 4T1 and inhibiting the lung metastasis process of breast cancer.[450] The DOX drug molecules were loaded onto the ND surface through noncovalent binding due to physical adsorption. The authors suggested that the binding of the DOX and the ND was due to electrostatic interactions between the protonated amine groups on the DOX and the carboxyl groups on the ND because the ND-DOX had a much higher zeta potential of −7.14 mV than that of the pristine ones with a negative value of −38.2 mV. Further conjugation of the DSPE−PEG 2K increased the zeta potential value to −1.46 mV that helped the ND nanocarriers to be highly stable in physiological environments. A high loading efficiency of 95% for the DOX onto the ND was obtained with an optimum mass ratio of 5:1 for the ND:DOX. It was shown that the release speed of the DOX a pH value of

DOI: 10.1021/acs.chemrev.9b00099
Chem. Rev. XXXX, XXX, XXX−XXX

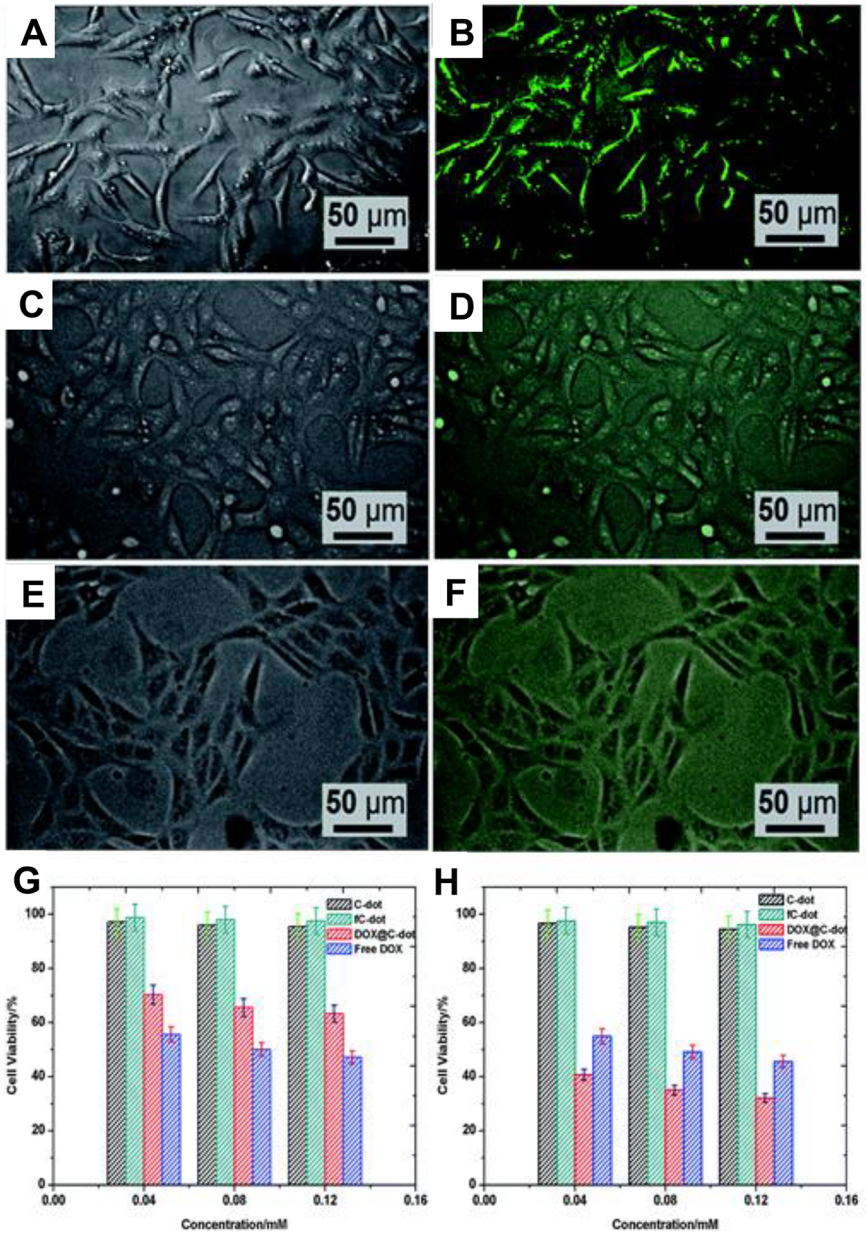

Figure 30. Left panels are the bright field images and right panels are the fluorescence images of HeLa cells treated with fC-dots-FA (A,B), HeLa cells treated with fC-dots (C,D), and Vero cells treated with fC-dots-FA (E,F). Cell viability of (G) Vero cells and (H) HeLa cells treated with different C-dot formulations. Reprinted with permission from ref 341. Copyright 2014 Royal Society of Chemistry.

7.4 from DSPE−PEG 2K-coated ND-DOX (25.5%) was much slower than that from ND-DOX (34.5%) after 24 h. This indicated that the DSPE−PEG 2K layer could act as physical barriers to limit the DOX diffusion and prevent the dissolution media to the PEG micelles. The cytotoxicities of free DOX drug molecules, ND-DOX and DSPE−PEG 2K-coated ND-DOX were investigated by incubating them with 4T1 cancer cells. The obtained IC_{50} values were respectively 9.48×10^{-4}, 4.93×10^{-4}, and 1.65×10^{-4} mg/mL. The 5.75 times improved anticancer efficacy of the DSPE−PEG 2K-coated ND-DOX than that of free DOX molecules was attributed to the enhanced targeting efficiency to the nucleus.

2.3.1.6. In Vitro Drug Delivery by Carbon Dots. Fluorescent C-dots have recently attracted great attention as promising candidates for nanomedicine applications.[451−456] They exhibit good aqueous solubility, high biocompatibility, low intrinsic toxicity, and tunable absorption and emission peak wavelengths. More importantly, the synthesis of the C-dots is usually performed in the absence of organic surfactants that are highly toxic.[457,458] The commonly used precursors for C-dots are nontoxic carbon sources like carbohydrates, citric acid, and urea. For example, Zhou et al. fabricated C-dots capped MSPs for the in vitro delivery of DOX drug molecules.[459] The novel nanocarriers showed low toxicity to the normal cells and also had strong fluorescence due to the presence of the C-dots. The C-dots with abundant carboxyl groups were negatively charged and could be attached onto the MSP surface through electrostatic interactions with their aminopropyl groups. The release of the DOX molecules of the C-dots capped MSPs was tuned by changing the pH values in the physiological environments. The 3.8 nm C-dots were prepared by calcining EDTA-2Na·2H_2O at high temperature in

DOI: 10.1021/acs.chemrev.9b00099
Chem. Rev. XXXX, XXX, XXX−XXX

a nitrogen atmosphere, followed by evaporation. The size of the C-dots was much larger than that of the MSP pore of 2.5 nm and could attach and block the pores. The quantum yield of the C-dots was estimated to be 11% based on the PL measurements. The MSPs with an average diameter of 130 nm were synthesized by a base-catalyzed sol−gel process. They were then functionalized with aminopropyl groups by reacting with APTES solutions. The DOX loaded onto the MSP surface could reach 0.073 mmol/g, which was determined through fluorescence quenching. A DOX release rate ranging from 13% to 85.6% was obtained by tuning the pH from 7.4 to 5.0. To study the anticancer efficacy of the DOX-loaded C-dots-MSPs, HeLa cancer cells were incubated respectively with free DOX drugs, DOX-loaded MSPs, and DOX-loaded C-dots-MSPs at different concentrations. The DOX-loaded C-dots-MSPs induced a significant decrease of the cell viability at all time points from 12 to 72 h, while the cell viability maintained at 90% with the pure nanocarriers even at a high concentration of 100 μg/mL.

Later, He et al. designed C-dots conjugated with ZIF-8 nanoparticles (C-dots@ZIF-8 NPs) as drug delivery nanocarriers.[460] The obtained C-dots nanoconjugates could emit green light due to their natural fluorescent property and thus could be used as multifunctional cancer therapy nanovectors for simultaneous pH-dependent chemotherapy and fluorescence tracking and imaging of the cancer cells. An anticancer drug molecule of 5-FU was employed as a cargo for the C-dots@ZIF-8 NPs carriers. The loading amount of the 5-FU was measured by the UV−vis absorption at 265 nm and determined to be 0.3 mg per mg. The release profile of the C-dots@ZIF-8 NPs was monitored at 37 °C at different pH values ranging from 7.4 to 5.5 in the PBS solutions. The release rate of 5-FU was found to be much higher under an acidic environment with a release amount of 92% after 48 h than that of 67% in the PBS solutions with a pH value of 7.4. The cytotoxicity of the C-dots@ZIF-8 NPs was studied with three different cell models including HeLa, fibroblast (L929), and prostate (DU145). The cell viability for all these cells maintained larger than 90% even at a high incubation concentration of 25 μg/mL after 24 h treatment of the pure carriers, while the viability decreased with the increased concentration of the 5-FU loaded C-dots@ZIF-8 NPs. The fluorescent imaging from the CLSM showed that the green emission of 5-FU loaded C-dots@ZIF-8 NPs was mainly localized the cytoplasm of the HeLa cells. This indicated that the cellular uptake of the nanocarriers was through endocytosis process rather than adsorption at the cell membranes.

FA-BSA functionalized C-dots for delivering DOX molecules to HeLa cancer cells were developed by Mewada and coworkers.[341] In this study, the C-dots were prepared by adding sorbitol into sodium hydroxide solutions followed by a microwave heating process. For the resulting C-dots after dialysis purification, there were two absorption peaks in the UV region respectively at 212 and 264 nm. These two peaks were originated from the $\pi \rightarrow \pi^*$ electron transition between the carbon bonds and the $n \rightarrow \pi^*$ transition of electrons due to the abundant carboxyl groups on the C-dot surface. BSA molecules were conjugated with the C-dots to enhance their biocompatibility and then further activated by the FA molecules as the target ligands. A maximum DOX drug loading efficiency up to 86% was achieved for the FA-BSA C-dot carriers. The DOX-loaded FA-BSA capped C-dots were shown to exhibit a higher release rate in the PBS solutions at a pH value of 5.8 than that at pH of 7.2 after 4 h. C-dot nanocarriers with FA and without FA functionalization were respectively injected into the cell culture media of the HeLa cells that were known to be overexpressed with FA receptors. Interestingly, only the HeLa cells treated with the FA-capped C-dots exhibited green fluorescence inside the cell, showing the selective cellular uptake of the nanocarriers (Figure 30A−F). Moreover, a much lower IC_{50} value of 0.04 mM for the DOX-loaded C-dot carriers was obtained in comparison to that of 0.08 mM for the free DOX drug molecules. The cytotoxicity of the pure C-dots carriers was also tested with Vero and HeLa cells. High cell viability rates of 95.5 and 94% for the FA-capped C-dots could be maintained even at a high concentration of 0.12 mM (Figure 30G,H).

Recently, Wang et al. demonstrated the use of PEG−chitosan functionalized C-dots for two-photon fluorescence imaging and controlled drug release by NIR light irradiation/pH regulation.[461] The chitosan capped on the C-dot surface was pH sensitive and could change from swelling to deswelling form for drug release at different pH conditions from 5.0 to 7.4. The polymerization of the nonlinear PEG nanogel networks on the C-dots carriers enable the thermosensitivity of the drug release where heat generated on the C-dots by NIR irradiation would increase the released drug amount. More specifically, the fluorescent C-dots were first obtained by sonication and heating of the glucose solution under an acid condition. The resulted C-dots were then mixed with MEO_2MA, MEO_5MA, PEGDMA, and chitosan to initiate the polymerization precipitation process. The DOX drug molecules were then conjugated to the hybrid C-dots nanogels by simple complexation reactions. On the basis of the absorption peak of the DOX drug molecules at 480 nm, the loading amount of the DOX onto the PEG−chitosan functionalized C-dots could be quantitatively determined with a maximum value of 33 mg/g. The release efficiency of the DOX molecules from the C-dot carriers was monitored at different pH conditions. A much higher release rate up to 49.2% was achieved for pH value of 5.0 in comparison to that of 25.4% and 20.8% for pH of 6.2 and 7.4 after 96 h. In addition, the release rate could be further speeded by only 5 min NIR light irradiation due to the increasing temperature of the solutions by 23 degrees. The PEG−chitosan functionalized C-dots with a high concentration of 100 μg/mL were injected into the cell culture media of the DU145 human prostate cancer cells. After 24 h incubation, the cell viability of the cells was 98%, which suggested the low cytotoxicity of the C-dots carriers without DOX loading. However, a significant cell death up to 40% was induced when the cells were treated with the DOX-loaded C-dots carriers even at a low concentration of 25 μg/mL.

In another report, Huang et al. prepared GQDs that were conjugated with FA and DOX drug molecules as nanovectors for multimodal cancer therapy.[335] The FA molecules were functionalized onto the GQD based on a classic carbodiimide cross-link process (EDC/NHS) where the carboxyl groups of the FA were bound to the amino groups on the GQDs. The cellular uptake of the GQDs was confirmed by the fluorescent imaging where most of them were located at the cytoplasm rather than the cell membrane. The DOX molecules were attached onto the GQD surface through strong π-stacking interactions. A high release percentage of 80% of the DOX molecules was achieved under acidic environment with a pH value of 5.0, while only 20% was observed for solutions at pH

DOI: 10.1021/acs.chemrev.9b00099
Chem. Rev. XXXX, XXX, XXX−XXX

of 7 after 48 h. The cytotoxicity of the pure FA-GQD nanocarriers was evaluated by using both HeLa and HepG2 cells as the targeted models. The cell viability for both cells maintained more than 90% after incubating with the FA-GQD nanocarriers even at a high concentration of 200 μg/mL for 24 h. The selectivity of the DOX-loaded FA-GQDs were then tested by respectively injecting into the cell culture media of FR-overexpressed HeLa cells as positive control and FR-normal expressed HepG2 cells as the negative control. It was observed that 90% decrease of the cell viability for the HeLa cells was achieved with DOX-loaded FA-GQDs at a concentration of 5 μg/mL, whereas only 30% cell inhibition was obtained for the HepG2 cells.

2.3.2. In Vitro Gene Delivery. Most commonly used nanocarbon materials for gene transfection studies are CNTs and GO. However, a few interesting studies also report gene delivery assisted by fullerenes, CNHs as well as NDs. This section illustrates the noteworthy contributions of different research groups in developing nanocarbon materials for in vitro nonviral gene delivery that is an indispensable approach for RNA interference-based cancer therapy. Various CNT-based delivery systems utilizing different surface functionalizations, charge ratio between positively charged f-CNTs, and negative charges of DNA, DNA condensation degree and f-CNTs surface area have been developed. Moreover, the effects of their physicochemical properties have been extensively studies on the transfection efficiency and degree of internalization.[516] Pantarotto et al. were the first to present CNTs as gene carriers.[517] They showed that charge density, hydrophobic character of the interaction, and the number of plasmid DNA molecules in the condensate determine the degree of plasmid condensation. Bianco et al. also showed the capacity of f-CNTs as delivery vector systems for transporting plasmid DNA pCMV-bGal expressing the β-galactosidase protein.[518] Next, MWCNTs were demonstrated as gene vectors with plasmid DNA expressing green fluorescent protein (GFP).[519]

Further, Singh et al. extended the study of ammonium-functionalized SWCNTs to ammonium functionalized MWCNTs and lysine-functionalized SWCNTs to transfect a human cell line with DNA. They pointed out that DNA binding ability is improved by the large surface of MWCNTs.[520] PAMAM−MWCNTs could also deliver DNA into COS7 and HeLa cells with transfection efficiency comparable or even higher than that of PEI and PAMAM used as positive controls.[521] Kam et al. showed highly efficient delivery of siRNA by phospholipids-f-MWCNTs via cleavable disulfide linkage.[522] Pristine SWCNTs complexed with siRNA targeted to hypoxia-inducible factor 1 alpha (HIF-1α) reported strong specific inhibition of cellular HIF-1α activity responsible for reduction of cell viability and increase of cell death in a large variety of cancer cell types.[523] SWCNTs functionalized by DSPE−PEG−amine bound siRNA targeting MDM2 (negative regulator of the p53 tumor suppressor gene). These complexes were successfully introduced into breast cancer cells and led to increased rates of cells proliferation inhibition and apoptosis.[524]

PEI-conjugated CNTs have shown excellent gene transfection efficiency with improved binding to DNA plasmids and siRNA.[523,525] CNT-based gene nanocarriers have demonstrated comparable or even high gene transfection efficiency and enhanced intracellular trafficking with reduced cytotoxicity. Interestingly, the SWCNT-based siRNA delivery was applicable to hard-to-transfect human T cells and primary cells, which were resistant to conventional cationic liposome-based transfection agents.[525] The CNT-based siRNA transfection has been further demonstrated in animal experiments for in vivo gene therapy, showing a tumor growth suppression effect after intratumoral injection of therapeutic CNT−siRNA complexes.[523,526] Ros et al. demonstrated immobilization of a therapeutic enzyme, laronidase, on CNTs.[527] They successfully showed internalization of the conjugate f4-MWCNTs (CNTs−laronidase) by fibroblasts from subjects affected with mucopolysaccharidosis type I and the capacity of the enzyme to retain its activity after internalization up to 48 h.

Feng et al. and Yin et al. reported analogous type of GO nanocarrier functionalized with both PEG and PEI that are able to carry EGFP-coding plasmid DNA (pDNA) and plasmid-based stat3 siRNA.[528,529] Chatterjee et al. developed a highly efficient nanocarrier based on dendron functionalized GO for gene delivery.[530,531] Polyamidoamine (PAMAM) dedrons were functionalized with nano GO (nGO) through click chemistry to enhance DNA loading capability and transfection efficiency. The group found that the transfection efficiency of dendron-functionalized GO was significantly higher as compared to bare nGO.

Zhang et al. prepared PEGylated rGO as a nanocarrier for the delivery of single-stranded ribonucleic acid (ssRNA). Their result indicates that the PEG−rGO has a better ssRNA loading and delivery potential than PEGylated GO.[532] Imani et al. studied the implementation of octaarginine-conjugated GO as nanovector for gene therapy. The group reported the enhancement of cellular uptake by conjugating cationic cell-penetrating peptide octaarginine with GO flakes.[533] In another report, Yang and co-workers prepared biocleavable organic−inorganic hybrid materials by decorating GO with poly(2-dimethylamino)ethyl methacrylate (PDMAEMA) using atom transfer radical polymerization method. This functionalization procedures allows targeted delivery and release of drugs and genes. The cleavable disulfide bond between GO and PDMAEMA allow the release of pDNA under reducible conditions.[534]

Guerra et al. prepared hybrid nanovectors comprising of CNHs as platform and various PAMAM dendrimers as siRNA graspers.[535] The employment of PAMAM dendrimers with several amino groups resulted in a more soluble and biocompatible CNHs. The hybrid nanocomplex does not exhibit cytotoxicity at high dosage of 25 lg/mL and was also found to possess high siRNA loading capability. Because of these virtues, the PAMAM−SWCNH nanovectors were loaded with siRNA through electrostatic interaction to specifically target mRNA expression of different proteins such as p42-MAPK and GADPH using PC-3 prostate cancer cells as the model cell.[536] In fact, the nanocomplex which composed of f-CNH3 and specific siRNA is able to reduce the housekeeping GAPDH mRNA levels and p42 mitogen-activated protein kinase, a type of protein directly involved in cancer progression.

Ceña and group prepared a nonviral delivery platform for gene delivery by functionalizing it with a fourth-generation polyamidoamine dendrimer (G4-PAMAM) to CNHs.[537] In their work, siRNA targeting cofilin-1, a key protein in the regulation of cellular cytoskeleton, was delivered into human prostate cancer cells (PCa). The CNHs were able to carry siRNA and the release can be triggered by the presence of excess polyanion heparin. After being treated with the CNHs nanocomplex, the cofilin-1 mRNA and protein levels decreased

DOI: 10.1021/acs.chemrev.9b00099
Chem. Rev. XXXX, XXX, XXX−XXX

to about 20% of the control values. The drug used for this treatment was docetaxel, which can generate a concentration-dependent activation of caspase-3, an increase in cell mortality assessed by lactate dehydrogenase release, cell cycle arrest, and inhibition of tumor cell proliferation.

The lack of toxicity combined with an adequate functionalization to avoid agglomeration, their high surface area, the possibility of the introduction of molecules within the cavities of oxSWCNHs, the absence of metallic particles, their regular size, and their inertness are some of the distinguishing features that make SWCNHs an attractive material for gene delivery.[52] Thus, more investigations will yield exciting outcomes for uncovering their full potential in cancer theranostics.

Meanwhile, the spherical-shaped fullerene hexa-adducts are found appealing for biological applications.[538] They offer two peculiar advantages for gene delivery applications. First, the spherical distribution of the substituents around the C_{60} core in hexa-adducts prevents the formation of amphiphilic compounds. Second, it shows high solubility in aqueous media without significant aggregation. Polycationic dendrimers with a fullerene hexa-adduct core were prepared from clickable building blocks and were treated with a large excess of trifluoroacetic acid to form trifluoroacetate salts.[539,540] These polycationic dendrimers were combined to plasmid DNA pCMVLuc to prepare polyplexes. Whereas the smallest compound showed only a moderate efficiency for pCMV-Luc gene delivery experiments conducted with HeLa cells, the two highest generation compounds had practically the same level of luciferase expression than that of JetSIt-ENDO (Polyplus-Transfection).

Badea and group developed lysine-conjugated nanodiamonds (lys-NDs) that can be well dispersed in water while preserving their physicochemical characteristics for at least 25 days.[447] The Lys-NDs would form a protein shell encapsulating the core upon interaction with serum which could stabilized the ND/siRNA complexes and enhances the cellular uptake. Cell transfected with diamoplexes obtained from aqueous dispersion of lys-NDs exhibited a significant increase in internalization of the labeled siRNA. The further supplement of serum to the formulation further improve the fluorescence, signifying that the protein corona can enhance the cellular uptake of diamoplexes.

Zhang et al. functionalized NDs with 800 Da polyethylenimine (PEI800) and further attached amine groups by covalent interaction for in vitro gene delivery.[541] The resultant nanocomplex exhibits superior high transfection efficiency due to the high molecular weight PEI (PEI25K) but with no cytotoxicity usually associated with PEI25K. They confirmed that the ND_PEI800 can serve as a biocompatible and effective gene carrier which can enhance the cellular internalization of the plasmid and also effectively transport DNA to the nucleus for translation.

2.4. In Vitro Multifunctional Combinatorial Imaging and Delivery

The current primary focus of the drug/gene delivery research community worldwide has been to design synthetic theranostic platforms that enable targeted drug/gene delivery at the site of interest with enhanced biocompatibility, more loading capacity, greater solubility, and immunity to enzymatic degradation. Hence, tremendous efforts have led to high efficiency and sustainable multifunctional theranostic systems based on carbon nanomaterials. The current section highlights a few examples of these systems.

Xu et al. demonstrated combinative anticancer therapy by using GO-hybridized nanogels (AGD) for delivery of the anticancer drug DOX, which simultaneously presented photothermal therapeutic effects against cancer cells.[542] They incorporated GO nanoplatelets into a biodegradable polymer (alginate) via a double emulsion approach using a disulfide molecule as cross-linker in situ to form the AGD nanogels and encapsulated DOX within them via electrostatic interactions. The hybrid nanogels presented pH/redox-dual sensitivity in accelerating the DOX release under reductive and acidic microenvironments mimicking extracellular solid tumor as well as intracellular compartments.

Huang and co-workers developed ligand-functionalized GQDs that can combine multiple therapeutic modalities such as selected cell labeling, targeted drug delivery, and real-tracking of cellular uptake synergistically.[334] GQDs were functionalized with FA, which can differentiate cancer cells (HeLa) cells from normal cells. DOX was also loaded onto the nanocomplex. The stable fluorescence of GQDs permit the real-time tracking of the uptake of DOX−GQD−FA and the subsequent intracellular DOX release in cancerous cells.

Chen et al. developed a unique GQDs-based FRET system for nucleus-targeted, real-time tracking of drug delivery.[543] This system comprised of GQDs that act as the drug delivery system as well as a donor of FRET pair (TAT) which facilitate the transport of the delivery platform to the nucleus. The group found that the functionalized TAT and small size of GQDs contributes to the nucleus-targeting effect, which results in improved intranuclear accumulation of therapeutic agent due to the high sensitivity of the FRET signal of the system. The GQD−TAT−DOX nanocomplex can kill HeLa cancer cells effectively, as shown by the 62.5% cell viability in the MTT assay.

Dong et al. developed a versatile nanocomposite consist of poly(L-lactide) (PLA) and PEGylated GQDs for synergistic intracellular microRNA (miRNA) imaging and gene therapy. GQDs have large surface to volume ratio which facilitates the adsorption of miRNA-21 and survivin. The simultaneous effect of miRNA-21 and survivin exhibit superior inhibition of cancer cell growth and higher apoptosis rate when compared to miRNA-21 or survivin treatment alone.[544]

Li and co-workers developed a chitosan-conjugated GO as a drug and gene delivery vehicle. The function of chitosan is to improve the aqueous solubility and biocompatibility of the nanocomplex. Water-insoluble anticancer drug, CPT, and plasmid DNA can be coloaded onto the nanocomplex, resulting in reasonable transfection efficacy at certain nitrogen to phosphate ratios using HeLa cells as the cell model.[495]

Xu et al. developed a hybrid nonviral vector consisting of AuNPs, gold nanorods (AuNRs), and GO.[545] The nanocomplex was formed by electrostatic self-assembly between the nanoparticles, thus stabilizing the nanocomposite. The AuNPs and AuNRs were modified with cetyltrimethylammonium bromide (CTAB), which provide subsequent modification with PEI. The PEI-modified GO encapsulating AuNPs displayed good transfection efficiency of 65% while maintaining 90% cell viability in HeLa cells.

Zhi et al. reported multipurpose nanographene oxide consist of PEI/poly(sodium 4-styrenesulfonate) (PSS)/GO for codelivery of siRNA targeting miR21 and anticancer drug adriamycin.[546] The group found that the viability of

DOI: 10.1021/acs.chemrev.9b00099
Chem. Rev. XXXX, XXX, XXX−XXX

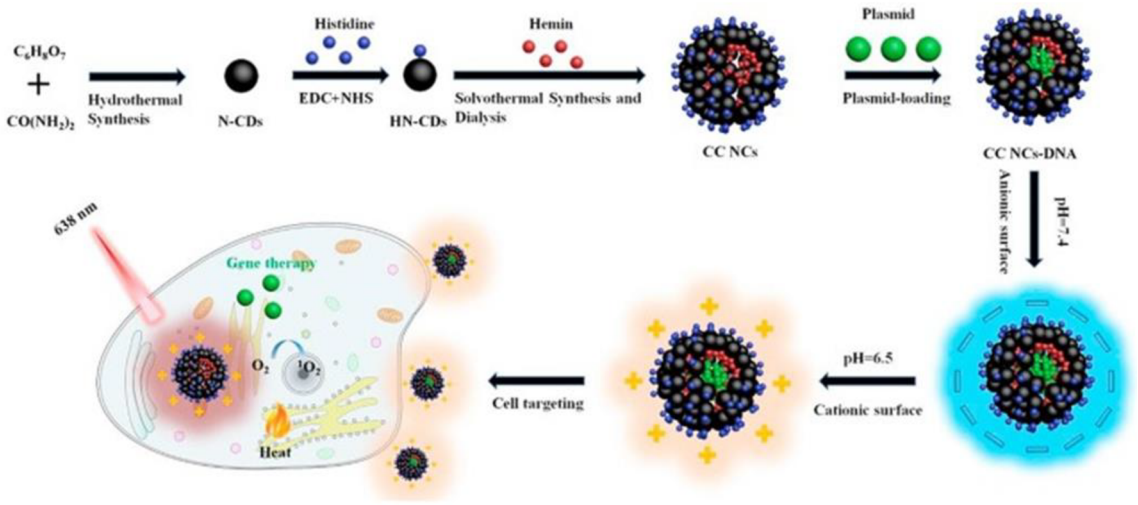

Figure 31. Schematic illustration of the synthesis and stimulated response of multifunctional charge convertible nanocomposites. Reprinted with permission from ref 551. Copyright 2018 Elsevier.

adriamycin-resistant MCF7 cells reduced considerably after being treated with the nanocomplex. In contrast, the cell viability was not significantly affected when the anticancer drug was delivered alone, indicating the capability of the nanocarrier to overcome drug-resistant in cancer cells. Moreover, exceptional reduction of cell viability was observed when drug and siRNA were codelivered, which indicates the promising future of synergistic therapies.

Kim and co-workers reported a photothermally responsive targeted gene delivery nanocarrier by functionalizing GO with low molecular weight branched PEI and PEG. This PEG−BPEI−rGO nanocomplex forms a stable nanosized complex with pDNA. In vitro cell study revealed that the nanocomplex showed a higher transfection efficacy without inducing significant cytotoxicity than naked ones in PC-3 and NIH/3t3 cells. Furthermore, this nanocomplex exhibited better gene transfection efficacy upon NIR light illumination, which is contributed by the locally induced heat which promotes accelerated endosomal escape of polyplexes.[547]

Zhang et al. demonstrated that a therapeutic effect can be enhanced by delivery of siRNA and an anticancer drug in successive order.[478] The group compared the therapeutic effect of anticancer drug DOX and Bcl-2-targeted siRNA by codelivery and sequential delivery to HeLa cells by using the PEI−GO nanocomplex. Under optimum conditions, the PEI−GO/BCl-2-targeted siRNA nanocomplex inhibited ∼70% of Bcl-2 expression level without inducing significant cytotoxicity, while the absence of PEI−GO/DOX resulted in cell viability of 92.5%.

A cationic gene carrier based on GO was successfully prepared by the combination of chemical modification with mPEG−NH2 and adsorption with PDMAEMA.[548] With the benefit of PEGylation, the mPEG−GO/PDMAEMA nanohybrids displayed acceptable cell viability. The mPEG−GO/PDMAEMA nanohybrids possessed a comparable gene-delivery efficiency to that of Lipofectamine 2000. In addition, compared to that of the original GO, the mPEG−GO/PDMAEMA nanohybrids displayed enhanced optical properties, indicating their use as a photothermal reagent. Thus, the mPEG−GO/PDMAEMA nanohybrids may be utilized for multifunctional therapeutic application, including gene therapy, drug delivery, and photothermal therapy.

Pei et al. synthesized Janus-like poly(methyl methacrylate)-*b*-poly(ethylene glycol)-FA block copolymer-grafted fluorescent carbon dots (CDs−PMMA−PEG−FA) via surface-initiated atom transfer radical polymerization of methyl methacrylate in ethanol with the modified carbon dots (CDs-Br) as initiator, followed by the PEGylation via click chemistry.[549] The DOX-loaded nanoassemblies could release N80% of DOX at pH 5.0 within 36 h, while that at pH 7.4 was only 2%, demonstrating the excellent on−off behavior on pH stimuli. Enhanced in vitro anticancer efficacy of the CDs−PMMA−PEG−FA/DOX nanoassemblies with folate receptor (FR)-mediated targeting function than the free DOX was revealed by the MTT assays, while the bare CDs−PMMA−PEG−FA nanoassemblies possessed good cytocompatibility. The fluorescence imaging results demonstrated that the CDs−PMMA−PEG−FA/DOX nanoassemblies could be effectively internalized into HepG2 cells and triggered DOX release into the cell nuclei by means of the FR-mediated targeting characteristics.

Yang et al. reported a facile method to prepare the water-soluble photoluminescent C-dots under the hydrothermal condition.[550] The as-obtained C-dots showed high quantum yield, excellent ability, and good biocompatibility. They used FA and PEI to prepare the C-dots with positive charges. The prepared C-dots could be directly applied in the imaging of cells without further functionalization and showed specific targeting ability to cancer cells that overexpressed the FA receptor. The positively charged C-dots could also link to plasmid DNA and efficiently transfect the therapeutic plasmid into cells.

In another work, Zhu and co-workers reported a tumor extracellular microenvironment responsive and photosensitive nanocomposite based on the combination of N-CDs, histidine, and hemin, possessing high-performance phototherapy for cancer (Figure 31).[551] The histidine grafted nanocomposites could undergo intriguing charge conversion from a negative-charged surface to a positive one in a mildly acidic tumor extracellular microenvironment (pH ∼ 6.5), leading to high affinity to negatively charged cancer cell membranes, which resulted in enhanced targeting ability of the nanocomposites. Meanwhile, the photothermal property of N-CDs and photodynamic ability of hemin were simultaneously enhanced

DOI: 10.1021/acs.chemrev.9b00099
Chem. Rev. XXXX, XXX, XXX−XXX

via the FRET effect in charge convertible nanocomposites, which endowed the synthesized nanocomposites with excellent biphototherapy for cancer cells. Moreover, the as-prepared nanocomposites could deliver plasmid into tumor cells for effective gene transfection, thus demonstrating the promising potential of the nanocomposites for multimodal cancer therapies.

Lim et al. developed PAMAM-functionalized NDs for E6/E7 siRNA delivery in HPV-positive carcinoma cells.[553] The PAMAM-NDs exhibited positive zeta potential in aqueous dispersion and an optimal size for gene delivery. The siRNA/PAMAM-NDs exhibited the highest inhibition effect at a concentration of 0.02 mg/mL, as shown in 4.6- and 4.0-fold increases in TP53 protein concentration for CaSki and HeLa cells, respectively. When the cellular uptake of siRNA was imaged using GFP fluorescence reporting engineered cell line, it was clear that PAMAM-decorated ND was highly effective at developing less toxic and more effective gene delivery vectors.

Chen et al. synthesized multifunctional photoluminescent CDs for induced neuronal differentiation of EMSCs via nonviral gene delivery and bioimaging.[554] These CDs enjoyed a high quantum yield (56.3%), excitation-dependent fluorescence, small size (<10 nm), spherical shape, uniform distribution, positive surface charge, low cytotoxicity, and excellent ability to condense macromolecular plasmid DNA. The synthesized CDs exhibited significantly higher transfection efficiency than the commonly used transfection reagents PEI (25 kDa) and Lipofectamine2000. Moreover, the induced cells showed obvious neurite extension and positive expression of neuron specific markers, and the CDs/pDNA nanoparticles exhibited more efficient neuronal differentiation of the EMSCs than the AT-RA-containing induction medium. Furthermore, the multiple pathways including both caveolae- and clathrin-mediated endocytosis were involved in the cellular uptake of the CDs/pDNA nanoparticles and acidic endosomes/lysosomes and cytoskeletal motors were responsible for their intracellular transport.

In another interesting work, Lou et al. prepared fluorine-doped CD C-6F by a one-step ring-opening polymerization−dehydrative carbonization (RPDC) approach based on low molecular weight polyethylenimine (PEI, 600 Da) and fluorinated diglycidyl ethers.[555] In vitro cell experiment results revealed that the CDs prepared from RPDC approach exhibited much higher transfection efficiency and cellular uptake than PEI 600 contrasts in various cell lines. Besides, these CDs exhibited good cell imaging capability under single wavelength excitation, making the materials suitable for cellular tracking and transfection mechanism studies.

Further, a nanocomplex was developed for combinatorial therapy using 5-fluorouracil (5-FU) as the chemotherapeutic drug and Au NRs which exhibit photothermal effect.[556] GO was used as the nanocarrier where hydroxyapatite and Au NRs were loaded. Hydroxyapatite, being sensitive to acidic pH, triggered the release of 5-FU in the lysosome region. Subsequently, 800 nm light irradiation was further used to exploit the photothermal effect of Au NRs for the additional release of 5-FU. Their study has shown that the resultant rGO/AU NR/hydroxyapatite-5FU exhibited selected targeting and transfection efficiency using HeLa cells as the cell model.

Cao et al. prepared CDs with low cytotoxicity by a one-step microwave-assisted pyrolysis of arginine and glucose, which were utilized as a novel, safe, highly efficient, dual-functional (gene delivery and self-tracking) cationic nano gene vector.[557] The synthesized CDs not only had high gene transfection efficiency but also enabled the intracellular tracking of the delivered molecules through tunable fluorescence studies. Furthermore, the CDs/pDNA nanoparticles could be internalized via both caveolae- and clathrin-mediated endocytosis and enter nuclei to achieve an effective gene expression.

These examples profoundly illustrate the vast potential of various nanocarbon materials for in vitro drug and gene delivery applications. Thus, the important role of nanocarbon materials in cancer theranostics is inevitable. On the basis of the encouraging results of in vitro research, scientists have sought to apply these nanomaterials for in vivo applications as well to validate and strengthen their capacity for clinical translation. The following section gives an overview of the important in vivo results with nanocarbon materials for imaging and drug delivery.

3. NANOCARBONS FOR IN VIVO APPLICATIONS: SENSING, IMAGING, AND DRUG DELIVERY

3.1. In Vivo Sensing

The intrinsic fluorescence of SWCNTs in the NIR II window has yielded enormously interesting results for in vitro sensing of biological analaytes. Owing to these advances, a few groups have demonstrated their useful applciations in the quantification of biological analytes in vivo. Strano's group synthesized NIR fluorescent, PEG-conjugated SWCNTs sensors that were stable for in vivo circulation and showed intravenous injection into mice and subsequent selective detection of local nitric oxide concentration with a detection limit of 1 mM.[558] Localization of the sensor in the liver tissue lasted for 4 h while it was cleared from the lungs within 2 h after injection, thus supporting in vivo nontoxicity of SWCNTs. The sensor was used to monitor the inflammatory response in a mouse liver induced by an injection of RcsX tumor cells, which results in the massive overproduction of nitric oxide over a predictable time course. The sensors showed a detection limit of 1 μM with an ultrastable response time (lasting over 400 days).

Landry and co-workers demonstrated NIR II fluorescent functionalized SWCNT nanosensors for the imaging of the neurotransmitter dopamine.[559] They estimated the quantum efficiency and the two-photon absorption cross section of the (6,5) chirality SWCNTs suspended in a sodium dodecyl sulfate solution, as 0.0023 and 216000 GM, respectively. They showed a 2-fold increase in SWCNT nanosensor fluorescence in the presence of 100×10^{-6} M dopamine and improved two-photon fluorescence spatial resolution while imaging 2 mm deep SWCNTs in a strongly scattering intralipid tissue phantom. Very recently, an example of ex vivo brain tissue imaging was demonstrated by the same group.[560] They synthesized catecholamine nanosensors from the noncovalent conjugation of SWCNTs with single-strand oligonucleotides. Utilizing the NIR fluorescent emission of the nanosensors in the 1000−1300 nm window, they were able to detect dopamine transmission in ex vivo brain slices in the presence of dopamine receptor agonists and antagonists using electrical and optogenetic methods.

3.2. In Vivo Imaging

In the past decade, fluorescent nanocarbon materials have shown tremendous potential for various in vivo imaging applications including one-photon/two-photon optical imaging, Raman imaging, and MRI.[561−564] Here, we describe their applications for in vivo imaging while highlighting various

DOI: 10.1021/acs.chemrev.9b00099
Chem. Rev. XXXX, XXX, XXX−XXX

Table 4. Summary of Carbon-Based Nanomaterials for in Vivo Imaging

animal model	imaging technique	material type	functional group/molecules	material scale	dose	ref
Embryo						
Drosophila melanogaster	wide-field fluorescence	ND	BSA and *N*−*V*	131 ± 60 nm	500 μg/mL	566
Mice						
athymic nude mice (sentinel lymph nodes)	wide-field fluorescence	ND	silica shell	100 nm	80 mg/mL	567
BALB/cAJcl-nu/nu	fluorescence	ND	nitrogen vacancy	<1 μm	100 μg/mL	568
ICR mice	MRI	SWCNH	Fe_3O_4 NPs (6 nm)	*D*: 100 nm	0.5 mg/mL	569
Kunming mice	MRI	GO	PEG−*β*-FeOOH	monolayer LD = 50−200 nm	1.0 mg/kg	570
	two-color fluorescence	C-Dot	hydroxyl group	2.5 ± 0.5 nm	100 μg/mL	230
Zebrafish						
wild-type	fluorescence	GO	PAA and FMA	40−60 nm	0.1 ng/nL	314
	dual-color fluorescence	CQD	C−N, N−H, Si−O, and −OH	3.6 ± 1.6 nm	456 μg/mL	333
A5-EGFP transgenic	fluorescence	GQD	annexin V (A5)	5 nm	2 mg/mL	305
Protists microorganisms						
T. thermophile	fluorescence	ND	carboxylic group	100 nm	20 μg/mL	571
Worm-nematode						
C. Elegans	fluorescence	ND	nitrogen vacancy and dextran or BSA	120 nm	1 mg/mL	572
	fluorescence	ND	nitrogen vacancy	<1 μm	1 mg/mL	568
	fluorescence	SWCNH	chitosan/CdTe QDs	60−80 nm	180 μg/mL	331
Breast cancer						
athymic nude mice(4T1)	fluorescence	GO	PEG−HPPH	monolayer LD < 50 nm	0.77 mg/kg	573
	PAT	GO	PEG−HPPH	monolayer and LD < 50 nm	0.77 mg/kg	573
	PET	GO	^{64}Cu-PEG−HPPH	monolayer LD < 50 nm	3.7 MBq	573
BALB/c mice (4T1)	MRI	GO	IONP−PEG	monolayer and LD < 50 nm	2 mg/mL	574
	fluorescence	rGO	Cy5 labeled IONP−PEG	50 nm	2 mg/mL	565
	MRI	rGO	IONP−PEG	50 nm	2 mg/mL	565
	PAT	rGO	IONP−PEG	50 nm	2 mg/mL	565
	MRI	rGO	IONP−Au−PEG	200 nm	4 mg/mL	465
	X-ray imaging	GO	IONP−Au−PEG	200 nm	4 mg/mL	465
	NIR II fluorescence	SWCNT	C_{18}PMH−PEG	*L* = 50−100 nm	0.2 mg/kg	575
	MRI	SWCNT	C_{18}PMH−PEG	*L* = 50−100 nm	0.2 mg/kg	575
	Raman imaging	SWCNT	C_{18}PMH−PEG	*L* = 50−100 nm	0.2 mg/kg	575
BALB/c mice (MCF-7)	PAT	rGO	BSA	monolayer LD = 70 ± 0.4 nm	1 mg/mL	576
SKH1 mice (MDA-MB231)	TD-DOT	GQD	carboxylic group	5 nm	2.5 mg/kg	577
BALB/c nude mice (BT474)	PAT	fullerene	chitosan and polyhydroxy	57 ± 4 nm	10 mg/mL	578
BALB/c *nu/nu* mice (231/H2N)	SPECT	GO	111In-BnDTPA and anti-HER2 (Tz)	mono and bilayer 64 nm	5 MBq	579
Tumor vasculature						
BALB/c mice (CD105)	PET/CT	GO	^{64}Cu and NOTA-TRC105	27.0 ± 0.9 nm	5−10 MBq	580
	PET	rGO	^{64}Cu and NOTA-TRC105	37.0 ± 7.2 nm	5−10 MBq	581
	PET/CT	GO	^{64}Ga and NOTA-TRC105	27.0 ± 0.9 nm	5−10 MBq	582
Cervical cancer						
athymic nude mice (HeLa)	two-photon luminescence	GO	coumarin and SS−DEAC		2 mg/mL	219
Glioblastoma						
athymic *nu/nu* mice (U87)	MRI	SWCNH	$Gd_3N@C_{80}$ and CdSe/ZnS QDs	40−200 nm	25 μg/mL	367
BALB/c nude mice (c6)	fluorescence	C-Dot	amide and carboxyl	3−4 nm	100 mg/kg	348
Lung carcinoma						
C57BL/6 mice (LLC)	NIR fluorescence	GO	Cy5-GPLGVRGC	monolayer LD = 200 nm	10 μg/mL	583
BALB/c mice (A549)	fluorescence	rGO	spiropyran and HA	196 nm	10 mg/kg	359

DOI: 10.1021/acs.chemrev.9b00099
Chem. Rev. XXXX, XXX, XXX−XXX

Table 4. continued

animal model	imaging technique	material type	functional group/molecules	material scale	dose	ref
Melanoma						
female C57 mice (B16−F10)	MRI	fullerene-C_{60}	IONP−PEG	187 ± 4.2 nm	100 μg/mL	584
Oral cancer						
Balb/c nude mice (KB)	MRI	MWCNT	PEI-FI-DOTA (Gd)-mPEG5K	D = 30−70 nm; L = 100 nm to 2 μm	20 mM	585
Ovarian cancer						
athymic *nu/nu* mice (OVCAR8)	NIR fluorescence	SWCNT	M13 virus and SPARC binding peptide	D = 0.7−1.5 nm; L = 880 nm	200 μg/kg	586
Prostate cancer						
Kunming mice (PC3)	ultrasound imaging	MWCNT	PEI(FITC)-mAb	D = 10−20 nm; LD = 150 nm	500 μg/mL	366
Sarcoma						
female BALB/c mice (S180)	MRI	fullerene-C_{60}	IONP−PEG−FA	163 ± 3.2 nm	10 mg/kg	54
Blood vessel						
BALB/c mice	fluorescence	GO	PEG	40 nm	0.2 mg/mL	315
BALB/c mice (lung cancer cell)	wild-field fluorescence	ND	N−V and carboxylic group	100 nm	100 μg/mL	587
Blood−brain barrier opening						
mice	MRI	GO	gadolinium and Let-7g/EPI	monolayer LD = 100−300 nm	1 mg/mL	490
Brain imaging						
Tg (Cspg4-DsRed.T1) 1Akik/J mice	two-photon luminescence	GO	PEG	40 nm	0.2 mg/mL	315
Peripheral vascular disease						
BALB/c mice	NIR fluorescence	GO	IR800−VEGF	20−50 nm	0.5 mg/mL	588

optimization strategies of the nanocarbon system to achieve long-term and real-time tracking and monitoring of cancer therapy and metastasis processes. We also discuss the surface functionalization of target molecules and inorganic nanoparticles to improve the specificity and resolution of the imaging effect at the deep tissue sites. Table 4 gives a systematic summary of carbon-based nanomaterials for in vivo imaging.

For instance, Yang et al. designed graphene-based nanoprobes for multimodal in vivo imaging by conjugating the rGOs with iron oxide nanoparticles (IONPs).[565] The nanoconjugates were further functionalized with PEG molecules to make them dispersible in water. These graphene nanoprobes were then used for targeted cellular imaging with multimodal techniques including fluorescent imaging, MRI, and photoacoustic imaging. Moreover, image-guided photothermal therapy was demonstrated to ablate the murine breast 4T1 tumor in mice models because the probes exhibited a strong absorption peak in the NIR region. Before the in vivo imaging studies, the cytotoxicity of the PEG-functionalized rGO−IONPs was evaluated by incubating the 4T1 cancer cells with a high concentration of to 200 μg/mL for 24 h. It was found that the cell viability and the ROS levels were maintained at the same levels. The photoacoustic signals at the tumor site of mice injected with the PEG−rGO−IONPs were much higher than those at the tumor sites of mice without the treatment of the nanoprobes. More importantly, there was no weight loss of the mice injected with the graphene probes after 40 days and histological analyses showed no organ abnormality or damage.

Later, Ma and co-workers conjugated the GOs with gadolinium labels and poly(amidoamine) dendrimer molecules as MRI nanoagents for analyzing the distribution of blood−brain barrier (BBB) opening and drug localization inside the tumor tissues.[490] The graphene probes were coloaded with miNRA and epirubicin cancer drug to achieve chemo/gene therapy. For the in vivo MRI, the BBB opening was induced by focused ultrasound (FUS). The gadolinium-GO probes were administered into the model mice and were shown to accumulate in the brain with a higher concentration at the BBB open area. These results confirmed that the Gd-GO nanoprobes could act as carriers for in vivo image-guided drug therapy and real-time monitoring and quantification of the chemo/gene therapy treatment.

Specifically, the NIR II fluorescence of SWCNTs, has been successfully employed in small animal imaging experiments due to mainly three advantages: (1) significantly less scattering of NIR II fluorescence photons than traditional fluorescence, (2) the nearly optically transparent NIR II window to endogenous chromophores (water and hemoglobins), and (3) reduced autofluorescence of endogenous biological molecules with increasing wavelengths.[589]

By taking advantage of these properties, Belcher's group presented an interesting application of NIR II fluorescent SWCNT probes. They showed in vivo targeting and fluorescence optical imaging of bacterial infections by conjugating SWCNT probes with a genetically engineered multifunctional vector called M13. The aqueous dispersed SWCNT probes showed specific targeting of *Staphylococcus aureus* infections in live-subjects, deep-tissue in vivo imaging capability on an endocarditis model of infection compared with traditional NIR-I dye fluorophores.[590]

Dai and group showed the long-tern in vivo stability of SWCNTs functionalized with phospholipids bearing PEG.[591] They coated the SWCNTs with PEG chains and linked them to an arginine−glycine−aspartic acid (RGD) peptide to demonstrate efficient targeting of integrin positive tumors in mice.[592] Owing to strong resonance Raman scattering of SWCNTs,[593] they have been used in combination with SERS nanoparticles to demonstrate noninvasive whole-body Raman imaging, nanoparticle pharmacokinetics, and in vivo tumor targeting in mice.[594,595] The same group later produced phospholipid−PEG coated carbon nanotubes by sonicating SWCNTs with sodium cholate. By using these brightly and biocompatibly, they demonstrated whole-animal in vivo deep-

DOI: 10.1021/acs.chemrev.9b00099
Chem. Rev. XXXX, XXX, XXX−XXX

tissue imaging of tumor vessels imaging using an InGaAs camera in the 1−1.7 μm spectral range by detecting the intrinsic NIR photoluminescence of the modified SWCNTs at a low dose of 17 mg/L.[596] Moreover, they also illustrated a dual application of intravenously injected SWCNTs as photoluminescent agents for in vivo tumor imaging in the 1.0−1.4 μm emission region and as NIR absorbers and heaters at 808 nm for photothermal tumor elimination at the lowest injected dose of 3.6 mg/kg and laser irradiation power of 0.6 W/cm^2.[597] They later used well-functionalized, biocompatible SWCNTs as NIR II fluorescent imaging agents to perform high-frame-rate video imaging of mice during intravenous injection of SWCNTs and investigated the path of SWCNTs through the mouse anatomy.[598] The group also used a synthetic polymer to solubilize SWCNTs with long blood circulation (half-life of ∼30 h) in vivo and achieved ultrahigh accumulation of ∼30% injected dose/g in 4T1 murine breast tumors in Balb/c mice. Upon the high accumulation of SWCNTs in the tumor region, they performed video-rate imaging of tumors based on the intrinsic fluorescence of SWCNTs in the NIR II window.[599] On the basis of these video-rate imaging experiments, they were successful in differentiating arterial vessels from venous vessels in the mouse hind limb during intravenous injection of SWCNTs.[600]

Zhuang Liu's group presented ultrasensitive in vivo detection of as few as 500 human mesenchymal stem cells (hMSCs) cells administrated into mice.[601] They functionalized SWCNTS with PEG and protamine and performed in vitro and in vivo Raman imaging of SWCNTs−PEG-protamine-labeled hMSCs. In addition, they utilized the metallic catalyst nanoparticles attached on SWCNTs as the T2-contrast agent in MRI of SWCNT-labeled hMSCs. Furthermore, they also performed in vivo photoacoustic imaging of hMSCs in mice. Huang Ngan et al. utilized SWCNTs to image murine hindlimb vasculature and blood flow in an experimental model of peripheral arterial disease by exploiting SWCNT fluorescence in the NIR II region.[602] These examples showcase the nonphotobleachable and deep tissue penetrating NIR II fluorescence of SWCNTs as a powerful in vivo imaging tool for accurate and reliable diseases theranostics.

It is important to note that inhomogeneities in the production of SWCNTs render them off-resonant with a wide range of diameters and chiralities. Thus, a typically high injection dose is required to produce a sufficient NIR II fluorescence signal for in vivo imaging, which in turn poses toxicity concerns. To address this practical concern, various groups have suggested techniques such as gel chromatography[603,604] and density gradient centrifugation[605,606] and demonstrated the chirality separated SWCNTs for in vivo NIR II fluorescence imaging at reduced doses.

With their extensive work on using SWCNTs photoluminescence in the NIR II window (1000−1700 nm) as in vivo imaging probes, Dai's group reported that by using a subwindow of 1.3−1.4 μm wavelength range (NIR IIa), it is possible to noninvasively image the mice brain by penetrating through the intact skin and skull through reduced tissue scattering.[607] More recently, Dai and group synthesized SWCNT NIR IIb emitters using by laser vaporization technique with a diameter range of approximately 0.96−1.24 nm to image blood vessels in the mouse hindlimb and in vivo tumor. The SWCNT probes exhibited strong fluorescence in the wavelength range of 1500−1700 nm with minimized photon scattering, high spatial resolution, deep tissue penetration, and high signal/background ratios for in vivo imaging.[608]

In a recent interesting study, Hammond's group showed the detection of orthotopic ovarian tumors in murine models using layer-by-layer assembled SWCNTs, among other NIR II probes including rare-earth based down-conversion nanoparticles, QDs, and small organic molecules.[609] They first created a negatively charged core comprising of sodium cholate stabilized SWCNTs and modified PAA. Biocompatible PLA and dextran sulfate were used as the barrier layers. They used HA as the outmost layer for targeting CD44 as well for further surface modifications. They did not record any observable damage in the liver or kidneys of mice treated with the layer-by-layer assembled imaging probes. The imaging results establish these optical probes as an efficient imaging tool to monitor tumor dissemination, metastasis, as well as real-time imaging-guided surgery.

An ultrastable SWCNT fluorescent probe with M13 bacteriophage for targeted tumor imaging was developed by Ghosh and co-workers.[586] Interestingly, this M13 virus-stabilized probe emitted fluorescence in longer wavelengths (950−1400 nm) at the NIR II region, making it suitable for noninvasive deep tissue imaging, most notably for the guidance of submillimeter tumor removal surgeries. The large interband difference between the emission and excitation wavelengths of these SWCNTs could minimize autofluorescence from the biological tissues and improve the signal-to-noise ratio required for small tumor nodule detection. The M13 virus used in the study was 6 nm in diameter and 880 nm in length and was modified with peptides to selectively target receptors in human ovarian tumor cells. Optical absorbance and emission peaks of the M13 virus functionalized SWCNTs were similar to those of unconjugated SWCNTs, suggesting that surface functionalization does not significantly modify the optical properties of the SWCNTs. Furthermore, no photobleaching was detected under continuous light excitation at 808 nm for 30 min. Using tumor fragments as an NIR imaging model, the penetration depths of the probes were estimated to be in the range of 9.7−18.2 mm. The M13 virus functionalized SWCNT nanoprobes could specifically target the ovarian tumor nodules overexpressed with secreted protein, acidity, and cysteines rich. To compare the in vivo imaging performance of the SWCNT probes with conventional fluorescent dyes, M13-SWCNTs and M13-AF750 dyes with a concentration of 1 mg/kg were respectively injected to the peritoneal cavity of the mice model bearing with ovarian tumors. From the fluorescent imaging results, the tumor to muscle ratio of the M13-SWCNTs was 5.5, which was higher than that of 3.1 for M13-AF750 dyes. The tumor-image background ratio (TBR) for M13-SWCNTs that was 24 times higher than that of M13-AF750 dyes. The specificity of the M13-SWCNTs was tested by implanting other tumor models into the mice including liver, spleen, and intestine nodules. The TBR value was found to be much lower as 4.6, 3.1, and 8.0 for the liver, spleen, and intestine tumors than that of 134.9 for the ovarian ones. To demonstrate the capability of M13-SWCNTs probes for improving the efficiency of tumor surgery through image guidance, the authors also calculated the number of excised tumor nodules with and without the imaging guidance of CNT probes. The number of excised submillimeter tumors during the surgeries was up to 30, which was much higher than that of 4 without the CNT imaging guidance. In addition, the diameters of the tumors excised from the CNT imaging guidance were much

DOI: 10.1021/acs.chemrev.9b00099
Chem. Rev. XXXX, XXX, XXX−XXX

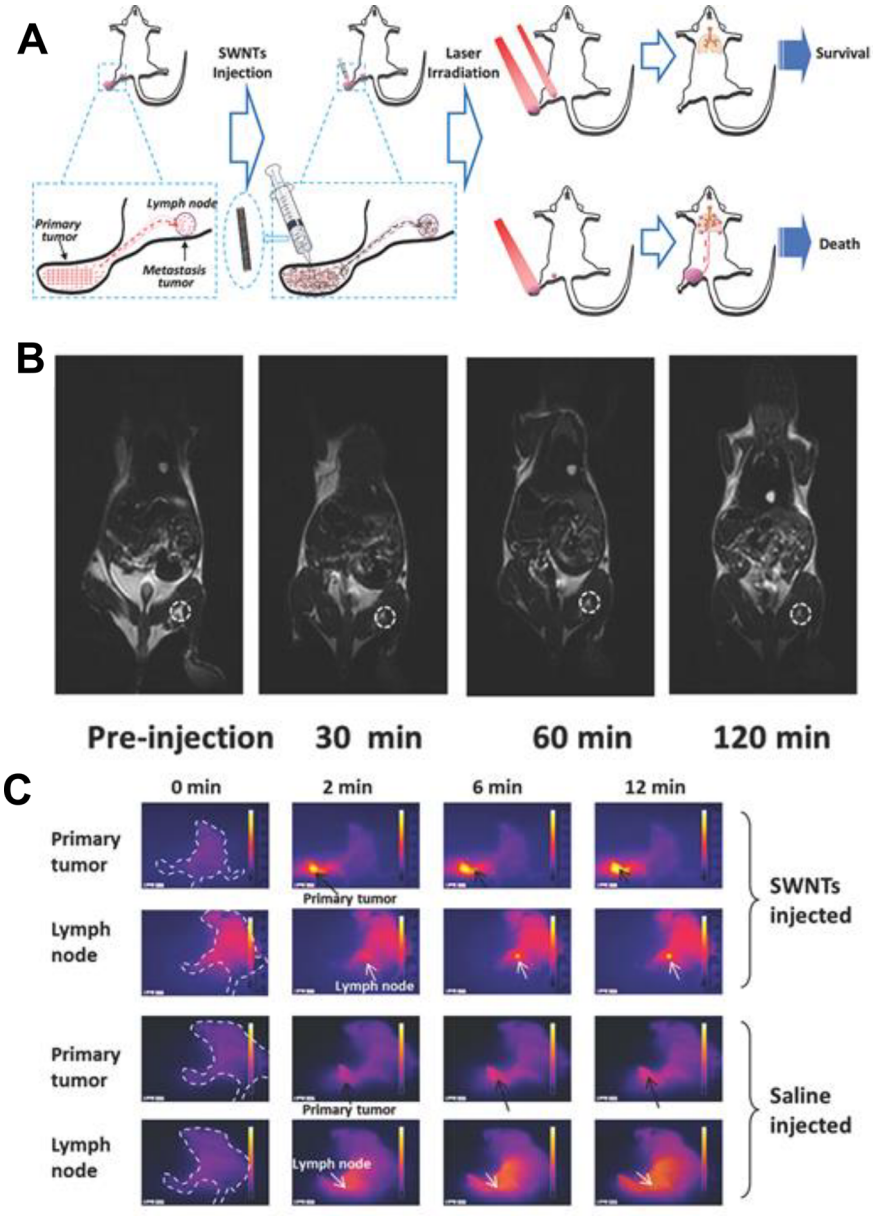

Figure 32. (A) Schematic illustration of the design of the animal experiment. (B) Fluorescent imaging in the NIR II range in a tumor-bearing mouse taken at different intervals after injection with SWCNT−PEG. (C) Infrared thermal images of 4T1 tumor-bearing mice with the primary tumor and the popliteal lymph node separately exposed to the NIR laser at 0.5 and 0.8 W cm^{-2}. Reprinted with permission from ref 575. Copyright 2014 John Wiley and Sons.

smaller than those with unguided ones that confirmed the improved accuracy of the surgical techniques.

Liang et al. employed SWCNT fluorescent nanoprobes for multimodal in vivo image-guided photothermal therapy of tumors in sentinel lymph nodes (Figure 32A).[575] This method could significantly extend the mice survival rate in comparison to the tumor elimination through direct surgery or traditional photothermal treatment. Moreover, the tumor metastasis was inhibited in the mice model. In this study, pristine SWCNTs were coated with amphiphilic polymer molecules of polyethylene glycol (PEG)-grafted poly(maleic anhydride-*alt*-1-octadecene) (C_{18}PMH−PEG) to improve their biocompatibility. The as-prepared SWCNTs exhibited fluorescence peaks centered from 1000 to 1700 nm under NIR excitation at 808 nm. Longer emission wavelengths lead to better spatial resolution of in vivo imaging. Here, Balb/c mice bearing with both murine breast 4T1 tumor and lymphatic metastases were administered with solutions containing PEG-functionalized SWCNTs. After 20 min, fluorescent signals were detected at the sentinel lymph nodes on the popliteal part of the mice. The signal intensity increased until 90 min postinjection, indicating probe migration from the primary tumor site to the sentinel lymph node through lymphatic vessels. The signal-to-noise ratio, a ratio of the lymph node and mouse muscle fluorescent intensities, was more than two times of the ratio obtained using the SWCNT-conjugated NIR I fluorescent dye Cy5.5 (Figure 32B). In vivo MRI showed darkening in T2-weighted images for solutions containing PEG−SWCNT, proportional to the SWCNT concentration. For the image-guided photothermal therapy, solutions containing PEG−SWCNTs with a dose of 0.2 mg/kg were administered from the paw of the mice model. The excitation

DOI: 10.1021/acs.chemrev.9b00099
Chem. Rev. XXXX, XXX, XXX−XXX

wavelength for the treatment was 808 nm, at which the SWCNTs had a high absorption coefficient of 7.9×10^6 M^{-1} cm^{-1}. Tuning the laser power density from 0.5 to 0.8 W/cm^2 facilitated modification in the targeting of ablation depth either at the lymph node, only a few mm under skin, or at the metastatic tumor within the deeper tissue. Following photothermal therapy at the sentinel lymph nodes and primary tumors, tumor metastasis was significantly inhibited compared to that of photoablation at primary tumor sites only (Figure 32C).

Recently, a fullerene-based magnetic nanoprobe for both in vivo optical and MR imaging was fabricated by Shi and co-workers.[54] The fullerene C_{60} nanoparticles were conjugated with IONPs and then functionalized with PEG and FA. By putting a magnet close to the dissolved nanoprobes in aqueous solutions, the magnetic effects of the conjugates were confirmed by the immediate attraction of the probes to the magnet and the solution change to transparent. For the in vivo imaging experiments, PEG-functionalized magnetic fullerenes were intravenously administered to female BALB/c mice bearing sarcoma S180 tumor models. Quantification of the darkened MRI signals were used to compare the effects induced by both FA-functionalized probes and pure PEG-magnetic fullerene probes. Interestingly, the intensity change of the FA-conjugated groups was 47% from the control group while it was only 26% for the group treated by probes without FA-functionalized capture molecules. The intensity change was further enhanced up to 78% with a magnet kept close to the tumor site for 3 h. Furthermore, under simultaneous PDT (20 min, 300 W) and radio frequency thermal treatment (10 min, 100 mW/cm^2), a high tumor growth inhibition rate of 80.2% was obtained for mice administered with FA-functionalized magnetic fullerene probes. However, no change in body weight of the mice models indicated the low toxicity of the probes under such multimodal treatments.

SWCNHs-based magnetic nanoprobes for in vivo imaging were also prepared by Miyawaki and co-workers.[552,569] The iron acetate coated on the nanohorn surface showed a strong darkening effect of the MRI signals that could be used for monitoring the uptake and accumulation behavior at the spleen and kidney sites of the SWCNH probes. In vivo toxicity experiments were studied with six-week-old mice models in a body mass of 35 g. Body weights of the mice were recorded on days 0, 1, 3, 5, 8, 12, and 15, and no weight difference and abnormality was detected between the mice groups treated with the SWCNT probes even at a high dose of 8 mg/kg and control groups injected with the same amount of PBS solutions. Ten-week-old mice models in a body mass of 40 g were employed as models for in vivo MRI. The dose injected to the mice tail vein was 0.5 mg/cm^3. Before injection, the solutions containing magnetic SWCNT probes were ultrasonicated to ensure a homogeneous dispersion in PBS solution. T2-weighted magnetic resonance images were collected every 30 min after the injection until 120 min. The image signals were darkened at the spleen and kidney, where the intensity increased with time following the injection. A follow-up histopathological analyses confirmed the accumulation of nanohorn probes in the spleen.

Later, Mohan et al. developed fluorescent NDs for long-term in vivo monitoring and imaging by using *Caenorhabditis elegans* (*C. elegans*) as test models.[572] The NDs were first oxidized by strong acids and then conjugated to dextran or BSA molecules through a standard carboxyl-to-amine cross-linking approach in the presence of EDC and sulfo-NHS. A wild-type *Caenorhabditis elegans* was tested as the in vivo model, where the worms were grown in the nematode media with *Escherichia coli* (*E. coli*). Different in vivo distributions from oral feeding were observed for the pure ND probe and dextran- or BSA-functionalized ND probes. Most of the pure NDs were found to be localized at the intestinal lumen of the *C. elegans*, while the dextran- or BSA-conjugated NDs were uptaken by the intestinal cells. Optical imaging showed a strong red fluorescent signal in the digestive lumen of the worms from the pharynx areas to anal parts after 12 h of oral feeding of bare ND probes. The long stay of NDs in the intestines suggested that NDs were resistant to digestive enzymes inside the worms. The number of NDs in the intestinal lumen was quantified through the fluorescent intensity as 1×10^6 particles/worm or 3 ng/worm. The in vivo photostability was also evaluated by excitation of the intestines for 48 h, with no observable photoblinking or photobleaching. As a complementary monitoring approach to passive oral feeding, NDs were also injected from gonads as an active introduction pathway. From this route, the NDs were delivered to the embryos and the next generation of hatched larvae. The probes were found to attach to the oocytes and maintained at the fertilized zygotes in the oogenesis process after only 30 min from injection. The fluorescence from NDs could be detected in the whole embryogenesis process. The toxicity of the ND probes was also evaluated by tracking the stress response in terms of related gene expression and protein distribution. No reduction in longevity and brood size indicated that the ROS level were retained at the same level after the injection of the ND probes.

More recently, Igarashi et al. demonstrated in vivo targeted imaging with high selectivity based on the NV centers present on the ND surface.[568] The fluorescence of the NDs were dependent on the NV centers that corresponded to the ground-state spin configuration. Thus, the ND fluorescence could be tuned by electron spin magnetic resonance. A custom-built optical imaging setup integrated a microwave irradiation unit that was used to tune the spin state occupation. By optimizing the frequency of the microwave, the fluorescent intensity from multiple NDs could be detected simultaneously. Moreover, the fluorescent intensity of each ND was observed to significantly decrease at a microwave frequency of 2.87 GHz due to alternating spin states of the magnetic resonance. The sensitivity of microscopy for detecting a single ND was confirmed by collecting the optically detected magnetic resonance spectra at different static magnetic fields and comparing the spot fluorescent intensity with those labeled by single Cy3 molecule. From the collected optically detected magnetic resonance spectra of single fluorescent spot, the selective imaging could distinguish the spot consisting of two NDs with different crystal lattice orientation. Here, both the mice model and *C. elegans* were used for in vivo monitoring of the NDs for a long duration. The in vivo selective imaging of the NDs was first carried out in *C. elegans* by comparing the fluorescent signals with the conventional fluorescent optical images. However, the in vivo selective imaging approach with microwave tunability could effectively reduce background noise and detect the NDs at the intestinal lumen. The nanoprobes were also injected into the flank of a mouse model at a tissue depth of 400 μm. High quality images of NDs could be collected within 320 ms and the high resolution could be maintained for 1 h, suitable for continuous long-term and real-time imaging. In addition, the sampling rate of the selective

DOI: 10.1021/acs.chemrev.9b00099
Chem. Rev. XXXX, XXX, XXX−XXX

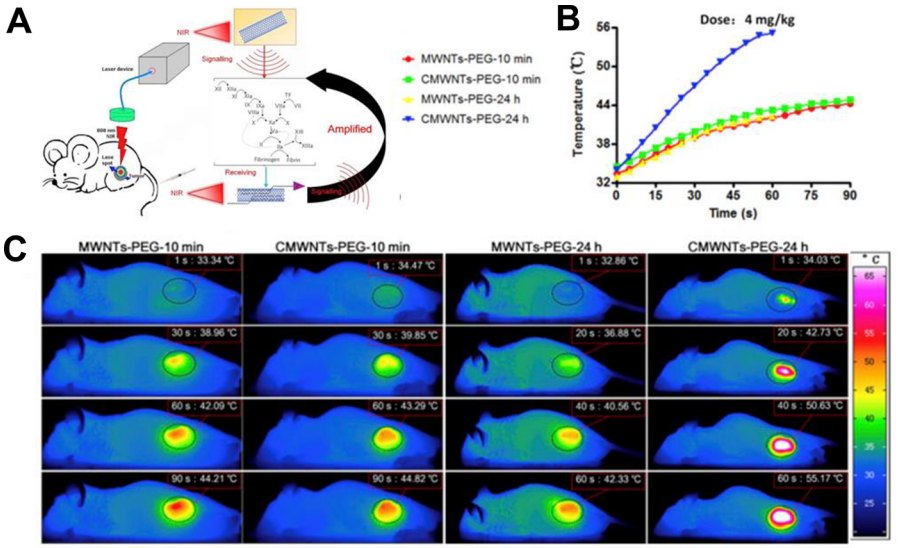

Figure 33. (A) Schematic describing the mechanism of the self-amplified targeting system. (B) Tumor temperature as a function of time of mouse models intravenously injected with 4 mg/kg CMWCNTs−PEG and treated with 808 nm NIR laser post administration. (C) Infrared thermal images as a function of NIR light irradiation time in tumor-bearing mouse models treated with 4 mg/kg MWCNTs. Reprinted with permission from ref 615. Copyright 2016 Elsevier.

image was faster than the animal respiration cycle, eliminating the contribution of respiration on the signals.

Fluorescent C-dots for in vivo imaging through a direct microwave approach by using ethylenediamine and citric acid as carbon source precursors were synthesized by Zhai and co-workers.[230] The preparation required only 5 min of microwave irradiation and resulted in a high quantum yield of 41.39%, paving the way for low-cost production of in vivo fluorescent labels on a large scale. No obvious fluorescent intensity change was detected when the pH of the C-dot solution changed from 3 to 11, showing the high stability of the C-dots. Before the in vivo experiments, the cytotoxicity of C-dots was analyzed by using human cervical HeLa cells as test models. The cell viability was maintained at levels higher than 90%, even for the cells labeled with a high concentration as 800 μg/mL of C-dots. A strong fluorescent signal for the in vitro cell cultures suggested a high uptake of C-dots by the cells. The fluorescence emission was tunable from bright blue to green by changing the excitation wavelength from UV and blue regions. For the in vivo investigation, Kunming mice models were subcutaneously injected with 100 μL of C-dot solutions and strong fluorescence emission was detected at the injection site. Furthermore, the C-dot probes were also injected through tail vein of the mice. At 2 h post injection, a bright emission in mice urine was observed which exponentially decayed within 4 h postinjection. These results indicated that the C-dots could be excreted from the mice body through urine and induced no in vivo toxicity and abnormality.

3.3. In Vivo Drug delivery

Followed by the illustration of nanocarbons as effective carriers in vitro drug delivery studies as detailed in the preceding sections, in vivo experiments to evaluate their fate, release mechanism, and therapeutic efficiencies have recently been demonstrated as well, and their high success rates would inevitably pave the way for their future clinical translation from the current target technology.[437,452,610−614] The overarching goal of any in vivo drug delivery system is to maximize its therapeutic efficiency while minimizing the negative side effects in normal tissues of the patient. Modification of the physicochemical properties of the nanocarrier is a flexible way and can be achieved by way of surface coating, carrier size, and hydrophobicity among others. The surface coating is instrumental in improving the in vivo efficacy compared to the controls. The variety of ligands for these applications is very diverse. In this section, we discuss the in vivo behavior of these nanocarbon carriers for cancer therapy in terms of their various physicochemical characteristics including the surface coating, sizes, hydrophobicity, etc. The optimization of the carbon-based drug delivery system would surely minimize the side effects to the normal tissues and organs in the cancer patients.

For instance, Song et al. functionalized GOs with HA molecules as the target drug nanocarriers for in vivo cancer chemotherapy.[496] Here, DOX drugs were employed as delivery cargos and first conjugated to the surface of GO through hydrogen bonding and π-stacking interaction. Because of the electrostatic charge screening, the DOX-loaded GOs were easy to be aggregated when dispersed in water. To overcome this challenge, ADH-modified HA molecules were then bound to the DOX-GOs by hydrogen bonding reaction between the amine groups of ADH-HA and epoxy groups of the GOs. The functional ADH-HAs served as target groups for recognizing the CD44 receptor of the cancer cells and could prevent the detachment from the GO surface in the presence of hyaluronidase. The hybrid carrier demonstrated a pH-dependent release profile, releasing DOX much faster in acidic conditions (pH = 5.3) than that in neutral conditions (pH 7.4), with tumor proliferation favoring acidic environments. Additionally, the slowed release of DOX indicated a continued and sustained release ability. The DOX-loaded HA-GO drug carriers were injected subcutaneously into mice models bearing H22 hepatic tumors, with different doses ranging from 4 to 6 mg/kg, and the tumor inhibition efficiencies of DOX and DOX-loaded HA-GOs was studied 12 days after implantation. Notably, the DOX-loaded HA-GOs exhibited more efficient anticancer properties compared to pure DOX and DOX-loaded GO carriers in the same treatment condition. The

DOI: 10.1021/acs.chemrev.9b00099
Chem. Rev. XXXX, XXX, XXX−XXX

inhibition rates for 4 mg/kg were 30.79% for the DOX, 18.83% for the DOX-loaded GOs, and 34.45% for the DOX-loaded HA-GOs, respectively, and increased to 36.92%, 32.02%, and 48.59% for a higher injection dose of 6 mg/kg.

PEG-functionalized CNTs conjugates with cysteine−arginine−glutamic acid−lysine−alanine (CREKA) peptides as the targeting groups for fibrin biomarkers of the tumor sites were designed by Zhang and co-workers.[615] Most notably, fibrin amplification in the clotting cascade results in a self-amplification of anticancer effects (Figure 33A). Fibrin is known as an end-product by the coagulation response process and can specifically localize at vascular injury sites. This coagulation effect is also observed in tumor vessels, where increasing fibrin presence in the thrombus slows blood flow to deprive cancer cells of oxygen and nutrition. Starving cancer cells are reported to be more effective to killing cells than using chemotherapeutic approaches.[616,617] The fibrin showed a high expression level in several tumor vessels to make them potential therapeutic targets. The fibrin targeting CREKA peptides were conjugated with the MWCNTs through the interaction of the thiol groups of the peptide and the maleimide groups at the end of the PEGs. MWCNTs, PEG−MWCNTs, and CREKA peptide/PEG−MWCNTs with different doses ranging from 2 to 4 mg/kg, were intravenously injected into the 8 mm tumor-bearing mice models. The temperature at the tumor site increased to 44 °C for both PEG−MWCNTs and CREKA peptide/PEG−MWCNTs with a dose of 4 mg/kg after the first NIR irradiation of 90 s. The temperature was elevated to 55 °C within 60 s following a second irradiation treatment at the tumor site for CREKA peptide/PEG−MWCNTs due to the coagulation response at the tumor vessels (Figure 33B,C). By contrast, groups with only pure PEG−MWCNTs saw comparatively lower heating at 42 °C. On the basis of the in vivo imaging and biodistribution results, the CREKA peptide/PEG−MWCNTs exhibited a 6.4 times concentration rate at the tumor sites compared to that of pure PEG−MWCNTs. This further confirms the targeting function of CREKA peptide to the fibrins. A 90% inhibition rate was obtained with the CREKA peptide/PEG−MWCNTs after four rounds of NIR illumination at the tumor sites while only a 31.8% tumor inhibition rate was achieved with the nontargeting PEG−MWCNTs.

Shi et al. demonstrated C_{60} fullerenes conjugated with PEI functional groups as biocompatible drug carriers for in vivo cancer therapy.[511] The C_{60} fullerenes were first reacted with ethylenediamine to enable their surface coating with amine groups, followed by cationic aziridine polymerization to conjugate with PEI. The PEI-fullerenes were further functionalized with FA molecules via an amide linker. The authors used docetaxel (*N*-debenzoyl-*N*-*tert*-butoxy-carbonyl-10-deacetyl, DTX) as a drug example for the delivery studies. The attachment of the DTX onto the fullerene could be achieved by physical adsorption due to π-stacking force and hydrophobic interaction. The drug loading efficiency for different mixing ratios between DTX and FA-PEI-C_{60} could be tuned from 37% to 220%. For the in vivo anticancer experiments, female BALB/c mice bearing S180 tumor models were used. The pure DTX drugs, DTX-loaded PEI-fullerene and DTX-loaded FA-PEI-fullerene carriers with doses of 11.96 mg/kg. were intravenously injected to the mice through the tail vein. They recorded a high tumor growth inhibition rate (up to 74.5%) for the DTX-loaded FA-PEI-fullerene drug carriers without any impact to the mice weight. More importantly, the biodistribution results of the DTX showed that the DTX concentrations for the DTX-loaded FA-PEI-fullerenes in the tumor sites were 7.5 times higher than the pure drugs after 3 h treatment, indicating a higher uptake rate of the DTX drugs through the functionalized C_{60} drug carriers. Later, the same group prepared DOX-loaded PEI fullerene as a dual-function drug carrier to achieve both in vivo chemotherapy and photodynamic therapy simultaneously.[513] For the study, DOX molecules were attached to the PEI-functionalized C_{60} through covalent binding via a pH-sensitive hydrazone linker molecule. As a result, the DOX release was strongly dependent on the pH condition in the physiological environment. They demonstrated significant reduction in tumor volume in the tumor bearing mice models treated with DOX-loaded PEI-fullerene with 532 nm light excitation. The tumor growth inhibition rate was 86.3% for the DOX-loaded PEI-fullerene under 532 nm light excitation, showing the high efficiency of the combined chemotherapy and PDT with C_{60} as the photosensitizer.

Using alternate structures, Nakamura and co-workers fabricated oxidized SWCNHs as carriers for anti-inflammatory glucocorticoid drugs of prednisolone and employed them to treat the joint of collagen-induced arthritis (CIA) rat models.[618] For the in vivo therapeutic experiments, type II collagens were used to immunize the rat models and followed by the injection of prednisolone-SWCNHs and PBS once a week. The prednisolone-SWCNHs were administered to the tarsal joints at the paw of CIA rats. The arthritis progression was observed to be retarded for the rat groups treated with prednisolone-SWCNHs in comparison to that of control groups treated with PBS and pure prednisolone on day 17. Moreover, the leukocyte and CRP concentration, as inflammation indicators, were also lower. From the immunohistological analyses, the number of CD68 positive multinucleated giant cells at the bone area of the ankle joint of the rats was significantly decreased by the injection of the prednisolone-SWCNHs, suggesting a minor bone destruction rate due to arthritis. The aggregation of the oxidized SWCNHs at the joints was confirmed by the black color depositions for the treated group, and none were shown in the control groups. The large number of SWCNHs located at the CD68 positive cells promised the immunosuppressive function of the released prednisolone inside the cells. In another work, lipid-functionalized ND as a drug carrier for sorafenib molecules was prepared by Zhang and co-workers to suppress the gastric cancer metastasis.[619] The sorafenib drugs were adsorbed onto the ND surface or their pores through noncovalent π-stacking or hydrophobic interaction. The authors studied the release profile of the sorafenib-NDs in a mimicked gastrointestinal fluid consisting of hydrochloric acid with a low pH value of 1.2 and PBS solutions with a pH value of 6.8, as the drugs need to be dissolved in the GI fluid first and then cross the membrane of the intestine after the oral administration. The sorafenib-NDs were released rapidly in the first few hours and then consistently increased in the culture media. The accumulative release rate of the sorafenib from the ND surface could reach to 80% after 6 h in the mimicked gastrointestinal fluid, which accelerated the absorption through the intestinal barriers and thu, enhanced the oral delivery efficiency. For the in vivo tests, the rat models were fasted overnight with free drinking water and then administered with a sorafenib-NDs dose of 20 mg/kg via oral gavage. The rat models were then xenografted with BGC-823 gastric tumors and orally administrated by both

DOI: 10.1021/acs.chemrev.9b00099
Chem. Rev. XXXX, XXX, XXX−XXX

Table 5. Summary of Carbon-Based Nanomaterials for in Vivo Drug Delivery

animal model	drug type	inhibition rate (%)	material type	functional group/molecules	material scale	dose	ref
Arthritis							
female DA/Slc mice prednisolone	prednisolone		SWCNH	carboxylic group	80−100 nm	10 mg/mL	618
Breast cancer							
BALB/c female mice (EMT6)	DOX	92	GO	PEG	LD = 100 nm	10 mg/kg	466
BALB/c female mice (4T1)	resveratrol	95	rGO	mPEG−NH_2	mono- and bilayer LD = 80 nm	10 mg/kg	417
	DOX	60	ND	carboxylic group	80 nm	100 μg	464
	DOX	65	SWCNH	DCA−HPCHS	164 nm	1 mg/mL (with NIR irradiation)	441
Cervical cancer							
BALB/c nude mice (HeLa)	DOX	71	GO	porphyrin and β-cyclodextrin	mono- and bilayer LD = 300−400 nm	1 mg/kg	620
Kunming mice (HeLa)	DOX	40	GO	hyaluronic acid	mono- and bilayer LD = 40−350 nm	6 mg/kg	416
Gastric cancer							
BALB/c nude mice (BGC-823)	sorafenib	80.59	ND	DSPE−PEG	127.6 ± 12.9 nm	20 mg/kg	619
Liver carcinoma							
ICR male mice (H22 hepatoma)	DOX	88.00	SWCNH	sodium alginate and anti-VEGF mAb	216 nm	2.5 mg/kg	473
Kunming mice (HepG2)	DOX	48.59	GO	hyaluronic acid	mono-and bilayer LD = 200−300 nm	6 mg/kg	496
	DOX	25	ND	carboxylic group	165 ± 1.7 nm	2 mg/kg	220
	oxaliplatin	91.30	CD	carboxylic group	2.28 ± 0.42 nm	0.72 mg/mL (20 μL)	621
Kunming mice (H22 hepatoma)	$[Gd@C_{82}(OH)_{22}]_n$	60	fullerene-C_{82}	Gd and hydroxylgroup	22 nm	100 nM/kg	622
	$C_{60}(OH)_x$	38.40	fullerene-C_{60}	hydroxyl group	40 nm	1 mg/kg	623
Lung carcinoma							
SCID mice (A549)	PTX	90	ND	carboxylic group	10 nm	10 μg/mL	501
BALB/c female mice (NCI-H460)	cisplatin	80	SWCNH	carboxylic group	100 nm	0.5 mg/kg	440
athymic nude mice (A549)	MWCNT(NIR)	90	MWCNT	PEG and CREKA peptide	10 nm	4 mg/kg	615
	DXR	35	SWCNH	PEG	80−100 nm	1.2 mg/kg	505
Prostate cancer							
athymic nude mice (CP-r PC-3)	cisplatin	46.70	fullerene-C_{82}	Gd and hydroxyl group	50 ± 12 nm	10 mg/k	493
Kunming mice (PC3)	DOX	76.90	MWCNT	PEI(FITC)-mAb	D = 10−20 nm; LD = 150 nm	5 mg/kg	366
Sarcoma							
female BALB/c mice (S180)	DTX	74.50	fullerene-C_{60}	PEI and FA	140 ± 2.7 nm	25.125 mg/kg	511
	DOX	83.30	SWCNT	lysine and thermosensitive liposome	232 ± 5.6 nm	10 mg/kg	497
Kunming mice (S180)	DTX	81.30	fullerene-C_{60} in micelles	diadduct malonic acid	47.7 ± 2.3 nm	15 mg/kg	482
Skin cancer							
Melanoma							
female C57 mice (B16F10)	DOX	86.30	fullerene-C_{60}	PEI and hydrazone	181 ± 4.7 nm	5 mg/kg	513
Squamous Carcinoma							
C3H/HeN mice (SCC7)	DOX	73	GO	PEG and Ce6	monolayer and LD = 148 ± 18 nm	5 mg/kg	414

sorafenib-NDs and pure sorafenib drug suspensions. Biodistribution analysis showed that the sorafenib concentration at the organs including stomach, colon, duodenum, and jejunum were 5.28, 5.33, 12.57, and 5.60 times, respectively, for the groups treated with sorafenib-NDs than those with pure sorafenib drugs. More importantly, the sorafenib levels at the tumor sites were up to 14.95 times higher for the sorafenib-NDs than that treated with pure sorafenib suspensions after single oral administration. At day 23, the tumor volume in the mice model was decreased to 33.75% of the one that was treated with sorafenib only.

DOI: 10.1021/acs.chemrev.9b00099
Chem. Rev. XXXX, XXX, XXX−XXX

In another ND investigation, Li et al. studied the function of pure NDs and DOX-loaded NDs chemodrugs for the in vivo anticancer treatment and compared their inhibition effect with that through the free DOX molecules.[220] DOX-loaded NDs showed a slow release and passive targeting manner which allowed them to effectively suppress tumor growth while maintaining low toxicity to the normal organs including kidneys, spleens, and livers. The NDs were directly mixed with DOX molecules at different pH conditions, and the maximum adsorption rate of the DOX (70.0 ± 2.3 μg/mg) was observed for the pH value of 10. Binding between the NDs and DOX may be attributed to the electrostatic interaction between of amine groups on the DOX and carboxyl groups on the ND surface. The release rate of the DOX from the ND surface was strongly dependent on the pH value of the physiological environment with a rapid release efficiency of 24% and 23% for pH 5.5 and 6.5 in the first 4 hours and 45% and 38% after 35 h. Interestingly, the pH values inside the tumors and endosomes of the cancer cells are around 6.5 and 5.5. Thus, the acidic release profile of the DOX-NDs would minimize the DOX release during the blood circulation and ensure the concentrated release at the tumor sites. In vivo experiments using mice models with H22 tumors and injected with free DOX, NDs, and DOX-loaded NDs showed an extended life expectancy of up to 57.5% for the mice treated with DOX-loaded NDs, which is almost four times of free DOX groups at 14.5% life expectancy. The results also indicated that the life span rate of 11.73% for the ND groups alone were still higher than that of negative control groups with saline solutions (1.12%). More importantly, the body weight of the mice treated with pure NDs or DOX-loaded NDs was maintained while an obvious weight loss was observed for the groups that were administered with the free DOXs.

More recently, Khan et al. reported the use of functionalized C-dots for delivering dopamine hydrochloride (DA) drugs to treat neuron diseases.[508] The DA molecules are known as the inotropic vasopressor for neurological dysfunctions.[503] In this work, C-dots were prepared by microwaving the citric acid mixture solutions with ethanol and sodium hydroxide and were later surface-functionalized with DA. The stable release time of DA from the C-dot surface could be extended to a long time of up to 60 h in a pH condition of 7.4. The cell viability was noted to be as high as 95% for the DA-loaded C-dots compared to that of 74% for the free DA molecules. This result suggested the higher water solubility and biocompatibility of the DA-loaded C-dots. The nanoconjugates were administered in mice models through the tail vein at a high concentration of 20 μg/mL for toxicity studies. No abnormality or lesions were observed from tissues of brain, liver, spleen, and kidney. In addition, the body weight of the mice was maintained after treatment even at day 45. Table 5 presents a systematic overview of the use of nanocarbon materials for in vivo drug delivery.

3.4. In Vivo Multifunctional Combinatorial Imaging and Delivery

While many works have focused on in vitro drug/gene transfection for designing nanocarbon platforms in cancer theranostic applications, few have reported on in vivo experiments that employ either a combinational therapeutic module or hybrid nanocarbon materials for achieving multiple theranostic objectives. This section outlines the interesting results of these multicombinatorial in vivo studies.

Khademhosseini and co-workers developed a unique GO/hydrogel based angiogenic gene delivery system for vasculogenesis and cardiac repair.[535] A biocompatible hydrogel was synthesized which efficiently delivered nanocomplexes of GO and vascular endothelial growth factor (VEGF)-165 pro-angiogenic gene for myocardial therapy. The effectiveness of the system was evaluated using a rat model with acute myocardial infarction. The therapeutic hydrogels were injected intramyocardially in the peri-infarct regions. Growth factor-165 from in vitro cardiomyocytes exhibited profound mitotic activities on endothelial cells. A significant increase in myocardial capillary density at the peri-infarct regions as well as reduction of the observable scar area in the infarcted heart was observed.

Yin et al. utilized multifunctionalized monolayer GO as a gene delivery system to efficiently codeliver HDAC1 and K-Ras siRNAs to specifically target MIAPaCa-2 pancreatic cancer cells.[624] The systematic mechanistic elucidation of the dual gene silencing effects indicated the inactivation of both the HDAC1 and the K-Ras gene, causing apoptosis, proliferation inhibition, and cell cycle arrest in treated MIA PaCa-2 cells. The synergistic combination of gene silencing and NIR light thermotherapy showed significant anticancer efficacy, inhibiting in vivo tumor volume growth by >80%. Furthermore, it was shown the GO could be metabolized in the mouse model within a reasonable period of time without obvious side effects.

In another use of GO, polyaniline (PANI) was loaded onto GO for a highly efficient nanodevice for photothermal therapy with 808 nm laser irradiation.[625] Loading DOX on GO−AU@PANI generated a very efficient nanoconstruct for the treatment of 4T1 cells as the strong NIR absorption induced a fast release of the cytotoxic drug. Furthermore, the presence of Au nanoparticles resulted in a strong SERS signal. For this reason, SERS, together with fluorescence spectroscopy, was used for real-time monitoring of the intracellular DOX release process. The study showed that nanoparticles remained confined into the cytoplasmic region, whereas DOX entered the nucleus. In vivo experiments performed on 4T1-tumor-bearing mice highlight how the combined use of DOX and photothermal therapy provides stringent controls on tumor mass growth.

Similarly, a GO nanohybrid with bismuth sulphide (Bi_2S_3) nanoparticles and polyvinyl pyrrolidone (PVP) was used for chemotherapeutic and photothermal treatment of tumors.[626] Bi_2S_3 nanoparticles ensured strong NIR absorption and a hyperthermal effect. The GO nanohybrid was prepared in a single step through a hydrothermal process starting from exfoliated GO, $Bi(NO_3)_3$, thioacetamide, and PVP. The resulting material was nontoxic toward several cell lines. Furthermore, the PVP−GO/Bi_2S_3 nanocomposite showed a high loading capacity of DOXO, up to 5 times its weight, and the final adduct proved to be an optimal device, both in vitro and in vivo. The PVP−rGO/Bi_2S_3 nanocomposite could be used as a theranostic, as its NIR and X-ray absorption ability could act as a dual-modal contrast agent for both photoacoustic tomography and CT imaging.

C-dots-based conjugates can also act as dual-function carriers for in vivo fluorescent imaging and drug delivery. Zheng and co-workers functionalized C-dots with anticancer drug of oxaliplatins based on the condensation interaction between the carboxyl groups of the oxaliplatin and the amino group on the C-dot surface.[605] With 50% of current chemotherapy drugs administered to cancer patients being

DOI: 10.1021/acs.chemrev.9b00099
Chem. Rev. XXXX, XXX, XXX−XXX

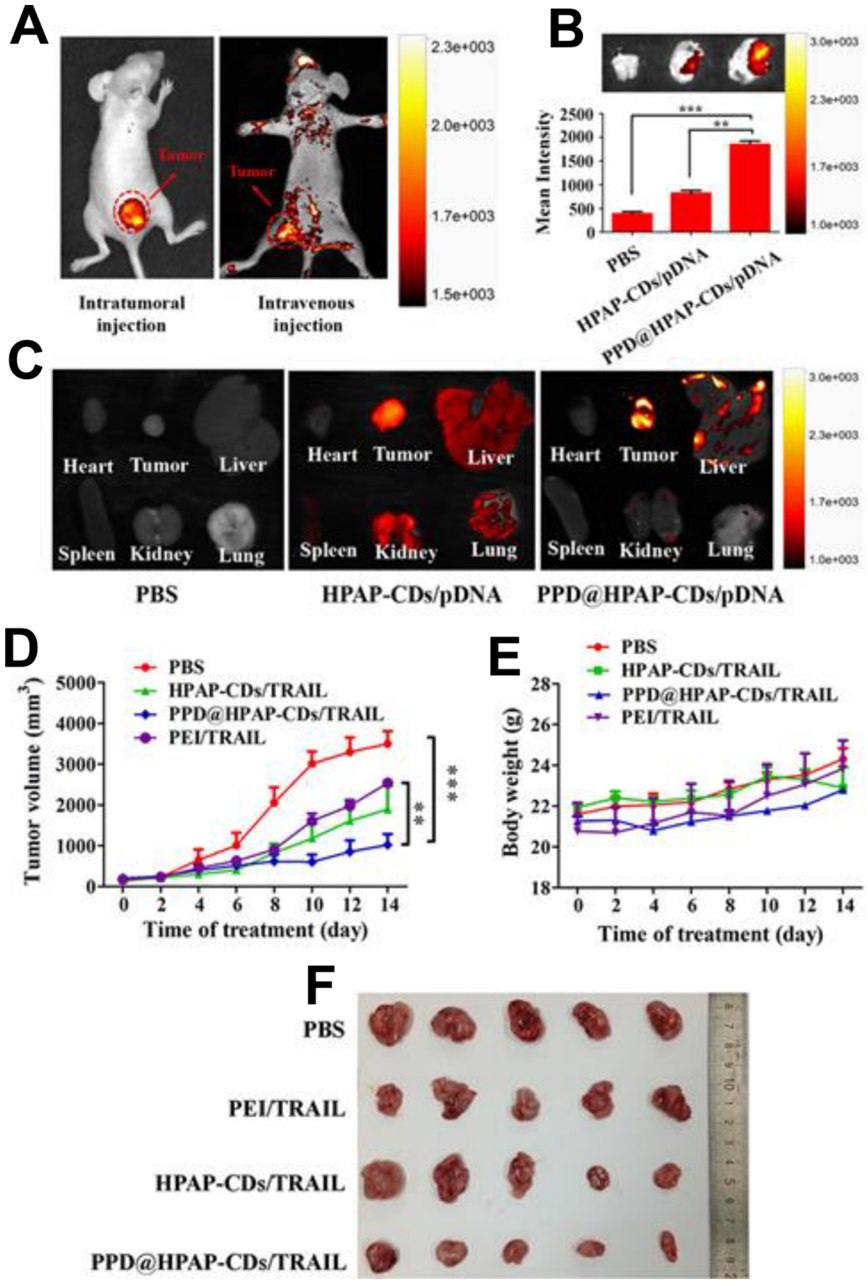

Figure 34. (A) In vivo imaging of tumor-bearing mice after injection with PPD@HPAP-CDs/pDNA via intratumoral injection (left) and intravenous injection (right) after 8 h. (B) Ex vivo imaging of accumulation of HPAP-CDs/pDNA complexes in tumor tissue after intravenous injections of different formulations (PBS, HPAP-CDs/pDNA, and PPD@HPAP-CDs/pDNA) and quantitative distribution analysis. (C) Ex vivo imaging of main organs and their corresponding fluorescence quantification data harvested after intravenous injection with different formulations after 8 h. In vivo antitumor studies of PPD@HPAP-CDs/pTRAIL and other formulations in nude Balb/c mice bearing MCF-7 cells in terms of (D) the tumor volume profiles and (E) the average body weight variations. (F) The sacrificed tumor tissue images from nude mice. Reprinted with permission from ref 627. Copyright 2018 American Chemical Society.

platinum-based, oxaliplatins have recently emerged as a new class of platinum-based drugs for the chemotherapy for metastatic colorectal cancers. To reduce the resistance and side effects of the drugs, Oxa(IV)-COOH of Pt(IV) complex is employed as a pro-drug that is formed through adding two axial ligand molecules to the Pt(II) drug. The Oxa(IV)-COOH drugs could be easily conjugated to the surface of C-dots and internalized by the cancer cells via endocytosis process. In this study, the C-dots were synthesized by thermally pyrolyzing the mixtures of polyene polyamine (PEPA) and citric acid (CA), where CA served as the carbon sources and PEPA as the passivation layers. Cell viability, determined by injecting different doses into the culture media of L929 fibroblast cells, was more than 75% even with a high concentration of the C-dots in 0.5 mg/mL. To investigate the in vivo anticancer effect of the Oxa-loaded C-dots, Kunming mice bearing hepatocarcinoma 22 liver tumors were employed as target models. The H22 tumors were xenografted at the anterior limb of the mice and then intralesionally injected with Oxa-loaded C-dots at a dose of 0.72 mg/mL of Pt. According to the imaging results, most of the tumors were necrotic after 72 h with only two times of C-dots carrier injection. This confirmed

DOI: 10.1021/acs.chemrev.9b00099
Chem. Rev. XXXX, XXX, XXX−XXX

the anticancer effect through the reduction of Pt(IV) into Pt(II) in the cancer cells which could maintain low toxicity to the normal organs. The tumor volume decreased from 6.5 to 1.2 cm^3, corresponding to a high inhibition ratio of 82.4%. Their body weights were observed to have a slight drop in the first 3 days and remained unchanged even after with multiple rounds of treatment.

More recently, Zhao et al. reported tumor-specific gene delivery with low side effects using a hybrid C-dots-based multifunctional theranostic nanoplatform (Figure 34).[627] The C-dots were prefunctionalized with PEI end-capped disulfide-bond-bearing hyperbranched poly(amido amine) (HPAP), yielding an enhanced fluorescent quantum yield (27%), intracellular degradability, and efficient gene delivery capability. Excellent in vivo antitumor activity was demonstrated in BALB/c nude mice models, where tumor growth in MCF-7 cells was inhibited by up to 70.84% upon treatment with the PPD@HPAP-CDs/TRAIL group compared with that of the PBS-treated cells.

Li et al. developed fluorescent CDs as an intranasal vaccine delivery system with bioimaging function.[628] The CDs/OVA formulation induced significantly higher IgG titer, IgA titer, splenocyte proliferation level, IFN-γ secretion level, and memory T cells. The immunization efficacy boost by the CDs/OVA formulation could be attributed to the permeation enhancement effect of the CDs and the promotion of antigen transport across the nasal mucosa layer.

Zhang et al. constructed novel amine-dotted hollow carbon nanospheres (HCNs) to serve as a versatile platform for the codelivery of siRNA targeting multidrug resistance gene (MDR1) mRNA (siMDR1) and chemotherapeutics (DOX or cisplatin) to fight drug-resistant cancers.[552] The HCNs showed enhanced loading capability for both siRNA and chemotherapeutics. The nanostructure down-regulated more than ~96% of MDR1 protein expression of DOX-resistant breast cancer (MCF-7/ADR cells) and led to ~90% reduction of weight of MCF-7/ADR tumor on mice.

4. TOXICITY

There is a compelling need to develop novel and effective clinical protocols that address the issue of safety, toxicity, and efficacy of nanocarbon materials at the clinical trials scale so that anticancer drugs formulated out of engineering nanocarbon materials sufficiently meet the expectations for clinical approvals. The following paragraphs detail the toxicity effects of the different nanocarbon materials discovered in various in vivo studies. The subsequent paragraphs outline the factors that drive the toxic mechanisms in these materials and how careful synthesis and functionalization approaches can help to better contain the toxicity effects within tolerable limits.

4.1. Cytotoxicity Effects of Different Nanocarbon materials

Evaluation of in vitro toxicity is a steppingstone toward the in vivo and clinical realization of nanocarbon-based biological carriers. In vitro assays are most commonly used to monitor and evaluate the effects on cellular activity such as mitochondrial function, reactive oxidative stress, and membrane stress. The cytotoxicity of nanocarbon materials are found to be dependent on factors such as morphology, including aggregation, cell line, concentration, and exposure time. These variations can be attributed to variable aspects such as the differing internalization mechanisms between cell types.

For example, graphene comprises of a monolayer of honeycomb lattice and is the basis of other morphologies in the nanocarbon material family.[29] Zhang et al. reported shape- and dose-dependent cytotoxic effects of a few-layer graphene (3−5 μm) when tested with MTT and LDH in neuronal PC12 cells.[629] The study found that lower concentrations of graphene resulted in stable metabolic activity. Significant disruptions of graphene to cellular membranes were seen at a relatively high concentration of 100 μg/mL. The flat morphology and sheet-like nature also afforded graphene improved metabolic activity at higher concentrations compared to other structures such as SWCNT, which has a more penetrating tubular shape. However, the aggregation of sheets can be detrimental to cellular activity. Where shape-dependence is concerned, the irreversible formation of graphene sheet aggregates saw a 9-fold increase in oxidative stresses for human skin fibroblast cells at concentrations of 25 μg/mL. Similarly, the higher toxicity of graphene sheets to adherent cells was attributed to the faster sedimentation, resulting in nutrient-deprivation and cell growth inhibition from the aggregation. The cytotoxicity of graphene is found to also be time-dependent, where longer exposure times saw significant interruptions with mitochondrial activity.[630] Few layer graphene sheets, exposed with concentrations between 0.005 and 90 μg/mL for up to 72 h, began introducing mitochondrial and membrane damages at 62.8 and 45.5 μg/mL, respectively, in skin keratinocytes. When exposed for 24 h, the HaCaT cells were unaffected with concentrations up to 100 μg/mL. However, 48 h exposures saw 16% reduction in mitochondrial activity with concentrations of 30 μg/mL or higher, which was also the concentration where significant cellular membrane damage was found. Interestingly, the lowered viability did not reduce the cell proliferation activity significantly, indicating the low cytotoxicity. Single layer graphene sheets with thickness of 0.8 nm showed a reduction in metabolic activity with a viability loss of 17% for a lower concentration of 1 μg/mL when exposed for 48 h to human hepatoma cells.[631]

CNTs, which can be single-walled or multiwalled, have been reported to have generally higher cytotoxic effects compared to other structures within the carbon family. The apparent higher cytotoxicity of the nanotubes for a variety of cell lines are well-documented in the literature.[632] It has been reported that the cytotoxicity is dependent on the nanomaterial mass basis, with SWCNT showing higher toxicity compared with MWCNTs.[633] SWCNT saw a reduction in the cell viability by 28% compared to graphene sheets (17%) in hepatoma cells.[631] Nanotubes also impacted the cell necrotic activity, by way of membrane damage, with a significant release of LDH activity seen in the study with PC12 cells.[629] The trends are consistent with other cell lines. In human keratinocytes, exposure to SWCNT concentrations of 0.06−0.24 mg/mL for 18 h introduced a host of oxidative stresses and cytotoxic effects, such as free radical formation, accumulation of peroxidase products, antioxidant depletion, and viability reduction.[634] It was found that dose-dependent cell separation and surface homogeneity alterations saw a reduction in cell viability up to 37.6%. In mouse lung epithelial cell lines, SWCNT slowed cell proliferation with a higher fraction of cells in the G1 phase of cell cycle compared to the S or G2 phase exposed for up to 72 h.[635] Clear cytotoxicity was seen in human dermal cell lines at a dose of 40 μg/mL with a near-50% cell viability reduction for the highest dose of 400 μg/mL from LDH release.[632] The main toxicity mechanism was

DOI: 10.1021/acs.chemrev.9b00099
Chem. Rev. XXXX, XXX, XXX−XXX

Table 6. Cytotoxicity Evaluation of Different Nanocarbon Materials

material	concentration	exposure time	sample/cell type	evaluation methods	conclusion	ref
graphene, SWCNT	0−100 μg/mL	24 h	PC12	assay: MTT, LDH (lactase dehyhrogenase release), ROS, caspase 3/7; visual morphology evaluation	• dependence on concentration and shape (include agglomeration)	629
graphene, SWCNT	1 μg/mL	48 h	human hepatoma/HepG2	assay: MTT, iTRAQ; LC-MS/MS	• viability loss for SWCNT, 26 ± 5%; graphene, 17 ± 3% • lowered metabolic activity	631
graphene, GO	FLG, 0.005−90 μg/mL; GO, 0.005−100 μg/mL	up to 72 h	skin keratinocytes/HaCaT	assay: WST-8, sulforhodamine B (SRB), PI uptake		630
graphene/chitosan	0−0.6%		L929	MTT, cell attachment	• no visible reduction in viability between the negative control and experimental groups at 24 and 48 h • good biological safety and almost no cytotoxicity	675
graphene sheet, GO	3.125−200 μg/mL		(1) EDTA-stabilized whole human blood samples; (2) human skin fibroblast/CRL-2522	assay: hemolysis, MTT, WST-8 viability; characterization: WXRD, AFM, XPS, DLS, zeta potential, microscopy	• state of graphene affects toxicity; dose-dependent hemolytic activity on RBCs • sonicated (smaller) GO has higher hemolytic activity than untreated (larger) GO • covering the GO sheets with chitosan eliminated their hemolytic activity	676
MWCNT, GO, ND	0, 5, 10, 20, 40, 80 μg/mL	2 h	HeLa	assay: MTT, LDH, SOD, MDA; ROS generation	• ND: least cytotoxic (91% cell viability at 80 μg/mL) and highest cell uptake ratio (25.6 ± 4.2%) • CNT, moderate uptake (13.3 ± 1.3%) • GO, lowest uptake ratio (7.8% ± 1.6%)	677
SWCNT, MWCNT, fullrene (C_{60})	SWCNTs and C_{60} were 0, 1.41, 2.82, 5.65, 11.30, 28.20, 56.50, 113.00, and 226.00 μg/cm^2, respectively; MWCNT10 were 0, 1.41, 2.82, 5.65, 11.30, and 22.60 μg/cm^2		alveolar macrophage	assay: MTT; phagocytic response by microscopy; TEM for structural alterations	• the cytotoxicity increases as high as ∼35% when the dosage of SWCNTs was increased by 11.30 μg/cm^2 • the cytotoxicity follows a sequence order on a mass basis: SWCNTs > MWCNT10 > quartz > C_{60} • the macrophages exposed to SWCNTs or MWCNT10 of 3.06 μg/cm^2 showed characteristic features of necrosis and degeneration	633
SWCNT	0.06, 0.12, or 0.24 mg/mL in KGM basal medium without phenol red	2, 4, 6, 8, and 18 h at 37 °C	human epidermal keratinocytes/HaCaT	ESR, free-radical generation; SEM, TEM, confocal microscopy; chemiluminescence of total antioxidant reserve; assay: AlmarBlue viability, HPLC of α-tocopherol, fluorescence for low molecular weight thiols and protein sulfhydryls, protein assay (Bradford method); spectrophotometric absorbance for peroxidative products	• SWCNT exposure produced oxidative stress and cellular toxicity, ultrastructural and morphological changes in cultured human cells • Unrefined SWCNT exposure results in accelerated oxidative stress and may produce dermal toxicity in exposed workers	634
fullerene derivative	0.24−2400 ppb	48 h	(1) Human dermal fibroblasts/HDF; (2) human liver carcinoma cells/HepG2	assay: live/dead, LDH, MTT	• cytotoxic to HDF and HepG2 cells at the 20 ppb level • water-soluble functional groups on the surface of a fullerene molecule dramatically decrease the toxicity of pristine C_{60} • after 30 h of exposure to nano-C_{60}, cells begin to exhibit signs of leaky membranes and lipid oxidation	641
SWCNT, fullerene (C_{60})	0 and 200 μg/mL for 24 h; long-term exposure (576 h) at 100 μg/mL	24 h; 576 h	FE1-MutaMouse lung epithelial cell line	assay: LDH (cytotoxicity), live/dead NucleoCounter, comet (DNA damage); cell cycle analysis (flow cytometry); ROS generation; mutagenicity analysis	• cell proliferation was slower with SWCNT exposure and a larger fraction of the cells were in the G1 phase • SWCNT and C_{60} are less genotoxic in vitro than carbon black and diesel exhaust particles	678
water-soluble fullerene	1−100 μg/mL	24 h	vascular endothelial cells (EC)	assay: LDH, proliferation, activity for 20S proteasome; Western blot analysis	• fullerenes changed morphology in a dose-dependent manner, only maximal doses of fullerenes caused cytotoxic injury and/or death and inhibited cell growth	
fullerene/nano-C_{60}	0.24, 2.4, 24, 240, and 2400 ppb	48 h	human dermal fibroblasts, human liver carcinoma cells (HepG2), and	assay: LDH, MTT, PicoGreen dsDNA quantitation solution; plasma membrane	• disrupts normal cellular function through lipid peroxidation	679

DOI: 10.1021/acs.chemrev.9b00099
Chem. Rev. XXXX, XXX, XXX−XXX

Table 6. continued

material	concentration	exposure time	sample/cell type	evaluation methods	conclusion	ref
			neuronal human astrocytes	monitoring by monitoring the uptake of fluorescein-derivatized dextrans; thiobarbituric acid assay for malondialdehyde (lipid peroxidation)	• ROS is responsible for the membrane damage • lipid peroxidation and resultant membrane damage are responsible for the cytotoxicity of nano-C_{60}	
fullerene (pristine, water-soluble polyhydroxylated)		short-term, 0.5−4 h; long-term, 18−24 h	(1) mouse fibrosarcoma cell line L929; (2) rat glioma cell line C6; (3) human glioma cell line U251	assay: crystal violet assay (viability), LDH, annexin V−FITC (apoptosis) and PI (necrosis), oxygen radical measurement, redox-sensitive dye dihydrorhodamine 123 (DHR) upon excitation at 488 nm' lipid peroxidation: colorimetric thiobarbituric acid assay for malondialdehyde (MDA)	• toxicity neither species/cell type specific • nano-C_{60} was at least 3 orders of magnitude more toxic than $C_{60}(OH)_n$ • nano-C_{60} caused rapid ROS-associated necrosis characterized by cell membrane damage without DNA fragmentation • in contrast, $C_{60}(OH)_n$ caused delayed, ROS-independent cell death with characteristics of apoptosis, including DNA fragmentation and loss of cell membrane asymmetry in the absence of increased permeability	640
single-walled carbon nanohorns	0.005, 0.010, 0.020, 0.039, 0.078, 0.156, 0.313, 0.625, 1.250, or 2.500 mg/mL of 5% suspension	24 or 48 h	clonal subline of a Chinese hamster lung fibroblast cell line CHL/IU	growth inhibition test; chromosome aberration test; reverse mutation test	• negative mutagenic and clastogenic potentials suggest that SWNHs are not carcinogenic • the acute peroral toxicity of SWNHs was found to be quite low	680
carbon dot	30−400 μg/100 μL		human kidney cells/293T	assay: MTT; Characterization: UV−vis, HRTEM, XPS	• no obvious reduction in cell viability	681
carbon dot	1, 5, 10, 20, 50, 100, or 200 μg/mL	24 h	(1) human breast cancer/MCF-7; (2) human colorectal adenocarcinoma/HT-29 cells	assay: cell mortality (trypan blue), MTT; cell proliferation	• lower proliferation (40%) for HT-29 cells at high concentration but generally suggest that C-dots are nontoxic to cells	682
nanodiamond	5−100 μg/mL		neuroblastoma cells, macrophages, keratinocytes, and PC-12 cells	MTT, ROS	• no significant difference in viability compared to controls at concentrations up to 100 μg/mL	645
SWCNT, MWCNT, nanodiamond	25−100 μg/mL	24 h	neuroblastoma cells, rat alveolar macrophages (NR8383 CRL-2192)	MTT, mitochondrial permeability, fluorescent imaging	• biocompatibility was found after incubation with NDs and both cell types followed the trend: ND > CB > MWCNT > SWCNT • macrophages were found to be more sensitive to the nanomaterials with up to five times the generation of ROS after incubation with MWCNTs or SWCNTs	646

reported to be DNA damage and apoptosis. It is thought that the physical nanotube form is a significant contributing factor to increased cytotoxicity, with shape affecting the ease of which cellular membrane damage can occur. These parameters include fiber dose, length, diameter, surface area, agglomeration, and dispersibility.[636−639] The higher mobility resulting from the needle-like shape of nanotubes may facilitate an easier penetration of the cell membrane compared to other geometries. The suspension quality is another consideration where poorly dispersed nanotubes result in agglomeration, posing a toxicological risk.[638] As nanotubes become more agglomerated, the structures become bigger, stiffer, and more solid, contributing to the overall toxicity.

For materials like carbon allotropes, their water solubility is an intrinsic challenge associated with their biological applications. Pristine C_{60} fullerenes, in contact with neutral water, form fullerene aggregates often known as "nano-C_{60}". One of the factors making nano-C_{60} highly cytotoxic is its strong oxidation property leading to cellular necrosis.[640] As a result, functional groups such as −OH, −COOH, and $-NH_2$ are added to its surfaces to render the structures water soluble. Over the years, several groups have studied the cytotoxicity in various animal and human cell lines with varied results. The surface chemistry profoundly impacts the manner in which the nanomaterial interacts with cells. In another report, Sayes et al. found that minor changes in the derivatization greatly affect the cytotoxic dosage. Two human cell lines were shown to alter this critical dosage by 7 orders of magnitude.[641] Cell exposure to lethal concentrations (20 ppb) of nano-C_{60}, the least derivatized, saw cytoplasmic membrane leakage as evidenced with an uptick in LDH concentration, whereas cell exposure to water-soluble polyhydroxylated fullerenes $[C_{60}(OH)_n]$ resulted in both antioxidant and cytoprotective properties with mild apoptotic activity that is independent of ROS.

NDs have been generating buzz among nanocarbon researchers, as they have been shown to be more biocompatible compared to others.[298,642−646] In a comparative study with carbon black, SWCNTs, and MWCNTs, NDs fare best in terms of biocompatibility.[646] Schrand et al. found that unfunctionalized NDs ranging in size from 2 to 10 nm were nontoxic to several cell types, such as neuroblastoma, macrophage, keratinocyte, and PC-12 cells. For concentrations from 1 to 100 μg/mL, inflammatory cytokines remained unstimulated in macrophages. To further this, the intact mitochondrial membrane coupled with the insignificant drop in oxidative stress generation suggests that NDs are unreactive

DOI: 10.1021/acs.chemrev.9b00099
Chem. Rev. XXXX, XXX, XXX−XXX

Table 7. Genotoxicity Evaluation of Different Nanocarbon Materials

material	concentration	exposure time	sample/cell type	evaluation methods	conclusion	ref
reduced graphene oxide nanoplatelets (rGONPs)	0.01−100 μg/mL	1, 24 h	human mesenchymal stem cells	assay: cell viability, ROS, Comet, RNA efflux; chromosomal aberration	• cell damage at 1 μg/mL but cytotoxic at maximal concentration • observed DNA fragmentation and chromosomal aberrations at <0.1 μg/mL	648
graphene oxide	1−100 μg/mL	24 h	human fetal fibroblast cells	assay: modified alkaline halo, LIVE/DEAD	• concentration-dependent genotoxicity • graphene among highest cell viability reduction compared to other nanomaterials	649
fullerenes (C_{60})	0.18−4.2 mg/L	3−6 h	human lymphocytes	assay: alkaline comet	• genotoxicity observed for all suspension solutions with lowest concentration down to 2.2 μg/L	683
CNTs, graphite nanofibers	3.8−380 μg/mL	24−72 h	human bronchial epithelial BEAS 2B cells	assay: Comet, micronucleus (cytokinesis-block method)	• morphological-dependent genotoxicity with observed micronucleation at select times	651
nanodiamond	5, 100 μg/mL	2−24 h	mouse embryonic cells	assay: WB, annexin V, AP detection	• observation of DNA damage markers, with indication of double-strand breakage • higher expression seen in oxidized NDs, with undetectable downstream markers in the pristine	653
carbon nanohorn	78−1250 μg/plate, 0.010−0.078 mg/mL	24−48 h	*Salmonella typhimurium* strains (TA100, TA1535, TA98, and TA1537) *E. coli* strain (WP2 uvrA) Chinese hamster lung fibroblast cell line	assay: bacterial reverse mutation (Ames), chromosomal aberration	• negative mutagenicity and clastogenicity	680

DOI: 10.1021/acs.chemrev.9b00099
Chem. Rev. XXXX, XXX, XXX−XXX

to cells, opening the possibility for their use as a control or benchmark material. Conversely, Li et al. have reported in their study that the cytotoxicity of the NDs depends on the presence of serum in the culture media.[449] It was found that HeLa cells in medium with serum did not show cytotoxicity. However, the opposite was true in serum-free medium, resulting in cell death 6 h following incubation of the nanomaterial. The authors postulated that the serum protein adsorption plays a protective role after ND uptake to result in the apparent nontoxicity of NDs in complete cell medium. In this instance, serum proteins adsorb onto the NDs as high as 48 wt % at 37 °C and work to improve hydrophilicity and stabilize the dispersion. Furthermore, the presence of serum proteins promoted cell proliferation. In the absence of serum, the ND dispersion showed aggregation, with sizes of 1359 nm compared to 304 nm for complete cell medium, possibly leading to a lower uptake as well. Table 6 summarizes the cytotoxicity effects of these nanocarbon materials.

4.2. Genotoxicity Effects of Different Nanocarbon Materials

Genotoxicity studies are concerned with the damage onto genetic materials as a result of nanomaterial exposure. This is an equally important aspect of conducting in vitro testing, as DNA damage can potentially result in mutations, apoptosis, and other effects in the cellular environment, where a correlation exists between DNA mutation and cancer.[647] However, the number of genotoxicity studies pale in comparison to cell death. Genotoxic evaluation can be assessed by assays such as the comet assay (single cell gel electrophoresis) for observing DNA strand breakage, or the micronucleus assay which stains the DNA of cells with 4′,6-diaminidino-2-phenylinodole (DAPI) to find changes in the cellular nuclei. The genotoxic evaluation draws parallels with its cytotoxicity counterpart, having factors such as material morphology, cell line, and dose affect the outcome, although the onset of each of those are independent of each other.

In reduced graphene oxide nanoplatelets (rGONPs), genotoxic effects were found to take place earlier than cytotoxic effects. rGONPs, exposed to human mesenchymal stem cells (hMSC) in concentrations of 0.01, 0.1, 1, 10, and 100 μg/mL for 24 h, caused DNA fragmentation and chromosomal aberration after 1 h which were concentration- and size-dependent.[648] The earliest onset was found at the lowest concentration and is associated with the penetration of nanosheets into the cell nucleus. The potency of graphene genotoxicity on human fetal fibroblast cells was seen in another study,[649] with GO measuring 2 μm laterally and 1.5 nm thick, outpacing other nanomaterials in DNA damage using the lowest tested concentration (1, 10, 100 μg/mL) for cells treated for a 24 h period.

Several researchers found that the more fibrous structures such as nanofiber and nanotube appear to more toxic compared to other morphologies, consistent with the higher cytotoxicity of such morphologies mentioned in the previous section. Despite these findings, exclusion from biological applications is unwarranted. However, understanding their effects in biological environments is essential to be able to exploit their properties for the intended application. For example, CNTs have been shown to be able to interact with biomolecules.[650] Lindberg et al. studied the genotoxicity to DNA and micronuclei in human bronchial epithelial cells, for CNTs and graphite nanofibers (GNFs).[651] The comet assay for CNTs (concentrations introduced between 3.8 and 380 μg/mL) showed statistically significant DNA damage for all doses administered, increasing accordingly with the administered dosage. However, the trends for the GNFs were not as obvious, with DNA damage seen in select doses based on the treatment period (24 h, 48 h, 72 h), with dose-dependent damage only at the 48 h treatment time. The micronucleus assay did not show any dose-dependence, however, in CNT damage observed for several doses and treatment times. The authors concluded that these materials appear to be toxic for CNTs and GNFs, likely due to the fibrous nature, in addition to possible catalyst metal presence on the surface.

NDs, despite being touted to be the most biocompatible of the nanocarbon family, are not exempt from genetic material damage either. Xing et al. showed that ND uptake by mouse embryonic cells (with concentration of 5 or 100 μg/mL) led to a higher expression of DNA damage marker proteins p53, MOGG-1, Rad51, and XRCC-4. p53, sometimes called "guardian of the genome",[652] activates in the event of DNA damage from irradiation or oxidative stresses among others and is seen at the beginnings of DNA damage.[653] MOGG-1 marks double-strand breakage, while Rad51 and XRCC-4 serve as repair markers. Damage marker expression was higher for oxidized NDs (oNDs) compared to the pristine. Both saw p53 expression at short and long time intervals. With pristine NDs, downstream markers were undetected, suggesting that minor repair was only required. oNDs after 24 h, however, showed MOGG-1 expression, indicating strand breakage, and showed signs of differentiation or apoptosis. From here, it can be seen that surface chemistry is an important parameter to consider for the nanomaterial design. Table 7 summarizes the genotoxicity effects of these nanocarbon materials.

4.3. In Vivo Toxicity Effects of Different Nanocarbon Materials and Their Biodistribution in Animal Models

In vivo toxicity is the next logical step following cellular level studies. The use of animal models has become a critical component of scientific research for improving understanding of the needs of an ever-changing healthcare landscape. More importantly, animal models can serve as the closest representative human model short of human trials to reveal the dynamical behaviors on a system-wide scale. The in vivo distribution depends on factors such as size, functionalization, and administration route. The utility of such studies is clear but requires care to conduct, ensuring to follow institutional ethics guidelines and performing due diligence on care of the animals. Although it is difficult to generalize in vivo toxicity studies because of the factors contributing to the outcome, in vivo studies also assist in determining the primary or secondary toxicity concerns and its causes as well as its distribution.

Many in vivo studies have been conducted over the years on a variety of carbon morphologies using both invertebrates such as *Caenorhabditis elegans*[654−656] and zebrafish,[657−659] and vertebrate animals such as mice,[652,618−620] rats,[592,660−662] and primates.[665] This section will discuss some of the relevant works categorized based on the animal model. The advantage of using invertebrate models are the ability to screen on a large scale (as per in vitro) while affording the visibility of active physiological functions. Vertebrate animal models require comparatively more care and can give an understanding of the accumulation profile and distribution of the nanomaterial in the organ structures within the body. The following section discusses the in vivo toxicity studies on animal models.

DOI: 10.1021/acs.chemrev.9b00099
Chem. Rev. XXXX, XXX, XXX−XXX

4.3.1. *Caenorhabditis elegans*. *Caenorhabditis elegans* or *C. elegans* is a saprophytic nematode species, generally found in soil and leaf litter. Its utility to perform as an in vivo animal model is characterized by genetic manipulability, well-defined genome, maintenance simplicity, short life cycle, and small size. The upkeep of this species can be done using standard in vitro processes with the distinct difference of having whole system information with metabolically active systems, including the digestive, reproductive, endocrine, and sensory systems.[666,667] GO was used to observe stress-induced toxicity in *C. elegans*.[654] The two dominant mechanisms in toxicity for the species boil down to an excess in hydroxyl radicals along with the formation of oxidizing intermediates.

In 2010, Mohan et al. conducted a toxicity assessment on the species using fluorescent NDs, administered orally or injected into the wild-type worm gonads to continually image the digestive system over the course of several days.[572] When fed, the uncoated NDs were found to remain within the intestinal lumen, while functionalized NDs got absorbed into intestinal cells thought to be resulting from endocytosis. The conjugated NDs which were absorbed remained in cells without causing changes in the worm's lifespan and reproduction. Meanwhile, injection served to introduce the nanomaterials within the reproductive system, hatching the next generation of larvae. Consistent with the trends of in vitro studies, introduction of NDs into the system did not introduce a detectable stress response and the NDs remained stable, suggesting their nontoxicity.

4.3.2. Zebrafish. Another invertebrate, zebrafish is a small and low maintenance species, with 100−200 offspring produced per weekly mating of an adult pair.[668] The species share physiological similarity to mammals.[669] With many genomic tools available for phenotype screening, and the ability to use in vitro tools while gaining physiological information has made zebrafish an attractive animal model. When administered to the species, carbon materials show some toxicity, requiring some optimization for the optimal doses. Developmental malformations with the zebrafish typically have dose and time dependencies and result in morphological changes to the standard zebrafish.

Usenko et al. reported the use of embryonic zebrafish to determine the toxicity of graded concentrations of fullerene types C_{60}, C_{70}, and $C_{60}(OH)_{24}$ in the early embryogenesis stage.[657] Concentrations between 100−500 ppb for C_{60} and C_{70} and 500−5000 ppb for $C_{60}(OH)_{24}$ in 100 ppb increments were used, and embryos were incubated in a 96-well plate with the nanomaterial solution until 96 h. Unlike $C_{60}(OH)_{24}$, the mortality rate was found to be 100% for embryos incubated in 200 ppb of C_{60} and C_{70} during the first 48 h. This rate was found at the higher concentration of 4000 ppb for the hydroxylated fullerene.

In another work, zebrafish embryos were used to evaluate the developmental toxicity of GO and its PEGylated derivatives.[658] It was found that both pristine and PEGylated GO, injected into, during the one or two cell stages of fertilized embryos, caused developmental defects which was found to be dose-dependent, providing evidence of the material toxicity. However, the extent of defects was lowered with the PEGylated GO as compared to the pristine, where some of the pristine GO-injected embryos showed signs of apoptosis. The PEG layer is thought to serve as a protection layer to ensure that the GO is more biocompatible. The doses tested in the study were 250, 500, and 750 pg. Following administration, a range of toxicity-related developmental problems ranging from mild to severe were found such as weakened circulation, underdevelopment of critical parts such as the brain and retina, and a curved spine, among others. These developmental defects increased in severity with higher injection does. Fluorescent imaging revealed that, unlike in mice, the accumulation of GOs within zebrafish occurs throughout the body, including the head region. It appears that the unlabeled materials nonspecifically bind and therefore have no targeting preference causing its distribution around the entire system.

Similarly, using pristine and BSA-tagged NDs as the fluorescent label, Lin et al. found some developmental defects in embryonic zebrafish microinjected with concentration of 1, 2, and 5 mg/mL, with the addition of BSA aiding in improving the dispersion of the solutions.[659] There were no development anomalies when using the lowest concentration. As concentration increased, the developmental anomalies began to increase, such as curvature of the caudal fin, indicating a dose-dependent effect as well.

4.3.3. Mice. Of the rodents, mouse models such as Kunming mice and BALB mice are arguably the most widely used animal model for in vivo evaluation of nanocarbon materials. Some of the more common tests for mouse studies include the blood biochemistry and hematology analysis, imaging, and histological examination. Blood biochemistry and hematology serve to look for any changes in marker levels that deviate from the control group. Imaging can be conducted by optical or tomographical means, where labels such as dyes or radioisotopes can be used. Finally, histological analysis reveals the distribution and accumulation profiles of the nanomaterial within organs in the body and pinpoints any abnormalities or lesions within the organs that could have arisen from treatment.

Using different functionalization formulations, SWCNTs were found to have little accumulation in reticuloendothelial system (RES) organs such as the liver.[592,670,671] Dai et al. functionalized SWCNTs with PEG and found the materials to be stable in vivo, exhibiting long blood circulation periods and low uptake by the RES. The authors did not find the material to be toxic at the doses administered, and the animals did not display negative health consequences such as weight loss or fatigue.[592] Interestingly, Wang et al. found that despite the large mean molecular weight, the hydroxylated SWCNTs used in the study behaved as small molecules, evidenced by the ease of movement between tissue and compartments within the body.[670] Furthermore, the excretion pathway for the material was 94% from urine as compared to feces. Singh et al. intravenously injected SWCNTs chelated with diethylentriaminepentaacetic and labeled with indium (^{111}In) for imaging.[671] Radioactive tracing found no retention in the RES. The blood clearance rate was found to be around 3 h, shorter than other materials such as fullerenes reporting at 6.8 h postinjection.

Carbon dots were studied over three months, injected in female BALB/C mice.[662] The 20 mg/kg dose used did not show any obvious sign of toxicity over the study time frame, with no weight loss or mortality from the administration. Liver function markers and hematology markers indicated normal results relative to the control. The dots were found to accumulate in the RES organs, while early accumulation was seen in the kidneys.

Yang et al. reported the long-term toxicity and biodistribution of nanographene sheets (NGS) intravenously

DOI: 10.1021/acs.chemrev.9b00099
Chem. Rev. XXXX, XXX, XXX−XXX

injected in BALB/C mice.[672] Blood biochemistry and hematology analysis indicated that no obvious toxicity was found with the results appearing to be normal compared to the control. The distribution of the materials is time-dependent, with uptake in several organs seen at certain time points. The long-term accumulation of NGS were found predominantly be in the RES, such as liver and spleen, and very low in other organs. Clearance is thought to be by both renal and fecal pathways as evidenced by uptake in the kidney and intestines, respectively. The authors did not find evidence of notable organ damage except for a color change in the liver and spleen. In other areas, bone uptake was observed in the early time points tested via bone marrow. The thyroid uptake occurred in the earliest time point (1 h), with subsequent uptake to be very low and nearly undetectable by day 3.

Zhang et al. reported the size-dependent biodistribution of nanohorns in mice.[673] It was found by tail vein injection, smaller nanohorn (S-CNH) aggregates (30−50 nm) accumulated at slower rates in RES organs compared to the larger (L-CNH) aggregates (100 nm), saturating at the spleen at 48 and 1 h, respectively, and >7 days and 48 h, respectively, for the liver. These movements are consistent with studies showing macrophage engulfment of S-CNH. Engulfment was slower for particles smaller than the micrometer range, which may be a cause for the slower accumulation. Inflammation markers were not found to be present, suggesting the low toxicity of the material in vivo.

4.3.4. Rats. Although not as common as mouse models, some research groups have used rats in the toxicity evaluation, using models such as Sprague−Dawley and Wistar strain rats. Some of the earlier works administered MWCNTs to Sprague−Dawley rats to better understand the inhalation risks and their effects on the relevant organs.[663,664] Muller and co-workers reported that MWCNTs are likely toxic, as evidenced by the increased inflammatory responses following intratracheal administration. CNT was present in the lungs 60 days post administration, with 40% remaining of the lowest dose tested. In addition, there was evidence of inflammatory and fibrotic reactions, with presence of TNF-α in the lung. In addition, large aggregates in the respiratory pathway, saw collagen-rich granuloma formation in the bronchial lumen 2 months later. On the basis of these results, it is imperative to implement appropriate protections, such as functionalization, and controlled doses for further in vivo trials.

Vaijayanthimala et al. used fluorescent 100 nm NDs to study the long-term stability and biocompatibility in rats.[674] The solution was intraperitoneally injected, and it was found that the solution had no apparent toxicity. The behaviors of the animal remained normal compared to the control, with no changes in consumption and weight. Furthermore, distribution of tissues showed that the NDs are nontoxic at doses up to 75 mg/kg body weight. The authors reported the stability of the solution, remaining unchanged over a 37-day period observed using fluorescence imaging.

4.3.5. Primates. Nonhuman primates are an important model, being genetically the most similar to humans. At this time, not many works use primates for in vivo toxicity testing, most likely due to the maintenance required and high costs. Nevertheless, they are highly valuable and the closest mimic human responses to drug administration.

Recently, Alidori and co-workers presented a multiorgan evaluation of fibrillar carbon nanotubes in nonhuman primates.[665] In cynomolgus macaques, fibrillar carbon nanotubes are considered nontoxic and biocompatible. The majority of CNTs accumulated in the kidneys and liver and were excreted in urine. The material was rapidly cleared from blood at a time of approximately 7 min. The solution thus appears to be nontoxic based on the lack of necrotic evidence in the histopathology and lack of inflammatory indicator of the macrophage.

4.4. Factors Affecting the Toxic Mechanisms

4.4.1. Choice of Raw Materials and Approach for Nanomaterial Synthesis. Graphene prepared by the chemical vapor deposition method has shown an increase in caspase-3 activity and generation of ROS in neural pheochromocytoma-derived PC12 cells.[589] Thus, it is important for researchers to focus on devising alternating synthetic approaches that are efficient and less detrimental. Moreover, careful examination of the structure and dynamics of the synthesized nanocarbon materials is necessary to accurately predict their physicochemical effects. As an example, transition metals, such as Fe, Ni, Mo, Y, Co, and Cr, and other catalyst residues were found in commercially available CNTs,[641−643] which were shown to affect the redox properties of nanocarbon materials significantly.

4.4.2. Physicochemical Properties of Nanocarbon Materials. Major studies have shown the prominent role of the physicochemical properties of carbon nanomaterials, such as size and stiffness, on their internalization, biodistribution, and cytotoxic effects.[642,644,645] For example, short or tangled MWCNTs can be easily engulfed by macrophages and thus easily cleared by the lymphatic system. In contrast, long and rigid MWCNTs are not completely phagocytized and thereby get accumulated in tissues, which might induce carcinogenesis.[646]

4.4.3. Effects of Chemical Modifications and Functionalizations. Functionalization of carbon nanomaterials is often performed to increase their solubility in physiological conditions. It makes a major contribution to longer circulation times, better internalization, and improved biocompatibility.[80,562,647−651] However, the different functional groups cast varying toxic effects depending on their surface chemistry with the nanocarbon material structure. For instance, polycyclic aromatic dyes are commonly used for good solubilization of graphene in aqueous media instead of organic solvents that are often harmful.[652] In addition, polyhydroxylated fullerenes and malonic acid derivatized fullerenes show excellent solubility and localization in mitochondria, generating ROS.[653] On the other hand, fullerenes functionalized with methyl radicals are capable of inhibiting the chain reaction of lipid peroxidation by scavenging peroxyl radicals.[654] Similarly, one study reported the cytotoxicity of GO, PEI−GO, PEG−GO, and lactobionic acid−polyethylene glycol (LA−PEG) functionalized GO on human lung fibroblast (HLF) cells and found that the order of cytotoxicity was PEG−GO < LA−PEG−GO < GO < PEI−GO, which confirms the varying biological effects due to surface chemistry of nanocarbon materials.[655]

5. DESIGN CONSIDERATIONS OF NANOCARBONS FOR THERANOSTIC APPLICATIONS

On the basis of current investigations of nanocarbon materials for theranostic applications, we can precisely outline the following key unifying themes that serve as building blocks for researchers to design and formulate nanocarbon materials as

DOI: 10.1021/acs.chemrev.9b00099
Chem. Rev. XXXX, XXX, XXX−XXX

well as hybrid plasmonic nanocarbon composites for imaging, sensing, and drug/gene delivery:

5.1. The Effects of Physicochemical Properties of the Different Nanocarbon Materials on Toxicokinetics and Pharmacokinetics

Toxicity effect of nanocarbon materials is indeed the foremost issue to address for their maximum utilization in nanomedicine and clinical translational research. Many studies have pointed out the distinct effect of physicochemical properties, such as size, shape, surface property, and purity of the different nanocarbon materials on both the in vivo and in vitro toxicokinetics and pharmacokinetics. Majority of the toxicity studies are based on in vitro studies and very little in vivo studies.

In particular, the size, stiffness, surface functionality, and aqueous dispersibility of CNTs do have major influences on the in vivo biodistribution, transfection ability, and solubility in the biological media.[689] Alterations in the physicochemical properties affect the optical and chemical properties of these nanomaterials, and thus it is important to consider these factors when we account the in vivo toxicity, nanomaterial accumulation, and drug delivery efficacy. However, we do need more detailed in vivo nanocarbon materials-concerned toxicity studies in zebrafish, aquatic frogs, mice, rats, and particularly, primates, so as to extrapolate and evaluate the immediate and long-term toxic effects in humans. More in vivo evaluation models would facilitate to lay out a structured protocol and strengthen the decision of biomedical scientists over the choice of these nanomaterials for theranostic applications.

5.2. Developing Ligands for Precise Tumor Targeting and Better Biodegradation in Vivo

The major concern for using nanocarbon materials for in vivo and clinical applications in their potential toxicity and low clearance.[704] To address these issues, it is necessary that researchers focus on developing ligands that are able to better define the tumor targeting capability of nanocarbon materials and at the same time endow these materials with significant biodegradable attributes in vivo. One of the approaches for conceptualizing these ligands is by careful investigations of the biological responses to the nanocarbon materials in vivo. As an example, certain ligands can drive the secretion of matrix metalloproteases (MMPs), which causes protein hydrolysis and aggravates metastasis.[705]

5.3. Evaluating the Merits of Using Combinatorial Therapy

Various chemical modifications on nanocarbon materials have been investigated for their suitable applications in numerous combinatorial therapies, for example, combined gene and chemotherapy,[690−696] codelivery for immunotherapy,[697] gene therapy,[624] photodynamic therapy[698] or photothermal therapy,[465] combined chemo and photothermal therapy,[556,625,626,699] and combined photodynamic chemotherapy.[700−702] Albeit a few of them include in vivo studies for characterizing their merits in terms of drug delivery efficacy and tissue accumulation effects,[703] more in vivo studies need to be evaluated before we can come up with a facile and targeted drug delivery protocol using nanocarbon materials.

5.4. Developing Ligands for Precise Tumor Targeting and Better Biodegradation in Vivo

The major concern for using nanocarbon materials for in vivo and clinical applications in their potential toxicity and low clearance.[704] To address these issues, it is necessary that researchers focus on developing ligands that are able to better define the tumor targeting capability of nanocarbon materials and at the same time endow these materials with significant biodegradable attributes in vivo. One of the approaches for conceptualizing these ligands is by careful investigations of the biological responses to the nanocarbon materials in vivo. As an example, certain ligands can drive the secretion of matrix metalloproteases (MMPs), which causes protein hydrolysis and aggravate metastasis.[705]

5.5. Executing Efficient in Vivo Gene Transfection with Respect to Toxicity, Specificity, and Side Effects

The domain of gene delivery with high transfection efficiency and low cytotoxicity is far underexplored with respect to nanocarbon materials. We certainly need large numbers of in vivo investigations for optimizing and realizing nanocarbon materials-assisted gene delivery systems with minimum cytotoxicity and harmful side effects. One possible solution toward successful clinical gene delivery would be employing combinatorial therapeutic strategies involving PDT, PTT, and photoacoustic therapies[706] that can be beneficial in terms of reduced side effects and overcoming chemo- and multidrug resistance.

5.6. Explicitly Defining the Tumor Targeting Pathways for the Different Nanocarbon Materials

Understanding the tumor microenvironment is essentially vital as is studying the physicochemical properties of different nanomaterials for developing nanomaterials-based cancer theranostic approaches. Tumor microenvironments are complex and serve as the habitat for cancer cells invasion, proliferation, and migration. The peculiar characteristics of tumor microenvironment such as enhanced permeability and retention effect, hypoxia, acidosis, extensive angiogenesis, and tumor-associated immune cells,[684] are the main impediment to the clinical efficacy of the numerous drug delivery modalities that show encouraging performance in the in vitro environment. It is thus typically essential to exploit the excellent tunability of nanomaterials for targeting definite characteristics of the tumor microenvironment and controlling the metastatic spread of cancer.

As an example, targeting the extracellular matrix (ECM) of the tumor cells could be a major factor in controlling cancer growth. Cancer-associated fibroblasts secrete matrix metalloproteinases and cause epithelium−mesenchymal transition.[685] Thus, the ECM undergoes remodeling as the epithelial cells gain migratory and invasive phenotypes. Therefore, developing nanocarbon materials for strengthening the ECM could be one of the primary targeting strategies for overcoming the challenges of tumor microenvironment in cancer therapy. Furthermore, targeting cytokines, such as CXCR-4 and CXCL-12, and growth factors, namely VEGF, FDG, DGF, and TGF-β, which dominantly promote angiogenesis and the metastatic spread of tumor, is a vital pathway for nanocarbon materials-assisted therapy.[686−688] By making use of the excellent drug/gene loading capability, strong binding capability to hydrophobic molecules, tunable surface chemistry, free dangling bonds, and longer circulation times, researchers are warranted to achieve outstanding results for tumor microenvironment-responsive nanocarbon materials formulations for better therapeutic outcomes.

These five key unifying themes will serve as a foundational first-principles for researchers to study and investigate so as to

DOI: 10.1021/acs.chemrev.9b00099
Chem. Rev. XXXX, XXX, XXX−XXX

Table 8. Summary of Biological Applications of Various Nanocarbon Materials

material	notable applications	pros	cons
Graphene oxide nanosheets	Flexible sensors, intracellular sensor	• Biomarker adsorption capability (pi-pi stacking) • High fluorescent quenching efficiency. • Strong photoluminescence under both one and two-photon excitation. • Can be used as photothermal agent. • The properties of resultant GO nanosheets can be tuned by choosing the starting precursors materials and modification during the oxidation process. • Stable photoluminescence.	• Molecule binding instability in protein-rich media. • Non-biodegradable. • Broad photoluminescence peaks.
Carbon Nanotubes	Drug delivery	• Photobleaching resistant (for continuous imaging labels, SWCNT). • NIR excitation for multiphoton excitation (lower toxicity). • Stable fluorescent emission (MWCNT) with short lifetime. • Exhibit large scattering cross-section and strong resonance Raman scattering. • Can be used for multimodal imaging.	• Generally higher toxicity compared to other nanocarbon materials. • Hydrophobic nature and lack of solubility in most biological medium. • Requires surface modification to control biodistribution, pharmacokinetics and minimize toxicity.
Fullerenes	Targeted imaging and drug delivery	• Cage-like structure to facilitate entrapment of compounds. • Molecularly modifiable for feature engineering.[708] • Well-developed morphology. • Exceptional free radical scavenging ability.	• Weaker fluorescence emission compared to other nanocarbon materials. • Water insoluble and aggregate in aqueous solution. • Require functionalization to improve water solubility and biocompatibility properties.
SWCNH	Targeted imaging and drug delivery	• Large loading capacity for other materials such as contrast agents (for multimodal imaging).	• Weaker fluorescent emission compared to other nanocarbon materials. • Potential metal ion leakage from weak affinity of other agents.
Nanodiamonds	Imaging label	• NIR emission range. • No photobleaching. • No photoblinking. • Fluorescent lifetime > 10 ns. • Higher resolution in 3D molecule imaging, less toxic than CNTs and GOs (for $d < 50$ nm). • Can be used as a Raman label for imaging and drug delivery tracing. • No alteration in fluorescence due to surface modification.	• Limited in vivo toxicity studies, especially those > 100 nm. • Aggregation issue especially for ND less than 50 nm.
C-dots	Imaging label	• Strong fluorescence in UV and visible range. • Better hemocompatibility compared to semiconductor QDs. • Can be prepared from green precursors.	• Insufficient range for *in vivo* imaging (centers around 400-500 nm for strong emitters). • Low PLQY for emission at longer wavelengths. • Lack of understanding on the formation mechanism from different precursors as well as the PL mechanism.

generate effective, biocompatible, and nontoxic nanocarbon materials-based models for cancer theranostics applications.

6. SUMMARY AND FUTURE OUTLOOK

In this comprehensive review, we summarized the sensing, imaging, and drug/gene delivery applications of various nanocarbon materials: graphene and GOs, carbon nanotubes, fullerenes, and carbon nanohorns and graphene nanoribbons, nanodiamonds, and carbon nanodots, while explicitly correlating their physical and chemical properties, toxicity, and biodegradability implications. Table 8 gives a quick summary of the biological applications of various nanocarbon materials with their distinct advantages and limitations.

GO nanosheets with abundant oxygen containing groups can adsorb many biomarkers including ssDNA sequences and peptides through either electrostatic or covalent binding. Thus, they can be suitably employed as flexible sensing nanoplatforms based on their high fluorescent quenching efficiency. Moreover, the PEG-functionalized GOs may serve as intracellular biosensors to monitor the pH variation and π protease activities that are important indicators for disease theranostics. However, it must be noted that the peptide molecules conjugated through noncovalent bindings (i.e., $\pi-\pi$ stacking and electrostatic interaction) to the graphene surface are not stable when dispersed in protein-abundant medium. Therefore, covalent attachment between the graphene nanosheets and target peptide probes is a preferred protocol for intracellular protease monitoring.

For drug delivery applications, it is important to obtain the targeted delivery efficacy through the drug nanocarriers. Conventionally, in vitro and in vivo tracking and monitoring of the effects of delivered drugs are normally achieved with fluorescent dyes as target labels. The fluorescent dyes exhibit photobleaching after a short period excitation time that impede their long-term evaluation of chemo/gene therapy efficiency. SWCNTs, on the other hand, are resistant to the photobleaching effect and can thus be used for continuous Raman scattering and fluorescent imaging labels. By using a laser scanning confocal Raman microscopy, one can clearly monitor and even quantify the cellular distribution and translocation of the antibody-conjugated SWCNT probes. More importantly, both SWCNTs and MWCNTs can be excited in the NIR region (700−1100 nm) through two-photon fluorescence microscopy. The multiphoton imaging shows lower phototoxicity to the biological tissues than that usually induced by single-photon excitation. Moreover, the MWCNTs are shown to be highly stable in the fluorescence emission with a short lifetime less than 100 ps. The short PL decay time of the MWCNTs can be used to distinguish their fluorescence from the traditional fluorophores through lifetime microscopy.

Fullerene nanoparticles are among the first batches of nanocarbon materials used for targeted imaging and drug delivery applications. However, the fluorescent emission from the fullerenes is much weaker compared to those of CNTs, NDs, and CDs. Optimizing the synthesis process of the fullerene nanoparticles can preferably result in strong fluorescent emission in the visible region (400−600 nm). To enhance the therapy efficacy of the fullerene probes as drug carriers, they could be conjugated with other biodegradable porous nanostructures such as poly(L-lactic acid) (PLLA) nanofiber to achieve imaging-guided drug therapy.

Fluorescent emissions from the SWCNHs were generally much weaker compared to those of CNTs, NDs, and CDs. The commonly used approach to enhance their fluorescence effect

DOI: 10.1021/acs.chemrev.9b00099
Chem. Rev. XXXX, XXX, XXX−XXX

is to conjugate them with semiconductor QDs. Because of their large loading capacity, multifunctional CNH probes can be fabricated by coloading the fluorescent QDs, Gd^{3+} containing magnetic resonance agents or iron oxide nanoparticles, and cancer drugs to achieve imaging-guided drug therapy. However, the present surface functionalization methods call for further modifications to strengthen the affinity of QDs to the CNH surface, especially for the complex in vivo biological environment because the leakage of heavy metal ions from the QDs induces severe toxic effects to cells and tissues. Also, the weight ratios between the CNHs and QDs need to be optimized to avoid fluorescent quenching of the QD.

Fluorescent NDs with NV centers are the most extensively studied probes as imaging labels. They have several advantages against the commercial fluorophores such as NIR emission ranging from 600 to 800 nm, no photobleaching and photoblinking, and long fluorescent lifetime longer than 10 ns. These unique properties make them promising candidates for long-term imaging and tracking, both in vitro and in vivo. The fluorescent NDs also exhibit higher resolution in 3D molecule imaging than that of organic dyes. Despite the encouraging performance of NDs in imaging and sensing applications, their in vivo toxicities are sparsely studied, especially for sizes larger than 100 nm. Although several studies have shown that the NDs with diameter less than 50 nm are less toxic than CNTs and GOs, pristine NDs with size larger than 100 nm were observed to kill cancer cells. Therefore, the toxicity of the NDs may vary according to their size, specific cancer models, and the administration approach (oral or intravenous).

Fluorescent C-dots are the newest nanocarbon materials with an average diameter less than 5 nm. They emit the strong fluorescence under UV and visible light excitation, mostly centered at 400−500 nm, which are not long enough for in vivo imaging. The development of new carbon precursors and surface functionalization approaches are still ongoing to fabricate C-dots that would emit at longer wavelengths. Fluorescent mechanisms of C-dots are still under investigation, and it is believed that doping the C-dots with nitrogen atoms could possibly improve their quantum yield. In general, the underlying mechanisms are based on either of the two assumptions: size-dependent quantum effect or degree of surface defects/surface oxidation. Carboxyl groups on the C-dot surface serve as surface states with their energy levels lying between the between π and π^* states. Therefore, the absorption band of C-dots may be attributed to the electron transition between one or more oxygen-containing groups. Interestingly, C-dots have been shown to exhibit a hemolysis rate of 12% at 6 h after injection, much lower than 19.4% in the case of semiconductor QDs at 4 h after injection, which demonstrates their good hemocompatibility for in vivo imaging and drug delivery applications.

Thus, this review highlights the in vitro and in vivo applications of the different nanocarbon materials for cancer theranostics applications. It lays particular emphasis on two design approaches that are essentially important for the development of clinically relevant nanocarbon materials-based theranostic models. The first approach involves the design of hybrid nanocomposites based on nanocarbons and plasmonic nanoparticles such as gold and silver nanoparticles for enhanced sensing/imaging and multifunctional imaging-guided cancer therapy. The second approach comprises multifunctional combinatorial imaging and therapeutic applications based on nanocarbon materials. Most importantly, the five design considerations outlined in this review serve as the key unifying themes that define the foundational principles for researchers to study and generate effective, biocompatible, and nontoxic nanocarbon materials-based models for cancer theranostics applications. The development of these promising nanotechnologies can thus lead us to a concrete pathway for achieving multiple detection and therapies based on functionalized nanocarbon materials.

AUTHOR INFORMATION

Corresponding Authors

*Xiaoyuan Chen: E-mail, shawn.chen@nih.gov.
*Ken-Tye Yong: E-mail, ktyong@ntu.edu.sg.
*Gaixia Xu: E-mail, xugaixia@szu.edu.cn.

ORCID

Kok Ken Chan: 0000-0002-0592-4427
Junle Qu: 0000-0001-7833-4711
Ken-Tye Yong: 0000-0001-7936-2941
Xiaoyuan Chen: 0000-0002-9622-0870

Author Contributions

#N.P. and A.M.S. contributed equally.

Notes

The authors declare no competing financial interest.

Biographies

Nishtha Panwar received her Ph.D. at the Nanyang Technological University (Singapore, 2018) in the area of miniature flow cytometry for applications in cancer theranostics. She graduated in Electrical Engineering at Jamia Millia Islamia (New Delhi, India, 2010) and received her Master's degree in Advanced Instrumentation at CSIR—Central Scientific Instruments Organisation (Chandigarh, India, 2012). She is currently pursuing postdoctoral research at NTU on the use of novel nanomaterials for RNA interference in cancer therapy. She is also exploring organ-on-a-chip studies for evaluating pancreatic cancer theranostics approaches.

Alana M. Soehartono received her B.Sc. (2011) and M.Sc. (2013) degrees in Electrical Engineering from the University of Wisconsin—Milwaukee, and is currently a Ph.D. Candidate at Nanyang Technological University, Singapore, under the supervision of Assoc Prof Ken-Tye Yong. Her research interests include nanomaterials and plasmonics for sensing applications.

Kok Ken Chan received his B. Eng in Electrical and Electronics Engineering from Universiti Tunku Abdul Rahman in 2011, and M. Sc in Power Engineering from Nanyang Technological University in 2012. He is currently a Ph.D. student at the same university under the supervision of Prof Ken-Tye Yong. His research interests include the synthesis, characterization, and applications of novel functional nanomaterials for sensing and biophotonic applications.

Shuwen Zeng received her Ph.D. from the School of Electrical and Electronic Engineering at Nanyang Technological University. She worked as a postdoctoral research fellow at CNRS International-NTU-THALES Research Alliance (CINTRA)/UMI 3288, Singapore. She is the recipient of the Chercheur−Marie Curie Fellow at XLIM, Université de Limoges, France. Her main research interests focus on nanomaterials preparation and their sensing applications.

Gaixia Xu received her Ph.D. in Biomedical Engineering in 2005 from Zhejiang University. From 2005 to 2007, she completed a

DOI: 10.1021/acs.chemrev.9b00099
Chem. Rev. XXXX, XXX, XXX−XXX

postdoctoral fellowship in the Institute of Optoelectronics, Shenzhen University. From 2007 to 2008, she completed a postdoctoral fellowship in the Institute of Laser, Photonics, and Biophotonics, Optoelectronics, State University of New York. She has joined Shenzhen University since 2008 and has been appointed full professor since 2013. Her current research interests include biomedical applications of multimode nanomaterials (CdSe, CdTe, InP, CuS, AIE, black phosphorus) and novel optical imaging methods.

Junle Qu is a Professor in the Center for Biomedical Photonics at Shenzhen University. His current research interests include nonlinear optical imaging, fluorescence lifetime imaging, superresolution optical imaging, and their applications in biomedicine and imaging guided optical therapy. He has published more than 250 papers in peer reviewed journals such as *Nature Photonics*, *Nature Communications*, *Chemical Society Reviews*, *Advanced Materials*, *Chem*, *PNAS*, *Optics Letters*, etc. He is the Fellow of SPIE and the director of Biomedical Photonics Committee of Chinese Optical Society. He serves in the editorial boards of JIOHS, Frontiers of Optoelectronics, etc.

Dr. Philippe Coquet received his doctoral degree in Electrical and Electronic Engineering in 1993 from the University of Rennes 1, France. From 1993 to 1994 he was a postdoctoral researcher at the National Institute of Information and Communications Technology (NiCT) in Tokyo. In 1994 he was appointed Assistant Professor at Ecole Normale Supérieure de Cachan, France. From 2002 to 2005 he was a visiting research fellow at the University of Tokyo in the frame of the Laboratory for Integrated Micro-Mechatronic Systems (LIMMS/CNRS). In 2005 he was appointed Professor at the University of Lille 1 and he joined the Institute for Electronics Microelectronics and Nanotechnology (IEMN/CNRS). In 2012 he has been seconded to CINTRA UMI 3288 in NTU Singapore and he is its director since September 2013 and an Adjunct Professor at the School of Electrical & Electronic Engineering at NTU. His research interests are on micro and nanotechnologies for high frequency and sensors applications. He has contributed to more than 125 publications in international journals and conferences and has filed 6 patents (co-inventor).

Dr. Yong is the Provost's Chair and Associate Professor in Electrical and Electronic Engineering at the Nanyang Technological University. Ken-Tye Yong earned his BS, M. Eng, and Ph.D. from State University of New York at Buffalo, USA. Prior to joining the Nanyang Technological University, he was a Samuel Stroum AACR research fellow, studying nanomedicine field where he engineered multimodal probes for pancreatic cancer detection and targeted gene and drug delivery therapy. He is the Fellow of Royal Society of Chemistry, Fellow of Royal Society of Biology, Overseas Fellow of Royal Society of Medicine, Fellow of Institute of Physics, Fellow of Materials, Minerals and Mining, and a Senior Member of IEEE. Ken-Tye is the recipient of 2017 Beilby Medal and Prize for his research work in using quantum dots and metal nanoparticles for nanomedicine, of 2018 Rosenhain Medal and Prize for his pioneering work in applying TENG devices, 2D materials, and AIE nanoparticles for biophotonics, and of 2018 Distinguished Lecturer Award from the IEEE Photonics Society. Currently, his research group interests include engineering nanomaterials for biophotonic and nanomedicine applications, nanotoxicity and pharmacokinetics of nanoparticles, fabricating miniaturized devices for drug delivery, developing nanosensors for biodetection, and creating devices for nanophotonics studies. Dr. Yong has published more than 195 articles in journals, 7 book chapters and 50 conference papers. He has filed more than 10 patents and some have been licensed.

Xiaoyuan (Shawn) Chen is a Senior Investigator and Chief of the Laboratory of Molecular Imaging and Nanomedicine (LOMIN) at the National Institute of Biomedical Imaging and Bioengineering (NIBIB), NIH. His current research interests include in vitro diagnostics, in vivo molecular imaging, and molecular therapeutics, including nanotheranostics. Dr. Chen has published over 760 peer-reviewed papers (H-index = 129, total citations >60000 based on Google Scholar) and numerous books and book chapters. He is the founding editor of journal *Theranostics* (2017 IF = 8.537).

ACKNOWLEDGMENTS

This work was supported by the Singapore Ministry of Education (grants tier 2 MOE2017-T2-2-002), the NTU-NHG Innovation Collaboration Grant (M4061202.040), the NTU-A*STAR Silicon Technologies, Centre of Excellence (11235100003), NEWRI EDB Funding, the NRF2017-NRF-ANR002-2DPS grant supported by the National Research Foundation, Singapore, and the Intramural Research Program, National Institute of Biomedical Imaging and Bioengineering (NIBIB), National Institutes of Health (NIH).

ABBREVIATIONS USED

HCPT	10-hydroxycamptothecin
MTT	3-(4,5-dimethylthiazol-2-yl)-2,5-diphenyltetrazolium bromide
APTES	3-aminopropyltriethoxysilane
DAPI	4′,6-diaminidino-2-phenylinodole
5-FU	5-fluorouracyl
A	adenine
ATP	adenosine triphosphate
ADH	adipic acid dihydrazide
ALP	alkaline phosphatase
AS	artesunate
AOx	ascorbate oxidases
BDD	boron-doped diamond
Bi_2S_3	bismuth sulfide
BBB	blood−brain barrier
BSA	bovine serum albumin
BP	buckypaper
CPT	camptothecin
CNH	carbon nanohorn
CNTs	carbon nanotubes
CTAB	cetyltrimethylammonium bromide
CRET	chemiluminescence resonance energy transfer
COS	chitooligosaccharide
Ce6	chlorin e6
CDDP	cisplatin
CA	citric acid
CLSM	confocal laser scanning microscopy
CRPs	C-reactive proteins
CVD	chemical vapor deposition
Cy-ALG−PEG	cytamine PEGylated alginate
C	cytosine
DCA−HPCHS	deoxycholic acid modified-hydropropyl chitosan
Gd-DTPA	diethylenetriaminepentaacetic acid gadolinium(III) dihydrogen salt hydrate
DA	dopamine hydrochloride
dsDNAs	double-stranded DNAs
DOX	doxorubicin

DOI: 10.1021/acs.chemrev.9b00099
Chem. Rev. XXXX, XXX, XXX−XXX

EDC	1-ethyl-3-(-3-(dimethylamino)propyl) carbodiimide hydrochloride
NHS	*N*-hydroxysuccinimide
ECL	electrochemiluminescence
EIS	electrolyte−insulator−semiconductor
ELISA	enzyme-linked immunosorbent assay
EPR	enhanced permeability and retention
ECM	extracellular matrix
Fib	fibrinogen
FETs	field-effect transistors
FAM	fluorescein amidite
FITC	fluorescein isothiocyanate
FOC	fluorescein isothiocyanate
FMA	fluorescein *o*-methacrylate
FA	folic acid
FRET	Förster resonance energy transfer
G4-PAMAM	fourth-generation polyamidoamine dendrimer
GCE	glassy carbon electrodes
GTX	gliotoxin
GOx	glucose oxidase
GLDH	glutamate dehydrogenase
GSH	glutathione
Au NPs	gold nanoparticles
AuNRs	gold nanorods
G-FET	graphene field-effect transistor
GNRs	graphene nanoribbons
GS	graphene nanosheet
GO	graphene oxide
GQDs	graphene quantum dots
G-FET	graphene-based field-effect transistor
GFP	green fluorescent protein
G	guanine
HCN	hollow carbon nanospheres
HRP	horseradish peroxidase
HA	hyaluronic acid
HE	hydroethidine
H_2O_2	hydrogen peroxide
HIF-1α	hypoxia-inducible factor 1 alpha
IgE	immunoglobulin E
IONPs	iron oxide nanoparticles
LDH	lactase dehydrogenase
L-cys	L-cysteine
MNPs	magnetite nanoparticles
MMPs	matrix metalloproteases
MSPs	mesoporous silica nanoparticles
MTX	methotrexate
mPEG-NH_2	methoxypolyethylene glycol amine
miR-141	microRNA-141
mAb	monoclonal antibody
MDR1	multidrug resistance gene
nGO	nanographene oxide
NDs	nanodiamonds
NGS	nanographene sheets
NIR	near-infrared
NADH	nicotinamide adenine dinucleotide
N-DNW	nitrogen-doped diamond nanowire
NV	nitrogen vacancy
oxMWCNTs	oxidized multiwall carbon nanotubes
pGOs	PEG-functionalized graphene oxides
PNA	peptide nucleic acid
PBS	phosphate buffered saline
PDT	photodynamic therapy
PEC	photoelectrochemical
PDMAEMA	poly(2-dimethylamino)ethyl methacrylate
PANI−PAMPSA	poly(aniline)−poly(2-acrylamido 2-methylpropanesulfonic acid)
PLA	poly(L-lactide)
PLLA	poly(L-lactide)
PVA	poly(vinyl alcohol)
PAA	poly(acrylic acid)
PAMAM	polyamidoamine
PANI	polyaniline
PEPA	polyene polyamine
PEG	polyethylene glycol
PET	polyethyleneterephthalate
PEI	polyethylenimine
PVP	polyvinylpyrrolidone
PI	propidium iodide
PSA	prostate-specific antigen
QD	quantum dot
RGD	arginine−glycine−aspartic acid
ROS	reactive oxygen species
rGONPs	reduced graphene oxide nanoplatelets
rGO	reduced graphene oxide
RES	reticuloendothelial system
SPCEs	screen-printed carbon electrodes
Ag NCs	silver nanoclusters
ssRNA	single-stranded ribonucleic acid
ssDNA	single-stranded DNA
SWCNHs	single-walled CNHs
SDS-PAGE	sodium dodecyl sulfate polyacrylamide gel electrophoresis
SERS	surface enhanced Raman spectroscopy
SPR	surface plasmon resonance
T	thymine
Tf	transferrin
TGF	transforming growth factor
VOC	volatile organic compounds
XPS	X-ray photoelectron spectroscopy
ZIFs	zeolitic imidazolate frameworks.

REFERENCES

(1) Rosi, N. L.; Mirkin, C. A. Nanostructures in biodiagnostics. *Chem. Rev.* **2005**, *105*, 1547−1562.

(2) Qian, X.; Peng, X.-H.; Ansari, D. O.; Yin-Goen, Q.; Chen, G. Z.; Shin, D. M.; Yang, L.; Young, A. N.; Wang, M. D.; Nie, S. *In vivo* tumor targeting and spectroscopic detection with surface-enhanced Raman nanoparticle tags. *Nat. Biotechnol.* **2008**, *26*, 83−90.

(3) Liu, Z.; Robinson, J. T.; Sun, X.; Dai, H. PEGylated nanographene oxide for delivery of water-insoluble cancer drugs. *J. Am. Chem. Soc.* **2008**, *130*, 10876−108777.

(4) Ye, L.; Yong, K. T.; Liu, L. W.; Roy, I.; Hu, R.; Zhu, J.; Cai, H. X.; Law, W. C.; Liu, J. W.; Wang, K.; Liu, J.; Liu, Y. Q.; Hu, Y. Z.; Zhang, X. H.; Swihart, M. T.; Prasad, P. N. A pilot study in non-human primates shows no adverse response to intravenous injection of quantum dots. *Nat. Nanotechnol.* **2012**, *7*, 453−458.

(5) Zeng, S.; Baillargeat, D.; Ho, H.-P.; Yong, K.-T. Nanomaterials enhanced surface plasmon resonance for biological and chemical sensing applications. *Chem. Soc. Rev.* **2014**, *43*, 3426−3452.

(6) Cheng, C.; Li, S.; Thomas, A.; Kotov, N. A.; Haag, R. Functional Graphene Nanomaterials Based Architectures: Biointeractions, Fabrications, and Emerging Biological Applications. *Chem. Rev.* **2017**, *117*, 1826−1914.

(7) Cai, K.; Wang, A. Z.; Yin, L.; Cheng, J. Bio-nano interface: The impact of biological environment on nanomaterials and their delivery properties. *J. Controlled Release* **2017**, *263*, 211−222.

DOI: 10.1021/acs.chemrev.9b00099
Chem. Rev. XXXX, XXX, XXX−XXX

(8) Xu, G.; Zeng, S.; Zhang, B.; Swihart, M. T.; Yong, K.-T.; Prasad, P. N. New Generation Cadmium-Free Quantum Dots for Biophotonics and Nanomedicine. *Chem. Rev.* **2016**, *116*, 12234−12327.
(9) Cheng, L.; Wang, C.; Feng, L.; Yang, K.; Liu, Z. Functional Nanomaterials for Phototherapies of Cancer. *Chem. Rev.* **2014**, *114*, 10869−10939.
(10) Biju, V. Chemical modifications and bioconjugate reactions of nanomaterials for sensing, imaging, drug delivery and therapy. *Chem. Soc. Rev.* **2014**, *43*, 744−764.
(11) Lim, E.-K.; Kim, T.; Paik, S.; Haam, S.; Huh, Y.-M.; Lee, K. Nanomaterials for Theranostics: Recent Advances and Future Challenges. *Chem. Rev.* **2015**, *115*, 327−394.
(12) Ulbrich, K.; Holá, K.; Šubr, V.; Bakandritsos, A.; Tuček, J.; Zbořil, R. Targeted Drug Delivery with Polymers and Magnetic Nanoparticles: Covalent and Noncovalent Approaches, Release Control, and Clinical Studies. *Chem. Rev.* **2016**, *116*, 5338−5431.
(13) Tibbitt, M. W.; Dahlman, J. E.; Langer, R. Emerging Frontiers in Drug Delivery. *J. Am. Chem. Soc.* **2016**, *138*, 704−717.
(14) Wilhelm, S.; Tavares, A. J.; Dai, Q.; Ohta, S.; Audet, J.; Dvorak, H. F.; Chan, W. C. W. Analysis of nanoparticle delivery to tumours. *Nat. Rev. Mater.* **2016**, *1*, 16014.
(15) Medintz, I. L.; Uyeda, H. T.; Goldman, E. R.; Mattoussi, H. Quantum dot bioconjugates for imaging, labelling and sensing. *Nat. Mater.* **2005**, *4*, 435−446.
(16) Yong, K.-T.; Ding, H.; Roy, I.; Law, W.-C.; Bergey, E. J.; Maitra, A.; Prasad, P. N. Imaging Pancreatic Cancer Using Bioconjugated InP Quantum Dots. *ACS Nano* **2009**, *3*, 502−510.
(17) Efros, A. L.; Nesbitt, D. J. Origin and control of blinking in quantum dots. *Nat. Nanotechnol.* **2016**, *11*, 661−671.
(18) Oh, E.; Liu, R.; Nel, A.; Gemill, K. B.; Bilal, M.; Cohen, Y.; Medintz, I. L. Meta-analysis of cellular toxicity for cadmium-containing quantum dots. *Nat. Nanotechnol.* **2016**, *11*, 479−486.
(19) Zeng, S.; Yong, K.-T.; Roy, I.; Dinh, X.-Q.; Yu, X.; Luan, F. A Review on Functionalized Gold Nanoparticles for Biosensing Applications. *Plasmonics* **2011**, *6*, 491−506.
(20) Cobley, C. M.; Chen, J.; Cho, E. C.; Wang, L. V.; Xia, Y. Gold nanostructures: a class of multifunctional materials for biomedical applications. *Chem. Soc. Rev.* **2011**, *40*, 44−56.
(21) Azubel, M.; Kornberg, R. D. Synthesis of Water-Soluble, Thiolate-Protected Gold Nanoparticles Uniform in Size. *Nano Lett.* **2016**, *16*, 3348−3351.
(22) Ali, M. R. K.; Wu, Y.; Ghosh, D.; Do, B. H.; Chen, K.; Dawson, M. R.; Fang, N.; Sulchek, T. A.; El-Sayed, M. A. Nuclear Membrane-Targeted Gold Nanoparticles Inhibit Cancer Cell Migration and Invasion. *ACS Nano* **2017**, *11*, 3716−3726.
(23) Chen, Y.; Xianyu, Y.; Jiang, X. Surface Modification of Gold Nanoparticles with Small Molecules for Biochemical Analysis. *Acc. Chem. Res.* **2017**, *50*, 310−319.
(24) Liu, Z.; Robinson, J. T.; Tabakman, S. M.; Yang, K.; Dai, H. Carbon materials for drug delivery & cancer therapy. *Mater. Today* **2011**, *14*, 316−323.
(25) Liu, Y.; Dong, X.; Chen, P. Biological and chemical sensors based on graphene materials. *Chem. Soc. Rev.* **2012**, *41*, 2283−2307.
(26) Mendes, R. G.; Bachmatiuk, A.; Buechner, B.; Cuniberti, G.; Ruemmeli, M. H. Carbon nanostructures as multi-functional drug delivery platforms. *J. Mater. Chem. B* **2013**, *1*, 401−428.
(27) Novoselov, K. S.; Geim, A. K.; Morozov, S. V.; Jiang, D.; Zhang, Y.; Dubonos, S. V.; Grigorieva, I. V.; Firsov, A. A. Electric field effect in atomically thin carbon films. *Science* **2004**, *306*, 666−669.
(28) Novoselov, K. S.; Geim, A. K.; Morozov, S. V.; Jiang, D.; Katsnelson, M. I.; Grigorieva, I. V.; Dubonos, S. V.; Firsov, A. A. Two-dimensional gas of massless Dirac fermions in graphene. *Nature* **2005**, *438*, 197−200.
(29) Geim, A. K.; Novoselov, K. S. The rise of graphene. *Nat. Mater.* **2007**, *6*, 183−191.
(30) Geim, A. K. Graphene: Status and Prospects. *Science* **2009**, *324*, 1530−1534.
(31) Allen, M. J.; Tung, V. C.; Kaner, R. B. Honeycomb Carbon: A Review of Graphene. *Chem. Rev.* **2010**, *110*, 132−145.
(32) Compton, O. C.; Nguyen, S. T. Graphene Oxide, Highly Reduced Graphene Oxide, and Graphene: Versatile Building Blocks for Carbon-Based Materials. *Small* **2010**, *6*, 711−723.
(33) Novoselov, K. S.; Fal'ko, V. I.; Colombo, L.; Gellert, P. R.; Schwab, M. G.; Kim, K. A roadmap for graphene. *Nature* **2012**, *490*, 192−200.
(34) Bao, Q.; Loh, K. P. Graphene Photonics, Plasmonics, and Broadband Optoelectronic Devices. *ACS Nano* **2012**, *6*, 3677−3694.
(35) Yang, K.; Feng, L.; Shi, X.; Liu, Z. Nano-graphene in biomedicine: theranostic applications. *Chem. Soc. Rev.* **2013**, *42*, 530−547.
(36) Feng, L.; Wu, L.; Qu, X. New Horizons for Diagnostics and Therapeutic Applications of Graphene and Graphene Oxide. *Adv. Mater. (Weinheim, Ger.)* **2013**, *25*, 168−186.
(37) Castro Neto, A. H.; Guinea, F.; Peres, N. M. R.; Novoselov, K. S.; Geim, A. K. The electronic properties of graphene. *Rev. Mod. Phys.* **2009**, *81*, 109−162.
(38) Wu, L.; Chu, H. S.; Koh, W. S.; Li, E. P. Highly sensitive graphene biosensors based on surface plasmon resonance. *Opt. Express* **2010**, *18*, 14395−14400.
(39) Zeng, S.; Hu, S.; Xia, J.; Anderson, T.; Dinh, X.-Q.; Meng, X.-M.; Coquet, P.; Yong, K.-T. Graphene−MoS_2 hybrid nanostructures enhanced surface plasmon resonance biosensors. *Sens. Actuators, B* **2015**, *207*, 801−810.
(40) Zeng, S.; Sreekanth, K. V.; Shang, J.; Yu, T.; Chen, C.-K.; Yin, F.; Baillargeat, D.; Coquet, P.; Ho, H.-P.; Kabashin, A. V.; Yong, K.-T. Graphene-Gold Metasurface Architectures for Ultrasensitive Plasmonic Biosensing. *Adv. Mater. (Weinheim, Ger.)* **2015**, *27*, 6163−6169.
(41) Giovannetti, G.; Khomyakov, P. A.; Brocks, G.; Karpan, V. M.; van den Brink, J.; Kelly, P. J. Doping Graphene with Metal Contacts. *Phys. Rev. Lett.* **2008**, *101*, 026803.
(42) Georgakilas, V.; Otyepka, M.; Bourlinos, A. B.; Chandra, V.; Kim, N.; Kemp, K. C.; Hobza, P.; Zboril, R.; Kim, K. S. Functionalization of Graphene: Covalent and Non-Covalent Approaches, Derivatives and Applications. *Chem. Rev.* **2012**, *112*, 6156−6214.
(43) Kuila, T.; Bose, S.; Mishra, A. K.; Khanra, P.; Kim, N. H.; Lee, J. H. Chemical functionalization of graphene and its applications. *Prog. Mater. Sci.* **2012**, *57*, 1061−1105.
(44) Goncalves, G.; Vila, M.; Portoles, M.-T.; Vallet-Regi, M.; Gracio, J.; Marques, P. A. A. P. Nano-Graphene Oxide: A Potential Multifunctional Platform for Cancer Therapy. *Adv. Healthcare Mater.* **2013**, *2*, 1072−1090.
(45) Liu, M.; Song, J.; Shuang, S.; Dong, C.; Brennan, J. D.; Li, Y. A Graphene-Based Biosensing Platform Based on the Release of DNA Probes and Rolling Circle Amplification. *ACS Nano* **2014**, *8*, 5564−5573.
(46) Xu, J.-J.; Zhao, W.-W.; Song, S.; Fan, C.; Chen, H.-Y. Functional nanoprobes for ultrasensitive detection of biomolecules: an update. *Chem. Soc. Rev.* **2014**, *43*, 1601−1611.
(47) Sun, X.; Liu, Z.; Welsher, K.; Robinson, J. T.; Goodwin, A.; Zaric, S.; Dai, H. Nano-Graphene Oxide for Cellular Imaging and Drug Delivery. *Nano Res.* **2008**, *1*, 203−212.
(48) Hummers, W. S.; Offeman, R. E. Preparation of graphitic oxide. *J. Am. Chem. Soc.* **1958**, *80*, 1339−1339.
(49) Liu, Z.; Tabakman, S.; Welsher, K.; Dai, H. Carbon Nanotubes in Biology and Medicine: *In vitro* and in vivo Detection, Imaging and Drug Delivery. *Nano Res.* **2009**, *2*, 85−120.
(50) Wong, B. S.; Yoong, S. L.; Jagusiak, A.; Panczyk, T.; Ho, H. K.; Ang, W. H.; Pastorin, G. Carbon nanotubes for delivery of small molecule drugs. *Adv. Drug Delivery Rev.* **2013**, *65*, 1964−2015.
(51) Zhu, S.; Xu, G. Single-walled carbon nanohorns and their applications. *Nanoscale* **2010**, *2*, 2538−2549.
(52) Guerra, J.; Herrero, M. A.; Vazquez, E. Carbon nanohorns as alternative gene delivery vectors. *RSC Adv.* **2014**, *4*, 27315−27321.

DOI: 10.1021/acs.chemrev.9b00099
Chem. Rev. XXXX, XXX, XXX−XXX

(53) Chen, Z.; Ma, L.; Liu, Y.; Chen, C. Applications of Functionalized Fullerenes in Tumor Theranostics. *Theranostics* **2012**, *2*, 238−250.
(54) Shi, J.; Wang, L.; Gao, J.; Liu, Y.; Zhang, J.; Ma, R.; Liu, R.; Zhang, Z. A fullerene-based multi-functional nanoplatform for cancer theranostic applications. *Biomaterials* **2014**, *35*, 5771−5784.
(55) Bolskar, R. D. Gadofullerene MRI contrast agents. *Nanomedicine* **2008**, *3*, 201−213.
(56) Nitta, N.; Seko, A.; Sonoda, A.; Ohta, S.; Tanaka, T.; Takahashi, M.; Murata, K.; Takemura, S.; Sakamoto, T.; Tabata, Y. Is the use of Fullerene in photodynamic therapy effective for atherosclerosis? *Cardiovasc. Intervent. Radiol.* **2008**, *31*, 359−366.
(57) Mody, V. V.; Nounou, M. I.; Bikram, M. Novel nanomedicine-based MRI contrast agents for gynecological malignancies. *Adv. Drug Delivery Rev.* **2009**, *61*, 795−807.
(58) Dellinger, A.; Zhou, Z.; Connor, J.; Madhankumar, A. B.; Pamujula, S.; Sayes, C. M.; Kepley, C. L. Application of fullerenes in nanomedicine: an update. *Nanomedicine* **2013**, *8*, 1191−1208.
(59) Kaur, R.; Badea, I. Nanodiamonds as novel nanomaterials for biomedical applications: drug delivery and imaging systems. *Int. J. Nanomed.* **2013**, *8*, 203−220.
(60) Balasubramanian, G.; Lazariev, A.; Arumugam, S. R.; Duan, D.-w. Nitrogen-Vacancy color center in diamond — emerging nanoscale applications in bioimaging and biosensing. *Curr. Opin. Chem. Biol.* **2014**, *20*, 69−77.
(61) Hsu, T.-C.; Liu, K.-K.; Chang, H.-C.; Hwang, E.; Chao, J.-I. Labeling of neuronal differentiation and neuron cells with biocompatible fluorescent nanodiamonds. *Sci. Rep.* **2015**, *4*, 5004.
(62) Wu, T.-J.; Tzeng, Y.-K.; Chang, W.-W.; Cheng, C.-A.; Kuo, Y.; Chien, C.-H.; Chang, H.-C.; Yu, J. Tracking the engraftment and regenerative capabilities of transplanted lung stem cells using fluorescent nanodiamonds. *Nat. Nanotechnol.* **2013**, *8*, 682−689.
(63) Hola, K.; Zhang, Y.; Wang, Y.; Giannelis, E. P.; Zboril, R.; Rogach, A. L. Carbon dots—Emerging light emitters for bioimaging, cancer therapy and optoelectronics. *Nano Today* **2014**, *9*, 590−603.
(64) Lin, L.; Rong, M.; Luo, F.; Chen, D.; Wang, Y.; Chen, X. Luminescent graphene quantum dots as new fluorescent materials for environmental and biological applications. *TrAC, Trends Anal. Chem.* **2014**, *54*, 83−102.
(65) Miao, P.; Han, K.; Tang, Y.; Wang, B.; Lin, T.; Cheng, W. Recent advances in carbon nanodots: synthesis, properties and biomedical applications. *Nanoscale* **2015**, *7*, 1586−1595.
(66) Lim, S. Y.; Shen, W.; Gao, Z. Carbon quantum dots and their applications. *Chem. Soc. Rev.* **2015**, *44*, 362−381.
(67) Liu, S.; Guo, X. Carbon nanomaterials field-effect-transistor-based biosensors. *NPG Asia Mater.* **2012**, *4*, e23.
(68) Green, N. S.; Norton, M. L. Interactions of DNA with graphene and sensing applications of graphene field-effect transistor devices: A review. *Anal. Chim. Acta* **2015**, *853*, 127−142.
(69) Yang, N.; Chen, X.; Ren, T.; Zhang, P.; Yang, D. Carbon nanotube based biosensors. *Sens. Actuators, B* **2015**, *207*, 690−715.
(70) Chen, H.-C.; Chen, Y.-T.; Tsai, R.-Y.; Chen, M.-C.; Chen, S.-L.; Xiao, M.-C.; Chen, C.-L.; Hua, M.-Y. A sensitive and selective magnetic graphene composite-modified polycrystalline-silicon nanowire field-effect transistor for bladder cancer diagnosis. *Biosens. Bioelectron.* **2015**, *66*, 198−207.
(71) Ping, J.; Zhou, Y.; Wu, Y.; Papper, V.; Boujday, S.; Marks, R. S.; Steele, T. W. J. Recent advances in aptasensors based on graphene and graphene-like nanomaterials. *Biosens. Bioelectron.* **2015**, *64*, 373−385.
(72) Biswas, C.; Lee, Y. H. Graphene Versus Carbon Nanotubes in Electronic Devices. *Adv. Funct. Mater.* **2011**, *21*, 3806−3826.
(73) Meric, I.; Han, M. Y.; Young, A. F.; Ozyilmaz, B.; Kim, P.; Shepard, K. L. Current saturation in zero-bandgap, topgated graphene field-effect transistors. *Nat. Nanotechnol.* **2008**, *3*, 654−659.
(74) Lin, Y.-M.; Dimitrakopoulos, C.; Jenkins, K. A.; Farmer, D. B.; Chiu, H.-Y.; Grill, A.; Avouris, Ph. 100-GHz Transistors from Wafer-Scale Epitaxial Graphene. *Science* **2010**, *327*, 662−662.
(75) Tung, V. C.; Allen, M. J.; Yang, Y.; Kaner, R. B. High-throughput solution processing of large-scale graphene. *Nat. Nanotechnol.* **2009**, *4*, 25−29.
(76) Lee, Y.; Bae, S.; Jang, H.; Jang, S.; Zhu, S.-E.; Sim, S. H.; Song, Y. Il; Hong, B. H.; Ahn, J.-H. Wafer-Scale Synthesis and Transfer of Graphene Films. *Nano Lett.* **2010**, *10*, 490−493.
(77) Tian, H.; Yang, Y.; Xie, D.; Cui, Y.-L.; Mi, W.-T.; Zhang, Y.; Ren, T.-L. Wafer-Scale Integration of Graphene-based Electronic, Optoelectronic and Electroacoustic Devices. *Sci. Rep.* **2015**, *4*, 3598.
(78) Boehm, H. P.; Clauss, A.; Fischer, G. O.; Hofmann, U. Dünnste Kohlenstoff-Folien. *Z. Naturforsch.* **1962**, *17*, 150−153.
(79) Cai, B.; Wang, S.; Huang, L.; Ning, Y.; Zhang, Z.; Zhang, G.-J. Ultrasensitive Label-Free Detection of PNA-DNA Hybridization by Reduced Graphene Oxide Field-Effect Transistor Biosensor. *ACS Nano* **2014**, *8*, 2632−2638.
(80) Ojeda, I.; Garcinuño, B.; Moreno-Guzmán, M.; González-Cortés, A.; Yudasaka, M.; Iijima, S.; Langa, F.; Yáñez-Sedeño, P.; Pingarrón, J. M. Carbon Nanohorns as a Scaffold for the Construction of Disposable Electrochemical Immunosensing Platforms. Application to the Determination of Fibrinogen in Human Plasma and Urine. *Anal. Chem.* **2014**, *86*, 7749−7756.
(81) Yu, C.; Li, X.; Zeng, F.; Zheng, F.; Wu, S. Carbon-Dot-Based Ratiometric Fluorescent Sensor for Detecting Hydrogen Sulfide in Aqueous Media and Inside Live Cells. *Chem. Commun.* **2013**, *49*, 403−405.
(82) Tran, H. V.; Piro, B.; Reisberg, S.; Huy Nguyen, L.; Dung Nguyen, T.; Duc, H. T.; Pham, M. C. An electrochemical ELISA-like immunosensor for miRNAs detection based on screen-printed gold electrodes modified with reduced graphene oxide and carbon nanotubes. *Biosens. Bioelectron.* **2014**, *62*, 25−30.
(83) Chen, D.; Feng, H.; Li, J. Graphene Oxide: Preparation, Functionalization, and Electrochemical Applications. *Chem. Rev.* **2012**, *112*, 6027−6053.
(84) Zhu, S.; Zhang, J.; Zhao, X.-e.; Wang, H.; Xu, G.; You, J. Electrochemical behavior and voltammetric determination of L-tryptophan and L-tyrosine using a glassy carbon electrode modified with single-walled carbon nanohorns. *Microchim. Acta* **2014**, *181*, 445−451.
(85) Valentini, F.; Ciambella, E.; Conte, V.; Sabatini, L.; Ditaranto, N.; Cataldo, F.; Palleschi, G.; Bonchio, M.; Giacalone, F.; Syrgiannis, Z.; Prato, M. Highly selective detection of Epinephrine at oxidized Single-Wall Carbon Nanohorns modified Screen Printed Electrodes (SPEs). *Biosens. Bioelectron.* **2014**, *59*, 94−98.
(86) Wei, Z.; Li, Z.; Sun, X.; Fang, Y.; Liu, J. Synergistic contributions of fullerene, ferrocene, chitosan and ionic liquid towards improved performance for a glucose sensor. *Biosens. Bioelectron.* **2010**, *25*, 1434−1438.
(87) Wu, H.; Fan, S.; Jin, X.; Zhang, H.; Chen, H.; Dai, Z.; Zou, X. Construction of a Zinc Porphyrin-Fullerene-Derivative Based Non-enzymatic Electrochemical Sensor for Sensitive Sensing of Hydrogen Peroxide and Nitrite. *Anal. Chem.* **2014**, *86*, 6285−6290.
(88) Zhang, W.; Patel, K.; Schexnider, A.; Banu, S.; Radadia, A. D. Nanostructuring of Biosensing Electrodes with Nanodiamonds for Antibody Immobilization. *ACS Nano* **2014**, *8*, 1419−1428.
(89) Zhang, M.; Yudasaka, M.; Ajima, K.; Miyawaki, A.; Iijima, S. Light-assisted oxidation of single-wall carbon nanohorns for abundant creation of oxygenated groups that enable chemical modifications with proteins to enhance biocompatibility. *ACS Nano* **2007**, *1*, 265−272.
(90) Jariwala, D.; Sangwan, V. K.; Lauhon, L. J.; Marks, T. J.; Hersam, M. C. Carbon nanomaterials for electronics, optoelectronics, photovoltaics, and sensing. *Chem. Soc. Rev.* **2013**, *42*, 2824−2860.
(91) Wang, W.; Lu, Y.-C.; Huang, H.; Wang, A.-J.; Chen, J.-R.; Feng, J.-J. Facile synthesis of N, S-codoped fluorescent carbon nanodots for fluorescent resonance energy transfer recognition of methotrexate with high sensitivity and selectivity. *Biosens. Bioelectron.* **2015**, *64*, 517−522.
(92) Zhu, S.; Liu, Z.; Hu, L.; Yuan, Y.; Xu, G. Turn-On Fluorescence Sensor Based on Single-Walled-Carbon-Nanohorn-Peptide Complex

DOI: 10.1021/acs.chemrev.9b00099
Chem. Rev. XXXX, XXX, XXX−XXX

for the Detection of Thrombin. *Chem. - Eur. J.* **2012**, *18*, 16556−16561.
(93) Lu, Q.; Hu, H.; Wu, Y.; Chen, S.; Yuan, D.; Yuan, R. An electrogenerated chemiluminescence sensor based on gold nanoparticles@C_{60} hybrid for the determination of phenolic compounds. *Biosens. Bioelectron.* **2014**, *60*, 325−331.
(94) Wang, N.; Wang, L.; Yang, H.; Xiong, T.; Xiao, S.; Zhao, J.; Du, W. Fluorescent Sensors Based on Organic Polymer-Capped Gold Nanoparticles for the Detection of Cr(VI) in Water. *Int. J. Anal. Chem.* **2019**, *2019*, 1756014.
(95) Carter, K. P.; Young, A. M.; Palmer, A. E. Fluorescent Sensors for Measuring Metal Ions in Living Systems. *Chem. Rev.* **2014**, *114*, 4564−601.
(96) Wang, F.; Gu, Z.; Lei, W.; Wang, W.; Xia, X.; Hao, Q. Graphene quantum dots as a fluorescent sensing platform for highly efficient detection of copper(II) ions. *Sens. Actuators, B* **2014**, *190*, 516−522.
(97) Ju, J.; Zhang, R.; He, S.; Chen, W. Nitrogen-doped graphene quantum dots-based fluorescent probe for the sensitive turn-on detection of glutathione and its cellular imaging. *RSC Adv.* **2014**, *4*, 52583−52589.
(98) Afreen, S.; Muthoosamy, K.; Manickam, S.; Hashim, U. Functionalized fullerene (C_{60}) as a potential nanomediator in the fabrication of highly sensitive biosensors. *Biosens. Bioelectron.* **2015**, *63*, 354−364.
(99) Ou, X.; Tan, X.; Wei, S.; Chen, S.; Zhang, J.; Liu, X. Electrochemiluminescence biosensor for cholesterol detection based on AuNPs/L-cys-C_{60} nanocomposites. *Anal. Methods* **2014**, *6*, 3804−3810.
(100) Ermakova, A.; Pramanik, G.; Cai, J. M.; Algara-Siller, G.; Kaiser, U.; Weil, T.; Tzeng, Y. K.; Chang, H. C.; McGuinness, L. P.; Plenio, M. B.; Naydenov, B.; Jelezko, F. Detection of a Few Metallo-Protein Molecules Using Color Centers in Nanodiamonds. *Nano Lett.* **2013**, *13*, 3305−3309.
(101) Lin, C.-T.; Loan, P. T. K.; Chen, T.-Y.; Liu, K.-K.; Chen, C.-H.; Wei, K.-H.; Li, L.-J. Label-Free Electrical Detection of DNA Hybridization on Graphene using Hall Effect Measurements: Revisiting the Sensing Mechanism. *Adv. Funct. Mater.* **2013**, *23*, 2301−2307.
(102) Li, F.; Huang, Y.; Yang, Q.; Zhong, Z.; Li, D.; Wang, L.; Song, S.; Fan, C. A graphene-enhanced molecular beacon for homogeneous DNA detection. *Nanoscale* **2010**, *2*, 1021−1026.
(103) Zhang, M.; Yin, B.-C.; Tan, W.; Ye, B.-C. A versatile graphene-based fluorescence "on/off" switch for multiplex detection of various targets. *Biosens. Bioelectron.* **2011**, *26*, 3260−3265.
(104) He, S.; Song, B.; Li, D.; Zhu, C.; Qi, W.; Wen, Y.; Wang, L.; Song, S.; Fang, H.; Fan, C. A Graphene Nanoprobe for Rapid, Sensitive, and Multicolor Fluorescent DNA Analysis. *Adv. Funct. Mater.* **2010**, *20*, 453−459.
(105) Liu, F.; Choi, J. Y.; Seo, T. S. Graphene oxide arrays for detecting specific DNA hybridization by fluorescence resonance energy transfer. *Biosens. Bioelectron.* **2010**, *25*, 2361−2365.
(106) Xu, Y.; Meng, X.; Liu, J.; Zhu, S.; Sun, L.; Shi, L. New nanoplatforms based on upconversion nanoparticles and single-walled carbon nanohorns for sensitive detection of acute promyelocytic leukemia. *RSC Adv.* **2016**, *6*, 1037−1041.
(107) Reuven, D. G.; Mihiri Shashikala, H. B.; Mandal, S.; Williams, M. N. V.; Chaudhary, J.; Wang, X.-Q. Supramolecular assembly of DNA on graphene nanoribbons. *J. Mater. Chem. B* **2013**, *1*, 3926−3931.
(108) Qiu, W.; Xu, H.; Takalkar, S.; Gurung, A. S.; Liu, B.; Zheng, Y.; Guo, Z.; Baloda, M.; Baryeh, K.; Liu, G. Carbon nanotube-based lateral flow biosensor for sensitive and rapid detection of DNA sequence. *Biosens. Bioelectron.* **2015**, *64*, 367−372.
(109) Qian, Z.; Shan, X.; Chai, L.; Chen, J.; Feng, H. Simultaneous Detection of Multiple DNA Targets by Integrating Dual-Color Graphene Quantum Dot Nanoprobes and Carbon Nanotubes. *Chem. - Eur. J.* **2014**, *20*, 16065−16069.
(110) Thavanathan, J.; Huang, N. M.; Thong, K. L. Colorimetric detection of DNA hybridization based on a dual platform of gold nanoparticles and graphene oxide. *Biosens. Bioelectron.* **2014**, *55*, 91−98.
(111) Shahrokhian, S.; Salimian, R.; Kalhor, H. R. A simple label-free electrochemical DNA biosensor based on carbon nanotube-DNA interaction. *RSC Adv.* **2016**, *6*, 15592−15598.
(112) Lu, C.-H.; Yang, H.-H.; Zhu, C.-L.; Chen, X.; Chen, G.-N. A Graphene Platform for Sensing Biomolecules. *Angew. Chem., Int. Ed.* **2009**, *48*, 4785−4787.
(113) Tao, Y.; Lin, Y.; Huang, Z.; Ren, J.; Qu, X. DNA-templated silver nanoclusters-graphene oxide nanohybrid materials: a platform for label-free and sensitive fluorescence turn-on detection of multiple nucleic acid targets. *Analyst* **2012**, *137*, 2588−2592.
(114) Zhu, S.; Liu, Z.; Zhang, W.; Han, S.; Hu, L.; Xu, G. Nucleic acid detection using single-walled carbon nanohorns as a fluorescent sensing platform. *Chem. Commun.* **2011**, *47*, 6099−6101.
(115) Tian, T.; Li, Z.; Lee, E.-C. Sequence-specific detection of DNA using functionalized graphene as an additive. *Biosens. Bioelectron.* **2014**, *53*, 336−339.
(116) Tao, Y.; Lin, Y.; Ren, J.; Qu, X. Self-assembled, functionalized graphene and DNA as a universal platform for colorimetric assays. *Biomaterials* **2013**, *34*, 4810−4817.
(117) Huang, P.-J. J.; Liu, J. DNA-Length-Dependent Fluorescence Signaling on Graphene Oxide Surface. *Small* **2012**, *8*, 977−983.
(118) Gaillard, C.; Girard, H. A.; Falck, C.; Paget, V.; Simic, V.; Ugolin, N.; Bergonzo, P.; Chevillard, S.; Arnault, J. C. Peptide nucleic acid-nanodiamonds: covalent and stable conjugates for DNA targeting. *RSC Adv.* **2014**, *4*, 3566−3572.
(119) Kang, T.; Choi, H.; Joo, S.-W.; Lee, S. Y.; Yoon, K.-A.; Lee, K. Peptide Nucleic Acid-Mediated Aggregation of Reduced Graphene Oxides and Label-Free Detection of DNA Mutation. *J. Phys. Chem. B* **2014**, *118*, 6297−6301.
(120) Li, F.; Peng, J.; Wang, J.; Tang, H.; Tan, L.; Xie, Q.; Yao, S. Carbon nanotube-based label-free electrochemical biosensor for sensitive detection of miRNA-24. *Biosens. Bioelectron.* **2014**, *54*, 158−164.
(121) Cao, H.; Liu, S.; Tu, W.; Bao, J.; Dai, Z. A carbon nanotube/quantum dot based photoelectrochemical biosensing platform for the direct detection of microRNAs. *Chem. Commun.* **2014**, *50*, 13315−13318.
(122) Chiu, N.-F.; Huang, T.-Y. Sensitivity and kinetic analysis of graphene oxide-based surface plasmon resonance biosensors. *Sens. Actuators, B* **2014**, *197*, 35−42.
(123) Lee, J. S.; Joung, H.-A.; Kim, M.-G.; Park, C. B. Graphene-Based Chemiluminescence Resonance Energy Transfer for Homogeneous Immunoassay. *ACS Nano* **2012**, *6*, 2978−2983.
(124) Lin, Y.; Tao, Y.; Pu, F.; Ren, J.; Qu, X. Combination of Graphene Oxide and Thiol-Activated DNA Metallization for Sensitive Fluorescence Turn-On Detection of Cysteine and Their Use for Logic Gate Operations. *Adv. Funct. Mater.* **2011**, *21*, 4565−4572.
(125) Wu, S.; Lan, X.; Huang, F.; Luo, Z.; Ju, H.; Meng, C.; Duan, C. Selective electrochemical detection of cysteine in complex serum by graphene nanoribbon. *Biosens. Bioelectron.* **2012**, *32*, 293−296.
(126) Wei, W.; Qu, K.; Ren, J.; Qu, X. Chiral detection using reusable fluorescent amylose-functionalized graphene. *Chem. Sci.* **2011**, *2*, 2050−2056.
(127) Shi, Y.; Pan, Y.; Zhang, H.; Zhang, Z.; Li, M.-J.; Yi, C.; Yang, M. A dual-mode nanosensor based on carbon quantum dots and gold nanoparticles for discriminative detection of glutathione in human plasma. *Biosens. Bioelectron.* **2014**, *56*, 39−45.
(128) Zhang, H.; Song, D.; Gao, S.; Zhang, H.; Zhang, J.; Sun, Y. Enhanced wavelength modulation SPR biosensor based on gold nanorods for immunoglobulin detection. *Talanta* **2013**, *115*, 857−862.
(129) Ohno, Y.; Maehashi, K.; Matsumoto, K. Label-Free Biosensors Based on Aptamer-Modified Graphene Field-Effect Transistors. *J. Am. Chem. Soc.* **2010**, *132*, 18012−18013.

DOI: 10.1021/acs.chemrev.9b00099
Chem. Rev. XXXX, XXX, XXX−XXX

(130) Li, L.-L.; Liu, K.-P.; Yang, G.-H.; Wang, C.-M.; Zhang, J.-R.; Zhu, J.-J. Fabrication of Graphene-Quantum Dots Composites for Sensitive Electrogenerated Chemiluminescence Immunosensing. *Adv. Funct. Mater.* **2011**, *21*, 869−878.
(131) Mao, S.; Lu, G.; Yu, K.; Bo, Z.; Chen, J. Specific protein detection using thermally reduced graphene oxide sheet decorated with gold nanoparticle-antibody conjugates. *Adv. Mater.* **2010**, *22*, 3521−3526.
(132) Zhang, H.; Sun, Y.; Gao, S.; Zhang, J.; Zhang, H.; Song, D. Novel Graphene Oxide-Based Surface Plasmon Resonance Biosensor for Immunoassay. *Small* **2013**, *9*, 2537−2540.
(133) Zhang, H.; Song, D.; Gao, S.; Zhang, J.; Zhang, H.; Sun, Y. Novel SPR biosensors based on metal nanoparticles decorated with graphene for immunoassay. *Sens. Actuators, B* **2013**, *188*, 548−554.
(134) Huang, C.-F.; Yao, G.-H.; Liang, R.-P.; Qiu, J.-D. Graphene oxide and dextran capped gold nanoparticles based surface plasmon resonance sensor for sensitive detection of concanavalin A. *Biosens. Bioelectron.* **2013**, *50*, 305−310.
(135) Khatayevich, D.; Page, T.; Gresswell, C.; Hayamizu, Y.; Grady, W.; Sarikaya, M. Selective Detection of Target Proteins by Peptide-Enabled Graphene Biosensor. *Small* **2014**, *10*, 1505−1513.
(136) Zhang, J.; Sun, Y.; Xu, B.; Zhang, H.; Gao, Y.; Zhang, H.; Song, D. A novel surface plasmon resonance biosensor based on graphene oxide decorated with gold nanorod-antibody conjugates for determination of transferrin. *Biosens. Bioelectron.* **2013**, *45*, 230−236.
(137) Jang, H.; Kim, Y.-K.; Kwon, H.-M.; Yeo, W.-S.; Kim, D.-E.; Min, D.-H. A Graphene-Based Platform for the Assay of Duplex-DNA Unwinding by Helicase. *Angew. Chem., Int. Ed.* **2010**, *49*, 5703−5707.
(138) Lu, C.-H.; Li, J.; Qi, X.-J.; Song, X.-R.; Yang, H.-H.; Chen, X.; Chen, G.-N. Multiplex detection of nucleases by a graphene-based platform. *J. Mater. Chem.* **2011**, *21*, 10915−10919.
(139) Wang, H.; Zhang, Q.; Chu, X.; Chen, T.; Ge, J.; Yu, R. Graphene Oxide-Peptide Conjugate as an Intracellular Protease Sensor for Caspase-3 Activation Imaging in Live Cells. *Angew. Chem., Int. Ed.* **2011**, *50*, 7065−7069.
(140) Li, J.; Lu, C.-H.; Yao, Q.-H.; Zhang, X.-L.; Liu, J.-J.; Yang, H.-H.; Chen, G.-N. A graphene oxide platform for energy transfer-based detection of protease activity. *Biosens. Bioelectron.* **2011**, *26*, 3894−3899.
(141) Feng, D.; Zhang, Y.; Feng, T.; Shi, W.; Li, X.; Ma, H. A graphene oxide-peptide fluorescence sensor tailor-made for simple and sensitive detection of matrix metalloproteinase. *Chem. Commun.* **2011**, *47*, 10680−10682.
(142) Zhang, M.; Yin, B.-C.; Wang, X.-F.; Ye, B.-C. Interaction of peptides with graphene oxide and its application for real-time monitoring of protease activity. *Chem. Commun.* **2011**, *47*, 2399−2401.
(143) Zhu, S.; Han, S.; Zhang, L.; Parveen, S.; Xu, G. A novel fluorescent aptasensor based on single-walled carbon nanohorns. *Nanoscale* **2011**, *3*, 4589−4592.
(144) Bhunia, S. K.; Jana, N. R. Peptide-Functionalized Colloidal Graphene *via* Interdigited Bilayer Coating and Fluorescence Turn-on Detection of Enzyme. *ACS Appl. Mater. Interfaces* **2011**, *3*, 3335−3341.
(145) Lee, E. G.; Park, K. M.; Jeong, J. Y.; Lee, S. H.; Baek, J. E.; Lee, H. W.; Jung, J. K.; Chung, B. H. Carbon nanotube-assisted enhancement of surface plasmon resonance signal. *Anal. Biochem.* **2011**, *408*, 206−211.
(146) Li, H.; He, J.; Li, S.; Turner, A. P. F. Electrochemical immunosensor with N-doped graphene-modified electrode for label-free detection of the breast cancer biomarker CA 15−3. *Biosens. Bioelectron.* **2013**, *43*, 25−29.
(147) Zhong, Z.; Wu, W.; Wang, D.; Wang, D.; Shan, J.; Qing, Y.; Zhang, Z. Nanogold-enwrapped graphene nanocomposites as trace labels for sensitivity enhancement of electrochemical immunosensors in clinical immunoassays: Carcinoembryonic antigen as a model. *Biosens. Bioelectron.* **2010**, *25*, 2379−2383.
(148) Tang, J.; Tang, D.; Niessner, R.; Chen, G.; Knopp, D. Magneto-Controlled Graphene Immunosensing Platform for Simultaneous Multiplexed Electrochemical Immunoassay Using Distinguishable Signal Tags. *Anal. Chem.* **2011**, *83*, 5407−5414.
(149) Chen, X.; Jia, X.; Han, J.; Ma, J.; Ma, Z. Electrochemical immunosensor for simultaneous detection of multiplex cancer biomarkers based on graphene nanocomposites. *Biosens. Bioelectron.* **2013**, *50*, 356−361.
(150) Jin, B.; Wang, P.; Mao, H.; Hu, B.; Zhang, H.; Cheng, Z.; Wu, Z.; Bian, X.; Jia, C.; Jing, F.; Jin, Q.; Zhao, J. Multi-nanomaterial electrochemical biosensor based on label-free graphene for detecting cancer biomarkers. *Biosens. Bioelectron.* **2014**, *55*, 464−469.
(151) Hu, W.; He, G.; Zhang, H.; Wu, X.; Li, J.; Zhao, Z.; Qiao, Y.; Lu, Z.; Liu, Y.; Li, C. M. Polydopamine-Functionalization of Graphene Oxide to Enable Dual Signal Amplification for Sensitive Surface Plasmon Resonance Imaging Detection of Biomarker. *Anal. Chem.* **2014**, *86*, 4488−4493.
(152) Wang, X.; Wang, C.; Qu, K.; Song, Y.; Ren, J.; Miyoshi, D.; Sugimoto, N.; Qu, X. Ultrasensitive and Selective Detection of a Prognostic Indicator in Early-Stage Cancer Using Graphene Oxide and Carbon Nanotubes. *Adv. Funct. Mater.* **2010**, *20*, 3967−3971.
(153) Feng, L.; Wu, L.; Wang, J.; Ren, J.; Miyoshi, D.; Sugimoto, N.; Qu, X. Detection of a Prognostic Indicator in Early-Stage Cancer Using Functionalized Graphene-Based Peptide Sensors. *Adv. Mater.* **2012**, *24*, 125−131.
(154) Myung, S.; Solanki, A.; Kim, C.; Park, J.; Kim, K. S.; Lee, K.-B. Graphene-encapsulated nanoparticle-based biosensor for the selective detection of cancer biomarkers. *Adv. Mater.* **2011**, *23*, 2221−2225.
(155) He, Y.; Xing, X.; Tang, H.; Pang, D. Graphene Oxide-Based Fluorescent Biosensor for Protein Detection *via* Terminal Protection of Small-Molecule-Linked DNA. *Small* **2013**, *9*, 2097−2101.
(156) Wu, L.; Wang, J.; Feng, L.; Ren, J.; Wei, W.; Qu, X. Label-Free Ultrasensitive Detection of Human Telomerase Activity Using Porphyrin-Functionalized Graphene and Electrochemiluminescence Technique. *Adv. Mater.* **2012**, *24*, 2447−2452.
(157) Han, J.; Zhuo, Y.; Chai, Y.; Yuan, R.; Xiang, Y.; Zhu, Q.; Liao, N. Multi-labeled functionalized C_{60} nanohybrid as tracing tag for ultrasensitive electrochemical aptasensing. *Biosens. Bioelectron.* **2013**, *46*, 74−79.
(158) Liu, F.; Xiang, G.; Yuan, R.; Chen, X.; Luo, F.; Jiang, D.; Huang, S.; Li, Y.; Pu, X. Procalcitonin sensitive detection based on graphene-gold nanocomposite film sensor platform and single-walled carbon nanohorns/hollow Pt chains complex as signal tags. *Biosens. Bioelectron.* **2014**, *60*, 210−217.
(159) Yang, M.; Javadi, A.; Li, H.; Gong, S. Ultrasensitive immunosensor for the detection of cancer biomarker based on graphene sheet. *Biosens. Bioelectron.* **2010**, *26*, 560−565.
(160) Li, H.; Wei, Q.; He, J.; Li, T.; Zhao, Y.; Cai, Y.; Du, B.; Qian, Z.; Yang, M. Electrochemical immunosensors for cancer biomarker with signal amplification based on ferrocene functionalized iron oxide nanoparticles. *Biosens. Bioelectron.* **2011**, *26*, 3590−3595.
(161) Yang, M.; Javadi, A.; Gong, S. Sensitive electrochemical immunosensor for the detection of cancer biomarker using quantum dot functionalized graphene sheets as labels. *Sens. Actuators, B* **2011**, *155*, 357−360.
(162) Xu, S.; Liu, Y.; Wang, T.; Li, J. Positive Potential Operation of a Cathodic Electrogenerated Chemiluminescence Immunosensor Based on Luminol and Graphene for Cancer Biomarker Detection. *Anal. Chem.* **2011**, *83*, 3817−3823.
(163) Li, T.; Yang, M.; Li, H. Label-free electrochemical detection of cancer marker based on graphene-cobalt hexacyanoferrate nanocomposite. *J. Electroanal. Chem.* **2011**, *655*, 50−55.
(164) Zhang, B.; Li, Q.; Cui, T. Ultra-sensitive suspended graphene nanocomposite cancer sensors with strong suppression of electrical noise. *Biosens. Bioelectron.* **2012**, *31*, 105−109.
(165) Shu, J.; Qiu, Z.; Zhou, Q.; Lin, Y.; Lu, M.; Tang, D. Enzymatic Oxydate-Triggered Self-Illuminated Photoelectrochemical Sensing Platform for Portable Immunoassay Using Digital Multimeter. *Anal. Chem.* **2016**, *88*, 2958−2966.

DOI: 10.1021/acs.chemrev.9b00099
Chem. Rev. XXXX, XXX, XXX−XXX

(166) Kim, D.-J.; Sohn, I. Y.; Jung, J.-H.; Yoon, O. J.; Lee, N. E.; Park, J.-S. Reduced graphene oxide field-effect transistor for label-free femtomolar protein detection. *Biosens. Bioelectron.* **2013**, *41*, 621−626.
(167) Du, D.; Wang, L.; Shao, Y.; Wang, J.; Engelhard, M. H.; Lin, Y. Functionalized Graphene Oxide as a Nanocarrier in a Multienzyme Labeling Amplification Strategy for Ultrasensitive Electrochemical Immunoassay of Phosphorylated p53 (S392). *Anal. Chem.* **2011**, *83*, 746−752.
(168) Li, Q.; Tang, D.; Tang, J.; Su, B.; Chen, G.; Wei, M. Magneto-controlled electrochemical immunosensor for direct detection of squamous cell carcinoma antigen by using serum as supporting electrolyte. *Biosens. Bioelectron.* **2011**, *27*, 153−159.
(169) Liu, M.; Zhao, H.; Quan, X.; Chen, S.; Fan, X. Distance-independent quenching of quantum dots by nanoscale-graphene in self-assembled sandwich immunoassay. *Chem. Commun.* **2010**, *46*, 7909−7911.
(170) Yang, F.; Han, J.; Zhuo, Y.; Yang, Z.; Chai, Y.; Yuan, R. Highly sensitive impedimetric immunosensor based on single-walled carbon nanohorns as labels and bienzyme biocatalyzed precipitation as enhancer for cancer biomarker detection. *Biosens. Bioelectron.* **2014**, *55*, 360−365.
(171) Wei, Q.; Mao, K.; Wu, D.; Dai, Y.; Yang, J.; Du, B.; Yang, M.; Li, H. A novel label-free electrochemical immunosensor based on graphene and thionine nanocomposite. *Sens. Actuators, B* **2010**, *149*, 314−318.
(172) Zhang, B.; Tang, D.; Liu, B.; Chen, H.; Cui, Y.; Chen, G. GoldMag nanocomposite-functionalized graphene sensing platform for one-step electrochemical immunoassay of alpha-fetoprotein. *Biosens. Bioelectron.* **2011**, *28*, 174−180.
(173) Zhao, C.; Lin, D.; Wu, J.; Ding, L.; Ju, H.; Yan, F. Nanogold-Enriched Carbon Nanohorn Label for Sensitive Electrochemical Detection of Biomarker on a Disposable Immunosensor. *Electroanalysis* **2013**, *25*, 1044−1049.
(174) Kwon, O. S.; Park, S. J.; Hong, J.-Y.; Han, A. R.; Lee, J. S.; Lee, J. S.; Oh, J. H.; Jang, J. Flexible FET-Type VEGF Aptasensor Based on Nitrogen-Doped Graphene Converted from Conducting Polymer. *ACS Nano* **2012**, *6*, 1486−1493.
(175) Lin, C.-W.; Wei, K.-C.; Liao, S.-s.; Huang, C.-Y.; Sun, C.-L.; Wu, P.-J.; Lu, Y.-J.; Yang, H.-W.; Ma, C.-C. M. A reusable magnetic graphene oxide-modified biosensor for vascular endothelial growth factor detection in Cancer diagnosis. *Biosens. Bioelectron.* **2015**, *67*, 431−437.
(176) He, Q.; Sudibya, H. G.; Yin, Z.; Wu, S.; Li, H.; Boey, F.; Huang, W.; Chen, P.; Zhang, H. Centimeter-Long and Large-Scale Micropatterns of Reduced Graphene Oxide Films: Fabrication and Sensing Applications. *ACS Nano* **2010**, *4*, 3201−3208.
(177) Liu, Q.; Yan, Y.; Yang, X.; Qian, J.; Cai, J.; Wang, K. Fe_3O_4-functionalized graphene nanoribbons: Preparation, characterization, and improved electrochemical activity. *J. Electroanal. Chem.* **2013**, *704*, 86−89.
(178) Pu, Y.; Zhu, Z.; Han, D.; Liu, H.; Liu, J.; Liao, J.; Zhang, K.; Tan, W. Insulin-binding aptamer-conjugated graphene oxide for insulin detection. *Analyst* **2011**, *136*, 4138−4140.
(179) Wang, Y.; Li, Z.; Hu, D.; Lin, C.-T.; Li, J.; Lin, Y. Aptamer/Graphene Oxide Nanocomplex for in Situ Molecular Probing in Living Cells. *J. Am. Chem. Soc.* **2010**, *132*, 9274−9276.
(180) Xu, S.; Man, B.; Jiang, S.; Yue, W.; Yang, C.; Liu, M.; Chen, C.; Zhang, C. Direct growth of graphene on quartz substrates for label-free detection of adenosine triphosphate. *Nanotechnology* **2014**, *25*, 165702.
(181) Tu, W.; Lei, J.; Ding, L.; Ju, H. Sandwich nanohybrid of single-walled carbon nanohorns-TiO_2-porphyrin for electrocatalysis and amperometric biosensing towards chloramphenicol. *Chem. Commun.* **2009**, *0*, 4227−4229.
(182) Goyal, R. N.; Gupta, V. K.; Chatterjee, S. Fullerene-C_{60}-modified edge plane pyrolytic graphite electrode for the determination of dexamethasone in pharmaceutical formulations and human biological fluids. *Biosens. Bioelectron.* **2009**, *24*, 1649−1654.
(183) Asadian, E.; Shahrokhian, S.; Zad, A. I.; Jokar, E. In-situ electro-polymerization of graphene nanoribbon/polyaniline composite film: Application to sensitive electrochemical detection of dobutamine. *Sens. Actuators, B* **2014**, *196*, 582−588.
(184) Li, Z.; Huang, Y.; Chen, L.; Qin, X.; Huang, Z.; Zhou, Y.; Meng, Y.; Li, J.; Huang, S.; Liu, Y.; Wang, W.; Xie, Q.; Yao, S. Amperometric biosensor for NADH and ethanol based on electro-reduced graphene oxide-polythionine nanocomposite film. *Sens. Actuators, B* **2013**, *181*, 280−287.
(185) Li, C.; Curreli, M.; Lin, H.; Lei, B.; Ishikawa, F. N.; Datar, R.; Cote, R. J.; Thompson, M. E.; Zhou, C. Complementary Detection of Prostate-Specific Antigen Using In_2O_3 Nanowires and Carbon Nanotubes. *J. Am. Chem. Soc.* **2005**, *127*, 12484−12485.
(186) Lanzellotto, C.; Favero, G.; Antonelli, M. L.; Tortolini, C.; Cannistraro, S.; Coppari, E.; Mazzei, F. Nanostructured enzymatic biosensor based on fullerene and gold nanoparticles: Preparation, characterization and analytical applications. *Biosens. Bioelectron.* **2014**, *55*, 430−437.
(187) Zhu, A.; Luo, Z.; Ding, C.; Li, B.; Zhou, S.; Wang, R.; Tian, Y. A two-photon "turn-on" fluorescent probe based on carbon nanodots for imaging and selective biosensing of hydrogen sulfide in live cells and tissues. *Analyst* **2014**, *139*, 1945−1952.
(188) Upan, J.; Reanpang, P.; Chailapakul, O.; Jakmunee, J. Flow injection amperometric sensor with a carbon nanotube modified screen printed electrode for determination of hydroquinone. *Talanta* **2016**, *146*, 766−771.
(189) Zhang, L.; Lei, J.; Zhang, J.; Ding, L.; Ju, H. Amperometric detection of hypoxanthine and xanthine by enzymatic amplification using a gold nanoparticles-carbon nanohorn hybrid as the carrier. *Analyst* **2012**, *137*, 3126−3131.
(190) Labroo, P.; Cui, Y. Flexible graphene bio-nanosensor for lactate. *Biosens. Bioelectron.* **2013**, *41*, 852−856.
(191) Martin, A.; Hernandez-Ferrer, J.; Vazquez, L.; Martinez, M.-T.; Escarpa, A. Controlled chemistry of tailored graphene nanoribbons for electrochemistry: a rational approach to optimizing molecule detection. *RSC Adv.* **2014**, *4*, 132−139.
(192) Chatterjee, J.; Cardenal, J.; Shellikeri, A. Engineered Carbon Nanotube Buckypaper: A Platform for Electrochemical Biosensors. *J. Biomed. Nanotechnol.* **2015**, *11*, 150−156.
(193) Dai, H.; Shi, Y.; Wang, Y.; Sun, Y.; Hu, J.; Ni, P.; Li, Z. A carbon dot based biosensor for melamine detection by fluorescence resonance energy transfer. *Sens. Actuators, B* **2014**, *202*, 201−208.
(194) Gasnier, A.; Laura Pedano, M.; Rubianes, M. D.; Rivas, G. A. Graphene paste electrode: Electrochemical behavior and analytical applications for the quantification of NADH. *Sens. Actuators, B* **2013**, *176*, 921−926.
(195) Ensafi, A. A.; Alinajafi, H. A.; Jafari-Asl, M.; Rezaei, B.; Ghazaei, F. Cobalt ferrite nanoparticles decorated on exfoliated graphene oxide, application for amperometric determination of NADH and H_2O_2. *Mater. Sci. Eng., C* **2016**, *60*, 276−284.
(196) Istrate, O.-M.; Rotariu, L.; Marinescu, V. E.; Bala, C. NADH sensing platform based on electrochemically generated reduced graphene oxide-gold nanoparticles composite stabilized with poly-(allylamine hydrochloride). *Sens. Actuators, B* **2016**, *223*, 697−704.
(197) Dai, H.; Yang, C.; Ma, X.; Lin, Y.; Chen, G. A highly sensitive and selective sensing ECL platform for naringin based on beta-Cyclodextrin functionalized carbon nanohorns. *Chem. Commun.* **2011**, *47*, 11915−11917.
(198) Shalini, J.; Sankaran, K. J.; Lee, C.-Y.; Tai, N.-H.; Lin, I. N. An amperometric urea bisosensor based on covalent immobilization of urease on N_2 incorporated diamond nanowire electrode. *Biosens. Bioelectron.* **2014**, *56*, 64−70.
(199) Siqueira, J. R., Jr.; Molinnus, D.; Beging, S.; Schoening, M. J. Incorporating a Hybrid Urease-Carbon Nanotubes Sensitive Nano-film on Capacitive Field-Effect Sensors for Urea Detection. *Anal. Chem.* **2014**, *86*, 5370−5375.
(200) Zehani, N.; Fortgang, P.; Lachgar, M. S.; Baraket, A.; Arab, M.; Dzyadevych, S. V.; Kherrat, R.; Jaffrezic-Renault, N. Highly sensitive electrochemical biosensor for bisphenol A detection based

DOI: 10.1021/acs.chemrev.9b00099
Chem. Rev. XXXX, XXX, XXX−XXX

on a diazonium-functionalized boron-doped diamond electrode modified with a multi-walled carbon nanotube-tyrosinase hybrid film. *Biosens. Bioelectron.* **2015**, *74*, 830−835.
(201) Dai, H.; Li, Y.; Zhang, S.; Gong, L.; Li, X.; Lin, Y. Delicate photoelectrochemical sensor for folic acid based on carbon nanohorns supported interwoven titanate nanotubes. *Sens. Actuators, B* **2016**, *222*, 120−126.
(202) Qian, Z. S.; Chai, L. J.; Huang, Y. Y.; Tang, C.; Shen, J. J.; Chen, J. R.; Feng, H. A real-time fluorescent assay for the detection of alkaline phosphatase activity based on carbon quantum dots. *Biosens. Bioelectron.* **2015**, *68*, 675−680.
(203) Paimard, G.; Gholivand, M. B.; Shamsipur, M. Determination of ganciclovir as an antiviral drug and its interaction with DNA at Fe3O4/carboxylated multi-walled carbon nanotubes modified glassy carbon electrode. *Measurement* **2016**, *77*, 269−277.
(204) Shoja, Y.; Rafati, A. A.; Ghodsi, J. Glassy carbon electrode modified with horse radish peroxidase/organic nucleophilic-functionalized carbon nanotube composite for enhanced electrocatalytic oxidation and efficient voltammetric sensing of levodopa. *Mater. Sci. Eng., C* **2016**, *58*, 835−845.
(205) Barberis, A.; Spissu, Y.; Fadda, A.; Azara, E.; Bazzu, G.; Marceddu, S.; Angioni, A.; Sanna, D.; Schirra, M.; Serra, P. A. Simultaneous amperometric detection of ascorbic acid and antioxidant capacity in orange, blueberry and kiwi juice, by a telemetric system coupled with a fullerene- or nanotubes-modified ascorbate subtractive biosensor. *Biosens. Bioelectron.* **2015**, *67*, 214−223.
(206) Nag, S.; Duarte, L.; Bertrand, E.; Celton, V.; Castro, M.; Choudhary, V.; Guegan, P.; Feller, J.-F. Ultrasensitive QRS made by supramolecular assembly of functionalized cyclodextrins and graphene for the detection of lung cancer VOC biomarkers. *J. Mater. Chem. B* **2014**, *2*, 6571−6579.
(207) Unnikrishnan, B.; Palanisamy, S.; Chen, S.-M. A simple electrochemical approach to fabricate a glucose biosensor based on graphene-glucose oxidase biocomposite. *Biosens. Bioelectron.* **2013**, *39*, 70−75.
(208) Liang, B.; Fang, L.; Yang, G.; Hu, Y.; Guo, X.; Ye, X. Direct electron transfer glucose biosensor based on glucose oxidase self-assembled on electrochemically reduced carboxyl graphene. *Biosens. Bioelectron.* **2013**, *43*, 131−136.
(209) Mani, V.; Devadas, B.; Chen, S.-M. Direct electrochemistry of glucose oxidase at electrochemically reduced graphene oxide-multiwalled carbon nanotubes hybrid material modified electrode for glucose biosensor. *Biosens. Bioelectron.* **2013**, *41*, 309−315.
(210) Tang, X.; Zhang, B.; Xiao, C.; Zhou, H.; Wang, X.; He, D. Carbon nanotube template synthesis of hierarchical $NiCoO_2$ composite for non-enzyme glucose detection. *Sens. Actuators, B* **2016**, *222*, 232−239.
(211) Terse-Thakoor, T.; Komori, K.; Ramnani, P.; Lee, I.; Mulchandani, A. Electrochemically Functionalized Seamless Three-Dimensional Graphene-Carbon Nanotube Hybrid for Direct Electron Transfer of Glucose Oxidase and Bioelectrocatalysis. *Langmuir* **2015**, *31*, 13054−13061.
(212) Zhao, S.; Wang, T.; Wang, L.; Xu, S. A non-enzymatic glucose amperometric biosensor based on a simple one-step electrodeposition of Cu microdendrites onto single-walled carbon nanohorn-modified electrode. *J. Solid State Electrochem.* **2015**, *19*, 831−839.
(213) Liu, X.; Shi, L.; Niu, W.; Li, H.; Xu, G. Amperometric glucose biosensor based on single-walled carbon nanohorns. *Biosens. Bioelectron.* **2008**, *23*, 1887−1890.
(214) Villalba, P.; Ram, M. K.; Gomez, H.; Kumar, A.; Bhethanabotla, V.; Kumar, A. GOX-functionalized nanodiamond films for electrochemical biosensor. *Mater. Sci. Eng., C* **2011**, *31*, 1115−1120.
(215) Dai, W.; Li, M.; Gao, S.; Li, H.; Li, C.; Xu, S.; Wu, X.; Yang, B. Fabrication of Nickel/nanodiamond/boron-doped diamond electrode for non-enzymatic glucose biosensor. *Electrochim. Acta* **2016**, *187*, 413−421.
(216) Singh, M.; Holzinger, M.; Biloivan, O.; Cosnier, S. 3D-nanostructured scaffold electrodes based on single-walled carbon nanotubes and nanodiamonds for high performance biosensors. *Carbon* **2013**, *61*, 349−356.
(217) Zhong, X.; Yuan, R.; Chai, Y. In situ spontaneous reduction synthesis of spherical Pd@Cys-C_{60} nanoparticles and its application in nonenzymatic glucose biosensors. *Chem. Commun.* **2012**, *48*, 597−599.
(218) Ye, C.; Zhong, X.; Yuan, R.; Chai, Y. A novel ECL biosensor based on C_{60} embedded in tetraoctylammonium bromide for the determination of glucose. *Sens. Actuators, B* **2014**, *199*, 101−107.
(219) Gao, Y.-F.; Yang, T.; Yang, X.-L.; Zhang, Y.-S.; Xiao, B.-L.; Hong, J.; Sheibani, N.; Ghourchian, H.; Hong, T.; Moosavi-Movahedi, A. A. Direct electrochemistry of glucose oxidase and glucose biosensing on a hydroxyl fullerenes modified glassy carbon electrode. *Biosens. Bioelectron.* **2014**, *60*, 30−34.
(220) Li, Y.; Tong, Y.; Cao, R.; Tian, Z.; Yang, B.; Yang, P. *In vivo* enhancement of anticancer therapy using bare or chemotherapeutic drug-bearing nanodiamond particles. *Int. J. Nanomed.* **2014**, *9*, 1065−1082.
(221) Wen, Y.; Xing, F.; He, S.; Song, S.; Wang, L.; Long, Y.; Li, D.; Fan, C. A graphene-based fluorescent nanoprobe for silver(I) ions detection by using graphene oxide and a silver-specific oligonucleotide. *Chem. Commun.* **2010**, *46*, 2596−2598.
(222) Ren, H.; Wang, C.; Zhang, J.; Zhou, X.; Xu, D.; Zheng, J.; Guo, S.; Zhang, J. DNA Cleavage System of Nanosized Graphene Oxide Sheets and Copper Ions. *ACS Nano* **2010**, *4*, 7169−7174.
(223) Liu, M.; Zhao, H.; Chen, S.; Yu, H.; Zhang, Y.; Quan, X. A "turn-on" fluorescent copper biosensor based on DNA cleavage-dependent graphene-quenched DNAzyme. *Biosens. Bioelectron.* **2011**, *26*, 4111−4116.
(224) Zhang, P.; Xue, Z.; Luo, D.; Yu, W.; Guo, Z.; Wang, T. Dual-Peak Electrogenerated Chemiluminescence of Carbon Dots for Iron Ions Detection. *Anal. Chem.* **2014**, *86*, 5620−5623.
(225) Salaam, A. D.; Hwang, P. T. J.; Poonawalla, A.; Green, H. N.; Jun, H.-w.; Dean, D. Nanodiamonds enhance therapeutic efficacy of doxorubicin in treating metastatic hormone-refractory prostate cancer. *Nanotechnology* **2014**, *25*, 425103.
(226) Chan, K. K.; Yang, C.; Chien, Y.-H.; Panwar, N.; Yong, K.-T. A facile synthesis of label-free carbon dots with unique selectivity-tunable characteristics for ferric ion detection and cellular imaging applications. *New J. Chem.* **2019**, *43*, 4734−4744.
(227) Li, M.; Zhou, X.; Ding, W.; Guo, S.; Wu, N. Fluorescent aptamer-functionalized graphene oxide biosensor for label-free detection of mercury(II). *Biosens. Bioelectron.* **2013**, *41*, 889−893.
(228) Zhang, H.; Cui, H. High-density assembly of chemiluminescence functionalized gold nanodots on multiwalled carbon nanotubes and their application as biosensing platforms. *Nanoscale* **2014**, *6*, 2563−2566.
(229) Yan, F.; Zou, Y.; Wang, M.; Mu, X.; Yang, N.; Chen, L. Highly photoluminescent carbon dots-based fluorescent chemosensors for sensitive and selective detection of mercury ions and application of imaging in living cells. *Sens. Actuators, B* **2014**, *192*, 488−495.
(230) Zhai, Y.; Zhu, Z.; Zhu, C.; Ren, J.; Wang, E.; Dong, S. Multifunctional water-soluble luminescent carbon dots for imaging and Hg^{2+} sensing. *J. Mater. Chem. B* **2014**, *2*, 6995−6999.
(231) Cui, X.; Zhu, L.; Wu, J.; Hou, Y.; Wang, P.; Wang, Z.; Yang, M. A fluorescent biosensor based on carbon dots-labeled oligodeoxyribonucleotide and graphene oxide for mercury (II) detection. *Biosens. Bioelectron.* **2015**, *63*, 506−512.
(232) Zhao, X.-H.; Kong, R.-M.; Zhang, X.-B.; Meng, H.-M.; Liu, W.-N.; Tan, W.; Shen, G.-L.; Yu, R.-Q. Graphene-DNAzyme Based Biosensor for Amplified Fluorescence "Turn-On" Detection of Pb^{2+} with a High Selectivity. *Anal. Chem.* **2011**, *83*, 5062−5066.
(233) Li, M.; Zhou, X.; Guo, S.; Wu, N. Detection of lead (II) with a "turn-on" fluorescent biosensor based on energy transfer from CdSe/ZnS quantum dots to graphene oxide. *Biosens. Bioelectron.* **2013**, *43*, 69−74.
(234) Liu, X.; Li, H.; Wang, F.; Zhu, S.; Wang, Y.; Xu, G. Functionalized single-walled carbon nanohorns for electrochemical biosensing. *Biosens. Bioelectron.* **2010**, *25*, 2194−2199.

DOI: 10.1021/acs.chemrev.9b00099
Chem. Rev. XXXX, XXX, XXX−XXX

(235) Gopalan, A. I.; Komathi, S.; Ai Anand, G.; Lee, K.-P. Nanodiamond based sponges with entrapped enzyme: A novel electrochemical probe for hydrogen peroxide. *Biosens. Bioelectron.* **2013**, *46*, 136−141.
(236) Vilian, A. T. E.; Veeramani, V.; Chen, S.-M.; Madhu, R.; Kwak, C. H.; Huh, Y. S.; Han, Y.-K. Immobilization of myoglobin on Au nanoparticle-decorated carbon nanotube/polytyramine composite as a mediator-free H_2O_2 and nitrite biosensor. *Sci. Rep.* **2015**, *5*, 18390.
(237) Yang, X.-L.; Zhang, Y.-S.; Yang, T.; Geng, F.-Y.; Li, D.; Xiao, B.-L.; Hong, J.; Moosavi-Movahedi, A. A.; Ghourchian, H. A soft-template nanostructured peroxidase based on cytochrome c and sodium decyl sulfate and its electrochemical properties on hydroxyl fullerenes modified glassy carbon electrode. *J. Iran. Chem. Soc.* **2016**, *13*, 471−479.
(238) Guo, C. X.; Zheng, X. T.; Lu, Z. S.; Lou, X. W.; Li, C. M. Biointerface by Cell Growth on Layered Graphene-Artificial Peroxidase-Protein Nanostructure for In Situ Quantitative Molecular Detection. *Adv. Mater.* **2010**, *22*, 5164−5167.
(239) Wu, P.; Cai, Z.; Gao, Y.; Zhang, H.; Cai, C. Enhancing the electrochemical reduction of hydrogen peroxide based on nitrogen-doped graphene for measurement of its releasing process from living cells. *Chem. Commun.* **2011**, *47*, 11327−11329.
(240) Wu, X.; Hu, Y.; Jin, J.; Zhou, N.; Wu, P.; Zhang, H.; Cai, C. Electrochemical Approach for Detection of Extracellular Oxygen Released from Erythrocytes Based on Graphene Film Integrated with Laccase and 2,2-Azino-bis(3-ethylbenzothiazoline-6-sulfonic acid). *Anal. Chem.* **2010**, *82*, 3588−3596.
(241) Gao, X.; Ding, C.; Zhu, A.; Tian, Y. Carbon-Dot-Based Ratiometric Fluorescent Probe for Imaging and Biosensing of Superoxide Anion in Live Cells. *Anal. Chem.* **2014**, *86*, 7071−7078.
(242) Zhang, J.; Lei, J.; Xu, C.; Ding, L.; Ju, H. Carbon Nanohorn Sensitized Electrochemical Immunosensor for Rapid Detection of Microcystin-LR. *Anal. Chem.* **2010**, *82*, 1117−1122.
(243) Jung, J. H.; Cheon, D. S.; Liu, F.; Lee, K. B.; Seo, T. S. A Graphene Oxide Based Immuno-biosensor for Pathogen Detection. *Angew. Chem., Int. Ed.* **2010**, *49*, 5708−5711.
(244) Liu, F.; Choi, K. S.; Park, T. J.; Lee, S. Y.; Seo, T. S. Graphene-based electrochemical biosensor for pathogenic virus detection. *BioChip J.* **2011**, *5*, 123−128.
(245) Cohen-Karni, T.; Qing, Q.; Li, Q.; Fang, Y.; Lieber, C. M. Graphene and Nanowire Transistors for Cellular Interfaces and Electrical Recording. *Nano Lett.* **2010**, *10*, 1098−1102.
(246) Hess, L. H.; Jansen, M.; Maybeck, V.; Hauf, M. V.; Seifert, M.; Stutzmann, M.; Sharp, I. D.; Offenhaeusser, A.; Garrido, J. A. Graphene Transistor Arrays for Recording Action Potentials from Electrogenic Cells. *Adv. Mater.* **2011**, *23*, 5045−5049.
(247) Kempaiah, R.; Chung, A.; Maheshwari, V. Graphene as Cellular Interface: Electromechanical Coupling with Cells. *ACS Nano* **2011**, *5*, 6025−6031.
(248) Song, Y.; Chen, Y.; Feng, L.; Ren, J.; Qu, X. Selective and quantitative cancer cell detection using target-directed functionalized graphene and its synergetic peroxidase-like activity. *Chem. Commun.* **2011**, *47*, 4436−4438.
(249) Feng, L.; Chen, Y.; Ren, J.; Qu, X. A graphene functionalized electrochemical aptasensor for selective label-free detection of cancer cells. *Biomaterials* **2011**, *32*, 2930−2937.
(250) Mannoor, M. S.; Tao, H.; Clayton, J. D.; Sengupta, A.; Kaplan, D. L.; Naik, R. R.; Verma, N.; Omenetto, F. G.; McAlpine, M. C. Graphene-based wireless bacteria detection on tooth enamel. *Nat. Commun.* **2012**, *3*, 763.
(251) Abdelhamid, H. N.; Wu, H.-F. Multifunctional graphene magnetic nanosheet decorated with chitosan for highly sensitive detection of pathogenic bacteria. *J. Mater. Chem. B* **2013**, *1*, 3950−3961.
(252) Hernandez, R.; Valles, C.; Benito, A. M.; Maser, W. K.; Xavier Rius, F.; Riu, J. Graphene-based potentiometric biosensor for the immediate detection of living bacteria. *Biosens. Bioelectron.* **2014**, *54*, 553−557.
(253) Mohanty, N.; Berry, V. Graphene-Based Single-Bacterium Resolution Biodevice and DNA Transistor: Interfacing Graphene Derivatives with Nanoscale and Microscale Biocomponents. *Nano Lett.* **2008**, *8*, 4469−4476.
(254) Wan, Y.; Lin, Z.; Zhang, D.; Wang, Y.; Hou, B. Impedimetric immunosensor doped with reduced graphene sheets fabricated by controllable electrodeposition for the non-labelled detection of bacteria. *Biosens. Bioelectron.* **2011**, *26*, 1959−1964.
(255) Kwun, J.; Yun, S.; Park, L.; Lee, J. H. Development of 1,1 '-oxalyldiimidazole chemiluminescent biosensor using the combination of graphene oxide and hairpin aptamer and its application. *Talanta* **2014**, *119*, 262−267.
(256) Pumera, M. Graphene in biosensing. *Mater. Today* **2011**, *14*, 308−315.
(257) Singh, M.; Holzinger, M.; Tabrizian, M.; Winters, S.; Berner, N. C.; Cosnier, S.; Duesberg, G. S. Noncovalently Functionalized Monolayer Graphene for Sensitivity Enhancement of Surface Plasmon Resonance Immunosensors. *J. Am. Chem. Soc.* **2015**, *137*, 2800−2803.
(258) Feng, T.; Qiao, X.; Wang, H.; Sun, Z.; Qi, Y.; Hong, C. An electrochemical immunosensor for simultaneous point-of-care cancer markers based on the host-guest inclusion of β-cyclodextrin-graphene oxide. *J. Mater. Chem. B* **2016**, *4*, 990−996.
(259) Pumera, M. Graphene-Based Nanomaterials and Their Electrochemistry. *Chem. Soc. Rev.* **2010**, *39*, 4146−4157.
(260) Swathi, R. S.; Sebastian, K. L. Resonance energy transfer from a dye molecule to graphene. *J. Chem. Phys.* **2008**, *129*, 054703.
(261) Rodrigo, D.; Limaj, O.; Janner, D.; Etezadi, D.; García de Abajo, F. J.; Pruneri, V.; Altug, H. Mid-infrared plasmonic biosensing with graphene. *Science* **2015**, *349*, 165−168.
(262) Landry, M. P.; Ando, H.; Chen, A. Y.; Cao, J.; Kottadiel, V. I.; Chio, L.; Yang, D.; Dong, J.; Lu, T. K.; Strano, M. S. Single-Molecule Detection of Protein Efflux From Microorganisms Using Fluorescent Single-Walled Carbon Nanotube Sensor Arrays. *Nat. Nanotechnol.* **2017**, *12*, 368−377.
(263) Chechetka, S. A.; Zhang, M.; Yudasaka, M.; Miyako, E. Physicochemically functionalized carbon nanohorns for multi-dimensional cancer elimination. *Carbon* **2016**, *97*, 45−53.
(264) Purbia, R.; Paria, S. A simple turn on fluorescent sensor for the selective detection of thiamine using coconut water derived luminescent carbon dots. *Biosens. Bioelectron.* **2016**, *79*, 467−475.
(265) Loo, A. H.; Sofer, Z.; Bouša, D.; Ulbrich, P.; Bonanni, A.; Pumera, M. Carboxylic Carbon Quantum Dots as a Fluorescent Sensing Platform for DNA Detection. *ACS Appl. Mater. Interfaces* **2016**, *8*, 1951−1957.
(266) Huang, H.; Bai, W.; Dong, C.; Guo, R.; Liu, Z. An ultrasensitive electrochemical DNA biosensor based on graphene/Au nanorod/polythionine for human papillomavirus DNA detection. *Biosens. Bioelectron.* **2015**, *68*, 442−446.
(267) Urbanová, V.; Holá, K.; Bourlinos, A. B.; Čépe, K.; Ambrosi, A.; Loo, A. H.; Pumera, M.; Karlický, F.; Otyepka, M.; Zbořil, R. Thiofluorographene−Hydrophilic Graphene Derivative with Semiconducting and Genosensing Properties. *Adv. Mater.* **2015**, *27*, 2305−2310.
(268) Wang, J.; Shi, A.; Fang, X.; Han, X.; Zhang, Y. An ultrasensitive supersandwich electrochemical DNA biosensor based on gold nanoparticles decorated reduced graphene oxide. *Anal. Biochem.* **2015**, *469*, 71−75.
(269) Li, H.; Wen, J.; Yu, R.; Meng, J.; Wang, C.; Wang, C.; Sun, S. Facile synthesis of a nanocomposite based on graphene and ZnAl layered double hydroxides as a portable shelf of a luminescent sensor for DNA detection. *RSC Adv.* **2015**, *5*, 9341−9347.
(270) Wei, W.; Gao, C.; Xiong, Y.; Zhang, Y.; Liu, S.; Pu, Y. A fluorescence method for detection of DNA and DNA methylation based on graphene oxide and restriction endonuclease HpaII. *Talanta* **2015**, *131*, 342−347.
(271) Lu, C.-H.; Li, J.; Liu, J.-J.; Yang, H.-H.; Chen, X.; Chen, G.-N. Increasing the sensitivity and single-base mismatch selectivity of the molecular beacon using graphene oxide as the "nanoquencher". *Chem. - Eur. J.* **2010**, *16*, 4889−4894.

DOI: 10.1021/acs.chemrev.9b00099
Chem. Rev. XXXX, XXX, XXX−XXX

(272) Hong, C.; Kim, D.-M.; Baek, A.; Chung, H.; Jung, W.; Kim, D.-E. Fluorescence-based detection of single-nucleotide changes in RNA using graphene oxide and DNAzyme. *Chem. Commun.* **2015**, *51*, 5641−5644.
(273) Zhu, D.; Zhang, L.; Ma, W.; Lu, S.; Xing, X. Detection of microRNA in clinical tumor samples by isothermal enzyme-free amplification and label-free graphene oxide-based SYBR Green I fluorescence platform. *Biosens. Bioelectron.* **2015**, *65*, 152−158.
(274) Ji, L.; Qian, Y.; Wu, P.; Zhang, H.; Cai, C. Fluorescence quenching of graphene oxide combined with the site-specific cleavage of restriction endonuclease for deoxyribonucleic acid demethylase activity assay. *Anal. Chim. Acta* **2015**, *869*, 74−80.
(275) Yan, F.; Zhang, M.; Li, J. Solution-gated graphene transistors for chemical and biological sensors. *Adv. Healthcare Mater.* **2014**, *3*, 313−331.
(276) Xu, G.; Abbott, J.; Qin, L.; Yeung, K. Y. M.; Song, Y.; Yoon, H.; Kong, J.; Ham, D. Electrophoretic and field-effect graphene for all-electrical DNA array technology. *Nat. Commun.* **2014**, *5*, 4866.
(277) Kakatkar, A.; Abhilash, T. S.; Alba, R. D.; Parpia, J. M.; Craighead, H. G. Detection of DNA and poly-l-lysine using CVD graphene-channel FET biosensors. *Nanotechnology* **2015**, *26*, 125502.
(278) Justino, C. I. L.; Rocha-Santos, T. A. P.; Duarte, A. C.; Rocha-Santos, T. A. P. Advances in point-of-care technologies with biosensors based on carbon nanotubes. *Trends Anal. Chem.* **2013**, *45*, 24−36.
(279) Guo, X. Single-Molecule Electrical Biosensors Based on Single-Walled Carbon Nanotubes. *Adv. Mater.* **2013**, *25*, 3397−3408.
(280) Shen, P.; Xia, Y. Synthesis-Modification Integration: One-Step Fabrication of Boronic Acid Functionalized Carbon Dots for Fluorescent Blood Sugar Sensing. *Anal. Chem.* **2014**, *86*, 5323−5329.
(281) Carbone, M.; Gorton, L.; Antiochia, R. An Overview of the Latest Graphene-Based Sensors for Glucose Detection: the Effects of Graphene Defects. *Electroanalysis* **2015**, *27*, 16−31.
(282) Martínez-García, G.; Agüí, L.; Yáñez-Sedeño, P.; Pingarrón, J. M. Multiplexed electrochemical immunosensing of obesity-related hormones at grafted graphene-modified electrodes. *Electrochim. Acta* **2016**, *202*, 209−215.
(283) Song, Y.; Luo, Y.; Zhu, C.; Li, H.; Du, D.; Lin, Y. Recent advances in electrochemical biosensors based on graphene two-dimensional nanomaterials. *Biosens. Bioelectron.* **2016**, *76*, 195−212.
(284) Gavalas, V. G.; Chaniotakis, N. A. 60 Fullerene-mediated amperometric biosensors. *Anal. Chim. Acta* **2000**, *409*, 131−135.
(285) Calvaresi, M.; Zerbetto, F. Baiting Proteins with C_{60}. *ACS Nano* **2010**, *4*, 2283−2299.
(286) Balasubramanian, K.; Kern, K. 25th Anniversary Article: Label-Free Electrical Biodetection Using Carbon Nanostructures. *Adv. Mater.* **2014**, *26*, 1154−1175.
(287) Nebel, C. E.; Rezek, B.; Shin, D.; Uetsuka, H.; Yang, N. Diamond for bio-sensor applications. *J. Phys. D: Appl. Phys.* **2007**, *40*, 6443−6466.
(288) Szunerits, S.; Nebel, C. E.; Hamers, R. J. Surface functionalization and biological applications of CVD diamond. *MRS Bull.* **2014**, *39*, 517−524.
(289) Magyar, A.; Hu, W.; Shanley, T.; Flatte, M. E.; Hu, E.; Aharonovich, I. Synthesis of luminescent europium defects in diamond. *Nat. Commun.* **2014**, *5*, 3523.
(290) Shu, Y.; Lu, J.; Mao, Q.-X.; Song, R.-S.; Wang, X.-Y.; Chen, X.-W.; Wang, J.-H. Ionic liquid mediated organophilic carbon dots for drug delivery and bioimaging. *Carbon* **2017**, *114*, 324−333.
(291) Russier, J.; Oudjedi, L.; Piponnier, M.; Bussy, C.; Prato, M.; Kostarelos, K.; Lounis, B.; Bianco, A.; Cognet, L. Direct visualization of carbon nanotube degradation in primary cells by photothermal imaging. *Nanoscale* **2017**, *9*, 4642−4645.
(292) Chen, X.; Zhang, W. Diamond nanostructures for drug delivery, bioimaging, and biosensing. *Chem. Soc. Rev.* **2017**, *46*, 734−760.
(293) Goryacheva, I. Y.; Sapelkin, A. V.; Sukhorukov, G. B. Carbon nanodots: Mechanisms of photoluminescence and principles of application. *TrAC, Trends Anal. Chem.* **2017**, *90*, 27−37.
(294) Chen, M.; Qin, X.; Zeng, G. Biodegradation of Carbon Nanotubes, Graphene, and Their Derivatives. *Trends Biotechnol.* **2017**, *35*, 836−846.
(295) Merson, T. D.; Castelletto, S.; Aharonovich, I.; Turbic, A.; Kilpatrick, T. J.; Turnley, A. M. Nanodiamonds with silicon vacancy defects for nontoxic photostable fluorescent labeling of neural precursor cells. *Opt. Lett.* **2013**, *38*, 4170−4173.
(296) Gokhale, R.; Singh, P. Blue Luminescent Graphene Quantum Dots by Photochemical Stitching of Small Aromatic Molecules: Fluorescent Nanoprobes in Cellular Imaging. *Part. Part. Syst. Charact.* **2014**, *31*, 433−438.
(297) Gong, J.; An, X.; Yan, X. A novel rapid and green synthesis of highly luminescent carbon dots with good biocompatibility for cell imaging. *New J. Chem.* **2014**, *38*, 1376−1379.
(298) Yu, S. J.; Kang, M. W.; Chang, H. C.; Chen, K. M.; Yu, Y. C. Bright fluorescent nanodiamonds: No photobleaching and low cytotoxicity. *J. Am. Chem. Soc.* **2005**, *127*, 17604−17605.
(299) Smith, B. R.; Niebert, M.; Plakhotnik, T.; Zvyagin, A. V. Transfection and imaging of diamond nanocrystals as scattering optical labels. *J. Lumin.* **2007**, *127*, 260−263.
(300) Fang, C.-Y.; Vaijayanthimala, V.; Cheng, C.-A.; Yeh, S.-H.; Chang, C.-F.; Li, C.-L.; Chang, H.-C. The Exocytosis of Fluorescent Nanodiamond and Its Use as a Long-Term Cell Tracker. *Small* **2011**, *7*, 3363−3370.
(301) Lien, Z.-Y.; Hsu, T.-C.; Liu, K.-K.; Liao, W.-S.; Hwang, K.-C.; Chao, J.-I. Cancer cell labeling and tracking using fluorescent and magnetic nanodiamond. *Biomaterials* **2012**, *33*, 6172−6185.
(302) Bajaj, P.; Mikoryak, C.; Wang, R.; Bushdiecker, D. K., II; Memon, P.; Draper, R. K.; Dieckmann, G. R.; Pantano, P.; Musselman, I. H. A carbon nanotube-based Raman-imaging immunoassay for evaluating tumor targeting ligands. *Analyst* **2014**, *139*, 3069−3076.
(303) Liu, K.; Zhang, J.-J.; Cheng, F.-F.; Zheng, T.-T.; Wang, C.; Zhu, J.-J. Green and facile synthesis of highly biocompatible graphene nanosheets and its application for cellular imaging and drug delivery. *J. Mater. Chem.* **2011**, *21*, 12034−12040.
(304) Wang, H.; Wang, Z.; Ye, M.; Zong, S.; Li, M.; Chen, P.; Ma, X.; Cui, Y. Optically encoded nanoprobes using single walled carbon nanotube as the building scaffold for magnetic field guided cell imaging. *Talanta* **2014**, *119*, 144−150.
(305) Roy, P.; Periasamy, A. P.; Lin, C.-Y.; Her, G.-M.; Chiu, W.-J.; Li, C.-L.; Shu, C.-L.; Huang, C.-C.; Liang, C.-T.; Chang, H.-T. Photoluminescent Graphene Quantum Dots for in vivo Imaging of Apoptotic Cells. *Nanoscale* **2015**, *7*, 2504−2510.
(306) Wang, Z.; Fu, B.; Zou, S.; Duan, B.; Chang, C.; Yang, B.; Zhou, X.; Zhang, L. Facile construction of carbon dots *via* acid catalytic hydrothermal method and their application for target imaging of cancer cells. *Nano Res.* **2016**, *9*, 214−223.
(307) Zhang, X.-Q.; Lam, R.; Xu, X.; Chow, E. K.; Kim, H.-J.; Ho, D. Multimodal Nanodiamond Drug Delivery Carriers for Selective Targeting, Imaging, and Enhanced Chemotherapeutic Efficacy. *Adv. Mater.* **2011**, *23*, 4770−4775.
(308) Whitney, J.; DeWitt, M.; Whited, B. M.; Carswell, W.; Simon, A.; Rylander, C. G.; Rylander, M. N. 3D viability imaging of tumor phantoms treated with single-walled carbon nanohorns and photothermal therapy. *Nanotechnology* **2013**, *24*, 275102.
(309) Zimmermann, K. A.; Inglefield, D. L.; Zhang, J.; Dorn, H. C.; Long, T. E.; Rylander, C. G.; Rylander, M. N. Single-walled carbon nanohorns decorated with semiconductor quantum dots to evaluate intracellular transport. *J. Nanopart. Res.* **2014**, *16*, 2078.
(310) Pramanik, A.; Chavva, S. R.; Fan, Z.; Sinha, S. S.; Nellore, B. P. V.; Ray, P. C. Extremely High Two-Photon Absorbing Graphene Oxide for Imaging of Tumor Cells in the Second Biological Window. *J. Phys. Chem. Lett.* **2014**, *5*, 2150−2154.
(311) Peng, C.; Hu, W.; Zhou, Y.; Fan, C.; Huang, Q. Intracellular Imaging with a Graphene-Based Fluorescent Probe. *Small* **2010**, *6*, 1686−1692.
(312) Chen, W.; Yi, P.; Zhang, Y.; Zhang, L.; Deng, Z.; Zhang, Z. Composites of Aminodextran-Coated Fe_3O_4 Nanoparticles and

DOI: 10.1021/acs.chemrev.9b00099
Chem. Rev. XXXX, XXX, XXX−XXX

Graphene Oxide for Cellular Magnetic Resonance Imaging. *ACS Appl. Mater. Interfaces* **2011**, *3*, 4085−4091.
(313) Liu, Q.; Wei, L.; Wang, J.; Peng, F.; Luo, D.; Cui, R.; Niu, Y.; Qin, X.; Liu, Y.; Sun, H.; Yang, J.; Li, Y. Cell imaging by graphene oxide based on surface enhanced Raman scattering. *Nanoscale* **2012**, *4*, 7084−7089.
(314) Gollavelli, G.; Ling, Y.-C. Multi-functional graphene as an in vitro and in vivo imaging probe. *Biomaterials* **2012**, *33*, 2532−2545.
(315) Qian, J.; Wang, D.; Cai, F.-H.; Xi, W.; Peng, L.; Zhu, Z.-F.; He, H.; Hu, M.-L.; He, S. Observation of Multiphoton-Induced Fluorescence from Graphene Oxide Nanoparticles and Applications in *In vivo* Functional Bioimaging. *Angew. Chem., Int. Ed.* **2012**, *51*, 10570−10575.
(316) Mao, X.; Li, H. Chiral imaging in living cells with functionalized graphene oxide. *J. Mater. Chem. B* **2013**, *1*, 4267−4272.
(317) Wang, Y.-W.; Fu, Y.-Y.; Peng, Q.; Guo, S.-S.; Liu, G.; Li, J.; Yang, H.-H.; Chen, G.-N. Dye-enhanced graphene oxide for photothermal therapy and photoacoustic imaging. *J. Mater. Chem. B* **2013**, *1*, 5762−5767.
(318) Liu, Z.; Guo, Z.; Zhong, H.; Qin, X.; Wan, M.; Yang, B. Graphene oxide based surface-enhanced Raman scattering probes for cancer cell imaging. *Phys. Chem. Chem. Phys.* **2013**, *15*, 2961−2966.
(319) Ma, X.; Qu, Q.; Zhao, Y.; Luo, Z.; Zhao, Y.; Ng, K. W.; Zhao, Y. Graphene oxide wrapped gold nanoparticles for intracellular Raman imaging and drug delivery. *J. Mater. Chem. B* **2013**, *1*, 6495−6500.
(320) Chen, M.-L.; He, Y.-J.; Chen, X.-W.; Wang, J.-H. Quantum-Dot-Conjugated Graphene as a Probe for Simultaneous Cancer-Targeted Fluorescent Imaging, Tracking, and Monitoring Drug Delivery. *Bioconjugate Chem.* **2013**, *24*, 387−397.
(321) Chang, Y.-R.; Lee, H.-Y.; Chen, K.; Chang, C.-C.; Tsai, D.-S.; Fu, C.-C.; Lim, T.-S.; Tzeng, Y.-K.; Fang, C.-Y.; Han, C.-C.; Chang, H.-C.; Fann, W. Mass production and dynamic imaging of fluorescent nanodiamonds. *Nat. Nanotechnol.* **2008**, *3*, 284−288.
(322) Chang, I. P.; Hwang, K. C.; Chiang, C.-S. Preparation of Fluorescent Magnetic Nanodiamonds and Cellular Imaging. *J. Am. Chem. Soc.* **2008**, *130*, 15476−15481.
(323) Fu, C.-C.; Lee, H.-Y.; Chen, K.; Lim, T.-S.; Wu, H.-Y.; Lin, P.-K.; Wei, P.-K.; Tsao, P.-H.; Chang, H.-C.; Fann, W. Characterization and application of single fluorescent nanodiamonds as cellular biomarkers. *Proc. Natl. Acad. Sci. U. S. A.* **2007**, *104*, 727−732.
(324) Faklaris, O.; Garrot, D.; Joshi, V.; Druon, F.; Boudou, J.-P.; Sauvage, T.; Georges, P.; Curmi, P. A.; Treussart, F. Detection of Single Photoluminescent Diamond Nanoparticles in Cells and Study of the Internalization Pathway. *Small* **2008**, *4*, 2236−2239.
(325) Faklaris, O.; Joshi, V.; Irinopoulou, T.; Tauc, P.; Sennour, M.; Girard, H.; Gesset, C.; Arnault, J.-C.; Thorel, A.; Boudou, J.-P.; Curmi, P. A.; Treussart, F. Photoluminescent Diamond Nanoparticles for Cell Labeling: Study of the Uptake Mechanism in Mammalian Cells. *ACS Nano* **2009**, *3*, 3955−3962.
(326) Weng, M.-F.; Chiang, S.-Y.; Wang, N.-S.; Niu, H. Fluorescent nanodiamonds for specifically targeted bioimaging: Application to the interaction of transferrin with transferrin receptor. *Diamond Relat. Mater.* **2009**, *18*, 587−591.
(327) Mkandawire, M.; Pohl, A.; Gubarevich, T.; Lapina, V.; Appelhans, D.; Roedel, G.; Pompe, W.; Schreiber, J.; Opitz, J. Selective targeting of green fluorescent nanodiamond conjugates to mitochondria in HeLa cells. *J. Biophotonics* **2009**, *2*, 596−606.
(328) McGuinness, L. P.; Yan, Y.; Stacey, A.; Simpson, D. A.; Hall, L. T.; Maclaurin, D.; Prawer, S.; Mulvaney, P.; Wrachtrup, J.; Caruso, F.; Scholten, R. E.; Hollenberg, L. C. L. Quantum measurement and orientation tracking of fluorescent nanodiamonds inside living cells. *Nat. Nanotechnol.* **2011**, *6*, 358−363.
(329) Tzeng, Y.-K.; Faklaris, O.; Chang, B.-M.; Kuo, Y.; Hsu, J.-H.; Chang, H.-C. Superresolution Imaging of Albumin-Conjugated Fluorescent Nanodiamonds in Cells by Stimulated Emission Depletion. *Angew. Chem., Int. Ed.* **2011**, *50*, 2262−2265.
(330) Nawa, Y.; Inami, W.; Lin, S.; Kawata, Y.; Terakawa, S.; Fang, C.-Y.; Chang, H.-C. Multi-Color Imaging of Fluorescent Nanodiamonds in Living HeLa Cells Using Direct Electron-Beam Excitation. *ChemPhysChem* **2014**, *15*, 721−726.
(331) Li, J.; He, Z.; Guo, C.; Wang, L.; Xu, S. Synthesis of carbon nanohorns/chitosan/quantum dots nanocomposite and its applications in cells labeling and in vivo imaging. *J. Lumin.* **2014**, *145*, 74−80.
(332) Hsiao, W. W.-W.; Hui, Y. Y.; Tsai, P.-C.; Chang, H.-C. Fluorescent Nanodiamond: A Versatile Tool for Long-Term Cell Tracking, Super-Resolution Imaging, and Nanoscale Temperature Sensing. *Acc. Chem. Res.* **2016**, *49*, 400−407.
(333) Huang, Y.-F.; Zhou, X.; Zhou, R.; Zhang, H.; Kang, K.-B.; Zhao, M.; Peng, Y.; Wang, Q.; Zhang, H.-L.; Qiu, W.-Y. One-pot synthesis of highly luminescent carbon quantum dots and their nontoxic ingestion by zebrafish for in vivo imaging. *Chem. - Eur. J.* **2014**, *20*, 5640−5648.
(334) Wang, X.; Sun, X.; Lao, J.; He, H.; Cheng, T.; Wang, M.; Wang, S.; Huang, F. Multifunctional graphene quantum dots for simultaneous targeted cellular imaging and drug delivery. *Colloids Surf., B* **2014**, *122*, 638−644.
(335) Huang, C.-L.; Huang, C.-C.; Mai, F.-D.; Yen, C.-L.; Tzing, S.-H.; Hsieh, H.-T.; Ling, Y.-C.; Chang, J.-Y. Application of paramagnetic graphene quantum dots as a platform for simultaneous dual-modality bioimaging and tumor-targeted drug delivery. *J. Mater. Chem. B* **2015**, *3*, 651−664.
(336) Zhou, L.; Zhou, L.; Ge, X.; Zhou, J.; Wei, S.; Shen, J. Multicolor imaging and the anticancer effect of a bifunctional silica nanosystem based on the complex of graphene quantum dots and hypocrellin A. *Chem. Commun.* **2015**, *51*, 421−424.
(337) Chandra, A.; Deshpande, S.; Shinde, D. B.; Pillai, V. K.; Singh, N. Mitigating the Cytotoxicity of Graphene Quantum Dots and Enhancing Their Applications in Bioimaging and Drug Delivery. *ACS Macro Lett.* **2014**, *3*, 1064−1068.
(338) Wang, W.; Lu, Y.-C.; Huang, H.; Feng, J.-J.; Chen, J.-R.; Wang, A.-J. Facile synthesis of water-soluble and biocompatible fluorescent nitrogen-doped carbon dots for cell imaging. *Analyst* **2014**, *139*, 1692−1696.
(339) Xu, Z.-Q.; Yang, L.-Y.; Fan, X.-Y.; Jin, J.-C.; Mei, J.; Peng, W.; Jiang, F.-L.; Xiao, Q.; Liu, Y. Low temperature synthesis of highly stable phosphate functionalized two color carbon nanodots and their application in cell imaging. *Carbon* **2014**, *66*, 351−360.
(340) Ding, H.; Zhang, P.; Wang, T.-Y.; Kong, J.-L.; Xiong, H.-M. Nitrogen-doped carbon dots derived from polyvinyl pyrrolidone and their multicolor cell imaging. *Nanotechnology* **2014**, *25*, 205604.
(341) Mewada, A.; Pandey, S.; Thakur, M.; Jadhav, D.; Sharon, M. Swarming carbon dots for folic acid mediated delivery of doxorubicin and biological imaging. *J. Mater. Chem. B* **2014**, *2*, 698−705.
(342) Chowdhury, S. M.; Surhland, C.; Sanchez, Z.; Chaudhary, P.; Suresh Kumar, M. A.; Lee, S.; Peña, L. A.; Waring, M.; Sitharaman, B.; Naidu, M. Graphene nanoribbons as a drug delivery agent for lucanthone mediated therapy of glioblastoma multiforme. *Nanomedicine* **2015**, *11*, 109−118.
(343) Roxbury, D.; Jena, P. V.; Williams, R. M.; Enyedi, B.; Niethammer, P.; Marcet, S.; Verhaegen, M.; Blais-Ouellette, S.; Heller, D. A. Hyperspectral Microscopy of Near-Infrared Fluorescence Enables 17-Chirality Carbon Nanotube Imaging. *Sci. Rep.* **2015**, *5*, 14167.
(344) Sheng, Y.; Tang, X.; Peng, E.; Xue, J. Graphene oxide based fluorescent nanocomposites for cellular imaging. *J. Mater. Chem. B* **2013**, *1*, 512−521.
(345) Datta, K. K. R.; Kozak, O.; Ranc, V.; Havrdova, M.; Bourlinos, A. B.; Safarova, K.; Hola, K.; Tomankova, K.; Zoppellaro, G.; Otyepka, M.; Zboril, R. Quaternized carbon dot-modified graphene oxide for selective cell labelling - controlled nucleus and cytoplasm imaging. *Chem. Commun.* **2014**, *50*, 10782−10785.
(346) Chen, T.; Lu, F.; Streets, A. M.; Fei, P.; Quan, J.; Huang, Y. Optical imaging of non-fluorescent nanodiamonds in live cells using transient absorption microscopy. *Nanoscale* **2013**, *5*, 4701−4705.
(347) Khalid, A.; Mitropoulos, A. N.; Marelli, B.; Simpson, D. A.; Tran, P. A.; Omenetto, F. G.; Tomljenovic-Hanic, S. Fluorescent

DOI: 10.1021/acs.chemrev.9b00099
Chem. Rev. XXXX, XXX, XXX−XXX

Nanodiamond Silk Fibroin Spheres: Advanced Nanoscale Bioimaging Tool. *ACS Biomater. Sci. Eng.* **2015**, *1*, 1104−1113.
(348) Ruan, S.; Qian, J.; Shen, S.; Zhu, J.; Jiang, X.; He, Q.; Gao, H. A simple one-step method to prepare fluorescent carbon dots and their potential application in non-invasive glioma imaging. *Nanoscale* **2014**, *6*, 10040−10047.
(349) Slegerova, J.; Hajek, M.; Rehor, I.; Sedlak, F.; Stursa, J.; Hruby, M.; Cigler, P. Designing the nanobiointerface of fluorescent nanodiamonds: highly selective targeting of glioma cancer cells. *Nanoscale* **2015**, *7*, 415−420.
(350) Akhavan, O.; Ghaderi, E.; Emamy, H. Nontoxic concentrations of PEGylated graphene nanoribbons for selective cancer cell imaging and photothermal therapy. *J. Mater. Chem.* **2012**, *22*, 20626−20633.
(351) Li, J.-L.; Bao, H.-C.; Hou, X.-L.; Sun, L.; Wang, X.-G.; Gu, M. Graphene Oxide Nanoparticles as a Nonbleaching Optical Probe for Two-Photon Luminescence Imaging and Cell Therapy. *Angew. Chem., Int. Ed.* **2012**, *51*, 1830−1834.
(352) Wang, C.; Chen, B.; Zou, M.; Cheng, G. Cyclic RGD-modified chitosan/graphene oxide polymers for drug delivery and cellular imaging. *Colloids Surf., B* **2014**, *122*, 332−340.
(353) Wang, C.; Li, J.; Amatore, C.; Chen, Y.; Jiang, H.; Wang, X.-M. Gold Nanoclusters and Graphene Nanocomposites for Drug Delivery and Imaging of Cancer Cells. *Angew. Chem., Int. Ed.* **2011**, *50*, 11644−11648.
(354) Liu, W.; Wei, J.; Chen, Y.; Huo, P.; Wei, Y. Electrospinning of Poly(L-lactide) Nanofibers Encapsulated with Water-Soluble Fullerenes for Bioimaging Application. *ACS Appl. Mater. Interfaces* **2013**, *5*, 680−685.
(355) Zhang, M.; Cao, Y.; Chong, Y.; Ma, Y.; Zhang, H.; Deng, Z.; Hu, C.; Zhang, Z. Graphene Oxide Based Theranostic Platform for T-1-Weighted Magnetic Resonance Imaging and Drug Delivery. *ACS Appl. Mater. Interfaces* **2013**, *5*, 13325−13332.
(356) Wen, T.; Yang, B.; Guo, Y.; Sun, J.; Zhao, C.; Zhang, S.; Zhang, M.; Wang, Y. Organosilane-functionalized graphene quantum dots and their encapsulation into bi-layer hollow silica spheres for bioimaging applications. *Phys. Chem. Chem. Phys.* **2014**, *16*, 23188−23195.
(357) Liu, W.; Wei, J.; Chen, Y. Electrospun poly(L-lactide) nanofibers loaded with paclitaxel and water-soluble fullerenes for drug delivery and bioimaging. *New J. Chem.* **2014**, *38*, 6223−6229.
(358) Kumar, V.; Singh, V.; Umrao, S.; Parashar, V.; Abraham, S.; Singh, A. K.; Nath, G.; Saxena, P. S.; Srivastava, A. Facile, rapid and upscaled synthesis of green luminescent functional graphene quantum dots for bioimaging. *RSC Adv.* **2014**, *4*, 21101−21107.
(359) Nahain, A.; Lee, J.-E.; Jeong, J. H.; Park, S. Y. Photoresponsive Fluorescent Reduced Graphene Oxide by Spiropyran Conjugated Hyaluronic Acid for in vivo Imaging and Target Delivery. *Biomacromolecules* **2013**, *14*, 4082−4090.
(360) Chen, T.; Yu, H.; Yang, N.; Wang, M.; Ding, C.; Fu, J. Graphene quantum dot-capped mesoporous silica nanoparticles through an acid-cleavable acetal bond for intracellular drug delivery and imaging. *J. Mater. Chem. B* **2014**, *2*, 4979−4982.
(361) Liu, W.; Yu, F.; Yang, J.; Xiang, B.; Xiao, P.; Wang, L. 3D Single-Molecule Imaging of Transmembrane Signaling by Targeting Nanodiamonds. *Adv. Funct. Mater.* **2016**, *26*, 365−375.
(362) Algarra, M.; Perez-Martin, M.; Cifuentes-Rueda, M.; Jimenez-Jimenez, J.; Esteves da Silva, J. C. G.; Bandosz, T. J.; Rodriguez-Castellon, E.; Lopez Navarrete, J. T.; Casado, J. Carbon dots obtained using hydrothermal treatment of formaldehyde. Cell imaging in vitro. *Nanoscale* **2014**, *6*, 9071−9077.
(363) Huynh, V. T.; Pearson, S.; Noy, J.-M.; Abboud, A.; Utama, R. H.; Lu, H.; Stenzel, M. H. Nanodiamonds with Surface Grafted Polymer Chains as Vehicles for Cell Imaging and Cisplatin Delivery: Enhancement of Cell Toxicity by POEGMEMA Coating. *ACS Macro Lett.* **2013**, *2*, 246−250.
(364) Feng, B.; Guo, L.; Wang, L.; Li, F.; Lu, J.; Gao, J.; Fan, C.; Huang, Q. A Graphene Oxide-Based Fluorescent Biosensor for the Analysis of Peptide-Receptor Interactions and Imaging in Somatostatin Receptor Subtype 2 Overexpressed Tumor Cells. *Anal. Chem.* **2013**, *85*, 7732−7737.
(365) Nigam, P.; Waghmode, S.; Louis, M.; Wangnoo, S.; Chavan, P.; Sarkar, D. Graphene quantum dots conjugated albumin nanoparticles for targeted drug delivery and imaging of pancreatic cancer. *J. Mater. Chem. B* **2014**, *2*, 3190−3195.
(366) Wu, H.; Shi, H.; Zhang, H.; Wang, X.; Yang, Y.; Yu, C.; Hao, C.; Du, J.; Hu, H.; Yang, S. Prostate stem cell antigen antibody-conjugated multiwalled carbon nanotubes for targeted ultrasound imaging and drug delivery. *Biomaterials* **2014**, *35*, 5369−5380.
(367) Zhang, J.; Ge, J.; Shultz, M. D.; Chung, E.; Singh, G.; Shu, C.; Fatouros, P. P.; Henderson, S. C.; Corwin, F. D.; Geohegan, D. B.; Puretzky, A. A.; Rouleau, C. M.; More, K.; Rylander, C.; Rylander, M. N.; Gibson, H. W.; Dorn, H. C. *In vitro* and in vivo Studies of Single-Walled Carbon Nanohorns with Encapsulated Metallofullerenes and Exohedrally Functionalized Quantum Dots. *Nano Lett.* **2010**, *10*, 2843−2848.
(368) Wu, Z.; Sun, W.-q.; Feng, T.; Tang, S. W.; Li, G.; Jiang, K.-l.; Xu, S.-y.; Ong, C. K. Imaging of soft material with carbon nanotube tip using near-field scanning microwave microscopy. *Ultramicroscopy* **2015**, *148*, 75−80.
(369) Perevedentseva, E.; Cheng, C.-Y.; Chung, P.-H.; Tu, J.-S.; Hsieh, Y.-H.; Cheng, C.-L. The interaction of the protein lysozyme with bacteria E-coli observed using nanodiamond labelling. *Nanotechnology* **2007**, *18*, 315102.
(370) Tyson, J. A.; Mirabello, V.; Calatayud, D. G.; Ge, H.; Kociok-Köhn, G.; Botchway, S. W.; Dan Pantoş, G.; Pascu, S. I. Thermally Reduced Graphene Oxide Nanohybrids of Chiral Functional Naphthalenediimides for Prostate Cancer Cells Bioimaging. *Adv. Funct. Mater.* **2016**, *26*, 5641−5657.
(371) Lin, J.; Chen, X.; Huang, P. Graphene-based nanomaterials for bioimaging. *Adv. Drug Delivery Rev.* **2016**, *105*, 242−254.
(372) Muazim, K.; Hussain, Z. Graphene oxide - A platform towards theranostics. *Mater. Sci. Eng., C* **2017**, *76*, 1274−1288.
(373) Sun, B.; Wu, J.; Cui, S.; Zhu, H.; An, W.; Fu, Q.; Shao, C.; Yao, A.; Chen, B.; Shi, D. In situ synthesis of graphene oxide/gold nanorods theranostic hybrids for efficient tumor computed tomography imaging and photothermal therapy. *Nano Res.* **2017**, *10*, 37−48.
(374) Frost, H. K.; Kodama, A.; Ekström, P.; Dahlin, L. B. G-CSF prevents caspase 3 activation in Schwann cells after sciatic nerve transection, but does not improve nerve regeneration. *Neuroscience* **2016**, *334*, 55−63.
(375) Dar, A. A.; Pradhan, T. N.; Kulkarni, D. P.; Shah, S. U.; Rao, K. V.; Chaukar, D. A.; D'Cruz, A. K.; Chiplunkar, S. V. Extracellular 2′5′-oligoadenylate synthetase 2 mediates T-cell receptor CD3-ζ chain down-regulation *via* caspase-3 activation in oral cancer. *Immunology* **2016**, *147*, 251−264.
(376) Xing, F.; Zhan, Q.; He, Y.; Cui, J.; He, S.; Wang, G. 1800 MHz Microwave Induces p53 and p53-Mediated Caspase-3 Activation Leading to Cell Apoptosis *In vitro*. *PLoS One* **2016**, *11*, No. e0163935.
(377) Zhu, W. P.; von dem Bussche, A.; Yi, X.; Qiu, Y.; Wang, Z. Y.; Weston, P.; Hurt, R. H.; Kane, A. B.; Gao, H. J. Nanomechanical mechanism for lipid bilayer damage induced by carbon nanotubes confined in intracellular vesicles. *Proc. Natl. Acad. Sci. U. S. A.* **2016**, *113*, 12374−12379.
(378) Nie, C.; Cheng, C.; Peng, Z.; Ma, L.; He, C.; Xia, Y.; Zhao, C. Mussel-inspired coatings on Ag nanoparticle-conjugated carbon nanotubes: bactericidal activity and mammal cell toxicity. *J. Mater. Chem. B* **2016**, *4*, 2749−2756.
(379) Ohfuchi, M.; Miyamoto, Y. Optical properties of oxidized single-wall carbon nanotubes. *Carbon* **2017**, *114*, 418−423.
(380) Zhu, S. J.; Yang, Q. L.; Antaris, A. L.; Yue, J. Y.; Ma, Z. R.; Wang, H. S.; Huang, W.; Wan, H.; Wang, J.; Diao, S.; Zhang, B.; Li, X. Y.; Zhong, Y. T.; Yu, K.; Hong, G. S.; Luo, J.; Liang, Y. Y.; Dai, H. J. Molecular imaging of biological systems with a clickable dye in the broad 800- to 1,700-nm near-infrared window. *Proc. Natl. Acad. Sci. U. S. A.* **2017**, *114*, 962−967.

DOI: 10.1021/acs.chemrev.9b00099
Chem. Rev. XXXX, XXX, XXX−XXX

(381) Cherukuri, P.; Bachilo, S. M.; Litovsky, S. H.; Weisman, R. B. Near-Infrared Fluorescence Microscopy of Single-Walled Carbon Nanotubes in Phagocytic Cells. *J. Am. Chem. Soc.* **2004**, *126*, 15638−15639.
(382) Cherukuri, P.; Gannon, C. J.; Leeuw, T. K.; Schmidt, H. K.; Smalley, R. E.; Curley, S. A.; Weisman, R. B. Mammalian Pharmacokinetics of Carbon Nanotubes Using Intrinsic Near-Infrared Fluorescence. *Proc. Natl. Acad. Sci. U. S. A.* **2006**, *103*, 18882−18886.
(383) Welsher, K.; Liu, Z.; Daranciang, D.; Dai, H. Selective Probing and Imaging of Cells with Single Walled Carbon Nanotubes as Near-Infrared Fluorescent Molecules. *Nano Lett.* **2008**, *8*, 586−590.
(384) Hong, G.; Tabakman, S. M.; Welsher, K.; Chen, Z.; Robinson, J. T.; Wang, H.; Zhang, B.; Dai, H. Near-Infrared-Fluorescence-Enhanced Molecular Imaging of Live Cells on Gold Substrates. *Angew. Chem., Int. Ed.* **2011**, *50*, 4644−4648.
(385) Fakhri, N.; Wessel, A. D.; Willms, C.; Pasquali, M.; Klopfenstein, D. R.; MacKintosh, F. C.; Schmidt, C. F. High-Resolution Mapping of Intracellular Fluctuations Using Carbon Nanotubes. *Science* **2014**, *344*, 1031−1035.
(386) Rubio, N.; Hirvonen, L. M.; Chong, E. Z.; Wang, J. T. W.; Bourgognon, M.; Kafa, H.; Hassan, H. A. F. M.; Al-Jamal, W. T.; McCarthy, D.; Hogstrand, C.; Festy, F.; Al-Jamal, K. T. Multiphoton luminescence imaging of chemically functionalized multi-walled carbon nanotubes in cells and solid tumors. *Chem. Commun.* **2015**, *51*, 9366−9369.
(387) Tan, L.; Wu, T.; Tang, Z.-W.; Xiao, J.-Y.; Zhuo, R.-X.; Shi, B.; Liu, C.-J. Water-soluble photoluminescent fullerene capped mesoporous silica for pH-responsive drug delivery and bioimaging. *Nanotechnology* **2016**, *27*, 315104.
(388) Xie, R.; Wang, Z.; Yu, H.; Fan, Z.; Yuan, F.; Li, Y.; Li, X.; Fan, L.; Fan, H. Highly Water-soluble and Surface Charge-tunable Fluorescent Fullerene Nanoparticles: Facile Fabrication and Cellular Imaging. *Electrochim. Acta* **2016**, *201*, 220−227.
(389) Rašović, I. Water-soluble fullerenes for medical applications. *Mater. Sci. Technol.* **2017**, *33*, 777−794.
(390) Yang, Z.; Mao, Z.; Xie, Z.; Zhang, Y.; Liu, S.; Zhao, J.; Xu, J.; Chi, Z.; Aldred, M. P. Recent advances in organic thermally activated delayed fluorescence materials. *Chem. Soc. Rev.* **2017**, *46*, 915−1016.
(391) E, Y.; Bai, L.; Fan, L.; Han, M.; Zhang, X.; Yang, S. Electrochemically generated fluorescent fullerene[60] nanoparticles as a new and viable bioimaging platform. *J. Mater. Chem.* **2011**, *21*, 819−823.
(392) Wang, J.; Wang, R.; Zhang, F.; Yin, Y.; Mei, L.; Song, F.; Tao, M.; Yue, W.; Zhong, W. Overcoming multidrug resistance by a combination of chemotherapy and photothermal therapy mediated by carbon nanohorns. *J. Mater. Chem. B* **2016**, *4*, 6043−6051.
(393) Chechetka, S. A.; Yuba, E.; Kono, K.; Yudasaka, M.; Bianco, A.; Miyako, E. Magnetically and Near-Infrared Light-Powered Supramolecular Nanotransporters for the Remote Control of Enzymatic Reactions. *Angew. Chem., Int. Ed.* **2016**, *55*, 6476−6481.
(394) Lv, L.; Li, D.; Cui, C.; Zhao, Y.; Guo, Z. Nuclease-aided target recycling signal amplification strategy for ochratoxin A monitoring. *Biosens. Bioelectron.* **2017**, *87*, 136−141.
(395) Merchant, K.; Sarkar, S. K. Fluorescent Nanodiamonds for Molecular and Cellular Bioimaging. *IEEE J. Sel. Top. Quantum Electron.* **2016**, *22*, 235−245.
(396) Reineck, P.; Francis, A.; Orth, A.; Lau, D. W. M.; Nixon-Luke, R. D. V.; Rastogi, I. D.; Razali, W. A. W.; Cordina, N. M.; Parker, L. M.; Sreenivasan, V. K. A.; Brown, L. J.; Gibson, B. C. Brightness and Photostability of Emerging Red and Near-IR Fluorescent Nanomaterials for Bioimaging. *Adv. Opt. Mater.* **2016**, *4*, 1549−1557.
(397) Nunn, N.; Torelli, M.; McGuire, G.; Shenderova, O. Nanodiamond: A high impact nanomaterial. *Curr. Opin. Solid State Mater. Sci.* **2017**, *21*, 1−9.
(398) Hui, Y. Y.; Hsiao, W. W.-W.; Haziza, S.; Simonneau, M.; Treussart, F.; Chang, H.-C. Single particle tracking of fluorescent nanodiamonds in cells and organisms. *Curr. Opin. Solid State Mater. Sci.* **2017**, *21*, 35−42.
(399) Chizhik, A. M.; Stein, S.; Dekaliuk, M. O.; Battle, C.; Li, W.; Huss, A.; Platen, M.; Schaap, I. A. T.; Gregor, I.; Demchenko, A. P.; Schmidt, C. F.; Enderlein, J.; Chizhik, A. I. Super-Resolution Optical Fluctuation Bio-Imaging with Dual-Color Carbon Nanodots. *Nano Lett.* **2016**, *16*, 237−242.
(400) Mao, Q.-X.; E, S.; Xia, J.-M.; Song, R.-S.; Shu, Y.; Chen, X.-W.; Wang, J.-H. Hydrophobic Carbon Nanodots with Rapid Cell Penetrability and Tunable Photoluminescence Behavior for in vitro and in vivo Imaging. *Langmuir* **2016**, *32*, 12221−12229.
(401) Lu, S.; Sui, L.; Liu, J.; Zhu, S.; Chen, A.; Jin, M.; Yang, B. Near-Infrared Photoluminescent Polymer−Carbon Nanodots with Two-Photon Fluorescence. *Adv. Mater.* **2017**, *29*, 1603443.
(402) Chan, K. K.; Yap, S. H. K.; Yong, K.-T. Biogreen Synthesis of Carbon Dots for Biotechnology and Nanomedicine Applications. *Nano-Micro Letters* **2018**, *10*, 72.
(403) Lopez-Chaves, C.; Soto-Alvaredo, J.; Montes-Bayon, M.; Bettmer, J.; Llopis, J.; Sanchez-Gonzalez, C. Gold nanoparticles: Distribution, bioaccumulation and toxicity. *In vitro* and in vivo studies. *Nanomedicine* **2018**, *14*, 1−12.
(404) Lam, P.-L.; Wong, W.-Y.; Bian, Z.; Chui, C.-H.; Gambari, R. Recent advances in green nanoparticulate systems for drug delivery: efficient delivery and safety concern. *Nanomedicine* **2017**, *12*, 357−385.
(405) Yao, X.; Niu, X.; Ma, K.; Huang, P.; Grothe, J.; Kaskel, S.; Zhu, Y. Graphene Quantum Dots-Capped Magnetic Mesoporous Silica Nanoparticles as a Multifunctional Platform for Controlled Drug Delivery, Magnetic Hyperthermia, and Photothermal Therapy. *Small* **2017**, *13*, 1602225.
(406) Wang, D.; Hou, C.; Meng, L.; Long, J.; Jing, J.; Dang, D.; Fei, Z.; Dyson, P. J. Stepwise growth of gold coated cancer targeting carbon nanotubes for the precise delivery of doxorubicin combined with photothermal therapy. *J. Mater. Chem. B* **2017**, *5*, 1380−1387.
(407) Masoudipour, E.; Kashanian, S.; Maleki, N. A targeted drug delivery system based on dopamine functionalized nano graphene oxide. *Chem. Phys. Lett.* **2017**, *668*, 56−63.
(408) Singh, S.; Mishra, A.; Kumari, R.; Sinha, K. K.; Singh, M. K.; Das, P. Carbon dots assisted formation of DNA hydrogel for sustained release of drug. *Carbon* **2017**, *114*, 169−176.
(409) Shim, G.; Kim, M.-G.; Park, J. Y.; Oh, Y.-K. Graphene-based nanosheets for delivery of chemotherapeutics and biological drugs. *Adv. Drug Delivery Rev.* **2016**, *105*, 205−227.
(410) Wei, Y.; Zhou, F.; Zhang, D.; Chen, Q.; Xing, D. A graphene oxide based smart drug delivery system for tumor mitochondria-targeting photodynamic therapy. *Nanoscale* **2016**, *8*, 3530−3538.
(411) He, Q.; Kiesewetter, D. O.; Qu, Y.; Fu, X.; Fan, J.; Huang, P.; Liu, Y.; Zhu, G.; Liu, Y.; Qian, Z.; Chen, X. NIR-Responsive On-Demand Release of CO from Metal Carbonyl-Caged Graphene Oxide Nanomedicine. *Adv. Mater.* **2015**, *27*, 6741−6746.
(412) Mo, R.; Jiang, T.; Sun, W.; Gu, Z. ATP-responsive DNA-graphene hybrid nanoaggregates for anticancer drug delivery. *Biomaterials* **2015**, *50*, 67−74.
(413) Jiang, T.; Sun, W.; Zhu, Q.; Burns, N. A.; Khan, S. A.; Mo, R.; Gu, Z. Furin-Mediated Sequential Delivery of Anticancer Cytokine and Small-Molecule Drug Shuttled by Graphene. *Adv. Mater.* **2015**, *27*, 1021−1028.
(414) Miao, W.; Shim, G.; Lee, S.; Lee, S.; Choe, Y. S.; Oh, Y.-K. Safety and tumor tissue accumulation of pegylated graphene oxide nanosheets for co-delivery of anticancer drug and photosensitizer. *Biomaterials* **2013**, *34*, 3402−3410.
(415) Kim, H.; Lee, D.; Kim, J.; Kim, T.-i.; Kim, W. J. Photothermally Triggered Cytosolic Drug Delivery *via* Endosome Disruption Using a Functionalized Reduced Graphene Oxide. *ACS Nano* **2013**, *7*, 6735−6746.
(416) Wu, H.; Shi, H.; Wang, Y.; Jia, X.; Tang, C.; Zhang, J.; Yang, S. Hyaluronic acid conjugated graphene oxide for targeted drug delivery. *Carbon* **2014**, *69*, 379−389.
(417) Chen, J.; Liu, H.; Zhao, C.; Qin, G.; Xi, G.; Li, T.; Wang, X.; Chen, T. One-step reduction and PEGylation of graphene oxide for

DOI: 10.1021/acs.chemrev.9b00099
Chem. Rev. XXXX, XXX, XXX−XXX

photothermally controlled drug delivery. *Biomaterials* **2014**, *35*, 4986−4995.
(418) Bianco, A.; Kostarelos, K.; Prato, M. Applications of carbon nanotubes in drug delivery. *Curr. Opin. Chem. Biol.* **2005**, *9*, 674−679.
(419) Boyer, P. D.; Shams, H.; Baker, S. L.; Mofrad, M. R. K.; Islam, M. F.; Dahl, K. N. Enhanced intracellular delivery of small molecules and drugs *via* non-covalent ternary dispersions of single-wall carbon nanotubes. *J. Mater. Chem. B* **2016**, *4*, 1324−1330.
(420) Spinato, C.; Giust, D.; Vacchi, I. A.; Menard-Moyon, C.; Kostarelos, K.; Bianco, A. Different chemical strategies to aminate oxidised multi-walled carbon nanotubes for siRNA complexation and delivery. *J. Mater. Chem. B* **2016**, *4*, 431−441.
(421) Yang, G.; Liu, J.; Wu, Y.; Feng, L.; Liu, Z. Near-infrared-light responsive nanoscale drug delivery systems for cancer treatment. *Coord. Chem. Rev.* **2016**, *320*, 100−117.
(422) Foldvari, M.; Bagonluri, M. Carbon nanotubes as functional excipients for nanomedicines: II. Drug delivery and biocompatibility issues. *Nanomedicine* **2008**, *4*, 183−200.
(423) Chen, J.; Chen, S.; Zhao, X.; Kuznetsova, L. V.; Wong, S. S.; Ojima, I. Functionalized Single-Walled Carbon Nanotubes as Rationally Designed Vehicles for Tumor-Targeted Drug Delivery. *J. Am. Chem. Soc.* **2008**, *130*, 16778−16785.
(424) Bhatnagar, I.; Venkatesan, J.; Kim, S.-K. Polymer Functionalized Single Walled Carbon Nanotubes Mediated Drug Delivery of Gliotoxin in Cancer Cells. *J. Biomed. Nanotechnol.* **2014**, *10*, 120−130.
(425) Sahoo, N. G.; Bao, H.; Pan, Y.; Pal, M.; Kakran, M.; Cheng, H. K. F.; Li, L.; Tan, L. P. Functionalized carbon nanomaterials as nanocarriers for loading and delivery of a poorly water-soluble anticancer drug: a comparative study. *Chem. Commun.* **2011**, *47*, 5235−5237.
(426) Prylutskyy, Y. I.; Petrenko, V. I.; Ivankov, O. I.; Kyzyma, O. A.; Bulavin, L. A.; Litsis, O. O.; Evstigneev, M. P.; Cherepanov, V. V.; Naumovets, A. G.; Ritter, U. On the Origin of C_{60} Fullerene Solubility in Aqueous Solution. *Langmuir* **2014**, *30*, 3967−3970.
(427) Panchuk, R. R.; Prylutska, S. V.; Chumak, V. V.; Skorokhyd, N. R.; Lehka, L. V.; Evstigneev, M. P.; Prylutskyy, Y. I.; Berger, W.; Heffeter, P.; Scharff, P.; Ritter, U.; Stoika, R. S. Application of C_{60} Fullerene-Doxorubicin Complex for Tumor Cell Treatment *In vitro* and *In vivo*. *J. Biomed. Nanotechnol.* **2015**, *11*, 1139−1152.
(428) Lee, E. J.; Lee, N. K.; Kim, I.-S. Bioengineered protein-based nanocage for drug delivery. *Adv. Drug Delivery Rev.* **2016**, *106*, 157−171.
(429) Shi, J.; Chen, Z.; Wang, L.; Wang, B.; Xu, L.; Hou, L.; Zhang, Z. A tumor-specific cleavable nanosystem of PEG-modified C_{60}@Au hybrid aggregates for radio frequency-controlled release, hyperthermia, photodynamic therapy and X-ray imaging. *Acta Biomater.* **2016**, *29*, 282−297.
(430) Partha, R.; Mitchell, L. R.; Lyon, J. L.; Joshi, P. P.; Conyers, J. L. Buckysomes: Fullerene-based nanocarriers for hydrophobic molecule delivery. *ACS Nano* **2008**, *2*, 1950−1958.
(431) Wei, P.; Zhang, L.; Lu, Y.; Man, N.; Wen, L. C_{60}(Nd) nanoparticles enhance chemotherapeutic susceptibility of cancer cells by modulation of autophagy. *Nanotechnology* **2010**, *21*, 495101.
(432) Fan, J.; Fang, G.; Zeng, F.; Wang, X.; Wu, S. Water-Dispersible Fullerene Aggregates as a Targeted Anticancer Prodrug with both Chemo- and Photodynamic Therapeutic Actions. *Small* **2013**, *9*, 613−621.
(433) Zhang, H.; Hou, L.; Jiao, X.; Ji, Y.; Zhu, X.; Zhang, Z. Transferrin-mediated fullerenes nanoparticles as Fe^{2+}-dependent drug vehicles for synergistic anti-tumor efficacy. *Biomaterials* **2015**, *37*, 353−366.
(434) Karousis, N.; Suarez-Martinez, I.; Ewels, C. P.; Tagmatarchis, N. Structure, Properties, Functionalization, and Applications of Carbon Nanohorns. *Chem. Rev.* **2016**, *116*, 4850−4883.
(435) Wang, R.; Cui, H.; Wang, J.; Li, N.; Zhao, Q.; Zhou, Y.; Lv, Z.; Zhong, W. Enhancing the antitumor effect of methotrexate in intro and in vivo by a novel targeted single-walled carbon nanohorn-based drug delivery system. *RSC Adv.* **2016**, *6*, 47272−47280.
(436) Iizumi, Y.; Okazaki, T.; Zhang, M.; Yuge, R.; Ichihashi, T.; Nakamura, M.; Ikehara, Y.; Iijima, S.; Yudasaka, M. Preparation and functionalization of boron nitride containing carbon nanohorns for boron neutron capture therapy. *Carbon* **2015**, *93*, 595−603.
(437) Chen, D.; Dougherty, C. A.; Zhu, K.; Hong, H. Theranostic applications of carbon nanomaterials in cancer: Focus on imaging and cargo delivery. *J. Controlled Release* **2015**, *210*, 230−245.
(438) Li, N.; Zhao, Q.; Shu, C.; Ma, X.; Li, R.; Shen, H.; Zhong, W. Targeted killing of cancer cells in vivo and in vitro with IGF-IR antibody-directed carbon nanohorns based drug delivery. *Int. J. Pharm.* **2015**, *478*, 644−654.
(439) Miyako, E.; Pichon, B. P.; Ménard-Moyon, C.; Vacchi, I. A.; Lefèvre, C.; Bégin-Colin, S.; Bianco, A. Design, synthesis, characterization and properties of magnetic nanoparticle−nanocarbon hybrids. *Carbon* **2016**, *96*, 49−56.
(440) Ajima, K.; Murakami, T.; Mizoguchi, Y.; Tsuchida, K.; Ichihashi, T.; Iijima, S.; Yudasaka, M. Enhancement of *In vivo* Anticancer Effects of Cisplatin by Incorporation Inside Single-Wall Carbon Nanohorns. *ACS Nano* **2008**, *2*, 2057−2064.
(441) Chen, D.; Wang, C.; Jiang, F.; Liu, Z.; Shu, C.; Wan, L.-J. *In vitro* and in vivo photothermally enhanced chemotherapy by single-walled carbon nanohorns as a drug delivery system. *J. Mater. Chem. B* **2014**, *2*, 4726−4732.
(442) Zheng, H.; Hu, Y.; Huang, W.; de Villiers, S.; Pentel, P.; Zhang, J.; Dorn, H.; Ehrich, M.; Zhang, C. Negatively Charged Carbon Nanohorn Supported Cationic Liposome Nanoparticles: A Novel Delivery Vehicle for Anti-Nicotine Vaccine. *J. Biomed. Nanotechnol.* **2015**, *11*, 2197−2210.
(443) Zhang, Y.; Cui, Z.; Kong, H.; Xia, K.; Pan, L.; Li, J.; Sun, Y.; Shi, J.; Wang, L.; Zhu, Y.; Fan, C. One-Shot Immunomodulatory Nanodiamond Agents for Cancer Immunotherapy. *Adv. Mater.* **2016**, *28*, 2699−2708.
(444) Cui, Z.; Zhang, Y.; Zhang, J.; Kong, H.; Tang, X.; Pan, L.; Xia, K.; Aldalbahi, A.; Li, A.; Tai, R.; Fan, C.; Zhu, Y. Sodium alginate-functionalized nanodiamonds as sustained chemotherapeutic drug-release vectors. *Carbon* **2016**, *97*, 78−86.
(445) Giammarco, J.; Mochalin, V. N.; Haeckel, J.; Gogotsi, Y. The adsorption of tetracycline and vancomycin onto nanodiamond with controlled release. *J. Colloid Interface Sci.* **2016**, *468*, 253−261.
(446) Chen, X.; Li, D.; Wang, H.; Jiao, Y.-y.; Wang, H.; Yu, Y.; Zhi, J. Fabrication of an EGF modified nanodiamonds-based anti-cancer drug targeted delivery system and drug carrier uptake visualization by 3D Raman microscopy. *RSC Adv.* **2016**, *6*, 44543−44551.
(447) Alwani, S.; Kaur, R.; Michel, D.; Chitanda, J. M.; Verrall, R. E.; Karunakaran, C.; Badea, I. Lysine-functionalized nanodiamonds as gene carriers: development of stable colloidal dispersion for in vitro cellular uptake studies and siRNA delivery application. *Int. J. Nanomed.* **2016**, *11*, 687−702.
(448) Wuest, K. N. R.; Trouillet, V.; Goldmann, A. S.; Stenzel, M. H.; Barner-Kowollik, C. Polymer Functional Nanodiamonds by Light-Induced Ligation. *Macromolecules* **2016**, *49*, 1712−1721.
(449) Li, J.; Zhu, Y.; Li, W.; Zhang, X.; Peng, Y.; Huang, Q. Nanodiamonds as intracellular transporters of chemotherapeutic drug. *Biomaterials* **2010**, *31*, 8410−8418.
(450) Xiao, J.; Duan, X.; Yin, Q.; Zhang, Z.; Yu, H.; Li, Y. Nanodiamonds-mediated doxorubicin nuclear delivery to inhibit lung metastasis of breast cancer. *Biomaterials* **2013**, *34*, 9648−9656.
(451) Zhao, A.; Chen, Z.; Zhao, C.; Gao, N.; Ren, J.; Qu, X. Recent advances in bioapplications of C-dots. *Carbon* **2015**, *85*, 309−327.
(452) Feng, T.; Ai, X.; An, G.; Yang, P.; Zhao, Y. Charge-Convertible Carbon Dots for Imaging-Guided Drug Delivery with Enhanced in vivo Cancer Therapeutic Efficiency. *ACS Nano* **2016**, *10*, 4410−4420.
(453) Wu, Y.-F.; Wu, H.-C.; Kuan, C.-H.; Lin, C.-J.; Wang, L.-W.; Chang, C.-W.; Wang, T.-W. Multi-functionalized carbon dots as theranostic nanoagent for gene delivery in lung cancer therapy. *Sci. Rep.* **2016**, *6*, 21170.
(454) Peng, H.; Li, Y.; Jiang, C.; Luo, C.; Qi, R.; Huang, R.; Duan, C.-G.; Travas-Sejdic, J. Tuning the properties of luminescent

DOI: 10.1021/acs.chemrev.9b00099
Chem. Rev. XXXX, XXX, XXX−XXX

nitrogen-doped carbon dots by reaction precursors. *Carbon* **2016**, *100*, 386−394.
(455) Permatasari, F. A.; Aimon, A. H.; Iskandar, F.; Ogi, T.; Okuyama, K. Role of C−N Configurations in the Photoluminescence of Graphene Quantum Dots Synthesized by a Hydrothermal Route. *Sci. Rep.* **2016**, *6*, 21042.
(456) Gong, X.; Zhang, Q.; Gao, Y.; Shuang, S.; Choi, M. M. F.; Dong, C. Phosphorus and Nitrogen Dual-Doped Hollow Carbon Dot as a Nanocarrier for Doxorubicin Delivery and Biological Imaging. *ACS Appl. Mater. Interfaces* **2016**, *8*, 11288−11297.
(457) Chien, Y. H.; Chan, K. K.; Anderson, T.; Kong, K. V.; Ng, B. K.; Yong, K. T. Advanced Near-Infrared Light-Responsive Nanomaterials as Therapeutic Platforms for Cancer Therapy. *Adv. Ther.* **2019**, *2*, 1800090.
(458) Chien, Y.-H.; Chan, K. K.; Yap, S. H. K.; Yong, K.-T. NIR-responsive nanomaterials and their applications; upconversion nanoparticles and carbon dots: a perspective. *J. Chem. Technol. Biotechnol.* **2018**, *93*, 1519−1528.
(459) Zhou, L.; Li, Z.; Liu, Z.; Ren, J.; Qu, X. Luminescent Carbon Dot-Gated Nanovehicles for pH-Triggered Intracellular Controlled Release and Imaging. *Langmuir* **2013**, *29*, 6396−6403.
(460) He, L.; Wang, T.; An, J.; Li, X.; Zhang, L.; Li, L.; Li, G.; Wu, X.; Su, Z.; Wang, C. Carbon nanodots@zeolitic imidazolate framework-8 nanoparticles for simultaneous pH-responsive drug delivery and fluorescence imaging. *CrystEngComm* **2014**, *16*, 3259−3263.
(461) Wang, H.; Di, J.; Sun, Y.; Fu, J.; Wei, Z.; Matsui, H.; del C. Alonso, A.; Zhou, S. Biocompatible PEG-Chitosan@Carbon Dots Hybrid Nanogels for Two-Photon Fluorescence Imaging, Near-Infrared Light/pH Dual-Responsive Drug Carrier, and Synergistic Therapy. *Adv. Funct. Mater.* **2015**, *25*, 5537−5547.
(462) Weaver, C. L.; LaRosa, J. M.; Luo, X.; Cui, X. T. Electrically Controlled Drug Delivery from Graphene Oxide Nanocomposite Films. *ACS Nano* **2014**, *8*, 1834−1843.
(463) Murakami, T.; Ajima, K.; Miyawaki, J.; Yudasaka, M.; Iijima, S.; Shiba, K. Drug-loaded carbon nanohorns: Adsorption and release of dexamethasone in vitro. *Mol. Pharmaceutics* **2004**, *1*, 399−405.
(464) Chow, E. K.; Zhang, X.-Q.; Chen, M.; Lam, R.; Robinson, E.; Huang, H.; Schaffer, D.; Osawa, E.; Goga, A.; Ho, D. Nanodiamond Therapeutic Delivery Agents Mediate Enhanced Chemoresistant Tumor Treatment. *Sci. Transl. Med.* **2011**, *3*, 73ra21.
(465) Shi, X.; Gong, H.; Li, Y.; Wang, C.; Cheng, L.; Liu, Z. Graphene-based magnetic plasmonic nanocomposite for dual bioimaging and photothermal therapy. *Biomaterials* **2013**, *34*, 4786−4793.
(466) Zhang, W.; Guo, Z.; Huang, D.; Liu, Z.; Guo, X.; Zhong, H. Synergistic effect of chemo-photothermal therapy using PEGylated graphene oxide. *Biomaterials* **2011**, *32*, 8555−8561.
(467) Zhang, L.; Xia, J.; Zhao, Q.; Liu, L.; Zhang, Z. Functional Graphene Oxide as a Nanocarrier for Controlled Loading and Targeted Delivery of Mixed Anticancer Drugs. *Small* **2010**, *6*, 537−544.
(468) Rana, V. K.; Choi, M.-C.; Kong, J.-Y.; Kim, G. Y.; Kim, M. J.; Kim, S.-H.; Mishra, S.; Singh, R. P.; Ha, C.-S. Synthesis and Drug-Delivery Behavior of Chitosan-Functionalized Graphene Oxide Hybrid Nanosheets. *Macromol. Mater. Eng.* **2011**, *296*, 131−140.
(469) Hu, H.; Yu, J.; Li, Y.; Zhao, J.; Dong, H. Engineering of a novel pluronic F127/graphene nanohybrid for pH responsive drug delivery. *J. Biomed. Mater. Res., Part A* **2012**, *100A*, 141−148.
(470) Xu, Z.; Wang, S.; Li, Y.; Wang, M.; Shi, P.; Huang, X. Covalent Functionalization of Graphene Oxide with Biocompatible Poly(ethylene glycol) for Delivery of Paclitaxel. *ACS Appl. Mater. Interfaces* **2014**, *6*, 17268−17276.
(471) Jung, H. S.; Lee, M.-Y.; Kong, W. H.; Do, I. H.; Hahn, S. K. Nano graphene oxide-hyaluronic acid conjugate for target specific cancer drug delivery. *RSC Adv.* **2014**, *4*, 14197−14200.
(472) Chen, M.; Pierstorff, E. D.; Lam, R.; Li, S.-Y.; Huang, H.; Osawa, E.; Ho, D. Nanodiamond-Mediated Delivery of Water-Insoluble Therapeutics. *ACS Nano* **2009**, *3*, 2016−2022.
(473) Ma, X.; Shu, C.; Guo, J.; Pang, L.; Su, L.; Fu, D.; Zhong, W. Targeted cancer therapy based on single-wall carbon nanohorns with doxorubicin in vitro and in vivo. *J. Nanopart. Res.* **2014**, *16*, 2497.
(474) Zhao, Q.; Li, N.; Shu, C.; Li, R.; Ma, X.; Li, X.; Wang, R.; Zhong, W. Docetaxel-loaded single-wall carbon nanohorns using anti-VEGF antibody as a targeting agent: characterization, in vitro and in vivo antitumor activity. *J. Nanopart. Res.* **2015**, *17*, 207.
(475) Lucafo, M.; Pacor, S.; Fabbro, C.; Da Ros, T.; Zorzet, S.; Prato, M.; Sava, G. Study of a potential drug delivery system based on carbon nanoparticles: effects of fullerene derivatives in MCF7 mammary carcinoma cells. *J. Nanopart. Res.* **2012**, *14*, 830.
(476) Moore, L.; Chow, E. K.-H.; Osawa, E.; Bishop, J. M.; Ho, D. Diamond-Lipid Hybrids Enhance Chemotherapeutic Tolerance and Mediate Tumor Regression. *Adv. Mater.* **2013**, *25*, 3532−3541.
(477) Toh, T.-B.; Lee, D.-K.; Hou, W.; Abdullah, L. N.; Nguyen, J.; Ho, D.; Chow, E. K.-H. Nanodiamond-Mitoxantrone Complexes Enhance Drug Retention in Chemoresistant Breast Cancer Cells. *Mol. Pharmaceutics* **2014**, *11*, 2683−2691.
(478) Zhang, L.; Lu, Z.; Zhao, Q.; Huang, J.; Shen, H.; Zhang, Z. Enhanced Chemotherapy Efficacy by Sequential Delivery of siRNA and Anticancer Drugs Using PEI-Grafted Graphene Oxide. *Small* **2011**, *7*, 460−464.
(479) Yang, X.; Wang, Y.; Huang, X.; Ma, Y.; Huang, Y.; Yang, R.; Duan, H.; Chen, Y. Multi-functionalized graphene oxide based anticancer drug-carrier with dual-targeting function and pH-sensitivity. *J. Mater. Chem.* **2011**, *21*, 3448−3454.
(480) Wen, H.; Dong, C.; Dong, H.; Shen, A.; Xia, W.; Cai, X.; Song, Y.; Li, X.; Li, Y.; Shi, D. Engineered Redox-Responsive PEG Detachment Mechanism in PEGylated Nano-Graphene Oxide for Intracellular Drug Delivery. *Small* **2012**, *8*, 760−769.
(481) Zhang, Q.; Yang, W.; Man, N.; Zheng, F.; Shen, Y.; Sun, K.; Li, Y.; Wen, L.-P. Autophagy-mediated chemosensitization in cancer cells by fullerene C_{60} nanocrystal. *Autophagy* **2009**, *5*, 1107−1117.
(482) Guo, X.; Ding, R.; Zhang, Y.; Ye, L.; Liu, X.; Chen, C.; Zhang, Z.; Zhang, Y. Dual Role of Photosensitizer and Carrier Material of Fullerene in Micelles for Chemo-Photodynamic Therapy of Cancer. *J. Pharm. Sci.* **2014**, *103*, 3225−3234.
(483) Guan, B.; Zou, F.; Zhi, J. Nanodiamond as the pH-Responsive Vehicle for an Anticancer Drug. *Small* **2010**, *6*, 1514−1519.
(484) Prabhakar, N.; Nareoja, T.; von Haartman, E.; Karaman, D. S.; Jiang, H.; Koho, S.; Dolenko, T. A.; Hanninen, P. E.; Vlasov, D. I.; Ralchenko, V. G.; Hosomi, S.; Vlasov, I. I.; Sahlgren, C.; Rosenholm, J. M. Core-shell designs of photoluminescent nanodiamonds with porous silica coatings for bioimaging and drug delivery II: application. *Nanoscale* **2013**, *5*, 3713−3722.
(485) Chechetka, S. A.; Pichon, B.; Zhang, M.; Yudasaka, M.; Begin-Colin, S.; Bianco, A.; Miyako, E. Multifunctional Carbon Nanohorn Complexes for Cancer Treatment. *Chem. - Asian J.* **2015**, *10*, 160−165.
(486) Huang, H.; Pierstorff, E.; Osawa, E.; Ho, D. Active nanodiamond hydrogels for chemotherapeutic delivery. *Nano Lett.* **2007**, *7*, 3305−3314.
(487) Shimkunas, R. A.; Robinson, E.; Lam, R.; Lu, S.; Xu, X.; Zhang, X.-Q.; Huang, H.; Osawa, E.; Ho, D. Nanodiamond-insulin complexes as pH-dependent protein delivery vehicles. *Biomaterials* **2009**, *30*, 5720−5728.
(488) Xi, G.; Robinson, E.; Mania-Farnell, B.; Vanin, E. F.; Shim, K.-W.; Takao, T.; Allender, E. V.; Mayanil, C. S.; Soares, M. B.; Ho, D.; Tomita, T. Convection-enhanced delivery of nanodiamond drug delivery platforms for intracranial tumor treatment. *Nanomedicine* **2014**, *10*, 381−391.
(489) Moore, T. L.; Podilakrishna, R.; Rao, A.; Alexis, F. Systemic Administration of Polymer-Coated Nano-Graphene to Deliver Drugs to Glioblastoma. *Part. Part. Syst. Charact.* **2014**, *31*, 886−894.
(490) Yang, H.-W.; Huang, C.-Y.; Lin, C.-W.; Liu, H.-L.; Huang, C.-W.; Liao, S.-S.; Chen, P.-Y.; Lu, Y.-J.; Wei, K.-C.; Ma, C.-C. M. Gadolinium-functionalized nanographene oxide for combined drug and microRNA delivery and magnetic resonance imaging. *Biomaterials* **2014**, *35*, 6534−6542.

DOI: 10.1021/acs.chemrev.9b00099
Chem. Rev. XXXX, XXX, XXX−XXX

(491) Zhao, L.; Xu, Y.-H.; Qin, H.; Abe, S.; Akasaka, T.; Chano, T.; Watari, F.; Kimura, T.; Komatsu, N.; Chen, X. Platinum on Nanodiamond: A Promising Prodrug Conjugated with Stealth Polyglycerol, Targeting Peptide and Acid-Responsive Antitumor Drug. *Adv. Funct. Mater.* **2014**, *24*, 5348−5357.
(492) Man, H. B.; Kim, H.; Kim, H.-J.; Robinson, E.; Liu, W. K.; Chow, E. K.-H.; Ho, D. Synthesis of nanodiamond-daunorubicin conjugates to overcome multidrug chemoresistance in leukemia. *Nanomedicine* **2014**, *10*, 359−369.
(493) Liang, X.-J.; Meng, H.; Wang, Y.; He, H.; Meng, J.; Lu, J.; Wang, P. C.; Zhao, Y.; Gao, X.; Sun, B.; Chen, C.; Xing, G.; Shen, D.; Gottesman, M. M.; Wu, Y.; Yin, J.-j.; Jia, L. Metallofullerene nanoparticles circumvent tumor resistance to cisplatin by reactivating endocytosis. *Proc. Natl. Acad. Sci. U. S. A.* **2010**, *107*, 7449−7454.
(494) Wang, X.; Low, X. C.; Hou, W.; Abdullah, L. N.; Toh, T. B.; Mohd Abdul Rashid, M.; Ho, D.; Chow, E. K.-H. Epirubicin-Adsorbed Nanodiamonds Kill Chemoresistant Hepatic Cancer Stem Cells. *ACS Nano* **2014**, *8*, 12151−12166.
(495) Bao, H.; Pan, Y.; Ping, Y.; Sahoo, N. G.; Wu, T.; Li, L.; Li, J.; Gan, L. H. Chitosan-Functionalized Graphene Oxide as a Nanocarrier for Drug and Gene Delivery. *Small* **2011**, *7*, 1569−1578.
(496) Song, E.; Han, W.; Li, C.; Cheng, D.; Li, L.; Liu, L.; Zhu, G.; Song, Y.; Tan, W. Hyaluronic Acid-Decorated Graphene Oxide Nanohybrids as Nanocarriers for Targeted and pH-Responsive Anticancer Drug Delivery. *ACS Appl. Mater. Interfaces* **2014**, *6*, 11882−11890.
(497) Zhu, X.; Xie, Y.; Zhang, Y.; Huang, H.; Huang, S.; Hou, L.; Zhang, H.; Li, Z.; Shi, J.; Zhang, Z. Thermo-sensitive liposomes loaded with doxorubicin and lysine modified single-walled carbon nanotubes as tumor-targeting drug delivery system. *J. Biomater. Appl.* **2014**, *29*, 769−779.
(498) An, J.; Gou, Y.; Yang, C.; Hu, F.; Wang, C. Synthesis of a biocompatible gelatin functionalized graphene nanosheets and its application for drug delivery. *Mater. Sci. Eng., C* **2013**, *33*, 2827−2837.
(499) Zakharian, T. Y.; Seryshev, A.; Sitharaman, B.; Gilbert, B. E.; Knight, V.; Wilson, L. J. A fullerene-paclitaxel chemotherapeutic: Synthesis, characterization, and study of biological activity in tissue culture. *J. Am. Chem. Soc.* **2005**, *127*, 12508−12509.
(500) Zhang, X.; Wang, S.; Liu, M.; Hui, J.; Yang, B.; Tao, L.; Wei, Y. Surfactant-dispersed nanodiamond: biocompatibility evaluation and drug delivery applications. *Toxicol. Res.* **2013**, *2* (5), 335−342.
(501) Liu, K.-K.; Zheng, W.-W.; Wang, C.-C.; Chiu, Y.-C.; Cheng, C.-L.; Lo, Y.-S.; Chen, C.; Chao, J.-I. Covalent linkage of nanodiamond-paclitaxel for drug delivery and cancer therapy. *Nanotechnology* **2010**, *21*, 315106.
(502) Zhang, X.; Wang, S.; Fu, C.; Feng, L.; Ji, Y.; Tao, L.; Li, S.; Wei, Y. PolyPEGylated nanodiamond for intracellular delivery of a chemotherapeutic drug. *Polym. Chem.* **2012**, *3*, 2716−2719.
(503) Ajima, K.; Yudasaka, M.; Murakami, T.; Maigne, A.; Shiba, K.; Iijima, S. Carbon nanohorns as anticancer drug carriers. *Mol. Pharmaceutics* **2005**, *2*, 475−480.
(504) Murakami, T.; Fan, J.; Yudasaka, M.; Iijima, S.; Shiba, K. Solubilization of single-wall carbon nanohorns using a PEG-doxorubicin conjugate. *Mol. Pharmaceutics* **2006**, *3*, 407−414.
(505) Murakami, T.; Sawada, H.; Tamura, G.; Yudasaka, M.; Iijima, S.; Tsuchida, K. Water-dispersed single-wall carbon nanohorns as drug carriers for local cancer chemotherapy. *Nanomedicine* **2008**, *3*, 453−463.
(506) Ma, D.; Lin, J.; Chen, Y.; Xue, W.; Zhang, L.-M. In situ gelation and sustained release of an antitumor drug by graphene oxide nanosheets. *Carbon* **2012**, *50*, 3001−3007.
(507) Kavitha, T.; Haider Abdi, S. I.; Park, S.-Y. pH-Sensitive nanocargo based on smart polymer functionalized graphene oxide for site-specific drug delivery. *Phys. Chem. Chem. Phys.* **2013**, *15*, 5176−5185.
(508) Khan, M. S.; Pandey, S.; Talib, T.; Bhaisare, M. L.; Wu, H.-F. Controlled delivery of dopamine hydrochloride using surface modified carbon dots for neuro diseases. *Colloids Surf., B* **2015**, *134*, 140−146.
(509) Kavitha, T.; Kang, I.-K.; Park, S.-Y. Poly(N-vinyl caprolactam) grown on nanographene oxide as an effective nanocargo for drug delivery. *Colloids Surf., B* **2014**, *115*, 37−45.
(510) Tripisciano, C.; Kraemer, K.; Taylor, A.; Borowiak-Palen, E. Single-wall carbon nanotubes based anticancer drug delivery system. *Chem. Phys. Lett.* **2009**, *478*, 200−205.
(511) Shi, J.; Zhang, H.; Wang, L.; Li, L.; Wang, H.; Wang, Z.; Li, Z.; Chen, C.; Hou, L.; Zhang, C.; Zhang, Z. PEI-derivatized fullerene drug delivery using folate as a homing device targeting to tumor. *Biomaterials* **2013**, *34*, 251−261.
(512) Salaam, A. D.; Hwang, P.; McIntosh, R.; Green, H. N.; Jun, H.-W.; Dean, D. Nanodiamond-DGEA peptide conjugates for enhanced delivery of doxorubicin to prostate cancer. *Beilstein J. Nanotechnol.* **2014**, *5*, 937−945.
(513) Shi, J.; Liu, Y.; Wang, L.; Gao, J.; Zhang, J.; Yu, X.; Ma, R.; Liu, R.; Zhang, Z. A tumoral acidic pH-responsive drug delivery system based on a novel photosensitizer (fullerene) for in vitro and in vivo chemo-photodynamic therapy. *Acta Biomater.* **2014**, *10*, 1280−1291.
(514) Pan, Y.; Bao, H.; Sahoo, N. G.; Wu, T.; Li, L. Water-Soluble Poly(N-isopropylacrylamide)-Graphene Sheets Synthesized *via* Click Chemistry for Drug Delivery. *Adv. Funct. Mater.* **2011**, *21*, 2754−2763.
(515) Cheng, L.; Li, Y.; Zhai, X.; Xu, B.; Cao, Z.; Liu, W. Polycation-b-Polyzwitterion Copolymer Grafted Luminescent Carbon Dots As a Multifunctional Platform for Serum-Resistant Gene Delivery and Bioimaging. *ACS Appl. Mater. Interfaces* **2014**, *6*, 20487−20497.
(516) Caoduro, C.; Hervouet, E.; Girard-Thernier, C.; Gharbi, T.; Boulahdour, H.; Delage-Mourroux, R.; Pudlo, M. Carbon nanotubes as gene carriers: Focus on internalization pathways related to functionalization and properties. *Acta Biomater.* **2017**, *49*, 36−44.
(517) Pantarotto, D.; Singh, R.; McCarthy, D.; Erhardt, M.; Briand, J.-P.; Prato, M.; Kostarelos, K.; Bianco, A. Functionalized Carbon Nanotubes for Plasmid DNA Gene Delivery. *Angew. Chem., Int. Ed.* **2004**, *43* (39), 5242−5246.
(518) Bianco, A.; Kostarelos, K.; Partidos, C. D.; Prato, M. Biomedical applications of functionalised carbon nanotubes. *Chem. Commun.* **2005**, *0*, 571−577.
(519) Gao, L.; Nie, L.; Wang, T.; Qin, Y.; Guo, Z.; Yang, D.; Yan, X. Carbon Nanotube Delivery of the GFP Gene into Mammalian Cells. *ChemBioChem* **2006**, *7*, 239−242.
(520) Singh, R.; Pantarotto, D.; McCarthy, D.; Chaloin, O.; Hoebeke, J.; Partidos, C. D.; Briand, J.-P.; Prato, M.; Bianco, A.; Kostarelos, K. Binding and Condensation of Plasmid DNA onto Functionalized Carbon Nanotubes: Toward the Construction of Nanotube-Based Gene Delivery Vectors. *J. Am. Chem. Soc.* **2005**, *127*, 4388−4396.
(521) Liu, M.; Chen, B.; Xue, Y.; Huang, J.; Zhang, L.; Huang, S.; Li, Q.; Zhang, Z. Polyamidoamine-Grafted Multiwalled Carbon Nanotubes for Gene Delivery: Synthesis, Transfection and Intracellular Trafficking. *Bioconjugate Chem.* **2011**, *22*, 2237−2243.
(522) Kam, N. W. S.; Liu, Z.; Dai, H. Functionalization of Carbon Nanotubes *via* Cleavable Disulfide Bonds for Efficient Intracellular Delivery of siRNA and Potent Gene Silencing. *J. Am. Chem. Soc.* **2005**, *127*, 12492−12493.
(523) Bartholomeusz, G.; Cherukuri, P.; Kingston, J.; Cognet, L.; Lemos, R.; Leeuw, T. K.; Gumbiner-Russo, L.; Weisman, R. B.; Powis, G. *In vivo* therapeutic silencing of hypoxia-inducible factor 1 alpha (HIF-1α) using single-walled carbon nanotubes noncovalently coated with siRNA. *Nano Res.* **2009**, *2*, 279−291.
(524) Chen, H.; Ma, X.; Li, Z.; Shi, Q.; Zheng, W.; Liu, Y.; Wang, P. Functionalization of single-walled carbon nanotubes enables efficient intracellular delivery of siRNA targeting MDM2 to inhibit breast cancer cells growth. *Biomed. Pharmacother.* **2012**, *66*, 334−338.
(525) Liu, Z.; Winters, M.; Holodniy, M.; Dai, H. siRNA Delivery into Human T Cells and Primary Cells with Carbon-Nanotube Transporters. *Angew. Chem., Int. Ed.* **2007**, *46*, 2023−2027.
(526) Zhang, Z.; Yang, X.; Zhang, Y.; Zeng, B.; Wang, S.; Zhu, T.; Roden, R. B. S.; Chen, Y.; Yang, R. Delivery of Telomerase Reverse

DOI: 10.1021/acs.chemrev.9b00099
Chem. Rev. XXXX, XXX, XXX−XXX

Transcriptase Small Interfering RNA in Complex with Positively Charged Single-Walled Carbon Nanotubes Suppresses Tumor Growth. *Clin. Cancer Res.* **2006**, *12*, 4933−4939.
(527) Da Ros, T.; Ostric, A.; Andreola, F.; Filocamo, M.; Pietrogrande, M.; Corsolini, F.; Stroppiano, M.; Bruni, S.; Serafino, A.; Fiorito, S. Carbon nanotubes as nanovectors for intracellular delivery of laronidase in Mucopolysaccharidosis type I. *Nanoscale* **2018**, *10*, 657−665.
(528) Feng, L.; Yang, X.; Shi, X.; Tan, X.; Peng, R.; Wang, J.; Liu, Z. Polyethylene Glycol and Polyethylenimine Dual-Functionalized Nano-Graphene Oxide for Photothermally Enhanced Gene Delivery. *Small* **2013**, *9*, 1989−1997.
(529) Yin, D.; Li, Y.; Lin, H.; Guo, B.; Du, Y.; Li, X.; Jia, H.; Zhao, X.; Tang, J.; Zhang, L. Functional graphene oxide as a plasmid-based Stat3 siRNA carrier inhibits mouse malignant melanoma growth in vivo. *Nanotechnology* **2013**, *24*, 105102.
(530) Sarkar, K.; Madras, G.; Chatterjee, K. Dendron conjugation to graphene oxide using click chemistry for efficient gene delivery. *RSC Adv.* **2015**, *5*, 50196−50211.
(531) Ghosal, K.; Sarkar, K. Biomedical Applications of Graphene Nanomaterials and Beyond. *ACS Biomater. Sci. Eng.* **2018**, *4*, 2653−2703.
(532) Zhang, L.; Wang, Z.; Lu, Z.; Shen, H.; Huang, J.; Zhao, Q.; Liu, M.; He, N.; Zhang, Z. PEGylated reduced graphene oxide as a superior ssRNA delivery system. *J. Mater. Chem. B* **2013**, *1*, 749−755.
(533) Imani, R.; Emami, S. H.; Faghihi, S. Synthesis and characterization of an octaarginine functionalized graphene oxide nano-carrier for gene delivery applications. *Phys. Chem. Chem. Phys.* **2015**, *17*, 6328−6339.
(534) Yang, X.; Zhao, N.; Xu, F.-J. Biocleavable graphene oxide based-nanohybrids synthesized *via* ATRP for gene/drug delivery. *Nanoscale* **2014**, *6*, 6141−6150.
(535) Paul, A.; Hasan, A.; Kindi, H. A.; Gaharwar, A. K.; Rao, V. T. S.; Nikkhah, M.; Shin, S. R.; Krafft, D.; Dokmeci, M. R.; Shum-Tim, D.; Khademhosseini, A. Injectable Graphene Oxide/Hydrogel-Based Angiogenic Gene Delivery System for Vasculogenesis and Cardiac Repair. *ACS Nano* **2014**, *8*, 8050−8062.
(536) Guerra, J.; Herrero, M. A.; Carrión, B.; Pérez-Martínez, F. C.; Lucío, M.; Rubio, N.; Meneghetti, M.; Prato, M.; Ceña, V.; Vázquez, E. Carbon nanohorns functionalized with polyamidoamine dendrimers as efficient biocarrier materials for gene therapy. *Carbon* **2012**, *50*, 2832−2844.
(537) Pérez-Martínez, F. C.; Carrión, B.; Lucío, M. I.; Rubio, N.; Herrero, M. A.; Vázquez, E.; Ceña, V. Enhanced docetaxel-mediated cytotoxicity in human prostate cancer cells through knockdown of cofilin-1 by carbon nanohorn delivered siRNA. *Biomaterials* **2012**, *33*, 8152−8159.
(538) Nierengarten, I.; Nierengarten, J.-F. The Impact of Copper-Catalyzed Alkyne−Azide 1,3-Dipolar Cycloaddition in Fullerene Chemistry. *Chem. Rec.* **2015**, *15*, 31−51.
(539) Sigwalt, D.; Holler, M.; Iehl, J.; Nierengarten, J.-F.; Nothisen, M.; Morin, E.; Remy, J.-S. Gene delivery with polycationic fullerene hexakis-adducts. *Chem. Commun.* **2011**, *47*, 4640−4642.
(540) Nierengarten, J.-F. Fullerene hexa-adduct scaffolding for the construction of giant molecules. *Chem. Commun.* **2017**, *53*, 11855−11868.
(541) Zhang, X.-Q.; Chen, M.; Lam, R.; Xu, X.; Osawa, E.; Ho, D. Polymer-Functionalized Nanodiamond Platforms as Vehicles for Gene Delivery. *ACS Nano* **2009**, *3*, 2609−2616.
(542) Xu, X.; Wang, J.; Wang, Y.; Zhao, L.; Li, Y.; Liu, C. Formation of graphene oxide-hybridized nanogels for combinative anticancer therapy. *Nanomedicine* **2018**, *14*, 2387−2395.
(543) Chen, H.; Wang, Z.; Zong, S.; Chen, P.; Zhu, D.; Wu, L.; Cui, Y. A graphene quantum dot-based FRET system for nuclear-targeted and real-time monitoring of drug delivery. *Nanoscale* **2015**, *7*, 15477−15486.
(544) Dong, H.; Dai, W.; Ju, H.; Lu, H.; Wang, S.; Xu, L.; Zhou, S.-F.; Zhang, Y.; Zhang, X. Multifunctional Poly(l-lactide)−Polyethylene Glycol-Grafted Graphene Quantum Dots for Intracellular MicroRNA Imaging and Combined Specific-Gene-Targeting Agents Delivery for Improved Therapeutics. *ACS Appl. Mater. Interfaces* **2015**, *7*, 11015−11023.
(545) Xu, C.; Yang, D.; Mei, L.; Lu, B.; Chen, L.; Li, Q.; Zhu, H.; Wang, T. Encapsulating Gold Nanoparticles or Nanorods in Graphene Oxide Shells as a Novel Gene Vector. *ACS Appl. Mater. Interfaces* **2013**, *5*, 2715−2724.
(546) Zhi, F.; Dong, H.; Jia, X.; Guo, W.; Lu, H.; Yang, Y.; Ju, H.; Zhang, X.; Hu, Y. Functionalized Graphene Oxide Mediated Adriamycin Delivery and miR-21 Gene Silencing to Overcome Tumor Multidrug Resistance *In vitro*. *PLoS One* **2013**, *8*, No. e60034.
(547) Kim, H.; Kim, W. J. Photothermally Controlled Gene Delivery by Reduced Graphene Oxide−Polyethylenimine Nanocomposite. *Small* **2014**, *10*, 117−126.
(548) Sun, Y.; Zhou, J.; Cheng, Q.; Lin, D.; Jiang, Q.; Dong, A.; Liang, Z.; Deng, L. Fabrication of mPEGylated graphene oxide/poly(2-dimethyl aminoethyl methacrylate) nanohybrids and their primary application for small interfering RNA delivery. *J. Appl. Polym. Sci.* **2016**, *133*, 43303.
(549) Pei, M.; Jia, X.; Liu, P. Design of Janus-like PMMA-PEG-FA grafted fluorescent carbon dots and their nanoassemblies for leakage-free tumor theranostic application. *Mater. Des.* **2018**, *155*, 288−296.
(550) Yang, X.; Wang, Y.; Shen, X.; Su, C.; Yang, J.; Piao, M.; Jia, F.; Gao, G.; Zhang, L.; Lin, Q. One-step synthesis of photoluminescent carbon dots with excitation-independent emission for selective bioimaging and gene delivery. *J. Colloid Interface Sci.* **2017**, *492*, 1−7.
(551) Yang, Z.; Hou, B.; Yang, Y.; Jiang, L.; Xie, A.; Shen, Y.; Zhu, M. A pH-induced charge convertible nanocomposite as novel targeted phototherapy agent and gene carrier. *Chem. Eng. J.* **2018**, *353*, 350−360.
(552) Zhang, L.; Yang, X.; Li, Y.; Zheng, W.; Jiang, X. Hollow carbon nanospheres as a versatile platform for co-delivery of siRNA and chemotherapeutics. *Carbon* **2017**, *121*, 79−89.
(553) Lim, D. G.; Rajasekaran, N.; Lee, D.; Kim, N. A.; Jung, H. S.; Hong, S.; Shin, Y. K.; Kang, E.; Jeong, S. H. Polyamidoamine-Decorated Nanodiamonds as a Hybrid Gene Delivery Vector and siRNA Structural Characterization at the Charged Interfaces. *ACS Appl. Mater. Interfaces* **2017**, *9*, 31543−31556.
(554) Chen, J.; Wang, Q.; Zhou, J.; Deng, W.; Yu, Q.; Cao, X.; Wang, J.; Shao, F.; Li, Y.; Ma, P.; Spector, M.; Yu, J.; Xu, X. Porphyra polysaccharide-derived carbon dots for non-viral co-delivery of different gene combinations and neuronal differentiation of ectodermal mesenchymal stem cells. *Nanoscale* **2017**, *9*, 10820−10831.
(555) Luo, T.-Y.; He, X.; Zhang, J.; Chen, P.; Liu, Y.-H.; Wang, H.-J.; Yu, X.-Q. Photoluminescent F-doped carbon dots prepared by ring-opening reaction for gene delivery and cell imaging. *RSC Adv.* **2018**, *8*, 6053−6062.
(556) Yang, Y.; Wang, Y.; Zhu, M.; Chen, Y.; Xiao, Y.; Shen, Y.; Xie, A. RGO/AuNR/HA-5FU nanocomposite with multi-stage release behavior and efficient antitumor activity for synergistic therapy. *Biomater. Sci.* **2017**, *5*, 990−1000.
(557) Cao, X.; Wang, J.; Deng, W.; Chen, J.; Wang, Y.; Zhou, J.; Du, P.; Xu, W.; Wang, Q.; Wang, Q.; Yu, Q.; Spector, M.; Yu, J.; Xu, X. Photoluminescent Cationic Carbon Dots as efficient Non-Viral Delivery of Plasmid SOX9 and Chondrogenesis of Fibroblasts. *Sci. Rep.* **2018**, *8*, 7057.
(558) Iverson, N. M.; Barone, P. W.; Shandell, M.; Trudel, L. J.; Sen, S.; Sen, F.; Ivanov, V.; Atolia, E.; Farias, E.; McNicholas, T. P.; Reuel, N.; Parry, N. M. A.; Wogan, G. N.; Strano, M. S. *In vivo* Biosensing *via* Tissue-Localizable Near-Infrared-Fluorescent Single-Walled Carbon Nanotubes. *Nat. Nanotechnol.* **2013**, *8*, 873−880.
(559) Bonis-O'Donnell, J. T. D.; Page, R. H.; Beyene, A. G.; Tindall, E. G.; McFarlane, I. R.; Landry, M. P. Dual Near-Infrared Two-Photon Microscopy for Deep-Tissue Dopamine Nanosensor Imaging. *Adv. Funct. Mater.* **2017**, *27*, 1702112.
(560) Beyene, A. G.; Delevich, K.; Del Bonis-O'Donnell, J. T.; Piekarski, D. J.; Lin, W. C.; Thomas, A. W.; Yang, S. J.; Kosillo, P.; Yang, D.; Wilbrecht, L.; Landry, M. P. Imaging Striatal Dopamine

DOI: 10.1021/acs.chemrev.9b00099
Chem. Rev. XXXX, XXX, XXX−XXX

Release Using A Non-Genetically Encoded Near-Infrared Fluorescent Catecholamine Nanosensor. *bioRxiv* **2018**, 356543.
(561) Rammohan, N.; MacRenaris, K. W.; Moore, L. K.; Parigi, G.; Mastarone, D. J.; Manus, L. M.; Lilley, L. M.; Preslar, A. T.; Waters, E. A.; Filicko, A.; Luchinat, C.; Ho, D.; Meade, T. J. Nanodiamond–Gadolinium(III) Aggregates for Tracking Cancer Growth *In vivo* at High Field. *Nano Lett.* **2016**, *16*, 7551–7564.
(562) Smith, B. R.; Gambhir, S. S. Nanomaterials for *In vivo* Imaging. *Chem. Rev.* **2017**, *117*, 901–986.
(563) Song, S.; Shen, H.; Yang, T.; Wang, L.; Fu, H.; Chen, H.; Zhang, Z. Indocyanine Green Loaded Magnetic Carbon Nanoparticles for Near Infrared Fluorescence/Magnetic Resonance Dual-Modal Imaging and Photothermal Therapy of Tumor. *ACS Appl. Mater. Interfaces* **2017**, *9*, 9484–9495.
(564) Kumar, S.; Rani, R.; Dilbaghi, N.; Tankeshwar, K.; Kim, K.-H. Carbon nanotubes: a novel material for multifaceted applications in human healthcare. *Chem. Soc. Rev.* **2017**, *46*, 158–196.
(565) Yang, K.; Hu, L.; Ma, X.; Ye, S.; Cheng, L.; Shi, X.; Li, C.; Li, Y.; Liu, Z. Multimodal Imaging Guided Photothermal Therapy using Functionalized Graphene Nanosheets Anchored with Magnetic Nanoparticles. *Adv. Mater.* **2012**, *24*, 1868–1872.
(566) Simpson, D. A.; Thompson, A. J.; Kowarsky, M.; Zeeshan, N. F.; Barson, M. S. J.; Hall, L. T.; Yan, Y.; Kaufmann, S.; Johnson, B. C.; Ohshima, T.; Caruso, F.; Scholten, R. E.; Saint, R. B.; Murray, M. J.; Hollenberg, L. C. L. *In vivo* imaging and tracking of individual nanodiamonds in drosophila melanogaster embryos. *Biomed. Opt. Express* **2014**, *5*, 1250–1261.
(567) Sarkar, S. K.; Bumb, A.; Wu, X.; Sochacki, K. A.; Kellman, P.; Brechbiel, M. W.; Neuman, K. C. Wide-field in vivo background free imaging by selective magnetic modulation of nanodiamond fluorescence. *Biomed. Opt. Express* **2014**, *5*, 1190–1202.
(568) Igarashi, R.; Yoshinari, Y.; Yokota, H.; Sugi, T.; Sugihara, F.; Ikeda, K.; Sumiya, H.; Tsuji, S.; Mori, I.; Tochio, H.; Harada, Y.; Shirakawa, M. Real-Time Background-Free Selective Imaging of Fluorescent Nanodiamonds in vivo. *Nano Lett.* **2012**, *12*, 5726–5732.
(569) Miyawaki, J.; Yudasaka, M.; Imai, H.; Yorimitsu, H.; Isobe, H.; Nakamura, E.; Iijima, S. *In vivo* magnetic resonance imaging of single-walled carbon nanohorns by labeling with magnetite nanoparticles. *Adv. Mater.* **2006**, *18*, 1010–1014.
(570) Chen, M.-L.; Shen, L.-M.; Chen, S.; Wang, H.; Chen, X.-W.; Wang, J.-H. In situ growth of beta-FeOOH nanorods on graphene oxide with ultra-high relaxivity for in vivo magnetic resonance imaging and cancer therapy. *J. Mater. Chem. B* **2013**, *1*, 2582–2589.
(571) Lin, Y.-C.; Perevedentseva, E.; Tsai, L.-W.; Wu, K.-T.; Cheng, C.-L. Nanodiamond for intracellular imaging in the microorganisms in vivo. *J. Biophotonics* **2012**, *5*, 838–847.
(572) Mohan, N.; Chen, C.-S.; Hsieh, H.-H.; Wu, Y.-C.; Chang, H.-C. *In vivo* Imaging and Toxicity Assessments of Fluorescent Nanodiamonds in Caenorhabditis elegans. *Nano Lett.* **2010**, *10*, 3692–3699.
(573) Rong, P.; Yang, K.; Srivastan, A.; Kiesewetter, D. O.; Yue, X.; Wang, F.; Nie, L.; Bhirde, A.; Wang, Z.; Liu, Z.; Niu, G.; Wang, W.; Chen, X. Photosensitizer Loaded Nano-Graphene for Multimodality Imaging Guided Tumor Photodynamic Therapy. *Theranostics* **2014**, *4*, 229–239.
(574) Ma, X.; Tao, H.; Yang, K.; Feng, L.; Cheng, L.; Shi, X.; Li, Y.; Guo, L.; Liu, Z. A functionalized graphene oxide-iron oxide nanocomposite for magnetically targeted drug delivery, photothermal therapy, and magnetic resonance imaging. *Nano Res.* **2012**, *5*, 199–212.
(575) Liang, C.; Diao, S.; Wang, C.; Gong, H.; Liu, T.; Hong, G.; Shi, X.; Dai, H.; Liu, Z. Tumor Metastasis Inhibition by Imaging-Guided Photothermal Therapy with Single-Walled Carbon Nanotubes. *Adv. Mater.* **2014**, *26*, 5646–5652.
(576) Sheng, Z.; Song, L.; Zheng, J.; Hu, D.; He, M.; Zheng, M.; Gao, G.; Gong, P.; Zhang, P.; Ma, Y.; Cai, L. Protein-assisted fabrication of nano-reduced graphene oxide for combined in vivo photoacoustic imaging and photothermal therapy. *Biomaterials* **2013**, *34*, 5236–5243.
(577) Nurunnabi, M.; Khatun, Z.; Reeck, G. R.; Lee, D. Y.; Lee, Y.-k. Photoluminescent Graphene Nanoparticles for Cancer Phototherapy and Imaging. *ACS Appl. Mater. Interfaces* **2014**, *6*, 12413–12421.
(578) Krishna, V.; Singh, A.; Sharma, P.; Iwakuma, N.; Wang, Q.; Zhang, Q.; Knapik, J.; Jiang, H.; Grobmyer, S. R.; Koopman, B.; Moudgil, B. Polyhydroxy Fullerenes for Non-Invasive Cancer Imaging and Therapy. *Small* **2010**, *6*, 2236–2241.
(579) Cornelissen, B.; Able, S.; Kersemans, V.; Waghorn, P. A.; Myhra, S.; Jurkshat, K.; Crossley, A.; Vallis, K. A. Nanographene oxide-based radioimmunoconstructs for in vivo targeting and SPECT imaging of HER2-positive tumors. *Biomaterials* **2013**, *34*, 1146–1154.
(580) Hong, H.; Yang, K.; Zhang, Y.; Engle, J. W.; Feng, L.; Yang, Y.; Nayak, T. R.; Goel, S.; Bean, J.; Theuer, C. P.; Barnhart, T. E.; Liu, Z.; Cai, W. *In vivo* Targeting and Imaging of Tumor Vasculature with Radiolabeled, Antibody-Conjugated Nanographene. *ACS Nano* **2012**, *6*, 2361–2370.
(581) Shi, S.; Yang, K.; Hong, H.; Valdovinos, H. F.; Nayak, T. R.; Zhang, Y.; Theuer, C. P.; Barnhart, T. E.; Liu, Z.; Cai, W. Tumor vasculature targeting and imaging in living mice with reduced graphene oxide. *Biomaterials* **2013**, *34*, 3002–3009.
(582) Hong, H.; Zhang, Y.; Engle, J. W.; Nayak, T. R.; Theuer, C. P.; Nickles, R. J.; Barnhart, T. E.; Cai, W. *In vivo* targeting and positron emission tomography imaging of tumor vasculature with Ga-66-labeled nano-graphene. *Biomaterials* **2012**, *33*, 4147–4156.
(583) Yue, Z.; Lv, P.; Yue, H.; Gao, Y.; Ma, D.; Wei, W.; Ma, G. Inducible graphene oxide probe for high-specific tumor diagnosis. *Chem. Commun.* **2013**, *49*, 3902–3904.
(584) Shi, J.; Yu, X.; Wang, L.; Liu, Y.; Gao, J.; Zhang, J.; Ma, R.; Liu, R.; Zhang, Z. PEGylated fullerene/iron oxide nanocomposites for photodynamic therapy, targeted drug delivery and MR imaging. *Biomaterials* **2013**, *34*, 9666–9677.
(585) Wen, S.; Zhao, Q.; An, X.; Zhu, J.; Hou, W.; Li, K.; Huang, Y.; Shen, M.; Zhu, W.; Shi, X. Multifunctional PEGylated Multiwalled Carbon Nanotubes for Enhanced Blood Pool and Tumor MR Imaging. *Adv. Healthcare Mater.* **2014**, *3*, 1568–1577.
(586) Ghosh, D.; Bagley, A. F.; Na, Y. J.; Birrer, M. J.; Bhatia, S. N.; Belcher, A. M. Deep, noninvasive imaging and surgical guidance of submillimeter tumors using targeted M13-stabilized single-walled carbon nanotubes. *Proc. Natl. Acad. Sci. U. S. A.* **2014**, *111*, 13948–13953.
(587) Hui, Y. Y.; Su, L.-J.; Chen, O. Y.; Chen, Y.-T.; Liu, T.-M.; Chang, H.-C. Wide-field imaging and flow cytometric analysis of cancer cells in blood by fluorescent nanodiamond labeling and time gating. *Sci. Rep.* **2015**, *4*, 5574.
(588) Sun, Z.; Huang, P.; Tong, G.; Lin, J.; Jin, A.; Rong, P.; Zhu, L.; Nie, L.; Niu, G.; Cao, F.; Chen, X. VEGF-loaded graphene oxide as theranostics for multi-modality imaging-monitored targeting therapeutic angiogenesis of ischemic muscle. *Nanoscale* **2013**, *5*, 6857–6866.
(589) Hong, G.; Diao, S.; Antaris, A. L.; Dai, H. Carbon Nanomaterials for Biological Imaging and Nanomedicinal Therapy. *Chem. Rev.* **2015**, *115*, 10816–10906.
(590) Bardhan, N. M.; Ghosh, D.; Belcher, A. M. Carbon Nanotubes as *In vivo* Bacterial Probes. *Nat. Commun.* **2014**, *5*, 4918.
(591) Liu, Z.; Davis, C.; Cai, W.; He, L.; Chen, X.; Dai, H. Circulation and Long-Term Fate of Functionalized, Biocompatible Single-Walled Carbon Nanotubes in Mice Probed by Raman Spectroscopy. *Proc. Natl. Acad. Sci. U. S. A.* **2008**, *105*, 1410–1415.
(592) Liu, Z.; Cai, W.; He, L.; Nakayama, N.; Chen, K.; Sun, X.; Chen, X.; Dai, H. *In vivo* Biodistribution and Highly Efficient Tumour Targeting of Carbon Nanotubes in Mice. *Nat. Nanotechnol.* **2007**, *2*, 47–52.
(593) Hong, G.; Antaris, A. L.; Dai, H. Near-Infrared Fluorophores for Biomedical Imaging. *Nat. Biomed. Eng.* **2017**, *1*, 0010.
(594) Keren, S.; Zavaleta, C.; Cheng, Z.; de la Zerda, A.; Gheysens, O.; Gambhir, S. S. Noninvasive Molecular Imaging of Small Living Subjects Using Raman Spectroscopy. *Proc. Natl. Acad. Sci. U. S. A.* **2008**, *105*, 5844–5849.

DOI: 10.1021/acs.chemrev.9b00099
Chem. Rev. XXXX, XXX, XXX–XXX

(595) Zavaleta, C.; de la Zerda, A.; Liu, Z.; Keren, S.; Cheng, Z.; Schipper, M.; Chen, X.; Dai, H.; Gambhir, S. S. Noninvasive Raman Spectroscopy in Living Mice for Evaluation of Tumor Targeting with Carbon Nanotubes. *Nano Lett.* **2008**, *8*, 2800−2805.
(596) Welsher, K.; Liu, Z.; Sherlock, S. P.; Robinson, J. T.; Chen, Z.; Daranciang, D.; Dai, H. A Route to Brightly Fluorescent Carbon Nanotubes for Near-Infrared Imaging in Mice. *Nat. Nanotechnol.* **2009**, *4*, 773−780.
(597) Robinson, J. T.; Welsher, K.; Tabakman, S. M.; Sherlock, S. P.; Wang, H.; Luong, R.; Dai, H. High Performance *In vivo* Near-IR (>1 μm) Imaging and Photothermal Cancer Therapy with Carbon Nanotubes. *Nano Res.* **2010**, *3*, 779−793.
(598) Welsher, K.; Sherlock, S. P.; Dai, H. Deep-Tissue Anatomical Imaging of Mice Using Carbon Nanotube Fluorophores in the Second Near-Infrared Window. *Proc. Natl. Acad. Sci. U. S. A.* **2011**, *108*, 8943−8948.
(599) Robinson, J. T.; Hong, G.; Liang, Y.; Zhang, B.; Yaghi, O. K.; Dai, H. *In vivo* Fluorescence Imaging in the Second Near-Infrared Window with Long Circulating Carbon Nanotubes Capable of Ultrahigh Tumor Uptake. *J. Am. Chem. Soc.* **2012**, *134*, 10664−10669.
(600) Hong, G.; Lee, J. C.; Robinson, J. T.; Raaz, U.; Xie, L.; Huang, N. F.; Cooke, J. P.; Dai, H. Multifunctional *In vivo* Vascular Imaging Using Near-Infrared II Fluorescence. *Nat. Med.* **2012**, *18*, 1841−1846.
(601) Wang, C.; Ma, X.; Ye, S.; Cheng, L.; Yang, K.; Guo, L.; Li, C.; Li, Y.; Liu, Z. Protamine Functionalized Single-Walled Carbon Nanotubes for Stem Cell Labeling and *In vivo* Raman/Magnetic Resonance/Photoacoustic Triple-Modal Imaging. *Adv. Funct. Mater.* **2012**, *22*, 2363−2375.
(602) Hong, G.; Lee, J. C.; Jha, A.; Diao, S.; Nakayama, K. H.; Hou, L.; Doyle, T. C.; Robinson, J. T.; Antaris, A. L.; Dai, H.; Cooke, J. P.; Huang, N. F. Near-Infrared II Fluorescence for Imaging Hindlimb Vessel Regeneration With Dynamic Tissue Perfusion Measurement. *Circ. Cardiovasc. Imaging* **2014**, *7*, 517−525.
(603) Diao, S.; Hong, G.; Robinson, J. T.; Jiao, L.; Antaris, A. L.; Wu, J. Z.; Choi, C. L.; Dai, H. Chirality Enriched (12,1) and (11,3) Single-Walled Carbon Nanotubes for Biological Imaging. *J. Am. Chem. Soc.* **2012**, *134*, 16971−16974.
(604) Antaris, A. L.; Robinson, J. T.; Yaghi, O. K.; Hong, G.; Diao, S.; Luong, R.; Dai, H. Ultra-Low Doses of Chirality Sorted (6,5) Carbon Nanotubes for Simultaneous Tumor Imaging and Photothermal Therapy. *ACS Nano* **2013**, *7*, 3644−3652.
(605) Ghosh, S.; Bachilo, S. M.; Weisman, R. B. Advanced Sorting of Single-Walled Carbon Nanotubes by Nonlinear Density-Gradient Ultracentrifugation. *Nat. Nanotechnol.* **2010**, *5*, 443−450.
(606) Green, A. A.; Hersam, M. C. Processing and Properties of Highly Enriched Double-Wall Carbon Nanotubes. *Nat. Nanotechnol.* **2009**, *4*, 64−70.
(607) Hong, G.; Diao, S.; Chang, J.; Antaris, A. L.; Chen, C.; Zhang, B.; Zhao, S.; Atochin, D. N.; Huang, P. L.; Andreasson, K. I.; Kuo, C. J.; Dai, H. Through-Skull Fluorescence Imaging of the Brain in a New Near-Infrared Window. *Nat. Photonics* **2014**, *8*, 723−730.
(608) Diao, S.; Blackburn, J. L.; Hong, G.; Antaris, A. L.; Chang, J.; Wu, J. Z.; Zhang, B.; Cheng, K.; Kuo, C. J.; Dai, H. Fluorescence Imaging *In vivo* at Wavelengths beyond 1500 nm. *Angew. Chem., Int. Ed.* **2015**, *54*, 14758−14762.
(609) Dang, X.; Gu, L.; Qi, J.; Correa, S.; Zhang, G.; Belcher, A. M.; Hammond, P. T. Layer-By-Layer Assembled Fluorescent Probes in the Second Near-Infrared Window for Systemic Delivery and Detection of Ovarian Cancer. *Proc. Natl. Acad. Sci. U. S. A.* **2016**, *113*, 5179−5184.
(610) Snyder-Talkington, B. N.; Dong, C.; Zhao, X.; Dymacek, J.; Porter, D. W.; Wolfarth, M. G.; Castranova, V.; Qian, Y.; Guo, N. L. Multi-walled carbon nanotube-induced gene expression in vitro: Concordance with in vivo studies. *Toxicology* **2015**, *328*, 66−74.
(611) Yang, K.; Feng, L.; Liu, Z. Stimuli responsive drug delivery systems based on nano-graphene for cancer therapy. *Adv. Drug Delivery Rev.* **2016**, *105*, 228−241.
(612) Kafa, H.; Wang, J. T.-W.; Rubio, N.; Klippstein, R.; Costa, P. M.; Hassan, H. A. F. M.; Sosabowski, J. K.; Bansal, S. S.; Preston, J. E.; Abbott, N. J.; Al-Jamal, K. T. Translocation of LRP1 targeted carbon nanotubes of different diameters across the blood−brain barrier in vitro and in vivo. *J. Controlled Release* **2016**, *225*, 217−229.
(613) Razzazan, A.; Atyabi, F.; Kazemi, B.; Dinarvand, R. *In vivo* drug delivery of gemcitabine with PEGylated single-walled carbon nanotubes. *Mater. Sci. Eng., C* **2016**, *62*, 614−625.
(614) Baldrighi, M.; Trusel, M.; Tonini, R.; Giordani, S. Carbon Nanomaterials interfacing with neurons: an in vivo perspective. *Front. Neurosci.* **2016**, *10*, 250.
(615) Zhang, B.; Wang, H.; Shen, S.; She, X.; Shi, W.; Chen, J.; Zhang, Q.; Hu, Y.; Pang, Z.; Jiang, X. Fibrin-targeting peptide CREKA-conjugated multi-walled carbon nanotubes for self-amplified photothermal therapy of tumor. *Biomaterials* **2016**, *79*, 46−55.
(616) von Maltzahn, G.; Park, J.-H.; Lin, K. Y.; Singh, N.; Schwöppe, C.; Mesters, R.; Berdel, W. E.; Ruoslahti, E.; Sailor, M. J.; Bhatia, S. N. Nanoparticles that communicate in vivo to amplify tumour targeting. *Nat. Mater.* **2011**, *10*, 545−552.
(617) Wang, J.-G.; Geddings, J. E.; Aleman, M. M.; Cardenas, J. C.; Chantrathammachart, P.; Williams, J. C.; Kirchhofer, D.; Bogdanov, V. Y.; Bach, R. R.; Rak, J.; Church, F. C.; Wolberg, A. S.; Pawlinski, R.; Key, N. S.; Yeh, J. J.; Mackman, N. Tumor-derived tissue factor activates coagulation and enhances thrombosis in a mouse xenograft model of human pancreatic cancer. *Blood* **2012**, *119*, 5543−5552.
(618) Nakamura, M.; Tahara, Y.; Ikehara, Y.; Murakami, T.; Tsuchida, K.; Iijima, S.; Waga, I.; Yudasaka, M. Single-walled carbon nanohorns as drug carriers: adsorption of prednisolone and anti-inflammatory effects on arthritis. *Nanotechnology* **2011**, *22*, 465102.
(619) Zhang, Z.; Niu, B.; Chen, J.; He, X.; Bao, X.; Zhu, J.; Yu, H.; Li, Y. The use of lipid-coated nanodiamond to improve bioavailability and efficacy of sorafenib in resisting metastasis of gastric cancer. *Biomaterials* **2014**, *35*, 4565−4572.
(620) Yang, Y.; Zhang, Y.-M.; Chen, Y.; Zhao, D.; Chen, J.-T.; Liu, Y. Construction of a Graphene Oxide Based Noncovalent Multiple Nanosupramolecular Assembly as a Scaffold for Drug Delivery. *Chem. - Eur. J.* **2012**, *18*, 4208−4215.
(621) Zheng, M.; Liu, S.; Li, J.; Qu, D.; Zhao, H.; Guan, X.; Hu, X.; Xie, Z.; Jing, X.; Sun, Z. Integrating Oxaliplatin with Highly Luminescent Carbon Dots: An Unprecedented Theranostic Agent for Personalized Medicine. *Adv. Mater.* **2014**, *26*, 3554−3560.
(622) Chen, C. Y.; Xing, G. M.; Wang, J. X.; Zhao, Y. L.; Li, B.; Tang, J.; Jia, G.; Wang, T. C.; Sun, J.; Xing, L.; Yuan, H.; Gao, Y. X.; Meng, H.; Chen, Z.; Zhao, F.; Chai, Z. F.; Fang, X. H. Multi hydroxylated $[Gd@C_{82}(OH)_{22}]_n$ nanoparticles: Antineoplastic activity of high efficiency and low toxicity. *Nano Lett.* **2005**, *5*, 2050−2057.
(623) Zhu, J.; Ji, Z.; Wang, J.; Sun, R.; Zhang, X.; Gao, Y.; Sun, H.; Liu, Y.; Wang, Z.; Li, A.; Ma, J.; Wang, T.; Jia, G.; Gu, Y. Tumor-inhibitory effect and immunomodulatory activity of fullerol $C_{60}(OH)_x$. *Small* **2008**, *4*, 1168−1175.
(624) Yin, F.; Hu, K.; Chen, Y.; Yu, M.; Wang, D.; Wang, Q.; Yong, K.-T.; Lu, F.; Liang, Y.; Li, Z. SiRNA Delivery with PEGylated Graphene Oxide Nanosheets for Combined Photothermal and Genetherapy for Pancreatic Cancer. *Theranostics* **2017**, *7*, 1133−1148.
(625) Chen, H.; Liu, Z.; Li, S.; Su, C.; Qiu, X.; Zhong, H.; Guo, Z. Fabrication of Graphene and AuNP Core Polyaniline Shell Nanocomposites as Multifunctional Theranostic Platforms for SERS Real-time Monitoring and Chemo-photothermal Therapy. *Theranostics* **2016**, *6*, 1096−104.
(626) Dou, R.; Du, Z.; Bao, T.; Dong, X.; Zheng, X.; Yu, M.; Yin, W.; Dong, B.; Yan, L.; Gu, Z. The polyvinylpyrrolidone functionalized rGO/Bi_2S_3 nanocomposite as a near-infrared light-responsive nanovehicle for chemo-photothermal therapy of cancer. *Nanoscale* **2016**, *8*, 11531−11542.
(627) Zhao, H.; Duan, J.; Xiao, Y.; Tang, G.; Wu, C.; Zhang, Y.; Liu, Z.; Xue, W. Microenvironment-Driven Cascaded Responsive Hybrid Carbon Dots as a Multifunctional Theranostic Nanoplatform for Imaging-Traceable Gene Precise Delivery. *Chem. Mater.* **2018**, *30*, 3438−3453.
(628) Li, S.; Guo, Z.; Zeng, G.; Zhang, Y.; Xue, W.; Liu, Z. Polyethylenimine-Modified Fluorescent Carbon Dots As Vaccine

DOI: 10.1021/acs.chemrev.9b00099
Chem. Rev. XXXX, XXX, XXX−XXX

Delivery System for Intranasal Immunization. *ACS Biomater. Sci. Eng.* **2018**, *4*, 142−150.
(629) Zhang, Y.; Ali, S. F.; Dervishi, E.; Xu, Y.; Li, Z.; Casciano, D.; Biris, A. S. Cytotoxicity Effects of Graphene and Single-Wall Carbon Nanotubes in Neural Phaeochromocytoma-Derived PC12 Cells. *ACS Nano* **2010**, *4*, 3181−3186.
(630) Pelin, M.; Fusco, L.; León, V.; Martín, C.; Criado, A.; Sosa, S.; Vázquez, E.; Tubaro, A.; Prato, M. Differential cytotoxic effects of graphene and graphene oxide on skin keratinocytes. *Sci. Rep.* **2017**, *7*, 40572.
(631) Yuan, J.; Gao, H.; Ching, C. B. Comparative protein profile of human hepatoma HepG2 cells treated with graphene and single-walled carbon nanotubes: An iTRAQ-coupled 2D LC−MS/MS proteome analysis. *Toxicol. Lett.* **2011**, *207*, 213−221.
(632) Patlolla, A.; Knighten, B.; Tchounwou, P. Multi-walled carbon nanotubes induce cytotoxicity, genotoxicity and apoptosis in normal human dermal fibroblast cells. *Ethn. Dis.* **2010**, *20*, 65−72.
(633) Jia, G.; Wang, H.; Yan, L.; Wang, X.; Pei, R.; Yan, T.; Zhao, Y.; Guo, X. Cytotoxicity of Carbon Nanomaterials: Single-Wall Nanotube, Multi-Wall Nanotube, and Fullerene. *Environ. Sci. Technol.* **2005**, *39*, 1378−1383.
(634) Shvedova, A.; Castranova, V.; Kisin, E.; Schwegler-Berry, D.; Murray, A.; Gandelsman, V.; Maynard, A.; Baron, P. Exposure to Carbon Nanotube Material: Assessment of Nanotube Cytotoxicity using Human Keratinocyte Cells. *J. Toxicol. Environ. Health, Part A* **2003**, *66*, 1909−1926.
(635) Jacobsen, N. R.; Pojana, G.; White, P.; Møller, P.; Cohn, C. A.; Smith Korsholm, K.; Vogel, U.; Marcomini, A.; Loft, S.; Wallin, H. Genotoxicity, cytotoxicity, and reactive oxygen species induced by single-walled carbon nanotubes and C_{60} fullerenes in the FE1-MutaMouse lung epithelial cells. *Environ. Mol. Mutagen.* **2008**, *49*, 476−487.
(636) He, X.; Young, S.-H.; Schwegler-Berry, D.; Chisholm, W. P.; Fernback, J. E.; Ma, Q. Multiwalled Carbon Nanotubes Induce a Fibrogenic Response by Stimulating Reactive Oxygen Species Production, Activating NF-κB Signaling, and Promoting Fibroblast-to-Myofibroblast Transformation. *Chem. Res. Toxicol.* **2011**, *24*, 2237−2248.
(637) Nagai, H.; Okazaki, Y.; Chew, S. H.; Misawa, N.; Yamashita, Y.; Akatsuka, S.; Ishihara, T.; Yamashita, K.; Yoshikawa, Y.; Yasui, H.; Jiang, L.; Ohara, H.; Takahashi, T.; Ichihara, G.; Kostarelos, K.; Miyata, Y.; Shinohara, H.; Toyokuni, S. Diameter and rigidity of multiwalled carbon nanotubes are critical factors in mesothelial injury and carcinogenesis. *Proc. Natl. Acad. Sci. U. S. A.* **2011**, *108*, E1330−E1338.
(638) Wick, P.; Manser, P.; Limbach, L. K.; Dettlaff-Weglikowska, U.; Krumeich, F.; Roth, S.; Stark, W. J.; Bruinink, A. The degree and kind of agglomeration affect carbon nanotube cytotoxicity. *Toxicol. Lett.* **2007**, *168*, 121−131.
(639) Kim, J. S.; Song, K. S.; Lee, J. H.; Yu, I. J. Evaluation of biocompatible dispersants for carbon nanotube toxicity tests. *Arch. Toxicol.* **2011**, *85*, 1499−1508.
(640) Isakovic, A.; Markovic, Z.; Todorovic-Markovic, B.; Nikolic, N.; Vranjes-Djuric, S.; Mirkovic, M.; Dramicanin, M.; Harhaji, L.; Raicevic, N.; Nikolic, Z.; Trajkovic, V. Distinct Cytotoxic Mechanisms of Pristine versus Hydroxylated Fullerene. *Toxicol. Sci.* **2006**, *91*, 173−183.
(641) Sayes, C. M.; Fortner, J. D.; Guo, W.; Lyon, D.; Boyd, A. M.; Ausman, K. D.; Tao, Y. J.; Sitharaman, B.; Wilson, L. J.; Hughes, J. B.; West, J. L.; Colvin, V. L. The Differential Cytotoxicity of Water-Soluble Fullerenes. *Nano Lett.* **2004**, *4*, 1881−1887.
(642) Zakrzewska, K. E.; Samluk, A.; Wierzbicki, M.; Jaworski, S.; Kutwin, M.; Sawosz, E.; Chwalibog, A.; Pijanowska, D. G.; Pluta, K. D. Analysis of the Cytotoxicity of Carbon-Based Nanoparticles, Diamond and Graphite, in Human Glioblastoma and Hepatoma Cell Lines. *PLoS One* **2015**, *10*, No. e0122579.
(643) Liu, K.-K.; Cheng, C.-L.; Chang, C.-C.; Chao, J.-I Biocompatible and detectable carboxylated nanodiamond on human cell. *Nanotechnology* **2007**, *18*, 325102.
(644) Huang, H.; Pierstorff, E.; Osawa, E.; Ho, D. Protein-Mediated Assembly of Nanodiamond Hydrogels into a Biocompatible and Biofunctional Multilayer Nanofilm. *ACS Nano* **2008**, *2*, 203−212.
(645) Schrand, A. M.; Huang, H.; Carlson, C.; Schlager, J. J.; Osawa, E.; Hussain, S. M.; Dai, L. Are Diamond Nanoparticles Cytotoxic? *J. Phys. Chem. B* **2007**, *111*, 2−7.
(646) Schrand, A. M.; Dai, L.; Schlager, J. J.; Hussain, S. M.; Osawa, E. Differential biocompatibility of carbon nanotubes and nanodiamonds. *Diamond Relat. Mater.* **2007**, *16*, 2118−2123.
(647) Agemy, L.; Sugahara, K. N.; Kotamraju, V. R.; Gujraty, K.; Girard, O. M.; Kono, Y.; Mattrey, R. F.; Park, J. H.; Sailor, M. J.; Jimenez, A. I.; Cativiela, C.; Zanuy, D.; Sayago, F. J.; Aleman, C.; Nussinov, R.; Ruoslahti, E. Nanoparticle-induced vascular blockade in human prostate cancer. *Blood* **2010**, *116*, 2847−56.
(648) Akhavan, O.; Ghaderi, E.; Akhavan, A. Size-dependent genotoxicity of graphene nanoplatelets in human stem cells. *Biomaterials* **2012**, *33*, 8017−8025.
(649) Qiao, Y.; An, J.; Ma, L. Single Cell Array Based Assay for in vitro Genotoxicity Study of Nanomaterials. *Anal. Chem.* **2013**, *85*, 4107−4112.
(650) Li, S.; He, P.; Dong, J.; Guo, Z.; Dai, L. DNA-Directed Self-Assembling of Carbon Nanotubes. *J. Am. Chem. Soc.* **2005**, *127*, 14−15.
(651) Lindberg, H. K.; Falck, G. C. M.; Suhonen, S.; Vippola, M.; Vanhala, E.; Catalán, J.; Savolainen, K.; Norppa, H. Genotoxicity of nanomaterials: DNA damage and micronuclei induced by carbon nanotubes and graphite nanofibres in human bronchial epithelial cells in vitro. *Toxicol. Lett.* **2009**, *186*, 166−173.
(652) Yong, K.-T.; Law, W.-C.; Hu, R.; Ye, L.; Liu, L.; Swihart, M. T.; Prasad, P. N. Nanotoxicity assessment of quantum dots: from cellular to primate studies. *Chem. Soc. Rev.* **2013**, *42*, 1236−1250.
(653) Xing, Y.; Xiong, W.; Zhu, L.; Osawa, E.; Hussin, S.; Dai, L. DNA Damage in Embryonic Stem Cells Caused by Nanodiamonds. *ACS Nano* **2011**, *5*, 2376−2384.
(654) Zhang, W.; Wang, C.; Li, Z.; Lu, Z.; Li, Y.; Yin, J.-J.; Zhou, Y.-T.; Gao, X.; Fang, Y.; Nie, G.; Zhao, Y. Unraveling Stress-Induced Toxicity Properties of Graphene Oxide and the Underlying Mechanism. *Adv. Mater.* **2012**, *24*, 5391−5397.
(655) Zanni, E.; De Bellis, G.; Bracciale, M. P.; Broggi, A.; Santarelli, M. L.; Sarto, M. S.; Palleschi, C.; Uccelletti, D. Graphite Nanoplatelets and Caenorhabditis elegans: Insights from an in vivo Model. *Nano Lett.* **2012**, *12*, 2740−2744.
(656) Wu, Q.; Zhao, Y.; Zhao, G.; Wang, D. microRNAs control of in vivo toxicity from graphene oxide in Caenorhabditis elegans. *Nanomedicine* **2014**, *10*, 1401−1410.
(657) Usenko, C. Y.; Harper, S. L.; Tanguay, R. L. *In vivo* evaluation of carbon fullerene toxicity using embryonic zebrafish. *Carbon* **2007**, *45*, 1891−1898.
(658) Jeong, J.; Cho, H.-J.; Choi, M.; Lee, W. S.; Chung, B. H.; Lee, J.-S. *In vivo* toxicity assessment of angiogenesis and the live distribution of nano-graphene oxide and its PEGylated derivatives using the developing zebrafish embryo. *Carbon* **2015**, *93*, 431−440.
(659) Lin, Y.-C.; Wu, K.-T.; Lin, Z.-R.; Perevedentseva, E.; Karmenyan, A.; Lin, M.-D.; Cheng, C.-L. Nanodiamond for biolabelling and toxicity evaluation in the zebrafish embryo in vivo. *J. Biophotonics* **2016**, *9*, 827−836.
(660) Yuan, Y.; Chen, Y.; Liu, J.-H.; Wang, H.; Liu, Y. Biodistribution and fate of nanodiamonds in vivo. *Diamond Relat. Mater.* **2009**, *18* (1), 95−100.
(661) Zhang, X.; Yin, J.; Kang, C.; Li, J.; Zhu, Y.; Li, W.; Huang, Q.; Zhu, Z. Biodistribution and toxicity of nanodiamonds in mice after intratracheal instillation. *Toxicol. Lett.* **2010**, *198*, 237−243.
(662) Tao, H.; Yang, K.; Ma, Z.; Wan, J.; Zhang, Y.; Kang, Z.; Liu, Z. *In vivo* NIR Fluorescence Imaging, Biodistribution, and Toxicology of Photoluminescent Carbon Dots Produced from Carbon Nanotubes and Graphite. *Small* **2012**, *8*, 281−290.
(663) Sayes, C. M.; Marchione, A. A.; Reed, K. L.; Warheit, D. B. Comparative Pulmonary Toxicity Assessments of C_{60} Water

DOI: 10.1021/acs.chemrev.9b00099
Chem. Rev. XXXX, XXX, XXX−XXX

Suspensions in Rats: Few Differences in Fullerene Toxicity in vivo in Contrast to in vitro Profiles. *Nano Lett.* **2007**, *7*, 2399−2406.
(664) Muller, J.; Huaux, F.; Moreau, N.; Misson, P.; Heilier, J.-F.; Delos, M.; Arras, M.; Fonseca, A.; Nagy, J. B.; Lison, D. Respiratory toxicity of multi-wall carbon nanotubes. *Toxicol. Appl. Pharmacol.* **2005**, *207*, 221−231.
(665) Alidori, S.; Thorek, D. L. J.; Beattie, B. J.; Ulmert, D.; Almeida, B. A.; Monette, S.; Scheinberg, D. A.; McDevitt, M. R. Carbon nanotubes exhibit fibrillar pharmacology in primates. *PLoS One* **2017**, *12*, No. e0183902.
(666) Hunt, P. R. The C. elegans model in toxicity testing. *J. Appl. Toxicol.* **2017**, *37*, 50−59.
(667) Leung, M. C. K.; Williams, P. L.; Benedetto, A.; Au, C.; Helmcke, K. J.; Aschner, M.; Meyer, J. N. Caenorhabditis elegans: an emerging model in biomedical and environmental toxicology. *Toxicol. Sci.* **2008**, *106*, 5−28.
(668) Raldúa, D.; Piña, B. *In vivo* zebrafish assays for analyzing drug toxicity. *Expert Opin. Drug Metab. Toxicol.* **2014**, *10*, 685−697.
(669) Caballero, M. V.; Candiracci, M. Zebrafish as screening model for detecting toxicity and drugs efficacy. *J. Unexplored Med. Data* **2018**, *3*, 4.
(670) Wang, H.; Wang, J.; Deng, X.; Sun, H.; Shi, Z.; Gu, Z.; Liu, Y.; Zhao, Y. Biodistribution of carbon single-wall carbon nanotubes in mice. *J. Nanosci. Nanotechnol.* **2004**, *4*, 1019−24.
(671) Singh, R.; Pantarotto, D.; Lacerda, L.; Pastorin, G.; Klumpp, C.; Prato, M.; Bianco, A.; Kostarelos, K. Tissue biodistribution and blood clearance rates of intravenously administered carbon nanotube radiotracers. *Proc. Natl. Acad. Sci. U. S. A.* **2006**, *103*, 3357−3362.
(672) Yang, K.; Wan, J.; Zhang, S.; Zhang, Y.; Lee, S.-T.; Liu, Z. *In vivo* Pharmacokinetics, Long-Term Biodistribution, and Toxicology of PEGylated Graphene in Mice. *ACS Nano* **2011**, *5*, 516−522.
(673) Zhang, M.; Yamaguchi, T.; Iijima, S.; Yudasaka, M. Size-dependent biodistribution of carbon nanohorns in vivo. *Nanomedicine* **2013**, *9*, 657−664.
(674) Vaijayanthimala, V.; Cheng, P.-Y.; Yeh, S.-H.; Liu, K.-K.; Hsiao, C.-H.; Chao, J.-I.; Chang, H.-C. The long-term stability and biocompatibility of fluorescent nanodiamond as an in vivo contrast agent. *Biomaterials* **2012**, *33*, 7794−7802.
(675) Fan, H.; Wang, L.; Zhao, K.; Li, N.; Shi, Z.; Ge, Z.; Jin, Z. Fabrication, Mechanical Properties, and Biocompatibility of Graphene-Reinforced Chitosan Composites. *Biomacromolecules* **2010**, *11*, 2345−2351.
(676) Liao, K.-H.; Lin, Y.-S.; Macosko, C. W.; Haynes, C. L. Cytotoxicity of Graphene Oxide and Graphene in Human Erythrocytes and Skin Fibroblasts. *ACS Appl. Mater. Interfaces* **2011**, *3*, 2607−2615.
(677) Zhang, X.; Hu, W.; Li, J.; Tao, L.; Wei, Y. A comparative study of cellular uptake and cytotoxicity of multi-walled carbon nanotubes, graphene oxide, and nanodiamond. *Toxicol. Res.* **2012**, *1*, 62−68.
(678) Yamawaki, H.; Iwai, N. Cytotoxicity of water-soluble fullerene in vascular endothelial cells. *Am. J. Physiol.* **2006**, *290*, C1495−C1502.
(679) Sayes, C. M.; Gobin, A. M.; Ausman, K. D.; Mendez, J.; West, J. L.; Colvin, V. L. Nano-C_{60} cytotoxicity is due to lipid peroxidation. *Biomaterials* **2005**, *26*, 7587−7595.
(680) Miyawaki, J.; Yudasaka, M.; Azami, T.; Kubo, Y.; Iijima, S. Toxicity of Single-Walled Carbon Nanohorns. *ACS Nano* **2008**, *2*, 213−226.
(681) Zhao, Q.-L.; Zhang, Z.-L.; Huang, B.-H.; Peng, J.; Zhang, M.; Pang, D.-W. Facile preparation of low cytotoxicity fluorescent carbon nanocrystals by electrooxidation of graphite. *Chem. Commun.* **2008**, *0*, 5116−5118.
(682) Yang, S.-T.; Wang, X.; Wang, H.; Lu, F.; Luo, P. G.; Cao, L.; Meziani, M. J.; Liu, J.-H.; Liu, Y.; Chen, M.; Huang, Y.; Sun, Y.-P. Carbon Dots as Nontoxic and High-Performance Fluorescence Imaging Agents. *J. Phys. Chem. C* **2009**, *113*, 18110−18114.
(683) Dhawan, A.; Taurozzi, J. S.; Pandey, A. K.; Shan, W.; Miller, S. M.; Hashsham, S. A.; Tarabara, V. V. Stable Colloidal Dispersions of C_{60} Fullerenes in Water: Evidence for Genotoxicity. *Environ. Sci. Technol.* **2006**, *40*, 7394−7401.
(684) Wang, M.; Zhao, J.; Zhang, L.; Wei, F.; Lian, Y.; Wu, Y.; Gong, Z.; Zhang, S.; Zhou, J.; Cao, K.; Li, X.; Xiong, W.; Li, G.; Zeng, Z.; Guo, C. Role of tumor microenvironment in tumorigenesis. *J. Cancer* **2017**, *8*, 761−773.
(685) Chang, H. Y.; Chi, J.-T.; Dudoit, S.; Bondre, C.; van de Rijn, M.; Botstein, D.; Brown, P. O. Diversity, topographic differentiation, and positional memory in human fibroblasts. *Proc. Natl. Acad. Sci. U. S. A.* **2002**, *99*, 12877−12882.
(686) Qiao, L.; Xu, Z.; Zhao, T.; Zhao, Z.; Shi, M.; Zhao, R. C.; Ye, L.; Zhang, X. Suppression of tumorigenesis by human mesenchymal stem cells in a hepatoma model. *Cell Res.* **2008**, *18*, 500.
(687) Wang, Y.; Chen, X.; Cao, W.; Shi, Y. Plasticity of mesenchymal stem cells in immunomodulation: pathological and therapeutic implications. *Nat. Immunol.* **2014**, *15*, 1009.
(688) Siegel, P. M.; Massagué, J. Cytostatic and apoptotic actions of TGF-β in homeostasis and cancer. *Nat. Rev. Cancer* **2003**, *3*, 807.
(689) Cifuentes-Rius, A.; Boase, N. R. B.; Font, I.; Coronas, N.; Ramos-Perez, V.; Thurecht, K. J.; Borrós, S. *In vivo* Fate of Carbon Nanotubes with Different Physicochemical Properties for Gene Delivery Applications. *ACS Appl. Mater. Interfaces* **2017**, *9*, 11461−11471.
(690) Herrero, M. A.; Toma, F. M.; Al-Jamal, K. T.; Kostarelos, K.; Bianco, A.; Da Ros, T.; Bano, F.; Casalis, L.; Scoles, G.; Prato, M. Synthesis and Characterization of a Carbon Nanotube−Dendron Series for Efficient siRNA Delivery. *J. Am. Chem. Soc.* **2010**, *132*, 1731−1731.
(691) Tao, Y.; Ju, E.; Ren, J.; Qu, X. Immunostimulatory oligonucleotides-loaded cationic graphene oxide with photothermally enhanced immunogenicity for photothermal/immune cancer therapy. *Biomaterials* **2014**, *35*, 9963−9971.
(692) Ding, X.; Su, Y.; Wang, C.; Zhang, F.; Chen, K.; Wang, Y.; Li, M.; Wang, W. Synergistic Suppression of Tumor Angiogenesis by the Co-delivering of Vascular Endothelial Growth Factor Targeted siRNA and Candesartan Mediated by Functionalized Carbon Nanovectors. *ACS Appl. Mater. Interfaces* **2017**, *9*, 23353−23369.
(693) Su, Y.; Hu, Y.; Wang, Y.; Xu, X.; Yuan, Y.; Li, Y.; Wang, Z.; Chen, K.; Zhang, F.; Ding, X.; Li, M.; Zhou, J.; Liu, Y.; Wang, W. A precision-guided MWCNT mediated reawakening the sunk synergy in RAS for anti-angiogenesis lung cancer therapy. *Biomaterials* **2017**, *139*, 75−90.
(694) Sanz, V.; Tilmacîu, C.; Soula, B.; Flahaut, E.; Coley, H. M.; Silva, S. R. P.; McFadden, J. Chloroquine-enhanced gene delivery mediated by carbon nanotubes. *Carbon* **2011**, *49*, 5348−5358.
(695) Sanz, V.; Coley, H. M.; Silva, S. R. P.; McFadden, J. Protamine and Chloroquine Enhance Gene Delivery and Expression Mediated by RNA-Wrapped Single Walled Carbon Nanotubes. *J. Nanosci. Nanotechnol.* **2012**, *12*, 1739−1747.
(696) Zeng, Y.; Yang, Z.; Li, H.; Hao, Y.; Liu, C.; Zhu, L.; Liu, J.; Lu, B.; Li, R. Multifunctional Nanographene Oxide for Targeted Gene-Mediated Thermochemotherapy of Drug-resistant. *Tumour. Sci. Rep.* **2017**, *7*, 43506.
(697) Hassan, H. A. F. M.; Smyth, L.; Wang, J. T. W.; Costa, P. M.; Ratnasothy, K.; Diebold, S. S.; Lombardi, G.; Al-Jamal, K. T. Dual stimulation of antigen presenting cells using carbon nanotube-based vaccine delivery system for cancer immunotherapy. *Biomaterials* **2016**, *104*, 310−322.
(698) Yang, Y.; Chen, S.; Liu, L.; Li, S.; Zeng, Q.; Zhao, X.; Li, H.; Zhang, Z.; Bouchard, L.-S.; Liu, M.; Zhou, X. Increasing Cancer Therapy Efficiency through Targeting and Localized Light Activation. *ACS Appl. Mater. Interfaces* **2017**, *9*, 23400−23408.
(699) Fu, X.; Wang, X.; Zhou, S.; Zhang, Y. IONP-doped nanoparticles for highly effective NIR-controlled drug release and combination tumor therapy. *Int. J. Nanomed.* **2017**, *12*, 3751−3766.
(700) Wu, C.; He, Q.; Zhu, A.; Li, D.; Xu, M.; Yang, H.; Liu, Y. Synergistic Anticancer Activity of Photo- and Chemoresponsive Nanoformulation Based on Polylysine-Functionalized Graphene. *ACS Appl. Mater. Interfaces* **2014**, *6*, 21615−21623.
(701) Zhou, L.; Zhou, L.; Wei, S.; Ge, X.; Zhou, J.; Jiang, H.; Li, F.; Shen, J. Combination of chemotherapy and photodynamic therapy

DOI: 10.1021/acs.chemrev.9b00099
Chem. Rev. XXXX, XXX, XXX−XXX

using graphene oxide as drug delivery system. *J. Photochem. Photobiol., B* **2014**, *135*, 7−16.
(702) Jang, H.; Choi, M.-H.; Yim, Y.; Kim, Y.-K.; Min, D.-H. Dual-Wavelength Irradiation and Dox Delivery for Cancer Cell Ablation with Photocatalytic Pr Doped TiO_2/NGO Hybrid Nanocomposite. *Adv. Healthcare Mater.* **2015**, *4*, 1833−1840.
(703) Biagiotti, G.; Fedeli, S.; Tuci, G.; Luconi, L.; Giambastiani, G.; Brandi, A.; Pisaneschi, F.; Cicchi, S.; Paoli, P. Combined therapies with nanostructured carbon materials: there is room still available at the bottom. *J. Mater. Chem. B* **2018**, *6*, 2022−2035.
(704) Saleem, J.; Wang, L.; Chen, C. Carbon-Based Nanomaterials for Cancer Therapy *via* Targeting Tumor Microenvironment. *Adv. Healthcare Mater.* **2018**, *7*, 1800525.
(705) Stuelten, C. H.; Byfield, S. D.; Arany, P. R.; Karpova, T. S.; Stetler-Stevenson, W. G.; Roberts, A. B. Breast cancer cells induce stromal fibroblasts to express MMP-9 *via* secretion of TNF-α and TGF-β. *J. Cell Sci.* **2005**, *118*, 2143−2153.
(706) Wang, L.; Sun, Q.; Wang, X.; Wen, T.; Yin, J.-J.; Wang, P.; Bai, R.; Zhang, X.-Q.; Zhang, L.-H.; Lu, A.-H.; Chen, C. Using Hollow Carbon Nanospheres as a Light-Induced Free Radical Generator To Overcome Chemotherapy Resistance. *J. Am. Chem. Soc.* **2015**, *137*, 1947−1955.
(707) Kwag, D. S.; Park, K.; Oh, K. T.; Lee, E. S. Hyaluronated Fullerenes with Photoluminescent and Antitumoral Activity. *Chem. Commun.* **2013**, *49*, 282−284.

DOI: 10.1021/acs.chemrev.9b00099
Chem. Rev. XXXX, XXX, XXX−XXX